

MONOTONIC AND CYCLIC PULLOUT RESISTANCE OF GEOSYNTHETICS

by

MUTHU RAJU

B.E., Bangalore University, 1986
M.E., Indian Institute of Science, Bangalore, 1988
M.A.Sc., The University of British Columbia, 1991

**A THESIS SUBMITTED IN PARTIAL FULFILMENT OF
THE REQUIREMENTS FOR THE DEGREE OF
DOCTOR OF PHILOSOPHY**

in

THE FACULTY OF GRADUATE STUDIES

DEPARTMENT OF CIVIL ENGINEERING

We accept this thesis as conforming

to the required standard

THE UNIVERSITY OF BRITISH COLUMBIA

March 1995

© Muthu Raju, 1995

In presenting this thesis in partial fulfilment of the requirements for an advanced degree at the University of British Columbia, I agree that the Library shall make it freely available for reference and study. I further agree that permission for extensive copying of this thesis for scholarly purposes may be granted by the head of my department or by his or her representatives. It is understood that copying or publication of this thesis for financial gain shall not be allowed without my written permission.

(Signature)

Department of CIVIL ENGINEERING

The University of British Columbia
Vancouver, Canada

Date March 20, 95

ABSTRACT

An evaluation of soil-geosynthetic interface strength for different types of loading is important to the design of any anchorage detail of a reinforced soil structure or membrane-lined waste containment facility. The imposed loadings may be classified as static, repeated non-dynamic or cyclic, and dynamic. The test method best suited to model the anchorage behaviour is the pullout test.

A large scale pullout apparatus was designed that accommodates a soil sample 1.30 m long x 0.64 m wide x 0.60 m thick. Samples of a uniformly-graded medium sand were prepared by air pluviation. A stress-controlled top boundary was used and tests performed for normal stresses in the range 4 to 30 kPa. Tests were performed on five types of geosynthetics: three geogrids, a smooth geomembrane and a textured geomembrane. A sophisticated electro-hydraulic control system was developed and two modes of testing were used to evaluate pullout resistance.

The response of the geosynthetic is characterized by a non-linear variation of tensile force along the specimen. Consequently the profile of shear stress variation is non-linear and is dependent on the magnitude of pullout displacement: interpretation of the pullout test to obtain an interaction factor for design should account for this extensible behaviour. A generalized method is proposed for use with independent measurements of force and strain. The application of the generalized method is demonstrated: it describes very well the variation of interaction factor with pullout displacement and suggests a unique value that is independent of normal stress.

Cyclic loading of the test specimen in most cases reveals that an interaction factor mobilized is equal to or slightly exceeds the value mobilized in corresponding DC test. A load

ABSTRACT

(continued)

ratio is defined as the ratio of the measured pullout load in cyclic pullout test to the corresponding DC test. A conceptual model is proposed that links a load ratio to stable and unstable behaviour in cyclic pullout, and identifies a threshold ratio above which an unstable behaviour results. The threshold ratio is observed to be influenced by the specimen characteristic, being >1 for a grid specimen with a relatively rigid bearing member, and $=1$ for all other test specimens except a few tests where a value <1 was observed. This implies that using a reduced value of interaction factor for dynamic loads in all cases is inappropriate, in that it does not properly describe the mobilized response.

TABLE OF CONTENTS

ABSTRACT	ii
LIST OF TABLES	xii
LIST OF FIGURES	xiii
1. INTRODUCTION.....	1
1.1 Use of Geosynthetics.....	1
1.2 Current Design Practice.....	1
1.3 Objectives	2
1.4 Thesis Organization.....	4
2. LITERATURE REVIEW	5
2.1 Introduction	5
2.2 Soil Reinforcement using Geosynthetics	5
2.3 Fluid/Gas Containment using Geosynthetics	6
2.4 Types of Imposed Loading.....	7
2.4.1 Construction Loading.....	8
2.4.2 Static Loading.....	8
2.4.3 Repeated Non-Dynamic Loading.....	8
2.4.4 Dynamic Loading.....	9
2.5 Analytical Methods used in Design.....	9
2.5.1 Limit Equilibrium Method.....	10
2.5.2 Strain Compatibility Design Method.....	11
2.5.3 Finite Element Method.....	12
2.5.4 Seismic Design.....	13

TABLE OF CONTENTS

(continued)

2.5.4.1 A Pseudo-Static Analysis	13
2.5.4.1.1 The Displacement-Controlled Design	16
2.6 Evaluation of Soil-Geosynthetic Interaction.....	16
2.6.1 Direct Shear Tests.....	17
2.6.2 Pullout Tests.....	19
2.6.2.1 Factors Influencing Pullout Resistance	25
2.6.2.1.1 Soil Characteristics	25
2.6.2.1.2 Test Specimen Characteristics.....	26
2.6.2.1.3 Test Apparatus and Procedure	27
2.6.2.1.3.1 Normal Stress	27
2.6.2.1.3.2 Boundary Effects	28
2.6.2.1.4 Loading Characteristics.....	31
2.6.2.2 Methods for Interpretation of the Pullout Test	34
2.6.2.2.1 Monotonic Pullout Tests.....	34
2.6.2.2.2 Cyclic Pullout Tests	35
2.6.2.3 Finite Element Modelling	37
2.6.3 Model Shake Table Tests	38
2.6.4 Behaviour of Field Structures.....	39
2.6.4.1 Pullout Tests.....	39
2.6.4.2 Dynamic Tests	40
2.7 Research Needs.....	41
3. APPARATUS.....	52

TABLE OF CONTENTS

(continued)

3.1 Introduction	52
3.2 Large Pullout Apparatus.....	52
3.2.1 Pullout Box.....	52
3.2.2 Hopper	55
3.2.3 Pullout Control Assembly.....	56
3.2.3.1 Clamp	57
3.2.4 Surcharge Pressure	58
3.2.4.1 Reaction	58
3.3 Instrumentation	59
3.3.1 Pullout Force	59
3.3.2 Pullout Displacement	59
3.3.3 Pressure on the Front Wall.....	60
3.3.4 Water Pressure Transducer	60
3.3.5 Strain Gauges	61
3.4 Data Acquisition System	61
4. MATERIAL PROPERTIES.....	71
4.1 Introduction.....	71
4.2 Sand.....	71
4.2.1 Angle of Friction.....	72
4.2.1.1 Direct Shear Tests.....	72
4.3 Geosynthetic Test Specimens	73
4.3.1 Geogrids.....	74

TABLE OF CONTENTS

(continued)

4.3.1.1 Tensar UX-1500	74
4.3.1.2 Miragrid 15T	74
4.3.1.3 Stratagrid 700	75
4.3.2 Geomembranes	76
4.4 Aluminum Sheet Test Specimen	76
4.5 Direct Shear Tests on the Sand and Test Specimens	77
5. TEST PROCEDURE	83
5.1 Introduction and Test Program.....	83
5.2 Test Preparation.....	84
5.2.1 Preparation of the Test Apparatus	84
5.2.2 Preparation of the Test Specimen.....	85
5.2.3 Placement of the Sand Sample and the Test Specimen.....	85
5.2.4 Application of Surcharge Load.....	86
5.2.5 Clamping of the Test Specimen	87
5.3 Test Procedure.....	87
5.4 Post Test Procedure	88
6. TEST RESULTS	91
6.1 Introduction	91
6.2 Displacement-Controlled Pullout Tests.....	91
6.2.1 Influence of Front Boundary	92
6.2.2 Influence of Rate of Displacement.....	94
6.2.3 Aluminum Test Specimen.....	94

TABLE OF CONTENTS

(continued)

6.2.3.1 Rough Aluminum Sheet	95
6.2.4 Geosynthetic Test Specimens	95
6.2.4.1 Geogrid	97
6.2.4.1.1 Pullout Resistance.....	97
6.2.4.1.2 Rib Strain	99
6.2.4.2 Geomembranes	101
6.2.4.2.1 Pullout Resistance.....	102
6.2.4.2.2 Local Strain	102
6.3 Load-Controlled Tests.....	103
6.3.1 Aluminum Test Specimen.....	104
6.3.1.1 Pullout Resistance.....	104
6.3.1.1.1 Displacement of the Embedded End	105
6.3.2 Geosynthetic Test Specimens	105
6.3.2.1 Geogrids.....	106
6.3.2.1.1 Pullout Resistance.....	106
6.3.2.1.2 Influence of Loading Frequency	107
6.3.2.1.3 Rib Strain	107
6.3.2.1.4 Displacement of the Embedded End	109
6.3.2.2 Geomembranes	109
6.3.2.2.1 Pullout Resistance.....	109
6.3.2.2.2 Local Strain	111
6.3.2.2.3 Displacement of the Embedded End	111

TABLE OF CONTENTS

(continued)

7. ANALYSIS OF THE TEST RESULTS	138
7.1 Introduction	138
7.2 Displacement-Controlled Pullout Tests	138
7.2.1 Influence of the Front Boundary	139
7.2.2 Mobilization of Pullout Resistance	141
7.2.3 Experimental Interaction Factors	144
7.2.3.1 Average Resistance Method	144
7.2.3.1.1 Total Area	145
7.2.3.1.2 Effective Area	146
7.2.3.1.3 Maximum Slope	147
7.2.3.1.4 Mobilising Process Method	147
7.2.3.2 Generalized Method	148
7.2.3.3 Application of the Generalized Method	152
7.2.3.3.1 Displacement of the Embedded End	153
7.2.3.3.2 Tensile Force	153
7.2.3.3.3 Shear Stress	155
7.2.3.3.4 Interaction Factors	157
7.2.3.3.4.1 Peak and Limiting Interaction Factors	159
7.2.4 Comparison of Interaction Factors With and Without Bearing Elements	161
7.2.5 Comparison of Theoretical and Experimental Interaction Factors	162
7.2.6 Comparison of Geogrid Interaction Factors with Other Laboratory and Field Data	164

TABLE OF CONTENTS

(continued)

7.3 Load-Controlled Pullout Tests.....	169
7.3.1 Incremental Displacement Response.....	170
7.3.2 Strain Response	172
7.3.3 Interaction Factors for Cyclic Loading	174
7.4 Comparison of Interaction Factors from DC and LC Tests	175
8. SUMMARY AND CONCLUSIONS	228
8.1 Summary.....	228
8.2 On the Pullout Test	229
8.2.1 Apparatus and Instrumentation.....	229
8.2.2 Materials and Test Procedure.....	230
8.2.3 Test Results and Interpretation.....	231
8.3 Implications for Selection of a Pullout Interaction Factor in Design	233
8.4 Recommendations for Future Studies	234
BIBLIOGRAPHY	236
A. TECHNIQUE OF STRAIN GAUGING PLASTICS.....	246
A.1 Introduction	246
A.2 Characteristics of the Strain Gauge	247
A.3 Strain Gauging Procedure.....	247
A.3.1 Chemicals for Surface Preparation.....	247
A.3.2 Adhesive Selection and Preparation.....	248
A.3.3 Geosynthetic Surface Preparation	248
A.3.4 Gauge Preparation.....	249

TABLE OF CONTENTS
(continued)

A.3.5 Application of the Gauge.....	250
A.3.6 Gauge Soldering.....	251
A.3.7 Gauge Protection	252
A.3.8 Analysis of Strain Data.....	253
B. RAW DATA OF PULLOUT RESISTANCE AND STRAIN	254

LIST OF TABLES

Table 2.1: Summary of the pullout test apparatus and testing characteristics	29
Table 4.1: Properties of the geogrid test specimens.....	75
Table 4.2: Properties of the geomembrane test specimens.....	76
Table 6.1: Summary of displacement-controlled tests on the geogrids.....	93
Table 6.2: Summary of displacement-controlled tests on the geomembrane and aluminum sheets.....	94
Table 6.3: Summary of the load-controlled pullout tests	104
Table 7.1: Geometric and interface friction characteristics of the test specimens.....	163
Table 7.2: Theoretical interaction factor for the grid specimens, USFHWA guidance.	163
Table 7.3: Stress ratio σ_v/σ_h from pullout tests on the geogrid	165
Table 7.4: Typical properties of the geogrid specimens.....	166
Table 7.5: Properties of soil used in the laboratory studies and field structure	166

LIST OF FIGURES

Figure 2.1: Typical examples of soil reinforcement applications (after Palmeira, 1987).	43
Figure 2.2: Failure mechanisms of reinforced soil structures (after Palmeira, 1987).....	43
Figure 2.3: Section showing the components of a liner system (after Udvari and Kittridge, 1986).....	44
Figure 2.4: Schematic illustration of potential failure modes in a containment facility (after Mitchell and Mitchell, 1992)	45
Figure 2.5: Forces acting on a reinforced soil wall (after Christopher et al., 1990).....	46
Figure 2.6: Schematic illustration of the multilayer liner system used in the Kettleman Hills landfill (after Seed et al., 1990).....	46
Figure 2.7: Mechanisms of load transfer (after Jewell et al., 1984).....	47
Figure 2.8: Bearing stresses on a grid reinforcement (after Jewell et al., 1984).....	48
Figure 2.9: Comparison of test results with predicted values of stress ratio (after Jewell, 1990)	49
Figure 2.10: Relationship between efficiency factor and confining stress for various geogrids (after Juran et al., 1988)	50
Figure 2.11: Effect of front wall roughness on pullout test results (after Palmeira and Milligan, 1989).....	51
Figure 2.12: A schematic of various interpretation methods for the pullout test.....	51
Figure 3.1: Components of the pullout apparatus.....	63
Figure 3.2: Photograph illustrating components of the pullout apparatus.....	64
Figure 3.3: Slot arrangement on the front wall of the apparatus	65
Figure 3.4: Top and side view of the hopper assembly	66

LIST OF FIGURES

(continued)

Figure 3.5: Principle components of closed-loop control.....	67
Figure 3.6: Schematic illustration of the closed-loop control system.....	67
Figure 3.7: Details of the clamp.....	68
Figure 3.8: Reaction frame and the pressurizing system	69
Figure 3.9: Location of pressure transducers on the front wall of the pullout box.....	70
Figure 3.10: Strain gauge locations with respect to the front wall of the apparatus.....	70
Figure 4.1: Grain size distribution curve of the sand before and after testing	78
Figure 4.2: Normalized shear stress relationship with shear displacement for direct shear tests on the sand.....	78
Figure 4.3: Relationship between normal displacement and shear displacement for the sand	79
Figure 4.4: Plane strain friction angle for the sand.....	79
Figure 4.5: Variation of constant volume plane strain friction angle with normal stress.	80
Figure 4.6: Measured dimensions of Tensar UX-1500	80
Figure 4.7: Instrumented Tensar UX-1500 test specimen with strain gauges	81
Figure 4.8: Photograph and measured dimensions of Miragrid 15T	81
Figure 4.9: Photograph and measured dimensions of Stratagrid 700.....	82
Figure 4.10: Shear stress and normal stress relationship of various interfaces from direct shear tests.....	82
Figure 5.1: Demand signal in the displacement-controlled mode	90
Figure 5.2: Demand signal in the load-controlled mode.....	90
Figure 6.1: Reference code for tests on the geogrids.....	112

LIST OF FIGURES

(continued)

Figure 6.2: Reference code for tests on the geomembranes and aluminum sheets	112
Figure 6.3: Pullout resistance of the Tensar grid with an aluminum or arborite surface on the front wall.....	113
Figure 6.4: Pullout resistance of the smooth and textured geomembranes with an aluminum or arborite surface on the front wall.....	113
Figure 6.5: Influence of displacement rate on mobilized pullout resistance for the Tensar grid.....	114
Figure 6.6: Relationship between d_c and d_e for the aluminum rough sheet.....	114
Figure 6.7: Pullout resistance of the aluminum rough sheet at $\sigma_n=4$ to 12 kPa.....	115
Figure 6.8: Relationship between d_c and d_e for the Tensar grid at $\sigma_n=4$ to 30 kPa.....	115
Figure 6.9: Relationship between d_c and d_e for the Stratagrid at $\sigma_n=4$ to 17 kPa	116
Figure 6.10: Relationship between d_c and d_e for the Miragrid at $\sigma_n=10$ and 17 kPa.....	116
Figure 6.11: Relationship between d_c and d_e for the smooth and textured geomembrane at $\sigma_n=4$ to 12 kPa.....	117
Figure 6.12: Pullout resistance of the Tensar grid at $\sigma_n=4$ to 30 kPa	117
Figure 6.13: Pullout resistance of the Miragrid at $\sigma_n=4$ to 17 kPa	118
Figure 6.14: A photograph illustrating the displacement pattern of transverse elements for the Miragrid.....	118
Figure 6.15: Pullout resistance of the Miragrid when tested in the cross-machine direction at $\sigma_n=4$ to 17 kPa.....	119
Figure 6.16: Pullout resistance of the Stratagrid at $\sigma_n=4$ to 17 kPa	119

LIST OF FIGURES

(continued)

Figure 6.17: Mobilization of strain with d_c for the Tensar grid at $\sigma_n=10$ kPa	120
Figure 6.18: Mobilization of strain with d_c for the Stratagrid at $\sigma_n=10$ kPa.....	120
Figure 6.19: Mobilization of strain with d_c for the Miragrid at $\sigma_n=10$ kPa.....	121
Figure 6.20: Mobilization of strain with d_c for the Miragrid at $\sigma_n=17$ kPa.....	121
Figure 6.21: Characteristic variation of strain with displacement d_c	122
Figure 6.22: Variation of strain with rate of pullout for the Tensar grid at $\sigma_n=20$ kPa.	122
Figure 6.23: Pullout resistance of the smooth geomembrane at $\sigma_n=4$ to 12 kPa.....	123
Figure 6.24: Pullout resistance of the textured geomembrane at $\sigma_n=4$ to 12 kPa.....	123
Figure 6.25: Mobilization of strain with d_c for the smooth geomembrane at $\sigma_n=4$ kPa	124
Figure 6.26: Mobilization of strain with d_c for the smooth geomembrane at $\sigma_n=8$ kPa	124
Figure 6.27: Mobilization of strain with d_c for the smooth geomembrane at $\sigma_n=12$ kPa	125
Figure 6.28: Pullout resistance of the rough aluminum sheet at $\sigma_n=8$ kPa and $f=0.01$ Hz.....	125
Figure 6.29: Detailed response at small displacement, from Figure 6.28	126
Figure 6.30: Relationship between d_c and d_c for the rough aluminum sheet in the LC tests at $\sigma_n=8$ kPa and $f=0.01$ Hz.	126
Figure 6.31: Pullout resistance of the Tensar grid in the DC and LC tests at $\sigma_n=4$ to 17 kPa and $f=0.01$ Hz	127

LIST OF FIGURES

(continued)

Figure 6.32: Pullout resistance of the Miragrid in the DC and LC tests at $\sigma_n=4$ to 17 kPa and $f=0.01$ Hz	127
Figure 6.33: Pullout resistance of the Stratagrid in the DC and LC tests at $\sigma_n=4$ to 17 kPa and $f=0.01$ Hz	128
Figure 6.34: Pullout resistance of the Stratagrid in the DC and LC tests at $\sigma_n=17$ kPa and $f=0.01$ Hz	128
Figure 6.35: Pullout resistance of the Tensar grid in the DC and LC tests at $\sigma_n=10$ kPa and $f=0.1$ Hz	129
Figure 6.36: Mobilization of strain for the Tensar grid in the LC tests at $\sigma_n=10$ kPa and $f=0.01$ Hz	129
Figure 6.37: Mobilization of strain for the Miragrid in the LC test at $\sigma_n=10$ kPa and $f=0.01$ Hz	130
Figure 6.38: Mobilization of strain for the Stratagrid in the LC tests at $\sigma_n=10$ kPa and $f=0.01$ Hz	130
Figure 6.39: Mobilization of strain for the Tensar grid in the LC tests at $\sigma_n=17$ kPa and $f=0.01$ Hz	131
Figure 6.40: Mobilization of strain for the Miragrid in the LC tests at $\sigma_n=17$ kPa and $f=0.01$ Hz	131
Figure 6.41: Mobilization of strain for the Stratagrid in the LC tests at $\sigma_n=17$ kPa and $f=0.01$ Hz	132

LIST OF FIGURES

(continued)

Figure 6.42: Relationship between d_c and d_e for the Tensar grid in the LC tests at $\sigma_n =$ 4, 10 and 17 kPa	132
Figure 6.43: Relationship between d_c and d_e for the Miragrid in the LC tests at $\sigma_n = 4$ kPa and 10 kPa	133
Figure 6.44: Relationship between d_c and d_e for the Stratagrid in the LC tests at $\sigma_n = 4,$ 10 and 17 kPa	133
Figure 6.45: Pullout resistance of the smooth geomembrane in the DC and LC tests ..	134
Figure 6.46: Pullout resistance of the textured geomembrane in the DC and LC test at $\sigma_n=8$ kPa and $f=0.01$ Hz.....	134
Figure 6.47: Pullout resistance of the textured geomembrane in the DC and LC tests at $\sigma_n=8$ kPa and $f=0.1$ Hz.....	135
Figure 6.48: Mobilization of strain for the smooth geomembrane in the LC test at $\sigma_n=8$ kPa.....	135
Figure 6.49: Mobilization of strain d_c for the smooth geomembrane in the LC test at $\sigma_n=12$ kPa.....	136
Figure 6.50: Relationship between d_c and d_e for the smooth geomembrane in the LC tests at $\sigma_n=8$ and 12 kPa.....	136
Figure 6.51: Relationship between d_c and d_e for the textured geomembrane in the LC tests at $\sigma_n=8$ and 12 kPa.....	137
Figure 7.1: Measured lateral stress and applied normal stresses at TPT-1 and TPT-6 locations.....	178

LIST OF FIGURES

(continued)

Figure 7.2: Measured lateral stress and pullout resistance for the Stratagrid at $\sigma_n=10$ kPa	178
Figure 7.3: Incremental lateral stress on the front wall for the smooth geomembrane and Tensar grid at similar normal stress.	179
Figure 7.4: Variation of normalised lateral stress ratio with depth ratio for the smooth geomembrane and Tensar grid at similar normal stress.....	179
Figure 7.5: Variation of normalised lateral stress ratio with depth ratio for the Tensar grid at $\sigma_n=4$ to 30 kPa.....	180
Figure 7.6: Variation of normalised lateral stress ratio with depth ratio for the Stratagrid at $\sigma_n=4$ to 17 kPa.....	180
Figure 7.7: Variation of normalised lateral stress ratio with depth ratio for the Miragrid tested in the machine direction at $\sigma_n=4$ to 17 kPa.....	181
Figure 7.8: Variation of normalised lateral stress ratio with depth ratio for the Miragrid tested in the cross-machine direction at $\sigma_n=4$ to 17 kPa	181
Figure 7.9: Variation of normalised lateral stress ratio with depth ratio for the smooth geomembrane at $\sigma_n=4$ to 12 kPa.....	182
Figure 7.10: Variation of normalised lateral stress ratio with depth ratio for the textured geomembrane at $\sigma_n=4$ to 12 kPa.....	182
Figure 7.11: Relationship between d_c and d_e for the Tensar grid in the DC test at.....	183
Figure 7.12: Strain profile for the Tensar grid in the DC test at $\sigma_n=10$ kPa.....	183

LIST OF FIGURES (continued)

Figure 7.13: Relationship between d_c and d_e for the Tensar grid in the DC test at $\sigma_n=30$ kPa	184
Figure 7.14: Strain profile for the Tensar grid in the DC test at $\sigma_n=30$ kPa.....	184
Figure 7.15: Strain profile for the Tensar grid in the DC test at $\sigma_n=20$ kPa and $r_d=0.50$ mm/min.....	185
Figure 7.16: Relationship between d_c and d_e for the Stratagrid in the DC test at $\sigma_n=10$ kPa	185
Figure 7.17: Strain profile for the Stratagrid in the DC test at $\sigma_n=10$ kPa.....	186
Figure 7.18: Strain profile for the Stratagrid in the DC test at $\sigma_n=17$ kPa.....	186
Figure 7.19: Relationship between d_c and d_e for the Miragrid in the DC test at $\sigma_n=17$ kPa	187
Figure 7.20: Strain profile for the Miragrid in the DC test at $\sigma_n=17$ kPa.....	187
Figure 7.21: Relationship between d_c and d_e for the smooth geomembrane in the DC test at $\sigma_n=8$ kPa.....	188
Figure 7.22: Strain profile for the smooth geomembrane in the DC test at $\sigma_n=8$ kPa ..	188
Figure 7.23: A schematic illustration of the interpretation of data by various resisting area methods (modified after Ochiai et al., 1992).....	189
Figure 7.24: Schematic illustration of nodes and elements for a) smooth geomembrane, b) Tensar grid and c) Stratagrid and Miragrid	190
Figure 7.25: Flow chart of the generalized method for interpretation of a pullout test	191

LIST OF FIGURES

(continued)

Figure 7.26: Comparison of measured and calculated displacements of the embedded end of the Tensar grid in the DC test at $\sigma_n=10$ kPa 192

Figure 7.27: Relationship between strain and tensile force per unit width for the Tensar grid 192

Figure 7.28: Relationship between tensile force at the clamped end and the measured strain at location SG-2 ($x/L_{ei}=0.106$) for the Stratagrid..... 193

Figure 7.29: Relationship between tensile force at the clamped end and the measured strain at location SG-1 ($x/L_{ei}=0.043$) for the Miragrid..... 193

Figure 7.30: Relationship between tensile force at the clamped end and the measured strain at location SG-1 ($x/L_{ei}=0.074$) for the smooth geomembrane in the DC tests 194

Figure 7.31: Profile of deduced tensile force/width and the generated polynomial fit for the Tensar grid at $\sigma_n=10$ kPa 194

Figure 7.32: Profile of deduced tensile force/width and the generated polynomial fit for the Tensar grid at $\sigma_n=20$ kPa and $r_d=0.5$ mm/min..... 195

Figure 7.33: Profile of deduced tensile force/width and the generated polynomial fit for Tensar grid at $\sigma_n=30$ kPa..... 195

Figure 7.34: Shear stress variation along the embedded length of the Tensar grid at $\sigma_n=10$ kPa 196

Figure 7.35: Shear stress variation along the embedded length of the Tensar grid at $\sigma_n=20$ kPa 196

LIST OF FIGURES (continued)

Figure 7.36: Shear stress variation along the embedded length of the Tensar grid at $\sigma_n=30$ kPa.....	197
Figure 7.37: Shear stress variation along the embedded length of the Stratagrid at $\sigma_n=10$ kPa.....	197
Figure 7.38: Shear stress variation along the embedded length of the Miragrid at $\sigma_n=17$ kPa	198
Figure 7.39: Shear stress variation along the embedded length of the smooth geomembrane at $\sigma_n=8$ kPa.....	198
Figure 7.40: Interaction factors for the Tensar grid: corrected total area method and generalized method	199
Figure 7.41: Interaction factors for the Tensar grid: generalized method.....	199
Figure 7.42: Interaction factor for the Stratagrid and Miragrid: corrected total area method and generalized method.....	200
Figure 7.43: Interaction factor for smooth geomembrane using the corrected area and generalized method	200
Figure 7.44: Relationship between average shear stress and normal stress for the grids and rough aluminum sheet.....	201
Figure 7.45: Influence of grid orientation on pullout behaviour of the Miragrid.....	201
Figure 7.46: Relationship between average shear stress and normal stress for the geomembranes and rough alumimun sheet	202

LIST OF FIGURES

(continued)

Figure 7.47: Relationship between average shear stress and normal stress for the Tensar grid and Miragrid with and without bearing elements.....	202
Figure 7.48: Details of the geogrid specimen (after Fannin et al. , 1994)	203
Figure 7.49: Comparison of Tensar grid interaction factors from laboratory pullout tests	203
Figure 7.50: Comparison of interaction factors from Figure 7.39 for small displacement	204
Figure 7.51: Comparison of interaction factor for Conwed G9027/Stratagrid 700.....	204
Figure 7.52: Strain profile deduced from the reported nodal displacements of Conwed grid at $\sigma_n=48.2$ kPa from Farrag et al. (1993).....	205
Figure 7.53: Reinforcement in the field structure (after Fannin et al., 1994)	205
Figure 7.54: A schematic diagram showing strain gauge locations (after Fannin, 1990).....	206
Figure 7.55: Strain in layer No. 7 of the field structure (after Fannin and Hermann, 1990)	206
Figure 7.56: Relationship between Δd_c and Δd_e for the Tensar grid at $\sigma_n=10$ kPa and $f=0.01$ Hz.....	207
Figure 7.57: Relationship between Δd_c and Δd_e for the Tensar grid at $\sigma_n=10$ kPa and $f=0.1$ Hz.....	208
Figure 7.58: Relationship between Δd_c and Δd_e for the Stratagrid at $\sigma_n=10$ kPa and $f=0.01$ Hz.....	209

LIST OF FIGURES (continued)

Figure 7.59: Relationship between Δd_c and Δd_e for the Miragrid at $\sigma_n=17$ kPa and $f=0.01$ Hz.....	210
Figure 7.60: Relationship between Δd_c and Δd_e for the smooth geomembrane at $\sigma_n=8$ kPa and $f=0.01$ Hz.....	211
Figure 7.61: Relationship between Δd_c and Δd_e for the textured geomembrane at $\sigma_n=8$ kPa and $f=0.01$ Hz.....	212
Figure 7.62: A conceptual model for the modes of behaviour observed in cyclic pullout testing.....	213
Figure 7.63: Mobilization of rib strain with number of cycles and increasing load ratio for the Tensar grid at $\sigma_n=10$ kPa and $f=0.01$ Hz.....	214
Figure 7.64: Strain profile with loading ratio at the end of the loading series for the Tensar grid at $\sigma_n=10$ kPa and $f=0.01$ Hz.....	214
Figure 7.65: Mobilization of rib strain with number of cycles and increasing load ratio for the Tensar grid at $\sigma_n=17$ kPa and $f=0.01$ Hz.....	215
Figure 7.66: Strain profile with loading ratio at the end of the loading series for the Tensar grid at $\sigma_n=17$ kPa and $f=0.01$ Hz.....	215
Figure 7.67: Mobilization of rib strain with number of cycles and increasing load ratio for the Miragrid at $\sigma_n=10$ kPa and $f=0.01$ Hz.....	216
Figure 7.68: Strain profile with loading ratio at the end of the loading series for the Miragrid at $\sigma_n=10$ kPa and $f=0.01$ Hz.....	216

LIST OF FIGURES

(continued)

Figure 7.69: Mobilization of rib strain with number of cycles and increasing load ratio for the Miragrid at $\sigma_n=17$ kPa and $f=0.01$ Hz.....	217
Figure 7.70: Strain profile with loading ratio at the end of the loading series for the Miragrid at $\sigma_n=17$ kPa and $f=0.01$ Hz.....	217
Figure 7.71: Mobilization of rib strain with number of cycles and increasing load ratio for the Stratagrid at $\sigma_n=10$ kPa and $f=0.01$ Hz.....	218
Figure 7.72: Strain profile with loading ratio at the end of the loading series for the Stratagrid at $\sigma_n=10$ kPa and $f=0.01$ Hz.....	218
Figure 7.73: Mobilization of rib strain with number of cycles and increasing load ratio for the Stratagrid at $\sigma_n=17$ kPa and $f=0.01$ Hz.....	219
Figure 7.74: Strain profile with loading ratio at the end of the loading series for the Stratagrid at $\sigma_n=17$ kPa and $f=0.01$ Hz.....	219
Figure 7.75: Cyclic pullout interaction factor from the generalized and corrected total area methods for the Tensar grid at $\sigma_n=10$ kPa and $f=0.01$ Hz	220
Figure 7.76: Comparison of interaction factors in the LC and DC tests for the Tensar grid at $\sigma_n=4$ kPa and $f=0.01$ Hz.....	220
Figure 7.77: Comparison of interaction factors in LC and DC tests for the Tensar grid at $\sigma_n=10$ kPa and $f=0.01$ Hz	221
Figure 7.78: Comparison of interaction factors in the LC and DC tests for the Tensar grid at $\sigma_n=10$ kPa and $f=0.1$ Hz.....	221

LIST OF FIGURES (continued)

Figure 7.79: Comparison of interaction factors in the LC and DC tests for the Tensar grid at $\sigma_n=17$ kPa and $f=0.01$ Hz.....	222
Figure 7.80: Comparison of interaction factors in the LC and DC tests for the Miragrid at $\sigma_n=4$ kPa and $f=0.01$ Hz.....	222
Figure 7.81: Comparison of interaction factors in the LC and DC tests for the Miragrid at $\sigma_n=10$ kPa and $f=0.01$ Hz.....	223
Figure 7.82: Comparison of interaction factors in the LC and DC tests for the Miragrid at $\sigma_n=17$ kPa and $f=0.01$ Hz.....	223
Figure 7.83: Comparison of interaction factors in the LC and DC tests for the Stratagrid at $\sigma_n=4$ kPa and $f=0.01$ Hz.....	224
Figure 7.84: Comparison of interaction factors in the LC and DC tests for the Stratagrid at $\sigma_n=10$ kPa and $f=0.01$ Hz.....	224
Figure 7.85: Comparison of interaction factors in the LC and DC tests for the Stratagrid at $\sigma_n=17$ kPa and $f=0.01$ Hz.....	225
Figure 7.86: Comparison of interaction factors in the LC and DC tests for the smooth geomembrane at $\sigma_n=8$ kPa and $f=0.01$ Hz.....	226
Figure 7.87: Comparison of interaction factors in the LC and DC tests for the smooth geomembrane at $\sigma_n=12$ kPa and $f=0.01$ Hz.....	226
Figure 7.88: Comparison of interaction factors in the LC and DC tests for the textured geomembrane at $\sigma_n=8$ kPa and $f=0.01$ Hz.....	227

LIST OF FIGURES

(continued)

Figure 7.89: Comparison of interaction factors in the LC and DC tests for the textured geomembrane at $\sigma_n=8$ kPa and $f=0.1$ Hz.....	228
Figure 7.90: Comparison of interaction factors in the LC and DC tests for the textured geomembrane at $\sigma_n=12$ kPa and $f=0.01$ Hz.....	228
Figure B.1: Mobilization of pullout resistance and strain with pullout displacement for the Tensar grid at $\sigma_n=4$ kPa.....	254
Figure B.2: Mobilization of pullout resistance and strain with pullout displacement for the Tensar grid at $\sigma_n=10$ kPa.....	254
Figure B.3: Mobilization of pullout resistance and strain with pullout displacement for the Tensar grid at $\sigma_n=10$ kPa: smooth arborite front boundary.....	255
Figure B.4: Mobilization of pullout resistance and strain with pullout displacement for the Tensar grid without bearing elements at $\sigma_n=4$ kPa.....	255
Figure B.5: Mobilization of pullout resistance and strain with pullout displacement for the Tensar grid without bearing elements at $\sigma_n=10$ kPa.....	256
Figure B.6: Mobilization of pullout resistance and strain with pullout displacement for the Tensar grid without bearing elements at $\sigma_n=17$ kPa.....	256
Figure B.7: Mobilization of pullout resistance and strain with pullout displacement for the Tensar grid without bearing elements at $\sigma_n=20$ kPa and $r_d=0.25$ mm/min.....	257

LIST OF FIGURES (continued)

Figure B.8: Mobilization of pullout resistance and strain with pullout displacement for the Tensar grid without bearing elements at $\sigma_n=20$ kPa and $r_d=0.50$ mm/min.....	257
Figure B.9: Mobilization of pullout resistance and strain with pullout displacement for the Tensar grid without bearing elements at $\sigma_n=20$ kPa and $r_d=1.00$ mm/min.....	258
Figure B.10: Mobilization of pullout resistance and strain with pullout displacement for the Stratagrid without bearing elements at $\sigma_n=17$ kPa.....	258
Figure B.11: Relationship between Δd_c and Δd_e for Tensar grid at $\sigma_n=4$ and 17 kPa...	259
Figure B.12: Relationship between Δd_c and Δd_e for Stratagrid at $\sigma_n=4$ and 17 kPa.....	260

LIST OF SYMBOLS

a	Factor
a_m	Maximum wall acceleration at the centroid of the active mass
a_o	Reference acceleration
B	Thickness of the bearing member
c	Cohesion
C	Effective unit perimeter, for sheets and grids it is 2
C_c	Coefficient of curvature
C_u	Coefficient of uniformity
CRD	Constant rate of displacement
CRL	Constant rate of loading
d_{ai}	average displacement of <i>i</i> th element
d_c	Clamped end displacement of the test specimen
d_e	Embedded end displacement of the test specimen
d_i	Displacement of the <i>i</i> th node
d₁₀	Particle size at 10 percent finer
d₅₀	Particle size at 50 percent finer or mean particle size
D	Depth of the pullout test apparatus
DC	Displacement-controlled testing mode
DI	Degree of interference
e_{max}	Maximum void ratio
e_{min}	Minimum void ratio

LIST OF SYMBOLS

(continued)

f	Frequency of cyclic loading
f_b	Generalized bond coefficient
F*	Pullout resistance (friction-bearing-interaction) factor
F	Non-dimensional stress factor
g	Gravitational acceleration (9.81 m/s ²)
H	Height of the retaining wall
h	Half thickness of soil sample
K	Ratio of the actual normal stress to the applied effective normal stress
K_o	Coefficient of lateral earth pressure at rest
K	Material constant
L	Length of the reinforcement in the retaining wall
L_e	Embedment or adherence length in the resisting zone behind the failure surface
L_{ea}	Actual embedment length of the test specimen
L_{ei}	Initial embedment length of the test specimen
L_r	Length of the test specimen
L_x	Length of the specimen between front wall of the apparatus and the section x
LC	Load-controlled testing mode
LR	Load ratio
LVDT	Linear variable differential transformer
N	Number of cycles
n	Number of bearing members
p_c	Corrected pullout resistance of the test specimen

LIST OF SYMBOLS (continued)

P_m	Maximum pullout resistance of the test specimen in CRD
P_{AE}	Horizontal dynamic thrust
P_b	Maximum pullout force for a grid with n bearing members
P_o	Maximum pullout force for an isolated bearing member
P_I	Horizontal inertia force acting at the centroid of the reinforced soil mass
P_{IA}	Inertia force
$P_{r,max}$	Pullout force measured at the clamped end of the specimen
$P_{r,x}$	Pullout force measured or estimated at a point x on the specimen
P_s	Skin friction component of the pullout resistance
r_d	Rate of displacement
r_l	Rate of loading
S	Spacing between bearing members
t_1, t_2, t_3	Real time
T	Tensile force
T_{max}	Pullout force measured at the clamped end of the specimen
T_x	Pullout force measured or estimated at the section x of the test specimen
TPT	Total pressure transducer
VRL	Variable rate of loading
W	Width of the test specimen
x	Distance of a point on the test specimen from the front wall of the apparatus
y	Distance of a point on the front wall from the middle of the slot
α	Scale effect correction factor

LIST OF SYMBOLS

(continued)

α_b	Fraction of the bearing area available for bearing
α_r, α_s	Fraction of the plan area of the test specimen that is solid
α_β	Structural geometric factor for bearing resistance
γ_r	Unit weight of the reinforced mass
γ_b	Unit weight of the retained soil
δ	Friction angle between soil and specimen surface
δ_{av}	Average interface friction angle mobilized along the test specimen
δ_{peak}	Peak interface friction angle mobilized along the test specimen
ϵ_{li}	Local strain in the element i
ϵ_{gl}	Global strain in the element i
ϵ_r	Rib strain
ϕ	Angle of internal friction
ϕ_{cv}	Constant volume friction angle
ϕ_{ds}	Direct shear friction angle
ϕ_{ps}	Plane strain friction angle
ϕ_{lps}	Large displacement plane strain friction angle
ϕ_{pps}	Peak plane strain friction angle
μ^*	Apparent friction coefficient
η_l	Normalised distance of the strain gauge from the front wall of the apparatus
σ'_n	Effective normal stress at the soil-test specimen interface

LIST OF SYMBOLS (continued)

σ'_b	Bearing stress acting on the embedded anchor
σ	Normal stress
τ	Shear stress
τ_{av}	Average interface shear stress mobilized along the test specimen
τ_{peak}	Peak interface shear stress mobilized along the test specimen
Δd_c	Incremental displacement of the clamped end
Δd_e	Incremental displacement of the embedded end
$\Delta p_m, \Delta p_{m1}, \Delta p_{m2}$	Amplitude of cyclic loading
$\Delta \sigma_h$	Incremental lateral (horizontal) stress

ACKNOWLEDGEMENTS

I am deeply indebted to my thesis supervisor Dr. Jonathan Fannin for his unfailing support, advice and engineering judgement throughout the study. Without his advice and understanding this research project would not have been possible.

I would like to express my sincere gratitude to Mr. Art Brookes, a technician in the civil engineering workshop, for his help in the fabrication of the large pullout test apparatus. I would also like to thank Mr. Harold Schemp for his assistance in modifying some parts of the apparatus, and Mr. Dick Postgate, chief technician in the civil engineering workshop, for his helpful suggestions. I wish to thank Mr. John Wong and Ron Dolling, electronic technicians for their help in the commissioning of the servo-hydraulic control system and the data acquisition testing system, often at short notice.

This research is funded by a Research Grant from the Natural Sciences and Engineering Research Council of Canada. I wish to express my thanks for the financial support provided. Thanks are also due to Nilex Geotechnical Products Inc., Armtec Construction Products, Gundle Lining Systems Inc., and Mirafi Inc., for providing materials used in the testing program.

Finally, I wish to express my sincere gratitude to my wife Suneetha for her constant support, patience and understanding throughout the thesis work.

CHAPTER 1

INTRODUCTION

1.1 Use of Geosynthetics

Polymeric materials such as geotextiles, geogrids and geomembranes that are used in geotechnical engineering applications are collectively termed “geosynthetics”. Five primary functions of geosynthetics are recognized (C.G.S., 1992): separation, filtration, drainage, reinforcement and fluid/gas containment. The last decade has seen a tremendous growth in the use of geosynthetics in engineering practice, and given recognition to these materials as an alternative to conventional solutions in design. Various factors, such as cost savings, ease of construction and quality control have made the use of geosynthetics attractive in foundation engineering. The increasing use has been supported by advances in analytical methods, and may be attributed to:

- research to evaluate design methodologies and fundamental behaviour;
- Standard Test methods that facilitate material specifications;
- regulatory guidance for construction practice.

Design using geosynthetics requires that consideration be given to appropriate analytical methods, material properties, material tests, interpretation of the manufacturer’s technical literature, and soil-geosynthetic interaction. The latter consideration of soil-geosynthetic interaction is the subject of this research study.

1.2 Current Design Practice

In the design of reinforced soil structures and membrane-lined containment facilities, an internal stability analysis includes examination of:

Chapter 1. Introduction

- a tensile failure of the geosynthetic;
- a tensile failure of any connections;
- a pullout failure of the geosynthetic.

Pullout failure of the geosynthetic is governed by the limiting soil-geosynthetic interface shear strength. A proper understanding of the development of interface resistance under different loading conditions is essential for computing the required embedment length of a geotextile or a geogrid in a reinforced soil structure, and of a geomembrane in the anchorage trench of a waste containment facility. Several parameters influence the mobilization of soil-geosynthetic interaction. In laboratory studies using a pullout apparatus, these parameters relate to the soil type, the type of geosynthetic, configuration of the test apparatus, nature of the loading characteristics, and the testing procedure. Although many test methods have been standardized for determining the material properties of geosynthetics, at the time of writing no standard test method has been approved for the pullout test.

Notwithstanding some significant research contributions on the subject of soil/geosynthetic interaction in pullout, there is a need for quality test data on behaviour in pullout at small relative displacements and under different types of loading. This need arises because most of the available pullout test data are from monotonic tests performed under a displacement-controlled mode.

1.3 Objectives

The objectives of this study were to:

Chapter 1. Introduction

- Design and commission a large pullout test apparatus, and associated controls to perform pullout tests under displacement-control and load-control;
- Develop a routine for cyclic loading of the test specimen, taking into account the current method for monotonic loading in pullout tests;
- Comprehensively describe the development of pullout resistance from instrumentation on the test specimen and on the test apparatus;
- Establish a method of interpretation for the response of the test specimen based on measurements of pullout load, and strain along the embedded length, that accounts for the extensible behaviour of geosynthetic test specimens;
- Compare and contrast the behaviour in pullout of grids and sheets;
- Contrast the results of this work with the limited experimental database for laboratory testing;
- Assess experimental and theoretical interaction factors for geosynthetic;
- Compare the behaviour in pullout testing with that for “in-service” conditions;
and
- Compare values of interaction factor for static and dynamic loading, and critically evaluate the current approach used in design for selection of an interaction factor.

To achieve these objectives, a large scale pullout apparatus was designed and commissioned at the University of British Columbia. The apparatus is used to replicate sand samples to a targeted density. Pullout tests were performed on embedded geosynthetic specimens confined at different values of normal stress. A sophisticated control system

Chapter 1. Introduction

allowed tests to be performed in a displacement-controlled or load-controlled mode. The apparatus and test specimen were instrumented to allow an examination of behaviour at small strains less than 0.5% that are representative of in-service conditions. Based on the experimental results, a generalized method is presented for interpretation of pullout test data. Implications of the results for design practice are discussed.

1.4 Thesis Organization

The state of the art for pullout testing and interpretation of the test results is reviewed in Chapter 2. Chapter 3 describes the design and fabrication of the pullout test apparatus used in this research study. Properties of the materials used in the program of testing are reported in Chapter 4. In Chapter 5 the experimental procedure followed in the pullout test preparation and performance is described. Pullout test results are reported in Chapter 6. In Chapter 7 an analysis and discussion of the results are presented. Some conclusions on the use and interpretation of the pullout test are drawn in Chapter 8, and recommendations made for further study.

CHAPTER 2

LITERATURE REVIEW

2.1 Introduction

In this chapter the literature is reviewed with an emphasis placed on: geosynthetic applications; various types of loading; current design practice; approaches used in the laboratory evaluation of design parameters; and behaviour of full scale structures. In concluding, a statement is made of the research needs arising from the state of the art and the state of the practice.

2.2 Soil Reinforcement using Geosynthetics

The technique of reinforcing soils with natural fibres is many thousands of years old, but the use of materials such as steel and plastic is more recent. Initially, galvanized steel strips and a granular backfill material were used in construction, though today geogrids and geotextiles are routinely used as reinforcing elements as well. In the analysis and design of such structures, a distinction is made between steel and polymeric materials because of their different stiffness: steel strips are considered to be inextensible inclusions, and polymeric materials are considered to be extensible inclusions. Typical examples of soil reinforcement applications are shown in Figure 2.1.

Placing reinforcement in a region of tensile strain, and orienting it in the direction of principal tensile strain, will best restrain the tensile stresses and increase the shear strength characteristics of the soil (McGown et al., 1978). The direction of principal strain is dependent on geometry, construction technique and type of load acting on the structure. The

Chapter 2. Literature Review

action of the reinforcement is mobilized by the stress field in operation, invoking a composite behaviour in which the “active zone” and the “restrained zone” in the soil mass are bonded (Schlosser, 1978).

The potential mechanism of failure that develops in a structure will determine which mode of soil-reinforcement interaction is critical (Palmeira, 1987), see Figure 2.2. In the case of failure along surface 1-2, sliding of soil on the plane of reinforcement occurs at A, and the test method best suited to model this behaviour is the direct shear test. If failure occurs along surface 3-4, then soil and reinforcement are sheared and the direct shear test, with proper orientation of reinforcement, best models the behaviour. In the case of failure along the surface 5-6, due to insufficient anchorage, sliding of the reinforcement inside the soil matrix takes place, and the test best suited to model this behaviour is the pullout test.

2.3 Fluid/Gas Containment using Geosynthetics

Geomembranes are used in the liner systems of waste containment facilities because of their low permeability and chemical resistance to many waste material leachates. In some countries, and for certain types of waste, their use is mandated by regulatory requirements. The facilities are designed and constructed to comply with US EPA regulations in the United States (US EPA, 1989) and B.C. Provincial Regulations (Waste Management Act, 1988) in the province of British Columbia. Emphasis in both the B.C. Provincial regulations and the US EPA guidance is placed firmly on two parameters for design: cross-plane permeability of the liners to prevent migration of leachates; and in-plane permeability of the drainage layers to facilitate collection of the leachate.

Chapter 2. Literature Review

Typically the geomembrane liner is taken up the side slope of a facility and anchored at the top in a trench, see Figure 2.3. A common failure mechanism of geomembrane lined side slopes of impoundments and reservoirs is by slippage between components of the liner system, Martin et al. (1984), or of the cover soil itself, Seed et al. (1990). A schematic illustration of the potential failure modes is given in Figure 2.4.

An analysis of slope stability requires:

- (i) data on limiting shear strength along the interface between soil and geosynthetic and between different geosynthetic layers;
- (ii) an understanding of tension in the liner system and its influence on overall slope stability;
- (iii) an understanding of slippage between soil, geomembrane and other construction materials, and its relationship to the general stress-strain behaviour of the materials.

The type of failure in a geomembrane-lined structure will determine the mechanism of soil-geosynthetic interaction that is developed. In the case of failure at the cover soil surface, or a geosynthetic-geosynthetic surface, the test method best suited to model the material interaction is the direct shear test. If failure occurs at the anchor trench, then the test best suited to model the interaction is the pullout test.

2.4 Types of Imposed Loading

The geosynthetic element in a structure may be subjected to various loading conditions during construction and its service life. The imposed loads are typically a result of construction techniques, self-weight of the structure and any live loading. Loads may be

Chapter 2. Literature Review

classified as static, repeated or dynamic in nature. The following sections describe these loads on the structure.

2.4.1 Construction Loading

The construction sequence in a typical application is to place the geosynthetic on a prepared surface, and then cover it with the soil. Placement and compaction of soil induce lateral spreading and invoke strain in the geosynthetic, and lead to a 'locking-in' of stresses (McGown et al., 1990). Consequently the rate and path of loading of an element are dependent on a number of factors, but during a particular stage of construction the load applied to the reinforcement will be either constant or changing monotonically at a reasonably slow rate (McGown et al., 1992).

2.4.2 Static Loading

The static loads acting on a structure are the permanent loads due to self-weight of the structure and any imposed load from the superstructure. They are essentially constant and independent of time. Load sharing between elements is governed by their arrangement and spacing. The stress distribution from imposed loads is computed by elastic theory or by assuming a load spread angle (Christopher et al., 1990).

2.4.3 Repeated Non-Dynamic Loading

A load is said to be repeated when there is an increase and decrease of magnitude with time. When inertia forces are negligible the load is termed non-dynamic. Some examples of repeated non-dynamic loads are: transient loads due to traffic on reinforced soil structures; variations of waste or water level in an impoundment; and severe wave loading on coastal structures.

Chapter 2. Literature Review

In reinforced soil structures that support highways and railways, the effect of a transient surcharge is to cause a simultaneous increase of vertical stress on the reinforcement and the horizontal stress within the structure. Wave loading on a reinforced structure imposes horizontal forces that vary in a cyclic manner. The additional increments of horizontal stress are resisted by shear stress mobilized at the soil-geosynthetic interface. Similarly, the variation of waste level in an impoundment induces varying tension in the geosynthetic liner, as well as a repeated loading and unloading sequence to the soil-geosynthetic interface in the anchorage trench.

2.4.4 Dynamic Loading

Dynamic loads are imparted to the geosynthetic element by a seismic event, blast loading or man- or machine- induced vibrations. A seismic event induces accelerations in the horizontal as well as the vertical direction. The horizontal component of the acceleration increases the lateral thrust on the soil geosynthetic structure due to acceleration of the active mass and the retained soil. The vertical component of the acceleration increases and decreases the normal stresses in a cyclic manner at the soil-geosynthetic interface. Blast loading or man- or machine- induced vibrations affect a structure by subjecting it to instantaneous transient loads (Yegian and Lahlaf, 1992). Again, the consequence of dynamic loading is to superimpose an increment of load on an element already loaded by self-weight.

2.5 Analytical Methods used in Design

Approaches used in design of geosynthetic structures may be classified as: limit equilibrium methods; strain compatibility design methods; and finite element methods. The limit equilibrium methods are simple and inexpensive, and consequently form the basis of most

Chapter 2. Literature Review

design. The current practice to account for dynamic loading is to perform a conventional pseudo-static analysis.

2.5.1 Limit Equilibrium Method

Many variations on the limit equilibrium method are proposed for design of walls and slopes, (Schneider and Holtz, 1986; Leschinsky and Perry, 1987; Schmertmann et al., 1987; Bonaparte et al., 1987; Bathurst and Simac, 1993). Reinforced soil structures are checked for two general modes of failure: external stability; and internal stability. In general, the external stability will govern the length of the reinforcement and internal stability will govern the vertical spacing of layers. A failure surface through the reinforced mass is assumed for internal stability analysis that establishes an active zone and a resistant zone. Reinforcement layers that extend beyond the postulated failure surface are considered to act as tension-resistant tiebacks for the failing mass. Force and moment equilibriums are used to calculate the mobilized tensile force in each layer of reinforcement. Limit equilibrium methods do not address wall deformations directly, and an empirical chart has been proposed for use in design (Christopher et al., 1990).

Claybourn and Wu (1993) compare several available methods when designing two walls, 3.6 m and 9.1 m high, with three different types of reinforcement. They conclude that the various design methods yield widely varying results. For the case of a 9.1 m high wall reinforced with the similar reinforcement, the ratio of largest design quantity (required reinforcement) to smallest design quantity was 12.5. However, this ratio was 2.5 when safety factors were not considered. Although some variation was attributed to differences in the

Chapter 2. Literature Review

analytical methods used in each design, significant variation was attributed to selection of an allowable reinforcement strength and appropriate factors of safety.

2.5.2 Strain Compatibility Design Method

The strain compatibility design method was proposed by Juran et al. (1990) to overcome limitations of the limit equilibrium method which (1) does not consider the fundamental requirements of strain compatibility between soil and reinforcement; and (2) does not allow for the influence of soil dilatancy, and extensibility of the reinforcement, on mobilized tension and stability of the structure.

The main assumptions in the strain compatibility design method are:(1) constitutive equations for the soil; (2) stress-strain relationships for the reinforcement; (3) soil-reinforcement interaction; (4) the strain path of elements on the potential sliding surface during construction; and (5) effects of the construction process on the initial state of strain.

Deutsch (1993) has presented a quantitative procedure for distributing the tensile load among the various geosynthetics within a lining system which assumes that there is no slippage between geosynthetic “sandwich” components. When designing a geosynthetic lining system, the usual practice is to assume that the most rigid material within the geosynthetic “sandwich” carries the developed tensile load. The assumption that the individual geosynthetic components act as a single block mass implies that the strain in each of the components is the same as the most rigid material. The consideration of strain compatibility between individual components within the lining system allows for distribution of load to each of the components based on the stress-strain relationships. Thus, the strain compatibility design method promotes an economical design.

Chapter 2. Literature Review

2.5.3 Finite Element Method

In comparison with the limit equilibrium method, the finite element method is a more powerful analytical tool for boundary value problems. A proper account of strain compatibility may only be made using a deformation analysis, and the finite element method is well suited for this purpose (Chan et al., 1993). It provides information such as the deformation, and stress-strain distribution in the structure and accounts for complex geometries and loading conditions.

Segrestin and Bastick (1988) modelled reinforced earth retaining walls using dynamic finite elements. The program used was SUPERFLUSH, a modification of the LUSH program of University of California, Berkeley. The elasto-plastic behaviour of soil is simulated by varying the modulus of elasticity as a function of observed deformations, this process being repeated until moduli and deformations are compatible.

Chalturnyk et al. (1990) performed nonlinear finite element analyses on an unreinforced embankment and a polymeric reinforced embankment, with 1:1 side slopes, on a simulated competent foundation. The soil behaviour was idealized as a hyperbolic nonlinear elastic material. The load-strain relationship for the reinforcement was defined by a nonlinear quadratic model. They conclude that significant reductions occur in shear, horizontal, and vertical strains within the slope because of the presence of the reinforcement. Also, for the example studied a circular-shaped slip surface was found to best represent the probable failure mechanism within the slope.

Yogendrakumar et al. (1992) review two methods used in current engineering practice for the dynamic response analysis of reinforced-soil retaining walls. The predictive capability

Chapter 2. Literature Review

of the iterative equivalent linear elastic approach, and the incremental elastic approach, is contrasted with reported field test data. The incremental elastic approach was reported to predict dynamic stress increments and accelerations at various locations that are similar to the measured values.

2.5.4 Seismic Design

Two approaches used in the design of reinforced soil structures to resist seismic forces are the conventional pseudo-static analysis and the displacement-controlled design. At present the displacement-controlled design is applied only to retaining walls.

2.5.4.1 A Pseudo-Static Analysis

The pseudo-static approach of the USFHWA for retaining walls (Christopher et al., 1990) proposes that the seismic forces be modelled as equivalent static forces using the Mononobe-Okabe approach.

During an earthquake the retained fill exerts a dynamic horizontal thrust on the reinforced soil wall, P_{AE} , that acts in addition to other lateral earth pressures, see Figure 2.5. A peak horizontal ground acceleration is selected based on the design earthquake. Due to the flexibility of the structure, an acceleration of greater magnitude is anticipated at the top of the wall. Based on finite element studies, Segrestin and Bastik (1988) recommend an expression for computing the maximum wall acceleration coefficient at the centroid of the active mass:

$$\frac{a_m}{g} = (1.45 - \frac{a_0}{g}) \frac{a_0}{g} \quad (2.1)$$

where a_m is the maximum wall acceleration at the centroid of the active mass, and a_0 is a reference acceleration between 0.05g and 0.5g

Chapter 2. Literature Review

For analysis of external stability, the horizontal inertial force P_I acting at the centroid of the reinforced soil mass is given by, Christopher et al. (1990):

$$P_I = \frac{a_m \gamma_r H L}{g} \quad (2.2)$$

where γ_r is the unit weight of the reinforced mass; H is the height of the wall; and L is the length of the reinforcement.

The horizontal dynamic thrust P_{AE} is calculated using the Mononobe-Okabe pseudo-static expression:

$$P_{AE} = 0.375 \frac{a_m}{g} \gamma_b H^2 \quad (2.3)$$

where γ_b is the unit weight of the retained soil. The force P_{AE} is assumed to act at the level $0.6H$ above the base of the wall, see Figure 2.5. The seismic thrust P_{AE} and 60% of the inertia force P_I are added to the static forces on the structure. The reduction of inertia force is justified by the fact that these two forces are unlikely to peak simultaneously. External stability is evaluated for sliding and overturning, taking the required minimum factors of safety to be 75% of the static factors of safety.

For analysis of internal stability, it is assumed the horizontal inertia force is taken up as an increment of dynamic load in each layer of geosynthetic. The inertia force acting on the reinforced soil mass is distributed between each layer of reinforcement in proportion to the resistant areas beyond the postulated failure surface. The increments of dynamic load are added to the existing static loads, and a check made for tensile failure of the geosynthetic and any connections for pullout failure. Again the minimum factors of safety are 75% of the

Chapter 2. Literature Review

corresponding factors for static loading. In addressing soil-geosynthetic interaction, it is proposed that the interaction factor in dynamic loading be taken as 80% of that for static loading (Segrestin and Bastik, 1988; Christopher et al. 1990). However, there is no experimental evidence to justify this assumption. Clearly, additional data are required to establish interaction factors for dynamic loading.

This issue of soil-geosynthetic interaction was also recognized by Bonaparte et al. (1986) in their pseudo-static analysis of slopes and embankments subjected to earthquake loading. In preparing a series of charts that compare the required tensile strength and length of reinforcement for seismic and gravity loading conditions, they concluded:

- Few additional layers of reinforcement are necessary to resist earthquake induced loads on slopes because
 - (1) the visco-elastic properties of geosynthetics permit the use of a higher available strength under conditions of rapid loading; and
 - (2) lower factors of safety are adopted for seismic design;
- The resultant dynamic increment of force should be distributed uniformly over the height of the slope;
- The allowable reinforcement tensile force for seismic design should: (1) consider the rapid rate of strain which occurs over a short duration; (2) ensure that brittle rupture of the reinforcement is precluded; and (3) result in working strains compatible with mobilization of soil strength at large displacement;

Chapter 2. Literature Review

- Few data are available on the influence of cyclic loading and deformation rates on the soil-geosynthetic interface.

2.5.4.1.1 The Displacement-Controlled Design

The displacement-controlled design method applied to gravity retaining walls was proposed to address the over-conservatism of conventional methods, Richards and Elms (1979). The analysis was based on the Mononobe-Okabe equations for active seismic pressures, and the Newmark sliding-block analysis for displacement of a block with a given coefficient of friction. More recently, Richards and Elms (1992) proposed an extension of the method to the design of tied-back walls based on model experiments. They observed that the acceleration response corresponding to the formation of a failure surface showed a pattern expected by the sliding-block model at a level roughly the same as that predicted by the Mononobe-Okabe equations using the residual friction angle. The method should be used with caution because the result is sensitive to wall friction, which is difficult to estimate accurately.

2.6 Evaluation of Soil-Geosynthetic Interaction

The common parameters for designing the geosynthetic structure using methods described in previous section are soil strength (cohesion, c , and angle of internal friction, ϕ), interface strength factors, and the allowable tensile strength of the geosynthetic. Soil strength parameters are typically obtained by performing conventional direct shear tests and/or triaxial tests. Interface strength factors are governed by the postulated failure mode in the structure, and measured in the shear test or pullout test. In 1992 the American Society for Testing and Materials established a test method for measurement of geosynthetic interface strength in

Chapter 2. Literature Review

direct shear (ASTM D5321-92). A standard test method for the pullout test is currently under development by ASTM.

2.6.1 Direct Shear Tests

Direct shear tests are used to model the failure behaviour observed along surface 1-2 and 3-4 of Figure 2.2. Martin et al. (1984) conducted modified direct shear tests on various geosynthetic-geosynthetic and geosynthetic-sand interfaces and concluded that the interface friction mobilized was between 65% and 90% of the peak friction angle for medium-dense sand samples. Eigenbrod and Locker (1987) report the results of direct shear tests on various geosynthetics and sand samples, performed on both dense and loose samples. Dilation of the dense samples was indicated by mobilization of a distinct peak and residual shear stress. Interface friction mobilized was between 55% and 85% of peak friction angle. Negussey et al. (1989) observed that interface sliding between a geomembrane and granular soils exhibits a peak and residual value, whereas sliding between a geomembrane and geotextile interface does not result in any such peak. Rinnie (1989), using the same ring shear apparatus, tested different types of geomembrane using an angular quartz sand and a rounded sand at high confining stresses. Geomembranes used in testing were polyvinylchloride (PVC), smooth high density polyethylene (HDPE) and textured HDPE. The soft PVC and textured HDPE mobilized a value of interface friction equal to the shear resistance of the sand, for both the angular and the rounded sand. In contrast, the smooth HDPE mobilized approximately 65% of the peak resistance of the rounded sand, and 90% of that for the angular sand.

O'Rourke et al. (1990) summarize the results of an experimental program involving over 450 direct shear tests of sand-polymer interfaces. Their results indicate that the interface

Chapter 2. Literature Review

frictional strength increases with soil density, but decreases with the Shore D Hardness of the polymer. The shear strength characteristics were found to vary as a function of the type of sand, but were independent of repeated loading, at least for polyethylene piping and linings. They expressed the shear strength characteristics of a polymer interface as the ratio of the interface angle of friction and the angle of friction in direct shear of the soil itself, in both cases at the residual state. It was observed that this ratio was relatively constant at 0.55-0.65 along high- and medium density polyethylene surfaces for different types of sand at various densities.

Takasumi et al. (1991) present a review of state-of-the-art testing procedures for soil-geosynthetic interface strength characteristics. Their review revealed that there is a wide range of interface strength characteristics reported and that there are significant variations in how interface testing is performed. Based on their study, they conclude that more testing is required to understand the influence of type and size of the apparatus on interface strength characteristics.

The importance of conditioning of the test specimen was emphasized in an investigation of the Kettleman Hills landfill failure, Seed et al. (1990). Failure developed by sliding along interfaces within the composite, multilayered geosynthetic-compacted clay liner system beneath the waste fill, see Figure 2.6. The materials used to construct the low permeability liner system at the facility involved contact surfaces between various geosynthetics including sheets of HDPE geomembrane, geonet and geotextile; and between these materials and the compacted clay liner. Based on a comprehensive series of testing it was concluded that the frictional resistance was affected by various properties, including the

Chapter 2. Literature Review

degree of polishing, whether the surfaces were wet or dry, and in some cases the relative orientation of the layers to the direction of shear-stress application. A decrease in frictional resistance was observed with an increase in degree of polishing. A wet interface gave a reduced interface friction when compared to dry condition. Also an increase in frictional resistance was exhibited when the relative orientation changed from aligned shear to transverse shear.

In discussion of the Kettleman Hills investigation and testing, Yegian and Lahlaf (1991) present data which illustrate the importance of specimen preparation. Static loading tests were performed to determine interface friction between two layers of HDPE geomembrane. Specimens were cleaned by two methods prior to testing: hand-wiping and towel-wiping. Results indicated that the residual friction angle was 11° when towel-wiped and about 6° when hand-wiped. This observation was attributed to a “dry” or “lubricated” condition of the geomembrane. They also noticed that when a geotextile was used with a HDPE geomembrane, the effect of hand-wiping the geomembrane was insignificant.

2.6.2 Pullout Tests

Soil-geosynthetic interaction in pullout is an important parameter in the design of a reinforced soil structure or a low permeability barrier. Jewell et al. (1984) refer to the mechanism of interaction for a grid structure in soil as “bond”, and propose the use of a bond coefficient. In a similar approach, Martin et al. (1984) and Eigenbrod and Locker (1987) use an efficiency factor when describing interaction of geomembranes and geotextiles. Soil-reinforcement interaction in pullout involves some or all the following general mechanisms of load transfer, see Figure 2.7.

Chapter 2. Literature Review

- lateral friction, where shear occurs on plane surface areas of the geosynthetic;
- passive earth pressure on transverse elements of geogrids, welded wire meshes, bar mats and woven geotextiles, as a result of soil bearing against surfaces normal to the direction of relative movement; and
- soil shearing over soil in the apertures of a grid.

The transfer of load between soil and geosynthetic in pullout is by mobilization of the first two components only, since there is no relative displacement between soil particles on either side of the element: the two components are lateral friction and passive resistance or bearing.

Jewell et al. (1984) derived an expression to describe pullout interaction between grid reinforcement and soil, so that a bond capacity could be calculated from the fundamental properties of the reinforcement geometry and angle of friction of the soil. The skin friction component of pullout resistance for a geosynthetic specimen is given by:

$$P_s = 2 \alpha_s L_r W_r \sigma_n' \tan \delta \quad (2.4)$$

where:

α_s is the fraction of the specimen plan area that is solid,

L_r and W_r are the length and width of the specimen,

σ_n' is the effective normal stress at the soil-inclusion surface, and

δ is the angle of interface friction

Chapter 2. Literature Review

Equation 2.4 is valid for geomembranes and planar geosynthetics without significant asperities out of the plane of the specimen.

Passive soil resistance developed against bearing surfaces normal to the direction of relative movement is similar to the pressure developed on deep foundations in soil. Jewell et al. (1984) modified an expression for deeply-embedded anchors to establish a theoretical contribution from bearing stresses. A lower bound to the expression is associated with a punching shear failure mode in the soil, (see Figure 2.8), is:

$$\frac{\sigma'_b}{\sigma'_n} = F_v = e^{(90+\phi)\tan\phi} \tan\left(45 + \frac{\phi}{2}\right) \quad (2.5)$$

where:

σ'_b is the effective bearing stress acting on the embedded anchor; and

F_v is a stress ratio.

An upper bound value is estimated by taking the conventional characteristic stress field for a footing rotated to the horizontal, and a horizontal boundary stress in the soil, where:

$$\frac{\sigma_b}{\sigma_n} = F_v = e^{\pi\tan\phi} \tan^2\left(45 + \frac{\phi}{2}\right) \quad (2.6)$$

It was suggested by Jewell et al. (1984) that the stress ratio be established directly from pullout tests, or estimated from curves summarizing test results in the literature. A comparison of the theoretical expressions with experimental data, Jewell (1990), shows good agreement despite the large spread and variability of the test results, see Figure 2.9. The stress ratio is used in the following expression to determine the bond coefficient, where:

$$P_r = 2L_r W_r \sigma'_n f_b \tan\delta \quad (2.7)$$

Chapter 2. Literature Review

and

$$f_b = \alpha_s \left[\frac{\tan \delta}{\tan \phi} \right] + \alpha_b \left[\frac{\sigma_b}{\sigma_n} \right] \frac{B}{S} \frac{1}{2 \tan \phi} \quad (2.8)$$

where:

P_r is the total pullout resistance,

f_b is the bond coefficient,

α_b is the fraction of the specimen bearing member width available for bearing,

B is the thickness of the bearing member, and

S is the spacing between bearing members

The effect of interference between transverse bars of a grid on the bond capacity in pullout has been analyzed for grid reinforcement by Palmeira (1987). A comparison of the value of the pullout load for a given grid (P_b) with the value obtained for an ideal grid (nP_o), defined as one having the sum of bearing pressure of a single isolated member (P_o) under similar conditions without interference, led to a parameter for degree of interference being defined as:

$$DI = 1 - \frac{P_b}{nP_o} \quad (2.9)$$

where:

P_b is the maximum pullout load for a grid with n bearing members, and

P_o is the maximum pullout load for an isolated bearing member of the same grid.

Thus an expression to calculate bond coefficient is proposed as follows:

$$f_b = \alpha_s \left[\frac{\tan \delta}{\tan \phi} \right] + \alpha_b \left[\frac{B}{S} \right] \left[\frac{\sigma_b}{\sigma_n} \right] \left[\frac{1 - DI}{2 \tan \phi} \right] \quad (2.10)$$

Chapter 2. Literature Review

Jewell (1990) suggests further modification to the above relation to account for the first bearing member which acts undisturbed on the sand, and subsequent bearing members for which interference can occur. For a grid with n bearing members, this gives:

$$DI = \left[1 - \frac{1}{n} \right] \left[1 - \frac{\frac{S}{\alpha_b B}}{\left(\frac{S}{\alpha_b B} \right)_\phi} \right] \quad (2.11)$$

where the ratio $\left(\frac{S}{\alpha_b B} \right)_\phi$ is defined as the grid geometry required to achieve a fully rough bond.

The FHWA manual of the U.S Department of Transportation (Christopher et al. 1990) for the design of reinforced soil structures recommends the following expression:

$$P_r = F^* \alpha \sigma_n' L_e C \quad (2.12)$$

where:

L_e is the embedment or adherence length in the resisting zone behind the failure surface,

C is the effective unit perimeter of the geosynthetic, which is 2 for planar sheets,

F^* is the pullout resistance (or friction-bearing-interaction) factor,

α is a scale effect correction factor, and

σ_n' is the effective normal stress at the soil-geosynthetic interface.

It is recommended that tests be performed to determine the pullout resistance factor F^* , which is very similar to the bond coefficient proposed by Jewell et al. (1984), and is given by:

$$F^* = F_v \alpha_\beta + K \mu' \alpha_f \quad (2.13)$$

Chapter 2. Literature Review

where:

F_v is the stress ratio,

K is a ratio of the actual normal stress to the effective normal stress; and is influenced by the geometry of the specimen,

α_β is a structural geometric factor for bearing resistance, where $\alpha_\beta = \frac{f_b}{2} \left[\frac{B}{S} \right]$; and

μ^* is an apparent friction coefficient for the specimen.

A value of 20 has been suggested for F_v based on limited experimental data (see also Figure 2.9). For geogrids, geomembranes and geotextiles, $K=1$ and $\mu^* = \tan \delta$. Recognising that the extensibility of geosynthetics leads to an interface shear stress that may not be uniformly mobilized along the total length of the geosynthetic, a scale effect correction factor α is introduced defined as:

$$\alpha = \frac{\tau_{av}}{\tau_{peak}} = \frac{\tan \delta_{av}}{\tan \delta_{peak}} \quad (2.14)$$

where τ_{av} and τ_{peak} are the average and ultimate interface shear stresses respectively, mobilized along the inclusion,

δ_{av} and δ_{peak} are the average and peak interface friction angles respectively.

The value of the scale effect correction factor is influenced by strain softening of the compacted granular backfill, extensibility of the geosynthetic material and the embedment length. The manual recommends a value of 0.6 in the absence of test results for extensible reinforcement; a realistic value may be in the range 0.6 to 1, with 1 being appropriate for an inextensible material. The factor can be obtained from pullout tests performed with different

Chapter 2. Literature Review

lengths of geosynthetic or derived using analytical or numerical load transfer models which have been “calibrated” against physical tests.

2.6.2.1 Factors Influencing Pullout Resistance

Typically the pullout resistance of a geosynthetic in laboratory testing is influenced by the type of soil, the material properties and geometry of the specimen, and the configuration of the test apparatus. Soil parameters of interest are: the particle size, shape and gradation; relative density; dilatancy; and water content. Test specimen parameters of interest are the geometry of the specimen (such as in-plane or out-of-plane transverse elements), orientation, tensile strength, extensibility, and creep behaviour. The influence of the test apparatus is a result of the loading system, the sample dimensions and its preparation, the boundary conditions and the testing procedure. A comparative summary of pullout test equipment and test materials is given in Table 2.1.

2.6.2.1.1 Soil Characteristics

In construction practice a well-graded free draining granular material is commonly specified for permanent reinforced soil structures because these soils develop a greater bond with the reinforcement. Since a high fines content will tend to restrict the free draining behaviour of a soil, an upper limit to the percentage of fines permitted in the backfill material is usually recommended, Brown et al. (1979). This is not to suggest that other soils cannot be used successfully in construction: Murray et al. (1979) used a silty clayey sand as backfill material for a reinforced soil wall and concluded that, despite construction difficulties and pore pressure development, cost savings could be achieved over granular backfills imported over substantial distances.

Chapter 2. Literature Review

Dense soils dilate during shearing, but with confinement from the surrounding soil they experience a restrained dilatancy. The dilatancy characteristics of dense sand and its effect on pullout resistance have been demonstrated for metallic reinforcements (Schlosser and Elias, 1978), where restrained dilatancy caused an increment of normal stress to act on the element, increasing its pullout resistance. The effect of such dilatancy is dependent on the magnitude of normal stress, surface texture of the reinforcement and the density of the soil.

Johnston (1985) evaluated the effect of dilatancy by placing pressure cells within the soil sample of a large pullout apparatus to monitor the applied normal stress on a Tensar SR-2 geogrid. A normal pressure on dense samples (at peak pullout load) some 1.5 to 3 times higher than the applied normal stress was measured. It was a result of the top boundary of the apparatus being rigid and restrained against upward displacement. In contrast pullout tests performed on loose samples (Figure 2.10) show efficiency factors to be independent of normal stress with $\tan\phi = \tan\delta$.

2.6.2.1.2 Test Specimen Characteristics

Characteristics of a test specimen which influence pullout resistance are: geometry, tensile strength and stiffness, and creep behaviour. Geosynthetics are thermo-viscoelastic materials, hence the load-strain characteristics are dependent not only on strain magnitude but also on strain rate and temperature. Creep is defined as continued strain at constant load, and the phenomenon is well-recognized in polymeric materials. The magnitude of any creep strain is influenced by:

- type of polymer;
- geosynthetic macro-structure;

Chapter 2. Literature Review

- manufacturing technique;
- magnitude of loading;
- temperature;
- time.

Therefore, an evaluation of long-term performance over the service life of a structure requires data describing the load-strain-time behaviour of the geosynthetic. Such data are typically presented as isochronous load-strain curves, from laboratory constant load-extension tests on unconfined samples, following an approach reported by McGown et al. (1984) and further described by Jewell (1985). The test method involves loading a series of test specimens in a rapid, smooth manner. Load is maintained throughout the test at $\pm 1\%$ of the targetted constant load, at a controlled temperature and humidity, and specimen elongation measured over time. The tests are performed for at least 10, 000 hrs or until failure, whichever is less. Data obtained from each test are plotted as strain against logarithm of time for each magnitude of load. A long-term design strength is selected based on a value of performance limit strain (identified from a plot of strain versus logarithm of strain rate) and extrapolation of the data from 1×10^4 hrs to 1×10^6 hrs, which is equivalent to a service life of 120 years.

2.6.2.1.3 Test Apparatus and Procedure

2.6.2.1.3.1 Normal Stress

The normal stress imposed on the test specimen strongly influences pullout, and the effect of any increase in stress is to increase the pullout resistance, while causing the length of the test specimen that is mobilized to decrease (Palmeira, 1987). At relatively high normal

Chapter 2. Literature Review

stresses, tests will tend toward a failure of the test specimen in tension, (Fannin and Raju, 1993). Pullout tests performed at high normal stresses may also cause particle breakage in some sands, and result in a small change in grain size distribution, (Raju, 1991).. In testing, the magnitude of normal stress is used as a control to promote a pullout failure, to simulate field conditions, or to develop very large strains in the test specimen if it tends towards a tensile failure rather than pulling out.

2.6.2.1.3.2 Boundary Effects

Typically a soil sample for pullout testing is prepared in a rectangular box with a rigid base and side walls. The top boundary may be rigid or flexible. The influence of a rigid boundary that was free to displace, and a flexible boundary, was examined by Palmeira (1987). A flexible top boundary, typically a surcharge bag filled with water, eliminates boundary shear stresses and for otherwise similar test conditions, leads to a smaller maximum peak pullout load. This behaviour is attributed to no restrained dilatancy.

Some experiences are reported in the literature regarding the influence of the rigid front wall of the apparatus on the measured pullout resistance. As the specimen is being pulled out from the box, lateral pressures develop against the front wall. Juran et al. (1988) postulate that arching of the soil over the specimen will reduce the normal stress on the test specimen close to the front boundary and, consequently decrease the pullout resistance. Tests performed to examine the influence of roughness of the front wall showed a marked effect, with a dramatic increase in pullout resistance attributed to an increase in normal stress on the sample caused by shear stresses developed on the front wall during pullout, Palmeira (1987), see Figure 2.11.

Chapter 2. Literature Review

Table 2.1: Summary of the pullout test apparatus and testing characteristics

Research Institution / Company	Dimensions in cm L x W x D	Soil Properties	Test Specimen	Boundary Preparation	Sample Preparation	Test Mode	Interpretation Method
The Reinforced Earth Co., (Cowell and Sprague, 1993)	152 x 61 x 30.4	Uniform fine sand with silt traces; $C_u=2.2$, $C_c=1.23$, $d_{10}=0.1$ mm	Geogrids and Geotextiles; woven from high tenacity polyester yarns	Lubricated tapered metal sleeve on front wall;	Sand placed at 95% of standard Proctor dry density and within 2% of optimum moisture content	Constant displacement rate of 1 mm/min	Total area, Effective area
Institute of Soils, Rocks and Foundations, Switzerland. (Kharchafi and Dysli, 1993)	80 x 55 x 20	Fine-grained sand; moist silt	Nonwoven heat bonded polypropylene continuous filament TYPAR geotextiles	Metal clamp buried in sand to avoid rigid front wall		Stopped at regular intervals to enable taking X-Ray shots	Total area, Effective area
Louisiana State University (Farrag et al. 1993)	152 x 90 x 76	Blasting sand, $d_{10}=0.26$ mm, varying density	Geogrids - Tensar SR-2 and Conwed 9027	Metal sleeve on front wall; minimum distance of 15 cm of sides to reduce side friction	Sand placed in four layers and each layer compacted using vibrating electric hammer	Constant rate of displacement- 6 mm/min; Step loading in load controlled mode.	Mobilising process
Kyushu University, Japan (Ochiai et al. 1992; Yasuda et al. 1992))	60 x 40 x 40	Toyoura sand, $D_r=30$ and 80; Two other well graded soil at 85 to 90% of Proctor maximum density	Geogrids Tensar SR-2 and SS-2		Compacted to achieve required densities	Constant rate of displacement of 1 mm/min; cyclic loading by cycling overburden pressure or adding cyclic loads over static	Total area
Netlon, U. K. (Nimmegern and Bush, 1991)	200 x 100 x 100	Well graded sandy gravel, $C_u=28$, maximum grain size= 30 mm	Geogrid Tensar SR-80			Load controlled : dynamic load superposed on static load at 5Hz frequency	---
Oxford University (Palmeira and Milligan, 1989)	100 x 100 x 100	Leighton Buzzard Sand 14/25, uniform coarse with a relative density 87%	Metallic grids, Tensar SR-1 and SR-2, Geolon, Stabiltenka 400	Sides and front:- Double layer of polyethylene with grease in between	Air pluviation with specially designed hopper	Constant rate of displacement 0.5 mm/min	Total area

Chapter 2. Literature Review

Research Institution / Company	Dimensions in cm L x W x D	Soil Properties	Test Specimen	Boundary Preparation	Sample Preparation	Test Mode	Interpre- tation Method
Public Works Research Institute, Tsukuba, Japan (Kuriara et al. 1988)	120 x 60 x 60 100 x 80 x 50	Air-dried Toyoura Sand; $d_p=0.16$ mm; relative density 20% and 60%	Tensor SR2	--	--	Constant rate of displacement 1 mm/min; staged load controlled test with 0.5tf/m for 12 hours	--
University of Missouri-Rolla (Lentz and Pyatt, 1988)	76.2 x 29.2 x 10	Fine sand and Coarse sand	Tensor SS1 and SR2	--	Placed using V- shaped hopper and each layer vibrated to densify	Constant rate of displacement 2.5 mm/min	--
Asian Institute of Technology (Bergado et al. 1987)	100 x 80 x 90	Light brown clayey sand and weathered clay	Tensor SR2 and Bamboo strips	--	Compacted to 95% if standard proctor at OMC, each layer 15 cm	Constant rate of displacement 1 mm/min	--
STS Consultants Ltd., Illinois, USA (Bonczkiewicz et al. 1986)	134 x 70 x 38	Fontainebleau sand (SP); dense sample	Tensor SS2 and SR2	A slot introduced to transfer the rigid front boundary into the box	Compacted using vibratory plate	Constant rate of displacement 1 mm/min	Total area, Effective area
Swedish Geotechnical Institute (Holtz, 1977)	190 x 70 x 70	Tullinge sand (Stockholm) G-12 sand (Denmark); medium dense sand	Woven polyester geotextile	To reduce the side effects, the test specimen was 5 cm narrower than the width of the box.	--	--	Total area, Effective area

Chapter 2. Literature Review

Various techniques have been tried to reduce or control the influence of the front boundary of the apparatus. Polyethylene sheets with grease in between have been used to create a low friction boundary (Palmeira, 1987; Lo, 1990). The influence of such an arrangement is to reduce boundary shear stresses, and hence the complimentary shear stresses on the specimen close to the front wall of the apparatus. In another approach the front boundary was essentially transferred into the soil mass by embedding a sleeve into the soil across the width of the pullout box, through which the specimen is pulled, Bonczkiewicz et al. (1986). To further address the issue, Juran et al. (1991) clamped the test specimen within the soil sample. Although the introduction of a sleeve mitigates the problem of front wall friction, it complicates the stress distribution within the soil mass at the edge of the sleeve, and the introduction of the clamp into the soil leads to further complexity. A rational understanding of the influence of the front wall will best be obtained through measurement of the distribution of lateral stress acting on it.

2.6.2.1.4 Loading Characteristics

Pullout tests on reinforcement installed in an experimental wall constructed with a uniformly graded sand, are reported by Murray et al. (1979). The tests were carried out under both static and dynamic loading conditions. Results showed a significant reduction in pullout resistance when vibration was applied to the surface of the fill. The measurement of vertical stress in close proximity to the reinforcement showed reductions of the overburden stress acting at the level of the interface: the observed reduction in pullout resistance was attributed to the temporary reduction of normal stress.

Chapter 2. Literature Review

When designing a structure to resist repeated non-dynamic loads, a knowledge of the material behaviour and load transfer characteristics of the interface is essential. At present, very few studies have addressed this issue. Al-Ashou and Hanna (1990) studied the effect of repeated loading on the life-span of metallic (inextensible) reinforcement. Displacement and stress distributions along the reinforcement element were measured after application of several series of load cycles. Results showed that a considerable amount of residual load was locked-in along the reinforcement, and a reversal of shear stress was generated during the loading cycles. Pullout behaviour was greatly influenced by the loading amplitude. Further, for the same amplitude of load, the static loading level was found to be the primary factor governing the pullout resistance.

Hanna and Touahmia (1991) performed static and slow repeated load tests on 4 m long smooth steel and polymeric grid reinforcing strips. A medium dense sand was placed by the air pluviation method to a relative density of 53%. Tests were performed at three levels of normal stress: 50, 75 and 100 kPa. On the basis of these results they conclude that the rate of accumulation of displacement of the test specimen increases with an increase in the number of load repetitions, load amplitude and load level. Failure by pullout occurred only with the smooth strip, despite testing to 10^5 load applications. The polymeric grid exhibited a greater pullout efficiency than either of smooth or ribbed steel strips under both static and repeated loading; it failed in tensile rupture.

In a limited study of the effects of transient surcharge loading due to traffic on reinforced soil structures, Nimmegern and Bush (1991) devised a dynamic pullout test to simulate in-situ conditions. The tests were carried out at low confining stress on polymeric

Chapter 2. Literature Review

grids in a large (1 m x 2 m in plan) pullout box, using a well-graded sandy gravel. In addition to a static surcharge pressure of 57 kPa, a dynamic surcharge pressure of 10 kPa was imposed at a frequency of 5 Hz. Results showed that the grid efficiently resisted the dynamic loads.

To simulate the loading regime prevalent during a seismic event, Yasuda et al. (1992) performed pullout tests on polymeric grids. Three types of soils were used in the testing series: a uniformly graded air-dried Toyoura sand at relative densities of 30% and 80%, and two well-graded volcanic ashes compacted to 85 to 90% of maximum density at optimum moisture content. Test specimens used were polymeric grids. Two types of loading were imposed. In the first mode, cyclic pullout loads were applied to the test specimen by increasing the amplitude of pullout load in stages until the specimen failed either in pullout or in tension. In the second mode, the normal stress was cycled, and simultaneously the specimen was pulled monotonically out of the box until it failed either in pullout or in tension. From the results they conclude:

- the maximum pullout loads under both modes of loading are affected by soil type and overburden pressure;
- the maximum pullout load under cyclic loading is greater than the load under monotonic loading; and
- the maximum pullout load under cyclic overburden pressure decreases with an increase of the amplitude of the cyclic pressure.

Chapter 2. Literature Review

2.6.2.2 Methods for Interpretation of the Pullout Test

2.6.2.2.1 Monotonic Pullout Tests

Juran and Chen (1988) present a soil-reinforcement load transfer model for interpreting pullout tests on extensible reinforcement. The model combines a constitutive equation for the reinforcement with interaction laws relating the shear stress mobilized at any point on the interface to the soil-reinforcement shear displacement. The procedure is derived from the “t-z” method that is commonly used in design of friction piles. They conclude that, for a meaningful interpretation of pullout test results on geosynthetics, an adequate estimation of the in-soil (confined) properties of the reinforcement is required. In addition, the extensibility of the specimen affects soil-reinforcement interaction, and extrapolation of test results to specimens of different dimensions requires a careful evaluation of scale effects.

More recently, to account for the non-uniform and non-linear shear stress distribution along the specimen length, three methods have been proposed based on the area of the specimen active in resistance (Ochiai et al., 1992, Bonczkiewicz et al., 1986), see Figure 2.12. The profile of shear stress distribution at any value of pullout resistance is used to evaluate the interaction factor in pullout using a value of average shear stress, hence the approach is termed the average resistance method. It may be classified into three methods:

1. Total Area Method, in which the pullout force at the front end and the whole area of the geogrid inside the pullout box are used;
2. Effective Area Method, in which the pullout force and effective area only are used; and

Chapter 2. Literature Review

3. **Maximum Slope Method**, in which the slope of an appropriate tangent to the load distribution curve is used.

The total area and effective area methods of evaluating pullout resistance proposed by Ochiai et al. (1992) are similar to the total area and corrected area method proposed by Bonczkiewicz et al. (1986). A determination of the mobilized length of the specimen by direct measurement during testing is utilized to calculate the corrected area. Analysis has shown that at low normal stresses both the effective area and total area methods give similar results.

In the mobilizing process method, the profile of tensile force along the embedded length of the specimen is determined indirectly from the strain measurements (Juran, 1991; and Ochiai, 1992). A common method used to obtain the strain distribution along the specimen is to attach a tell-tale to various nodes. This method of deducing strain is appropriate for specimens with well defined nodes. A generalized technique for measuring strain and an appropriate method for interpreting pullout data are necessary for tests at low normal stress and small strain.

2.6.2.2.2 Cyclic Pullout Tests

Hanna and Touahmia (1991) observed a deterioration in the pullout resistance of metallic strips subjected to repeated loads. The test data demonstrated a complex response to loading, and the authors attributed the behaviour to several partly understood factors including, (i) changes in load transfer along the embedded length, (ii) changes in the normal stress along the specimen with increase in the number of load repetitions, (iii) “compaction” of the sand due to local shear reversals causing a breakdown of particles, (iv) locked-in stresses changing after each load cycle. To better understand these complex and interrelated factors,

Chapter 2. Literature Review

they identify a need for further development of a unified theory to explain and interpret results from cyclic pullout loading.

The interface behaviour under cyclic loading depends on the surface characteristics of the specimen. If the surface is a planar surface the relevant theory for predicting the performance would be that used for soil-pile interaction under cyclic loading. Swinianski and Sawicki (1992) proposed a model for a soil-pile system subjected to vertical cyclic loading. This model, based on the classical t-z concept and compaction of granular materials, was used to study the reduction of shearing resistance around a shaft owing to cyclic loading. The redistribution of loads carried by the shaft and tip of a pile was predicted by the model. Turner and Kulhawy (1990) present results from an experimental study illustrating the effects of repeated axial loading on the drained uplift capacity of drilled shafts in granular soils. Their results indicate that changes in the uplift capacity depend primarily upon the magnitude of cyclic displacement. Critical levels of repeated loading (CLRL) are established, above which shafts fail in uplift and below which failure under repeated loading does not occur.

If a bearing component, rather than skin friction component, is predominant in the measured pullout resistance of the geosynthetic, consideration must be given to bearing capacity and rate effects. The effects of variation of the loading rate on the bearing capacity of footings on sand were studied by Vesic et al. (1965). Observations showed a limited effect of variation of rate of displacement on the bearing capacity of dry sand: there was some decrease, as the rate increases to moderate values of about 0.05 mm/min, followed by an increase for faster tests.

Chapter 2. Literature Review

2.6.2.3 Finite Element Modelling

Chan et al. (1993) used the finite element method to simulate pullout tests and investigated the effect of progressive shearing on the calculation of the shear stiffness of the soil-reinforcement interface. The reinforcing elements were 3 noded elements capable of sustaining only tensile stress. The interface was modelled by 6 node elements. Eight node isoparametric elements were used to simulate the soil. The numerical simulation performed at 51 kPa normal stress reproduced the highly non-uniform shear stress distribution along the specimen. A discrepancy between true stiffness and apparent stiffness was evident when the force-displacement response of the pullout test was used to obtain a value of tensile shear stiffness. This discrepancy was found to depend on the relative stiffness between the interface and the specimen. It was concluded that an appropriate stiffness correction was necessary to obtain true values of stiffness from the pullout test data.

Wilson-Fahmy and Koerner (1993) modelled the pullout test by deriving an incremental finite-element formulation to simulate the non-linear response of a geogrid to pullout. Polynomial and hyperbolic functions were used to represent the load-extension behaviour of the geogrid and the soil-geogrid interaction properties in friction and bearing. Three models were used in the analysis to simulate the deformation of the transverse ribs in bearing. Highly flexible transverse ribs were assumed to take a parabolic shape and to act as strings, whereas short stiff ribs were considered not to deflect during pulling. Intermediate cases were analyzed by assuming the ribs to behave as beams deflecting under load. Typical results indicated that the contribution of the transverse ribs to pullout resistance was greatly affected by their flexibility, especially at low normal stress.

Chapter 2. Literature Review

Yogarajah and Yeo (1994) measured load and strain distributions along a geogrid reinforcement during a pullout test by experiments and numerically modeled the response using the CRISP finite element program. Load and strain along the test specimen were measured using load cells and strain gauges respectively. They used variable elastic moduli for the test specimen and conclude that the use of a single elastic modulus over the entire length is inappropriate due to the visco-elastic nature of the polymeric reinforcement, which is to be expected.

2.6.3 Model Shake Table Tests

Several investigators have attempted to simulate dynamic loading in the laboratory using the shaking table for: reinforced embankments, Koga et al. (1988); reinforced retaining walls, Richards and Elms (1992), Sommers and Wolfe (1988); and to study the interface behaviour of geomembranes and geotextiles, Yegian and Lahlaf (1992).

Sommers and Wolfe (1988) investigated the effects of different input motions on the measured amplification ratios and displacements of model gravity walls. The experiments showed that at low levels of excitation, the model walls behaved as damped elastic structures. Magnification factors were found to be somewhat higher for input motions near the natural frequency of the model. All displacements were shown to be a function of the level of base acceleration with a minimum level of input acceleration required to induce permanent displacement. For all walls tested, a minimum acceleration of approximately 0.25g had to be exceeded before any measurable relative movement between the top of the wall and its base was observed. This yield acceleration was seen to be relatively insensitive to a specific type or frequency of base motion.

Chapter 2. Literature Review

Yegian and Lahlaf (1992) performed shaking table tests to measure the dynamic interface shear strength properties between geotextiles and geomembranes. From the test results it was observed that there was a limiting shear stress, that can be transmitted from one geosynthetic to another. Thereafter a relative displacement occurs along the geosynthetic interface. They conclude that the primary concern about the dynamic response of a geotechnical facility that incorporates geosynthetics should be the permanent relative displacement that may accumulate along the geosynthetic interfaces. The measured dynamic friction angles at the onset of relative displacement between the geosynthetics were not appreciably different from those obtained from static tests.

2.6.4 Behaviour of Field Structures

2.6.4.1 Pullout Tests

Field pullout tests were performed by Ochiai et al. (1988) on polymer grids embedded in an embankment. Based on a comparison of the results with laboratory tests they conclude that the basic characteristics of pullout resistance observed in each case are very similar.

Bonczkiewicz et al. (1991) performed laboratory and field pullout tests on Mirafi 5T (a continuous filament polyester yarn formed into a biaxial grid by a knitting process) to evaluate stress transfer in geogrids exhibiting a low junction strength. Resistance strain gauges were mounted on geogrid sections to obtain strain data. A pullout rate of 1 mm/min was used in testing. Grid displacement was measured using a dial gauge near the face of the wall, and eight strain gauges were used to measure local strains. Again, the behaviour observed during pullout tests in the field was similar to that observed in the laboratory.

Chapter 2. Literature Review

In comparing the laboratory and field pullout tests Bergado et al. (1992) noted that the influence of arching effects on the field response was more pronounced.

2.6.4.2 Dynamic Tests

Richardson et al. (1975, 1977) conducted dynamic tests by subjecting a full-scale instrumented reinforced soil wall to random excitations at the University of California, Los Angeles. The test wall was 6.1 m high and reinforced with steel strips 4.88 m long placed at equal vertical spacings of 0.76 m. Instrumentation in the wall measured acceleration-time histories at selected locations in the wall and dynamic force histories along the steel strips. The input acceleration to the base of the wall was measured by an accelerometer placed at the toe of the wall. They conclude that the Mononobe-Okabe pseudo-static seismic coefficient was found to give reasonable predictions of the location of the postulated failure plane in the backfill, but seriously underestimated the magnitude of the maximum tie forces developed in reinforced earth walls during seismic loading.

Qualitative observations of the field performance of geosynthetic structures, when subjected to a seismic event, are reported by Collin et al. (1992). The performance of five reinforced slopes and walls that experienced the Loma Prieta earthquake of 1989 were evaluated. In the Watsonville wall, a uniaxial Tensar geogrid was used as a primary reinforcement and a biaxial grid used to stabilize the soil at the face of the slope between primary layers. The wall was designed for a maximum horizontal acceleration of 0.1-0.2g. The estimated horizontal acceleration at the site was 0.4g. Visual observations at the site indicated no sign of movement or cracks in the wall, and similar observations are reported at the other sites where very little if any distress occurred in the composite structures.

2.7 Research Needs

From the literature review it is evident that the field response of geosynthetic structures to seismic loading is excellent. This fact makes the use of geosynthetics in practice attractive. However, the available data on soil-geosynthetic interaction under various loading conditions are very limited. Moreover the use and understanding of the pullout apparatus to characterize soil-geosynthetic response in anchorage is an essential requirement.

White and Holtz (1992) review current methods for the analysis of geosynthetic reinforced earth slopes that are subjected to earthquake shaking and conclude that seismic design procedures are very limited. They also observe that despite design procedures being conservative, building code officials are hesitant to approve the technology of steep geosynthetic earth slopes. This was attributed to a lack of published research regarding the seismic stability of steep geosynthetic reinforced slopes. Therefore, they conclude that the seismic design of geosynthetic reinforced slopes and walls are among the “high priority” research needs.

The review of literature reveals that there is a need for a better understanding of soil-geosynthetic interaction, and the following specific research needs are identified:

- comprehensively describe the development of pullout resistance from instrumentation on the test specimen and on the test apparatus;
- describe soil-geosynthetic interaction under monotonic loading, and at small strain;

Chapter 2. Literature Review

- develop a procedure for load-controlled (cyclic) loading on specimens, taking into account the current method for displacement-controlled (monotonic) loading in pullout tests;
- study the influence of an instantaneous increase of load due to a dynamic event on mobilized pullout resistance, and characterize soil-geosynthetic interaction under cyclic loading;
- account for the extensible behaviour of geosynthetic specimens, which are visco-elastic materials by establishing a method of interpretation based on measurements of pullout load, and strain along the test specimen;
- adopt a strain gauging technique for use in pullout testing on grids and sheets;
- compare laboratory derived interaction factors with theoretical factors proposed for design, for both static and dynamic loading conditions;
- assess experimental and theoretical interaction factors; and
- compare pullout test behaviour with in-service conditions.

The present study of monotonic and cyclic pullout resistance of geosynthetics is undertaken to better understand soil-geosynthetic interaction when geosynthetics are subjected to various loading conditions, and make recommendations for both materials testing and design practice.

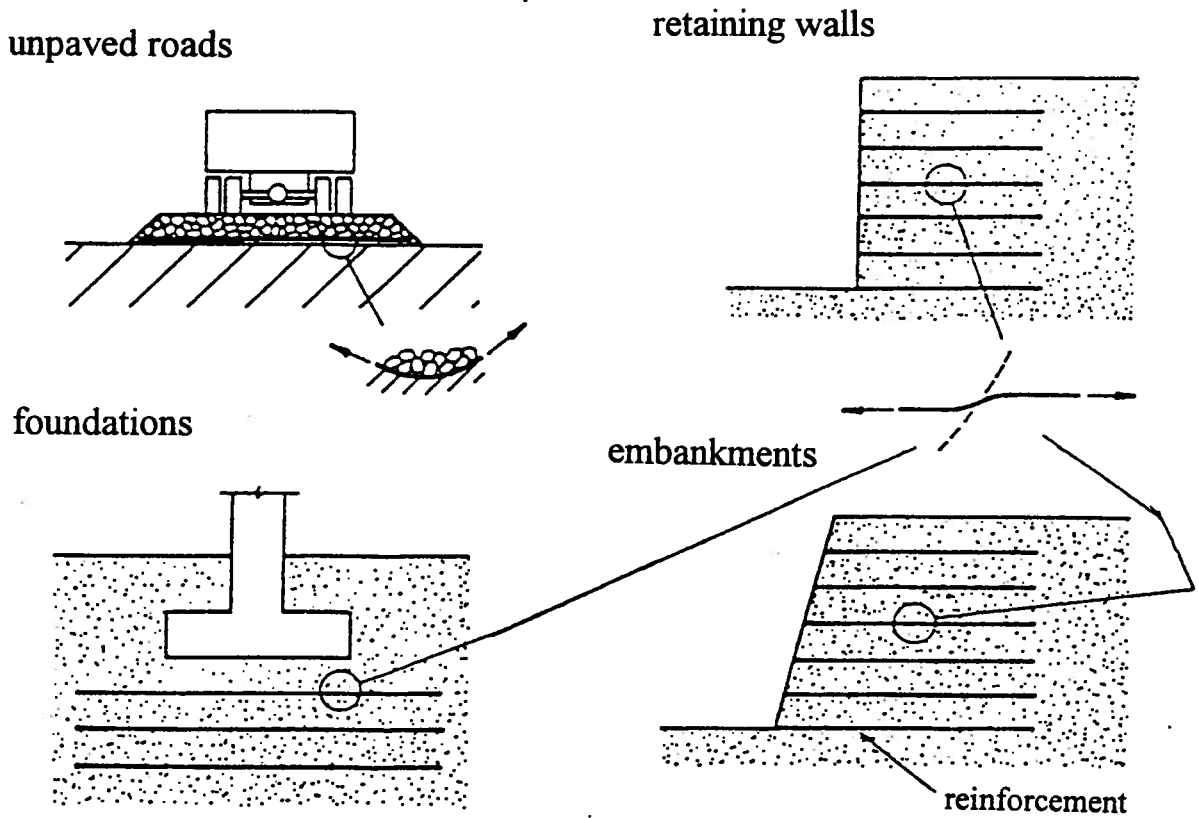


Figure 2.1: Typical examples of soil reinforcement applications (after Palmeira, 1987)

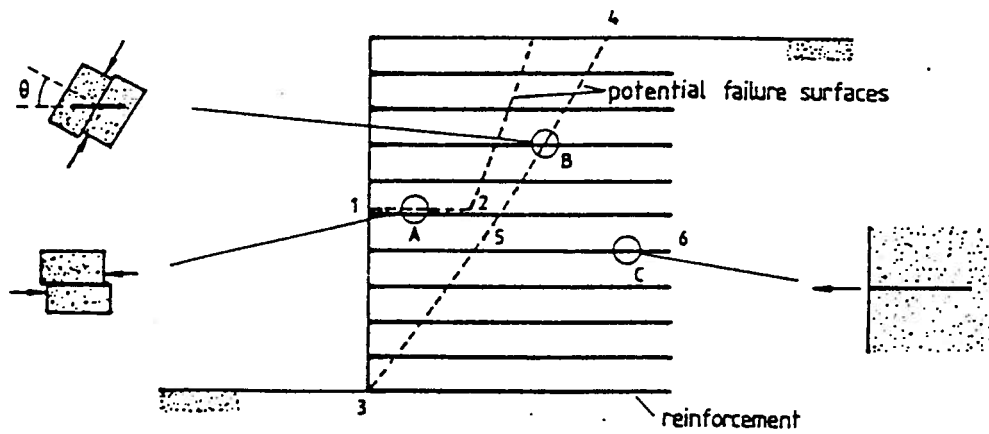


Figure 2.2: Failure mechanisms of reinforced soil structures (after Palmeira, 1987)

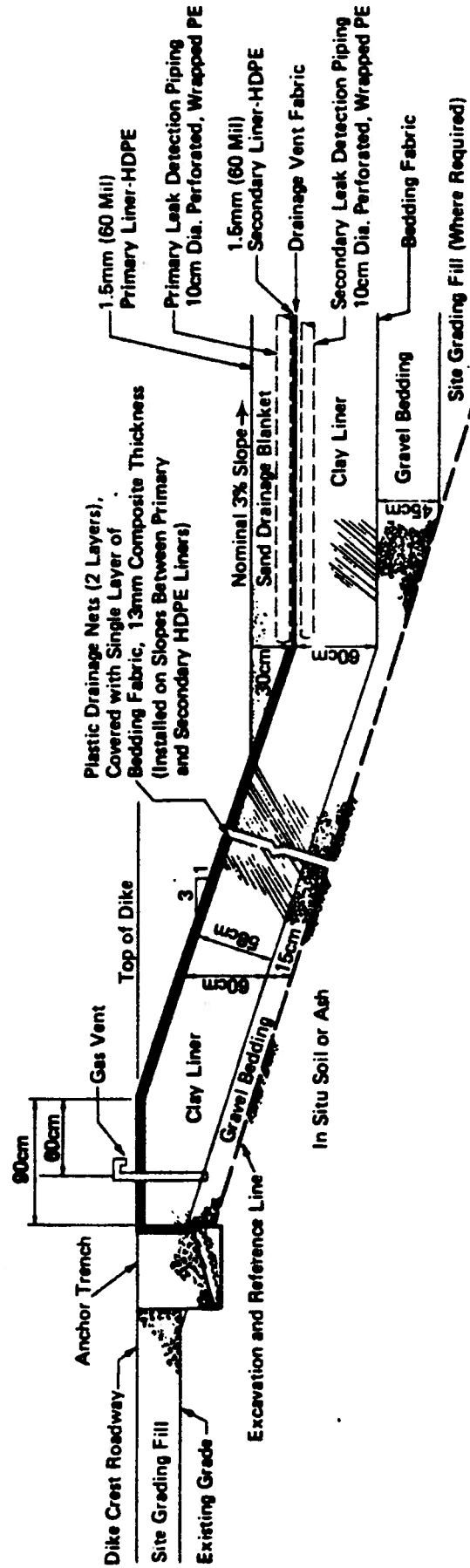


Figure 2.3: Section showing the components of a liner system (after Udvari and Kittridge, 1986)

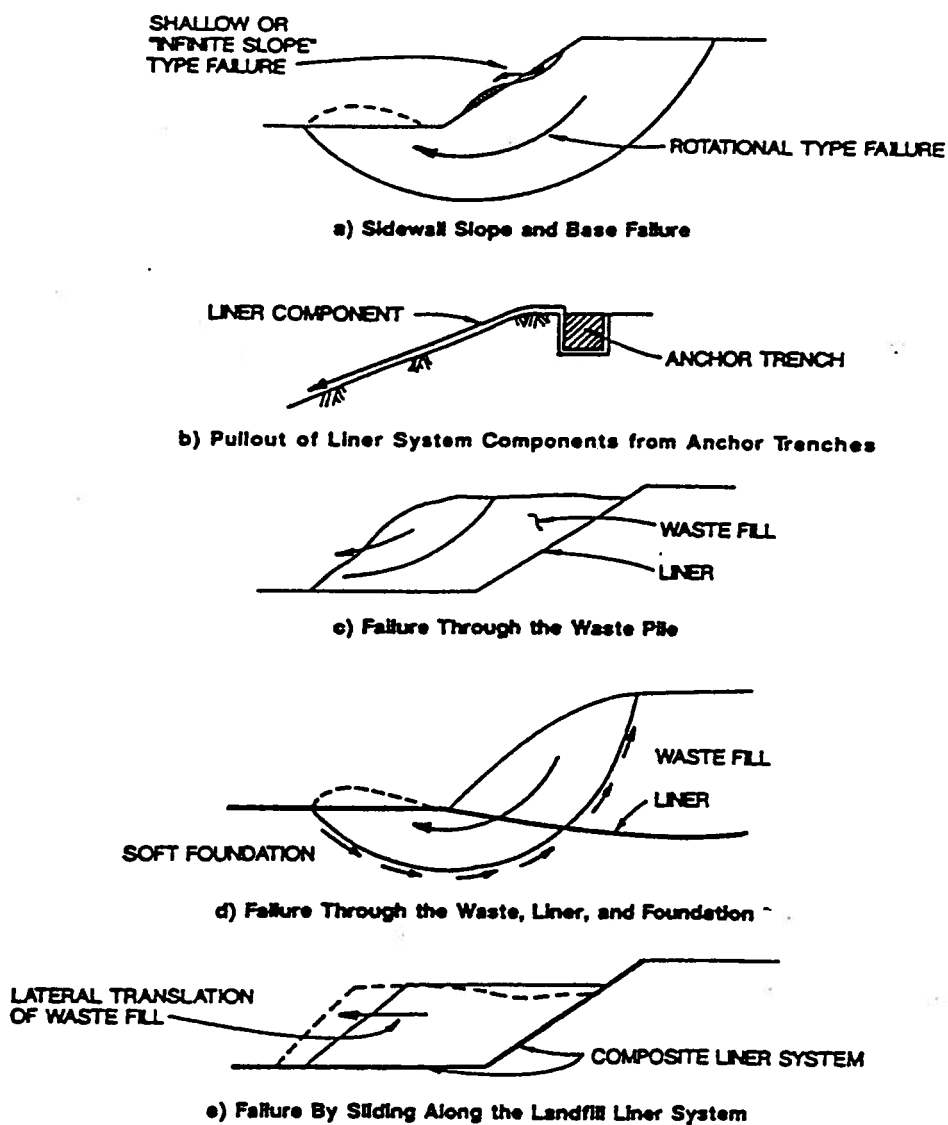


Figure 2.4: Schematic illustration of potential failure modes in a containment facility (after Mitchell and Mitchell, 1992)

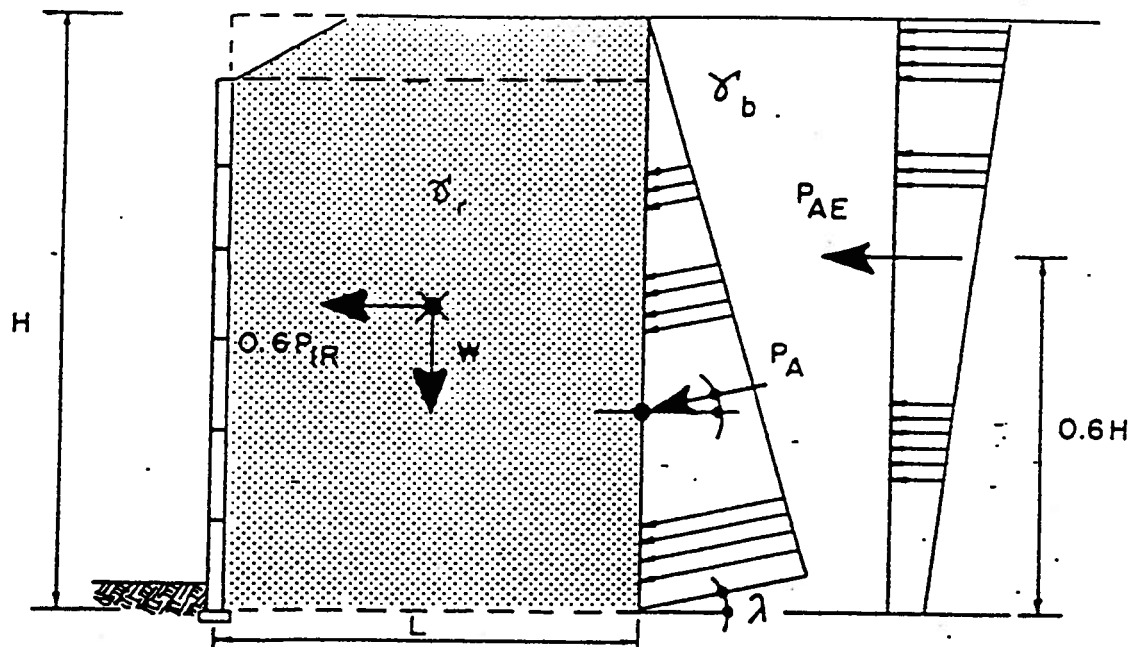


Figure 2.5: Forces acting on a reinforced soil wall (after Christopher et al., 1990)

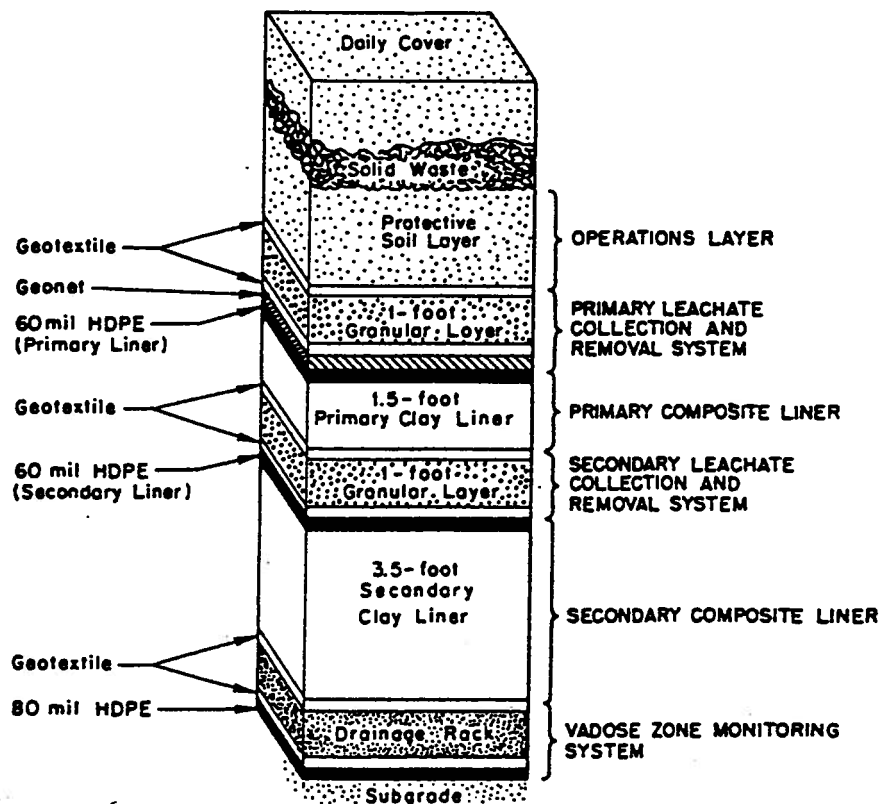


Figure 2.6: Schematic illustration of the multilayer liner system used in the Kettleman Hills landfill (after Seed et al., 1990)

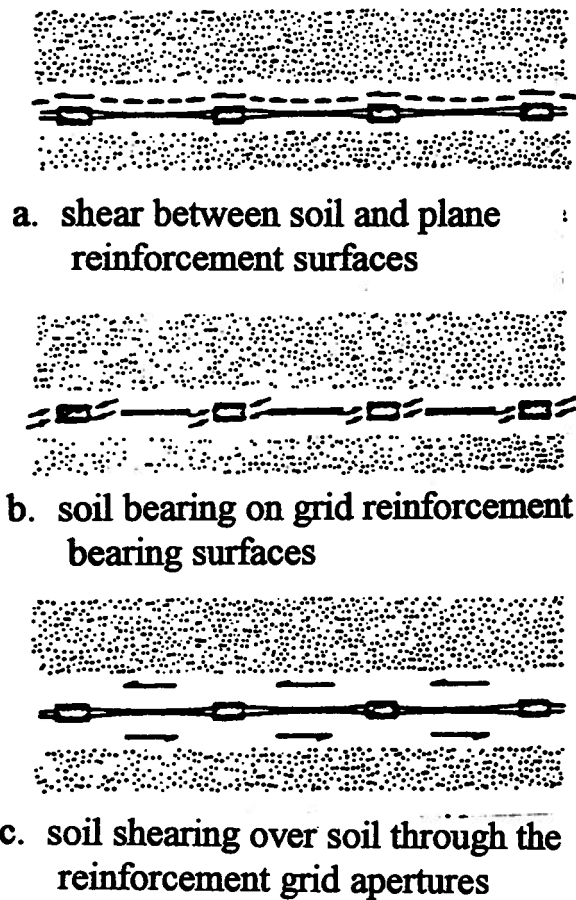


Figure 2.7: Mechanisms of load transfer (after Jewell et al., 1984)

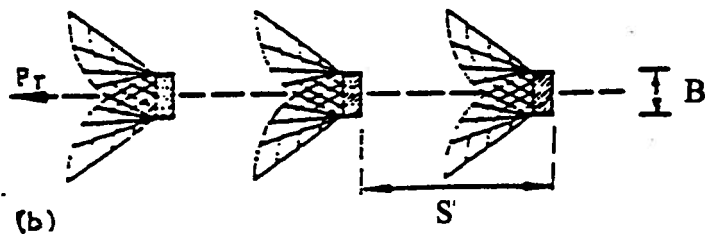
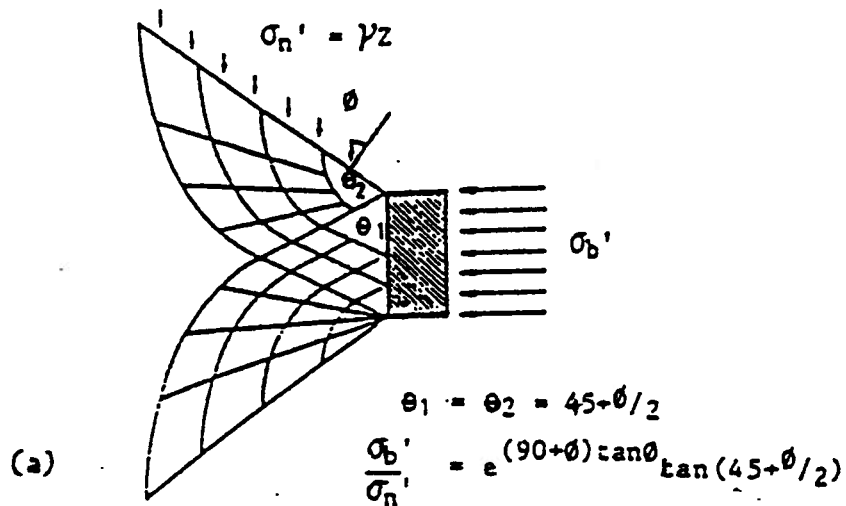
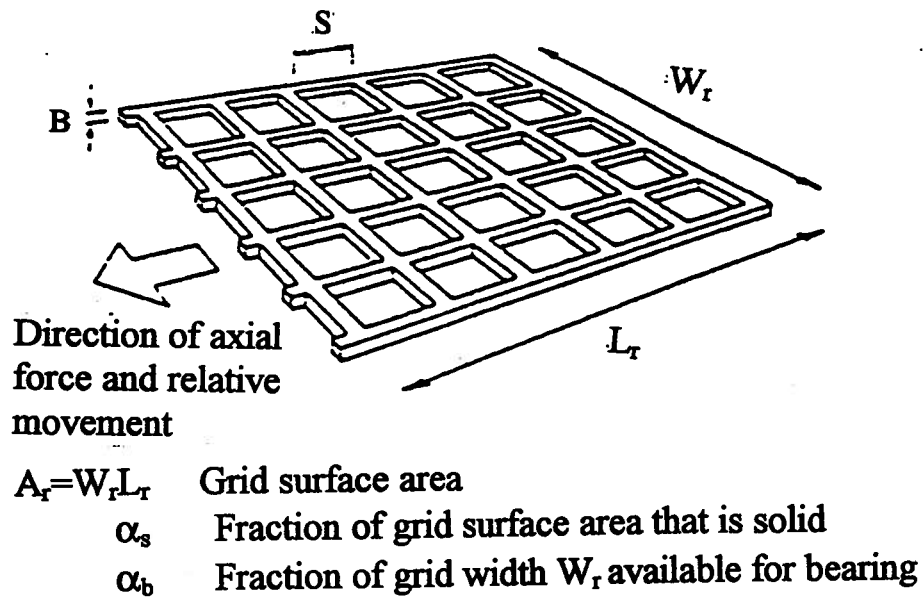


Figure 2.8: Bearing stresses on a grid reinforcement (after Jewell et al., 1984)

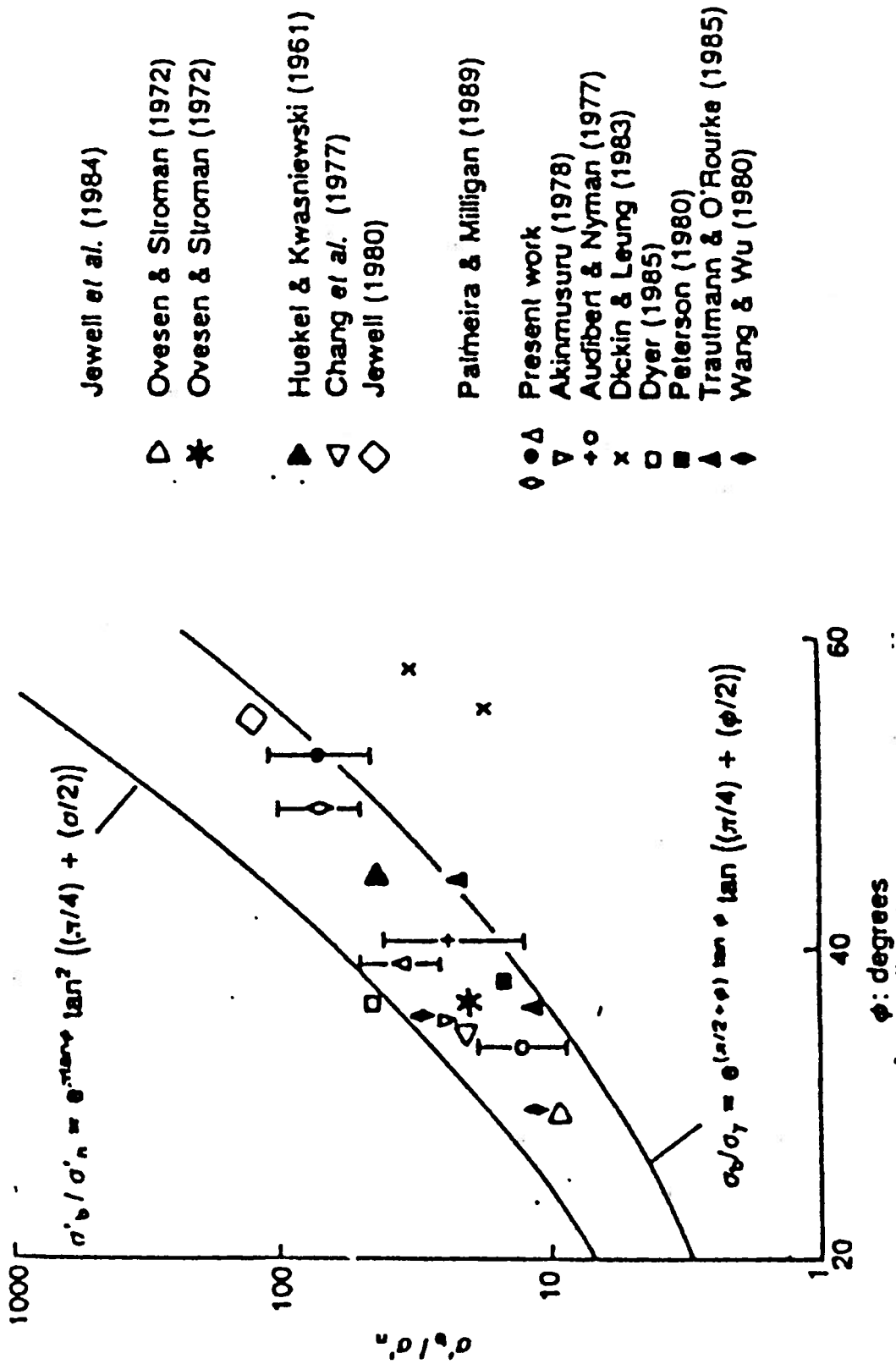


Figure 2.9: Comparison of test results with predicted values of stress ratio (after Jewell, 1990)

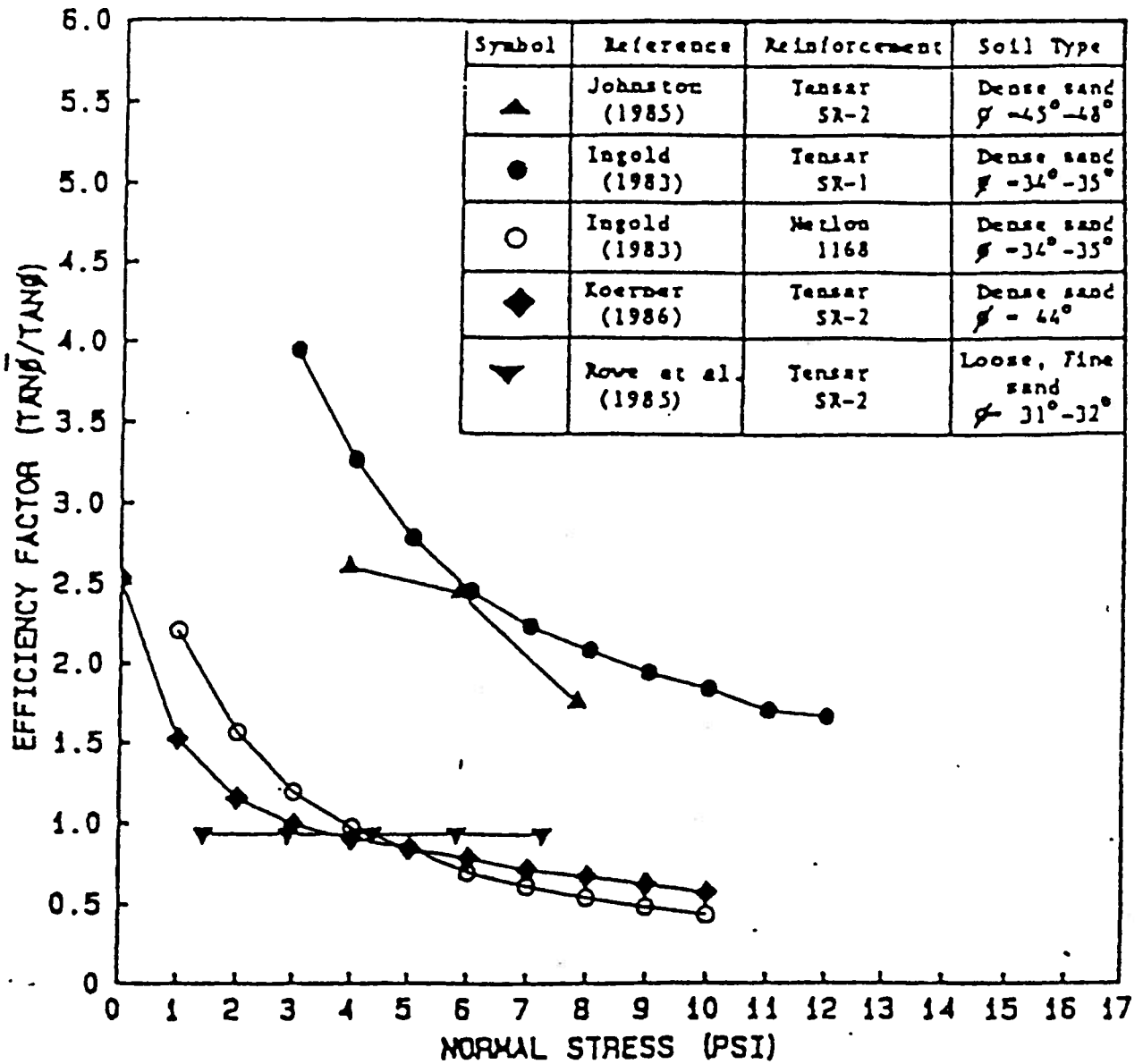


Figure 2.10: Relationship between efficiency factor and confining stress for various geogrids (after Juran et al., 1988)

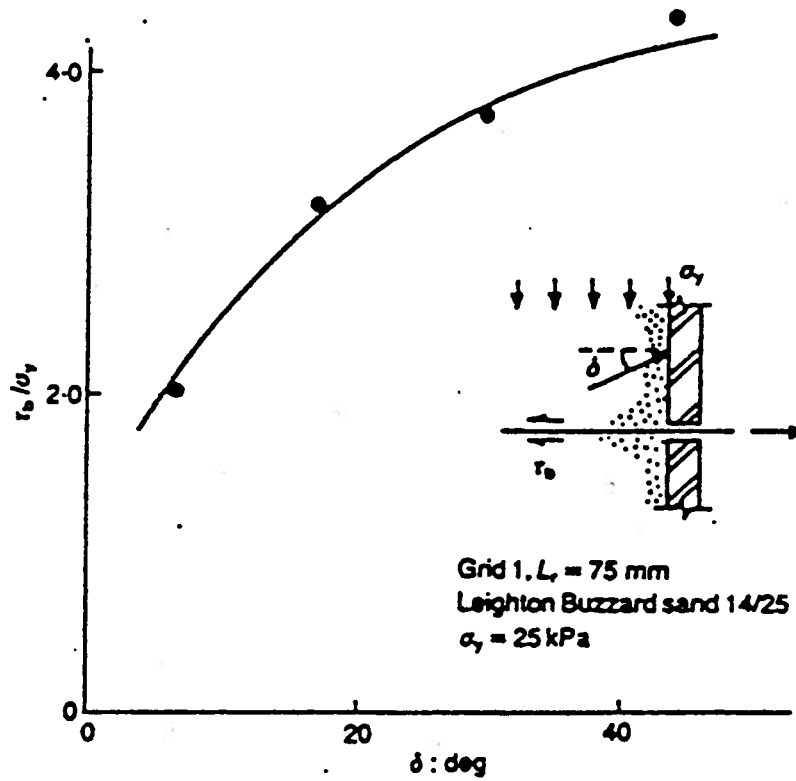


Figure 2.11: Effect of front wall roughness on pullout test results (after Palmeira and Milligan, 1989)

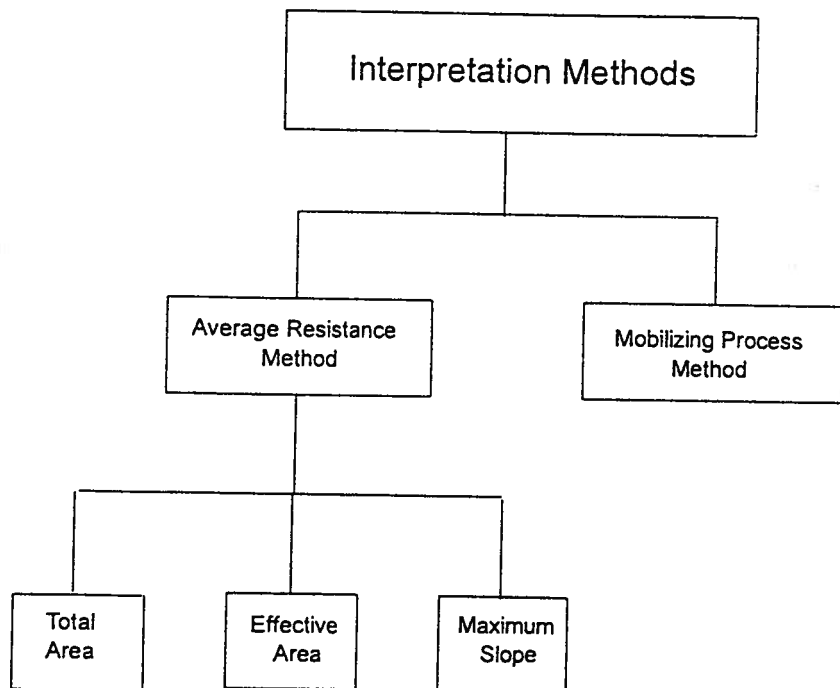


Figure 2.12: A schematic of various interpretation methods for the pullout test

CHAPTER 3

APPARATUS

3.1 Introduction

A large pullout apparatus that was designed and constructed at the University of British Columbia a preliminary study, Raju (1991), was modified substantially for the present study. The apparatus is used to evaluate the development of pullout resistance with increasing displacement of the geosynthetic specimen, and is described in section 3.2. Instrumentation is used to measure pullout force, pullout displacement at the clamped end and embedded end of the test specimen, lateral pressure on the front wall of the apparatus, and the strain in the geosynthetic specimen. The instrumentation scheme and data acquisition system are described in section 3.3.

3.2 Large Pullout Apparatus

The apparatus comprises several components: a pullout box which contains the soil sample and geosynthetic test specimen; a hopper for controlled placement of soil in the box to a targeted density; ; a clamp assembly for gripping the geosynthetic test specimen; a servo-controlled, electro-hydraulic system to mobilize pullout resistance through control of displacement or load on the specimen; and a reaction frame. They are described in detail below.

3.2.1 Pullout Box

The internal dimensions of the pullout box were selected to meet the following criteria:

Chapter 3. Apparatus

- (1) the box should be long enough to accommodate a geosynthetic test specimen representative of the material used in field structures;
- (2) the box should accept test specimens of length to width ratio up to 2; and
- (3) the width and the depth of the pullout box should be large enough to minimize the effect of boundary shear stresses.

The first two criteria help establish the dimensions of the test specimen: a minimum length of the reinforcement in the resistant or anchorage zone beyond any postulated slip surface in a reinforced soil structure is commonly taken as 1 m or 3 ft (Christopher et al., 1990). Therefore, a test specimen of dimension 1 m in length and 0.5 m in width was selected as a basis for testing. The third criterion implies that the pullout box dimensions in plan view should be sufficiently larger than the test specimen and the box deep enough to reduce the influence of the side, top and bottom boundaries respectively. Little experience was available on this matter of clearance at the time of design and fabrication. In the absence of specific guidance the internal dimensions of the pullout box were chosen to be: 1.3 m long, 0.64 m wide and 0.63 m deep, and the influence of specimen dimensions assessed in the program of testing. The box accommodates a soil sample 1.3 m long, 0.64 m wide and 0.6 m deep, and provides a clearance of 7.5 cm between the specimen and the side wall of the apparatus. It gives a clearance of 0.03 m to seat a surcharge bag on top of the soil sample that is in contact with the top plate of the pullout box. In a recent ASTM draft proposal for pullout testing, the minimum dimension for the pullout box is proposed to be: 0.76 m long, 0.46 m wide and 0.305 m deep. Also a minimum clearance on the sides is proposed to be 7.5 cm or 15 cm when the side wall friction is minimized, or not minimized, respectively. Based on a parametric study Farrag et al. (1993) concluded that a minimum clearance of 150 mm is

Chapter 3. Apparatus

necessary in their pullout box to reduce the effect of the side boundary friction. The ASTM draft proposal further recommends the use of a metal sleeve to minimize the influence of the front boundary. The pullout apparatus used in this research meets the requirements of the ASTM draft proposal except for the metal sleeve recommendation: this was to permit measurements of horizontal stress on the front wall of the pullout box.

The pullout box comprises a base frame, base plate, two side frames, and two end plates with supporting frame work, see Figures 3.1 and 3.2. The base frame is made of 76 mm x 76 mm mild steel tube. It supports the pullout box and provides a reaction for the pullout force and the applied normal stress on the test specimen. The base plate of the pullout box is made of 13 mm thick aluminum plate. It provides a rigid lower boundary for the sample, and supports the two side frames and two end frames. The side frames are also made of 7.6 cm x 7.6 cm mild steel tube. A 2.5 cm thick plexiglas sheet, that is fixed to the side frame, forms the side walls of the test box. A 0.3 cm thick glass sheet is glued to the inside face of the plexiglas to minimize friction between the sand sample and side walls. The front wall of the apparatus is made of two 13 mm thick aluminum plates mounted on the end frame with a 12 mm slot between them at the mid-height of the soil sample, through which the test specimen is pulled. Details of the slot arrangement are illustrated in Figure 3.3. The back wall of the apparatus is a 13 mm thick aluminum plate: a small hole of diameter 16 mm is centrally located through which wires from the instrumentation on the test specimen are taken out of the box.

The pullout reaction frame of the apparatus is made of mild steel flats and bars, and bolts to the base frame. It supports the pullout assembly used to load the test specimens.

Chapter 3. Apparatus

Bending restraint to the pullout frame is provided by a pair of stiffeners at 45° to the base frame, see Figure 3.2. Two hollow circular tubes, connected between the pullout frame and the side frame of the apparatus, are used to transfer bending stresses to the side frames.

3.2.2 Hopper

A hopper is used for controlled placement of the sand sample to a targeted density in the pullout box. Characteristics of the hopper are shown in Figure 3.4. It comprises an aluminum frame that supports two perforated mild steel plates that are overlapped to create a regular pattern of apertures of constant size. The opening size can be altered to suit the type of sand, and therefore grain size used in testing.

Selection of height of fall, and the size of aperture, was based on a study reported by Vaid and Negussey (1988) of factors influencing the maximum achievable density of a uniformly graded Ottawa sand by air pluviation. The rate of placement was varied by adjusting the diameter of aperture, and an optimum value established to minimize interference between falling particles. It was also recognized that a critical height of fall exists for a given particle of sand to impart a terminal velocity and hence achieve a maximum increase in density. Consequently a series of trials were performed in which the sand for testing was air pluviated into a small mould, and variations of the sieve opening size and the height of fall used to determine an optimum configuration. As a result the hopper is fixed on legs above the pullout box to give a height of fall in the range 1.4 m to 0.8 m for the 0.6 m thick sand sample. Two mild steel plates, with apertures of 6 mm diameter on a triangular spacing of 13 mm, are overlapped to give approximately 50% openings. Pneumatically operated cylinders control a

Chapter 3. Apparatus

trap door beneath the perforated plates and initiate pluviation. Dispersion of any dust is prevented by thin plexiglas curtain walls on the hopper assembly.

3.2.3 Pullout Control Assembly

The pullout load assembly comprises a double-acting hydraulic actuator with an associated electro-hydraulic servo-controlled system, and a clamp that connects the rod of the actuator to the test specimen. The hydraulic actuator is bolted to the longitudinal cross-piece of the pullout frame, such that the centre of the piston is in alignment with the slot in the pullout box. The hydraulic system comprises a pump and several control valves that are used to control delivery of oil to the actuator. The hydraulic power supply, manufactured by the MTS systems corporation, operates at 3 gallons per minute and is capable of delivering oil at pressures in the range 20.7 to 34.5 MPa (3000 to 5000 psi). The hydraulic actuator, manufactured by the Cunningham Cylinder Co., has a 82.5 mm diameter rod with a stroke of 152.4 mm. A servo valve, model 760-912A manufactured by Moog Hydraulics, mounts directly on the actuator and interfaces between the electric and hydraulic control.

A closed-loop servo-controlled system is used for control of the movement of the actuator: the principle components are illustrated in Figure 3.5. In closed-loop control, the function to be controlled is continuously measured and used as a feedback for comparison with the demand signal for that function. The difference between feedback and demand, termed error, is then used to correct the system.

Pullout tests are performed under displacement or load control. For displacement-controlled (DC) tests, the feedback signal comes from a displacement transducer monitoring the position of the actuator rod. Tests performed under load-control (LC) use a feedback

Chapter 3. Apparatus

signal from a load cell measuring the tensile force imposed on the test specimen. The two closed-loop control options are illustrated schematically in Figure 3.6. The demand signal for the control system, in either displacement or load control, is generated from software on a 386-SX personal computer, see section 3.4. For tests in which a constant rate of displacement (CRD) or a constant rate of load (CRL) is applied to the test specimen, the demand signal generated is a ramp function. If the requirement of testing is to impose a repeated load, then the demand signal is a waveform. Digital to analog conversion of the demand signal is made using a D/A board in the computer, and the signal is then output to a controller. The controller, manufactured by the MTS systems corporation, is used to amplify the feedback signal, compare it with the demand signal, and generate the error signal for the servo valve. The entire control system was specifically designed and commissioned for this study.

3.2.3.1 Clamp

The clamp used to connect the actuator rod to the test specimen is made of aluminum and comprises three pieces: a lower jaw, an upper jaw and a central insert, see Figure 3.7. The lower jaw is connected to the actuator rod by a self aligning swivel joint, which eliminates any transfer of moment. The inside surface of the lower jaw, which grips the test specimen during testing, is serrated to provide a good grip. The upper jaw fixes to the lower jaw with four screws.

The central insert is a wedge shaped bar that bears against a stainless steel rod mounted in the inside face of the upper jaw. Serrations on the lower face of the insert grip the test specimen. To increase the efficiency of clamping for some test specimens, the central insert was drilled and tapped to accept a series of studs that seat into the apertures of the

Chapter 3. Apparatus

Tensor geogrid specimens or pre-drilled holes in the aluminum test specimen. During testing the upper and the lower jaw move as a rigid piece: any attempt by the jaws to open is prevented by G-clamps placed at four locations across the clamp.

The clamp moves on a support table, see Figure 3.1. It rests directly on a mild steel roller plate, 25.4 mm x 152.4 mm, which translates on ball bearings located at a triangular pitch of 25.4 mm. This roller plate mounts between two arborite surfaces: one glued to the lower jaw of the clamp, and the other to the support table.

3.2.4 Surcharge Pressure

Surcharge pressure is applied to the sand sample by pressurizing a flexible bag filled with water, see Figure 3.8. The bag is 1300 mm long, 640 mm wide and 25.4 mm thick, and is made of PVC. It is pressurized by maintaining a constant head of water for low surcharge pressures (8 to 25 kPa), and by use of an air-water interface chamber for higher pressure.

The air-water interface chamber, modified from a triaxial cell, has two ports on the top and bottom plates. One of the ports on the top plate serves as a vent to the atmosphere while filling the bag with water, whereas the other port acts as a pressure inlet to the reservoir during testing. A regulator on the pressure inlet from the laboratory air supply is used to maintain a constant pressure during testing.

3.2.4.1 Reaction

Reaction to the applied surcharge pressure on the sand sample is provided by a 25.4 mm thick top plate resting on the pullout box, which is held in place by two cross-beams and four tie bars attached to the base frame of the apparatus. The top plate, 147 mm x 777 mm,

Chapter 3. Apparatus

seats on the pullout box and is bolted in position prior to the application of surcharge pressure. The cross beams are fabricated using 76 mm x 76 mm channel sections placed back-to-back, and welded together at the ends using 13 mm thick mild steel plates. Four 25.4 mm diameter high yield steel bars are used to connect the base frame and the top plate.

3.3 Instrumentation

Instrumentation is used to measure pullout force, pullout displacement at the clamped and the embedded end, total pressure on the front wall of the pullout box, water pressure in the surcharge bag and strain in the geosynthetic test specimen.

3.3.1 Pullout Force

Pullout force is measured using a load cell connected between the clamp and the hydraulic actuator. Three load cells were used in the program of testing, all manufactured by Interface Inc.: model 1210AF and 1210AF-1K with a capacity of 44.5 kN (10,000 lbs) and 22.25 kN (5000 lbs) respectively, and S type with 4.45 kN (1000lbs) capacity. All three load cells are powered with a 10V DC supply.

3.3.2 Pullout Displacement

Pullout displacement of the clamped end of geosynthetic specimen is measured using a linear variable differential transformer (LVDT) mounted on each end of the central insert of the clamp. They are both DC-DC types SE 373/100, manufactured by SE LABS, with a 100 mm stroke. They are mounted independently of the base frame using a separate frame that rests on the floor. Displacement of the insert is taken as the mean of these two measurements.

Chapter 3. Apparatus

Displacement of the embedded end of the specimen is monitored by a tell-tale cable connected to a LVDT that is mounted outside the back wall of the box, see Figure 3.1. The LVDT, a DC-DC type, manufactured by Transtek, has a total stroke of 100 mm. The other end of the tell-tale cable is connected to some test specimens with a screw (aluminum sheets and Tensar geogrid) and to all others using glue.

3.3.3 Pressure on the Front Wall

Six total pressure transducers (TPT) were used to measure the distribution of lateral stress on the front wall of the pullout box: their locations are shown in Figure 3.9. The transducers, type AB/HP manufactured by Data Instruments, are bonded semiconductor strain gauge pressure transducers. Three transducers are mounted above the slot and three below it along a vertical axis through the centre line of the sample. Two transducers have a range 0-100 kPa; three have a range 0-50 kPa; and one has a range 0-25 kPa. They are mounted flush with the inside surface of the front wall of the pullout box. Transducers at locations TPT-3 and TPT-4 are of the 0 to 100 kPa range, while those at locations TPT-2, TPT-4 and TPT-5 are 0 to 50 kPa. The most sensitive transducer, with a range 0 to 25 kPa, was used at location TPT-1. Each transducer was calibrated in contact with soil using a separate device that applies air pressure via bellofram to small chamber in which the transducer is mounted.

3.3.4 Water Pressure Transducer

A gauge pressure transducer, type SP100-15G, manufactured by Magnetek Transducer Products, was used to monitor the pressure in the surcharge bag during the experiment. The range of the transducer is 0 to 100 kPa. The transducer is mounted on a bracket that is fixed at the same level as the surcharge bag. The body of the transducer was

Chapter 3. Apparatus

dismantled, and connected by immersing in water, to ensure that the cavity is free of air. Full saturation of connecting tubing was ensured by using a hypodermic syringe to fill the connecting hoses.

3.3.5 Strain Gauges

Strain gauges were fixed on the geosynthetic specimen to measure tensile strain during testing. A full description of the gauges, type EP-08-250BF-350 OPTION E, manufactured by the Micro-Measurements Division of Measurements Group Inc., and the procedure for bonding them was developed after Bathurst (1990) and is reported in Appendix-A. The wires connect to the data acquisition system through a circuit completion box, where dummy gauges are used to complete a full Wheatstone bridge.

A schematic illustration of the strain gauge locations (SG-1 to SG-5) is given in Figure 3.10. The mounting locations of the gauges on a test specimen are dependent on the type of specimen. Hence, in the reporting of a gauge location, the distance from the front wall is normalized with respect to the initial embedded length of the geosynthetic test specimen (x/L_{ei}).

3.4 Data Acquisition System

The data acquisition system consists of a DAS-16 board, a 386-SX desktop microcomputer, a signal conditioning unit, and a data acquisition program. The DAS-16 board is a multifunction, high speed A/D (analog/digital), I/O (input/output) expansion board, manufactured by the Metrabyte Corp. It includes a 12-bit successive approximation converter and user-selectable gain, and accommodates 16 single-ended channels or 8 double-ended (differential) channels. The signal conditioning unit was designed and built at UBC. It

Chapter 3. Apparatus

supplies DC. input to the transducers, and amplifies the output using a variable gain on each channel. The transducer signals from the signal conditioning unit are taken to the DAS-16 that converts the signal from analog to digital. A digital to analog converter channel of the DAS-16 board is used to apply a demand signal to the servo-control valve.

A data acquisition program was written using Quick Basic to support the program of testing. Features of the program are:

- **Program input:-** The test initialization file is read before starting the program. The input parameters include: test name, length and width of the test specimen, and calibration coefficients of all the transducers. For cyclic loading tests, additional input parameters are: frequency of loading and expected maximum pullout resistance of the test specimen from a CRD test.
- **Scan before testing:-** Continuous scanning of all channels before testing, and recording of initial readings of the transducers.
- **Scan during testing:-** Continuous scanning of all channels during testing. The demand and the measured displacement or load are written to the computer screen as a real time plot, together with displacement of the clamped end, to allow monitoring of test progression.

The test is terminated automatically when actuator travel distance exceeds 76 mm in the case of displacement-controlled tests. In load-controlled tests, the test continues until the specimen fails in pullout or in tension. A data reduction program was developed to reduce the results to engineering units.

Chapter 3. Apparatus

- | | |
|---------------------------|-----------------------|
| 1 Soil sample | 9 Servo valve |
| 2 Test specimen | 10 LVDT |
| 3 Base frame | 11 Hydraulic actuator |
| 4 Support table for clamp | 12 Pullout frame |
| 5 Clamp | 13 Load cell |
| 6 Surcharge bag | 14 LVDT |
| 7 Top plate | |
| 8 Reaction frame | |

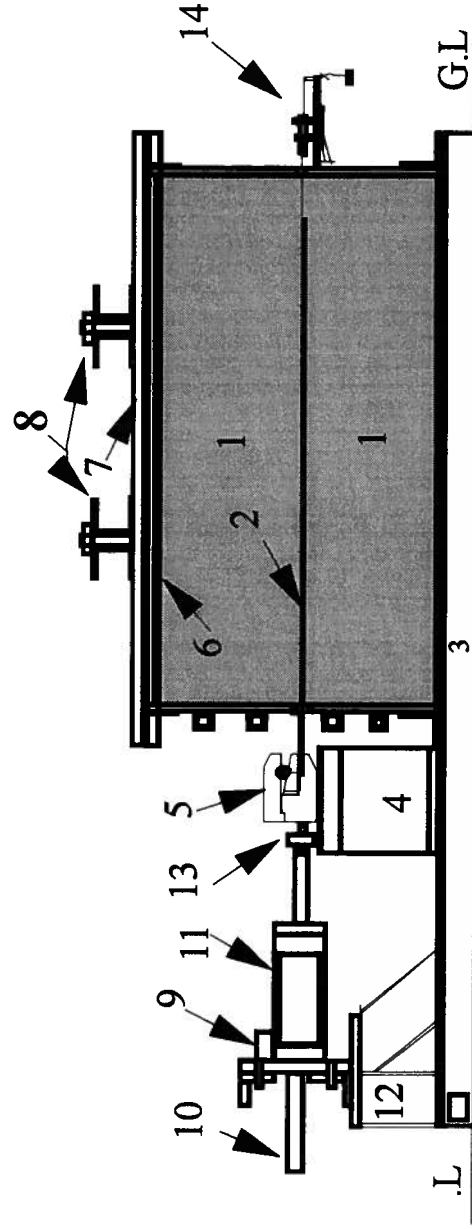


Figure 3.1: Components of the pullout apparatus

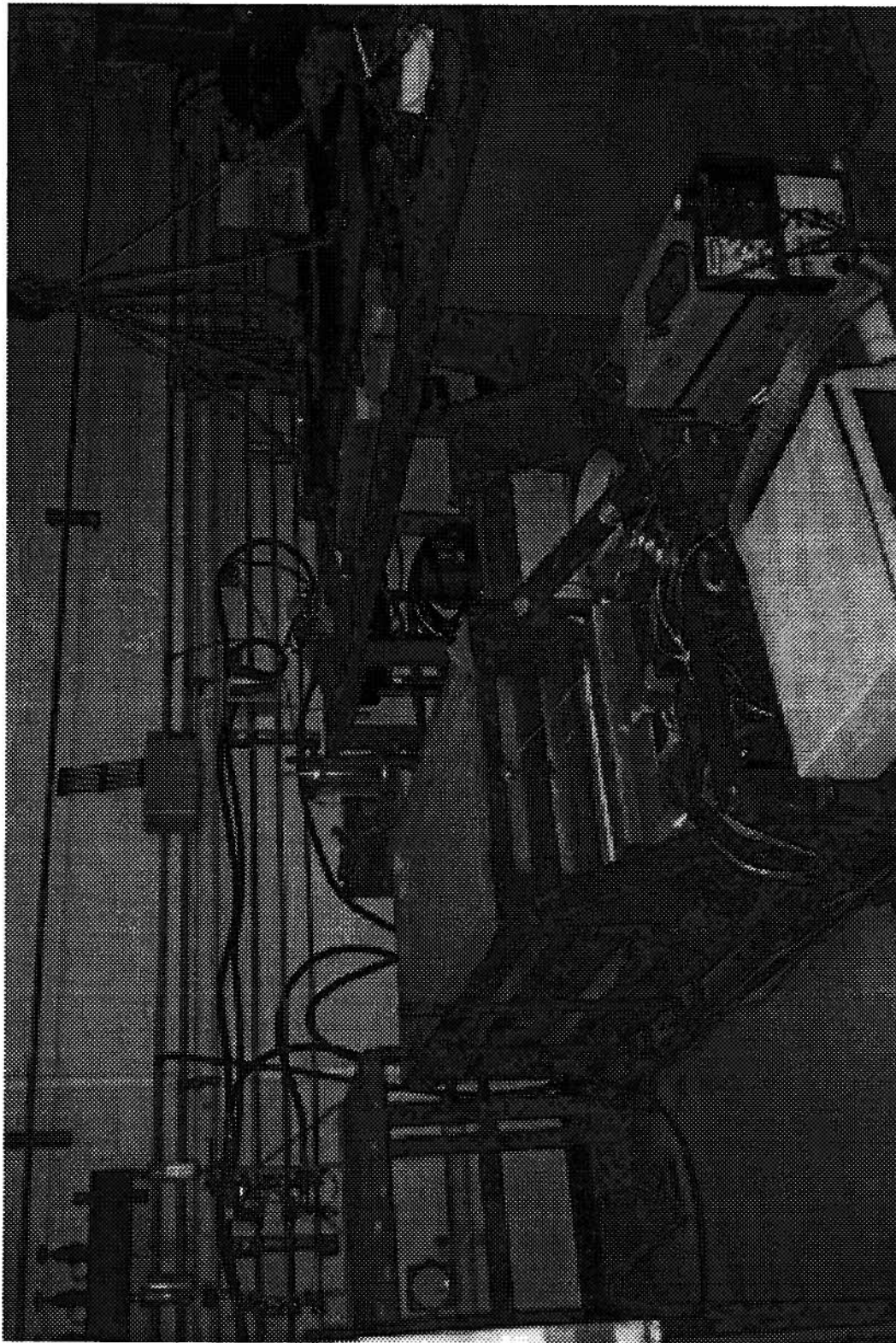


Figure 3.2: Photograph illustrating components of the pullout apparatus

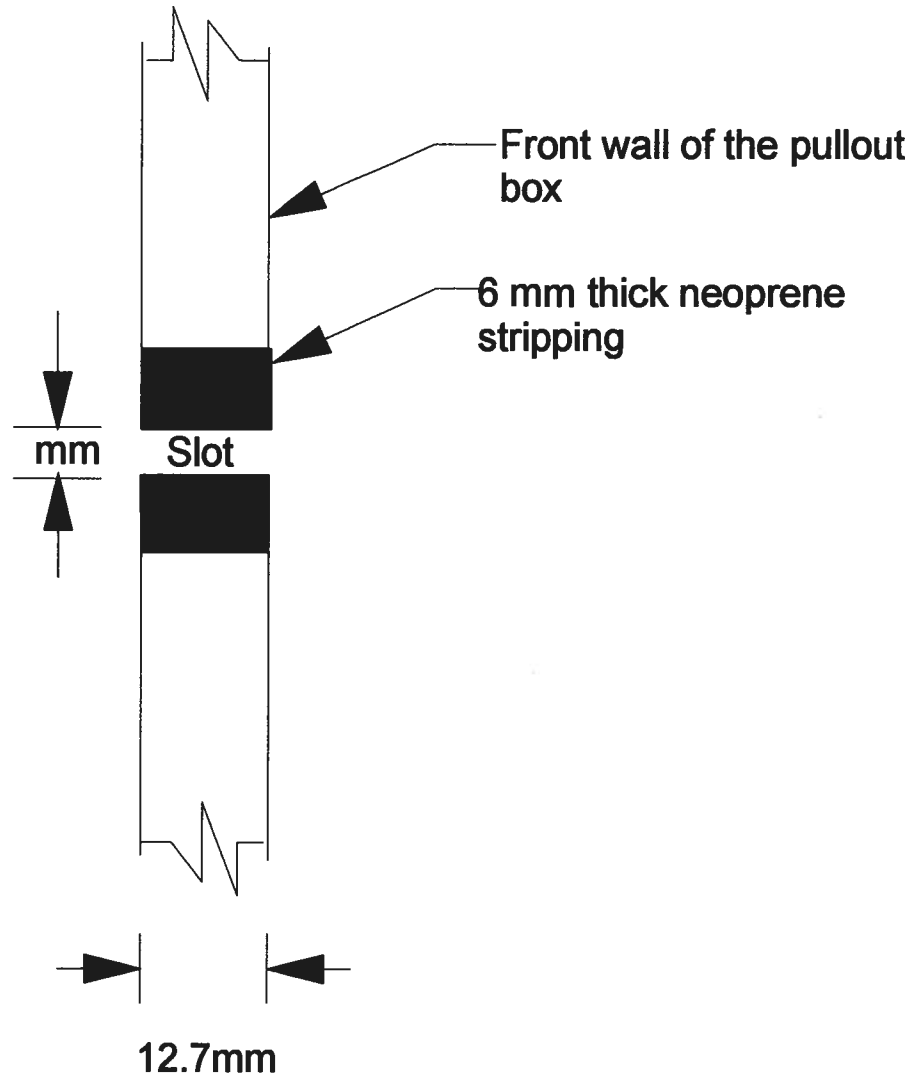
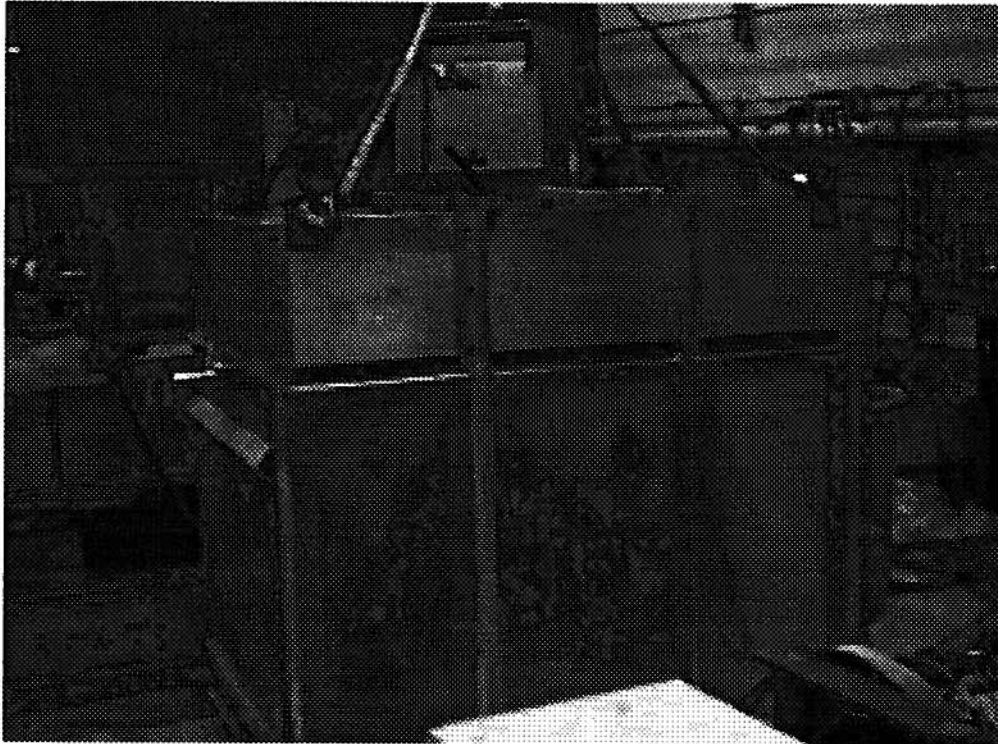


Figure 3.3: Slot arrangement on the front wall of the apparatus

Chapter 3. Apparatus

Side view



Top view

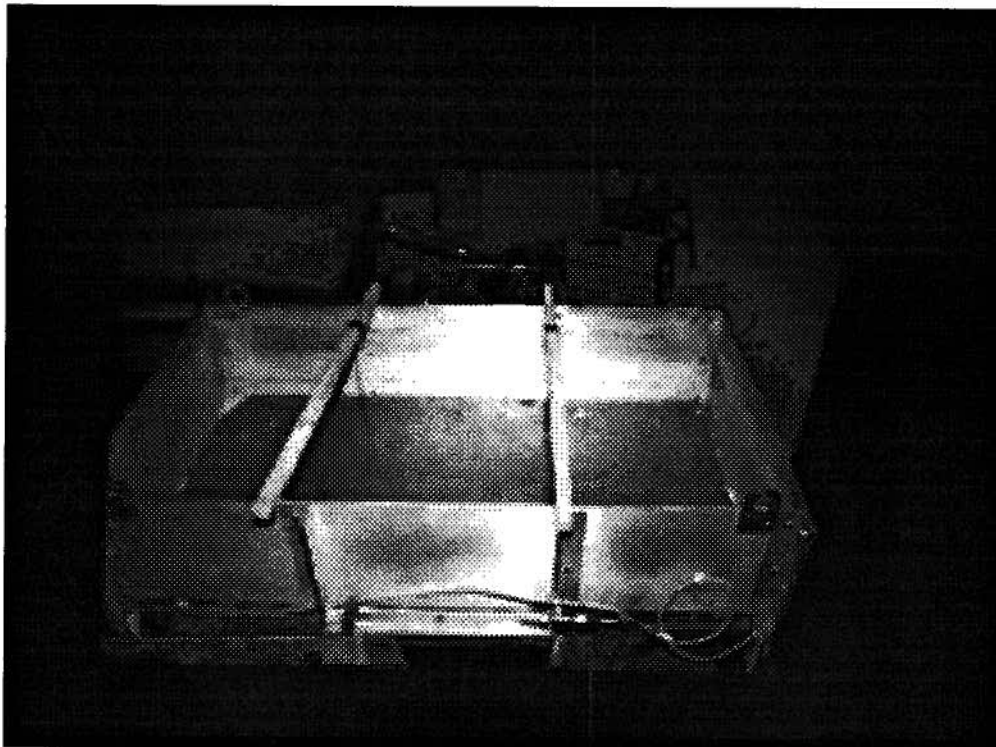


Figure 3.4: Top and side view of the hopper assembly

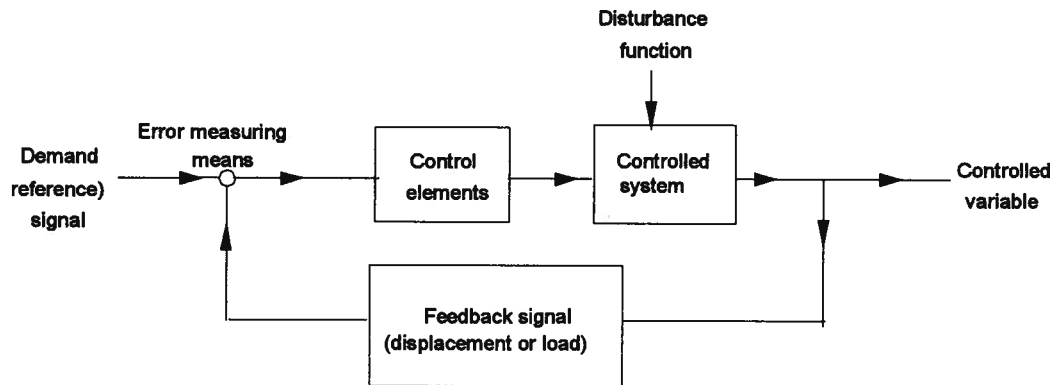


Figure 3.5: Principle components of closed-loop control

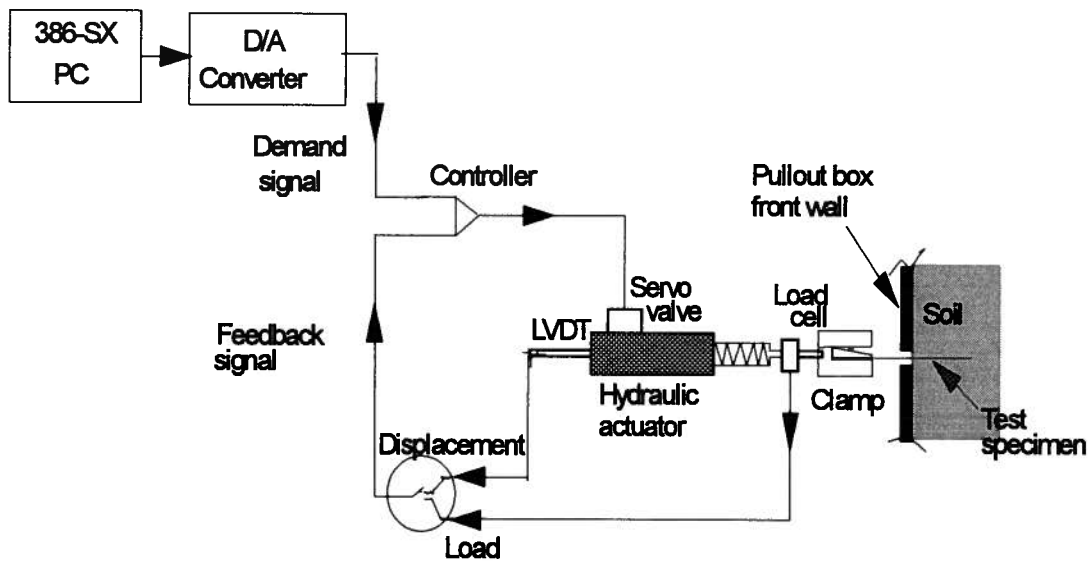


Figure 3.6: Schematic illustration of the closed-loop control system

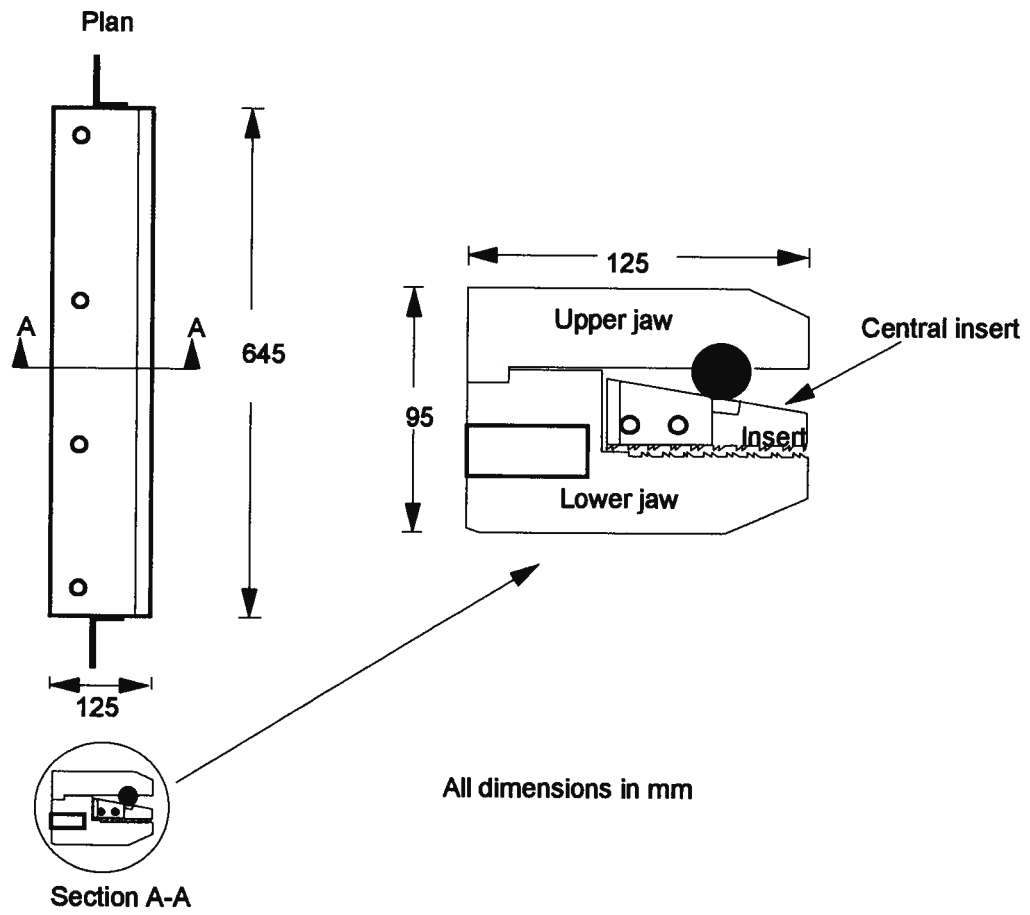


Figure 3.7: Details of the clamp

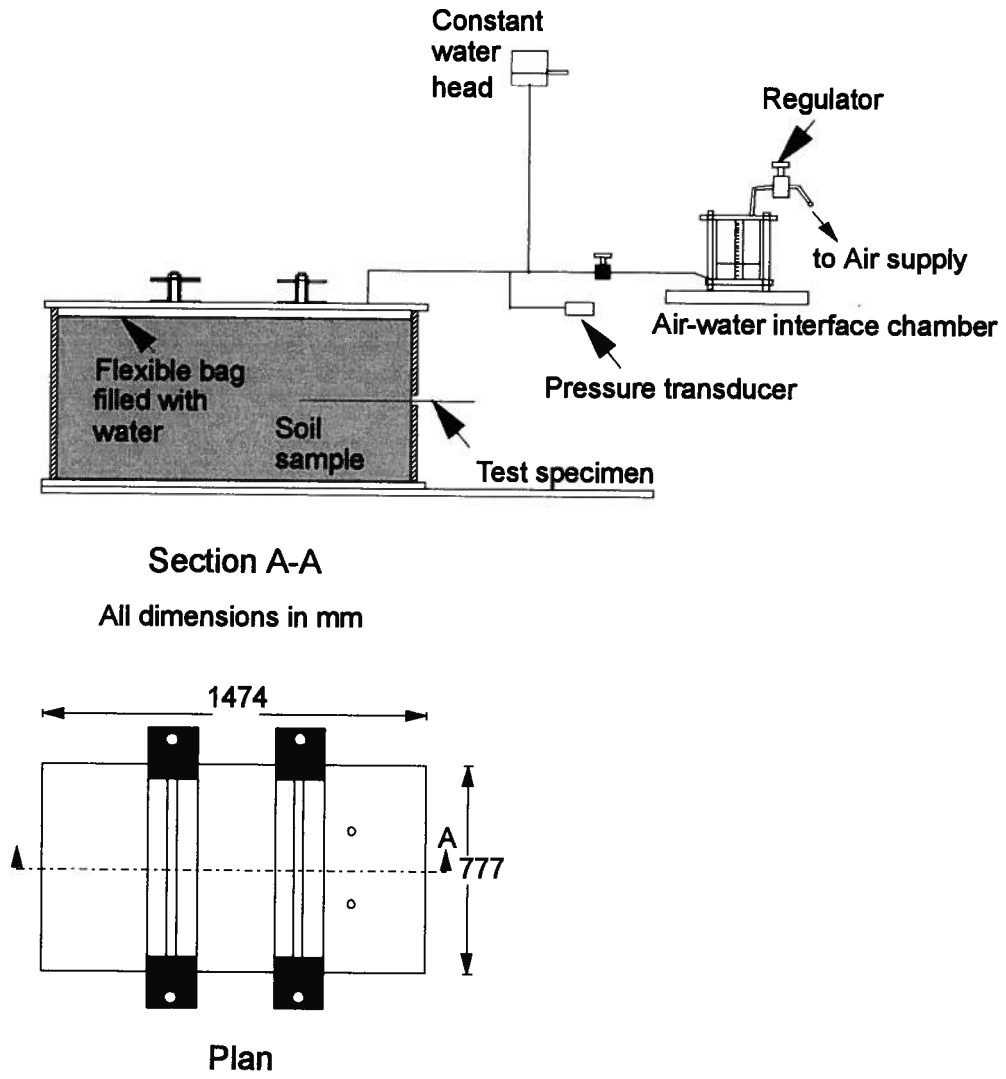


Figure 3.8: Reaction frame and the pressurizing system

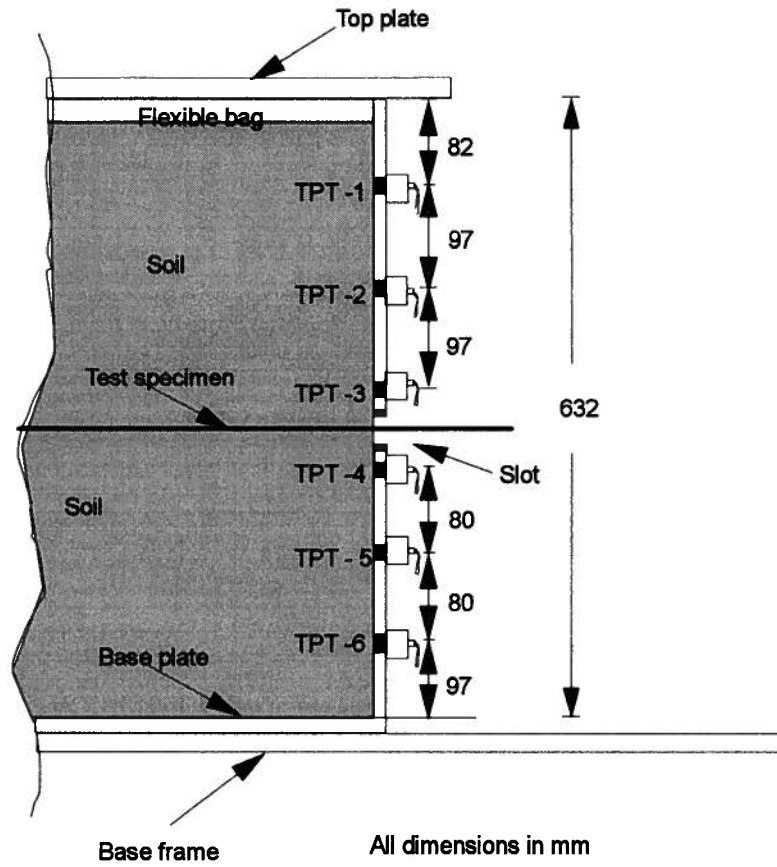


Figure 3.9: Location of pressure transducers on the front wall of the pullout box

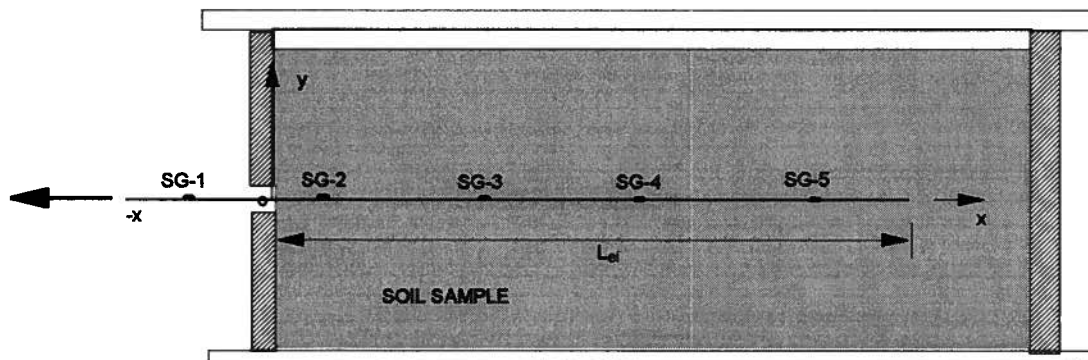


Figure 3.10: Strain gauge locations with respect to the front wall of the apparatus

CHAPTER 4

MATERIAL PROPERTIES

4.1 Introduction

Materials used in the program of pullout testing are the soil, and the pullout test specimens which are classified as either extensible inclusions, or inextensible inclusions. The extensible inclusions are the geosynthetic specimens: geogrids and geomembranes. The inextensible inclusion is a rough aluminum sheet that was used for comparative purposes. Some material properties that are relevant to the present study are reported in the following sections based on laboratory testing and the manufacturers' technical literature.

4.2 Sand

The soil used in the present study is a rounded silica sand, supplied from a source in Minnesota, USA, by the Badger Mining Corporation. This sand was chosen because of its high crush strength and gradation, based on experiences with degradation of an angular sand used in earlier work (Muthu, 1991). Grain size distribution curves determined for samples prior to, and at the end of the program of testing are presented in Figure 4.1. It is a uniformly graded sand ($C_u=1.5$) with little or no fines. Particle size diameters are in the range 0.1 mm to 2 mm, with a value of d_{50} between 0.8 and 0.9 mm. Inspection showed the particles to be subrounded to rounded. The similarity of grain size distribution curves indicates there was no significant particle breakage or crushing during testing. Determinations of a minimum and maximum void ratio according to ASTM D 4253-93 and ASTM D 4254-91 gave $e_{\min} = 0.49$ and $e_{\max} = 0.62$ respectively.

Chapter 4. Material Properties

4.2.1 Angle of Friction

Direct shear tests were performed to establish the angle of internal friction of the sand (ϕ_{ds}). A plane strain friction angle (ϕ_{ps}) for the sand is determined knowing the angle of dilation during shearing as shown in the following section. The plane strain friction angle at large displacement corresponds to the constant volume friction angle of the sand.

4.2.1.1 Direct Shear Tests

A small scale laboratory shear box, 76 mm x 76 mm in plan, was used to study behaviour of the sand in direct shear at large displacement. Sand samples were prepared by air pluviation which resulted in relative densities between 40 and 60%. Although lower than the initial relative density of the pullout tests (85-90%), the objective was to allow a comparison of residual strength values. Tests were performed at normal stresses between 5 kPa and 30 kPa, a range chosen to encompass that applied to the soil samples during pullout testing. Results are reported as a normalized stress ratio (τ/σ) against shear displacement in Figure 4.2. A maximum stress ratio for the densities tested is observed at all stress levels at a similar shear displacement of approximately 1.4 mm. As shearing continues, the stress ratio decreases to a constant value. The magnitude of stress ratio at large displacement appears to be dependent on stress level: a higher value is observed at the lower stresses (4 and 10 kPa).

The relationship between normal displacement and shear displacement shows a similar response for all tests, see Figure 4.3. An initial, slight tendency to contract changes rapidly to a dilative behaviour at a shear displacement of 0.6 mm. Dilation continues to a shear displacement of 3 mm, and thereafter shearing takes place at essentially constant volume.

Chapter 4. Material Properties

Considering the stress ratio and the dilatancy characteristics, a plane strain friction angle for the sand, (ϕ_{ps}), is obtained using the following expression, after Jewell and Wroth (1987):

$$\sin \phi_{ps} = \frac{\tan \phi_{ds}}{\cos \psi (1 + \tan \phi_{ds} \tan \psi)} \quad (4.1)$$

where:

ψ is the angle of dilation in the soil; and

$\tan \phi_{ds} = \tau/\sigma$ is the normalized stress ratio in direct shear.

The change in plane strain friction angle with increased shear displacement is shown in Figure 4.4. Residual values at large displacement are in the range 29° to 36° : the variation is attributed to slight stress dependency, see Figure 4.5.

4.3 Geosynthetic Test Specimens

Geosynthetics are polymeric materials, and exhibit a marked visco-elastic behaviour. Consequently the load-extension behaviour is governed by temperature, strain magnitude and rate of strain. Common polymers used in the manufacture of geosynthetics are polyethylene, polypropylene, polyester and polyvinylchloride. Carbon black is added to protect against degradation in the presence of UV radiation.

Five types of geosynthetic specimens were used in the testing program to investigate the influence of structural geometry and tensile strength of the specimen. They are broadly classified in two categories: geogrids and geomembranes.

Chapter 4. Material Properties

4.3.1 Geogrids

The three geogrids used in testing are termed uniaxial grids because the material properties vary with the machine direction (MD) and cross machine direction (CMD) due to the manufacturing process. All of them comprise longitudinal ribs and transverse bars. Some physical and mechanical properties of the geogrids are reported in Table 4.1 from manufacturers' technical literature.

4.3.1.1 Tensar UX-1500

Tensar UX-1500, manufactured by the Tensar Earth Technologies Corp. of Atlanta, Georgia, is a uniaxial grid that is formed by punching small holes in a solid sheet of extruded HDPE and stretching it preferentially in one direction. This action causes the holes to elongate and form the apertures of the grid which exhibits a monolithic structure with high junction strength. Measured dimensions of the geogrid are as shown in Figure 4.6; a test specimen with strain gauges mounted is illustrated in Figure 4.7

4.3.1.2 Miragrid 15T

Miragrid 15T, manufactured by the Mirafi Inc. (now Nicolon/Mirafi Inc.) is a bi-directional grid made of polyester multifilament yarns which are interlocked by weaving to create a stable network such that the yarns retain their relative position. In contrast to the Tensar geogrid this product is more flexible in bending and exhibits a relatively lower junction strength. Measured dimensions of the grid are as shown in Figure 4.8.

Chapter 4. Material Properties

4.3.1.3 Stratagrid 700

Stratagrid 700, manufactured by Strata Systems Inc., of Atlanta, Georgia, is also produced from a polyester yarn. Measured dimensions of the geogrid are illustrated in Figure 4.9. The yarns are bonded, and interwoven at the junctions to form a dimensionally stable structure, with a uniform network of apertures providing significant tensile strength in one principal direction.

Table 4.1: Properties of the geogrid test specimens

Property	Unit	TENSAR UX-1500	MIRAGRID 15T	STRATAGRID 700
Test code		GT	GM	GS
Interlock				
Apertures:				
Machine Direction (MD)	cm	14.478	2.286	5.766
Cross Machine Direction (CMD)	cm	1.676	2.16	1.981
Open area	%	60	60	46
Thickness:				
Ribs	cm	0.127	0.16	0.185
Junctions	cm	0.432	0.16	0.205
Tensile strength				
Wide width strip tensile strength (D4595-86):				
(i) at 5% strain	kN/m	52.4	34.0	32.0
(ii) Ultimate strength	kN/m	86.0	124.0	146.0
Long term design load in MD (GRI GGR)	kN/m	29.2	50.0	68.1
Material				
High Density Polyethylene (HDPE)	%	97.5	---	----
Polyester (PET)	%	---	100	100
Carbon Black	%	2.0	coating	coating
Creep Reduction Factor (CRF)				
Manufacturer's Test Results	ratio	.35 - .39	.55 - .65	.55 - .65
AASHTO Default Values	ratio	.20	.40	.40
Dimensions				
Roll length	m	29.87	45.72	45.72
Roll width	m	1.0 & 1.31	4.05	1.83
Weight/unit area	kN/m ²	0.00746	0.00516	0.00654

Chapter 4. Material Properties

4.3.2 Geomembranes

Two types of geomembranes were used in testing. The smooth membrane was a Novex HDPE sheet, 1.5 mm thick, supplied by Nilex Geotechnical Products Inc; the textured geomembrane was a Gundline HDT, 2 mm thick, manufactured by Gundline Lining Systems Inc., from high density polyethylene. Some physical and mechanical properties of the geomembranes are reported in Table 4.2 from the manufacturers' technical literature.

Table 4.2: Properties of the geomembrane test specimens

Property	Test Method	Unit	Novex-Smooth	Gundline-Textured
Test code			MS	MT
Density (min)	ASTM D1505	g/cc	0.94	0.94
Minimum Tensile Properties:				
Tensile Strength at Break (min)	ASTM D638	kN/m	41	6
Tensile Strength at Yield (min)		kN/m	20.7	29
Elongation at Break (min)		%	700	--
Elongation at Yield (min)		%	10	13
Modulus of Elasticity		MPa	770	--
Tear Strength	ASTM D1004, Die C	kN	0.2	0.27

4.4 Aluminum Sheet Test Specimen

Tests were performed on a rigid test specimen to allow a comparison of behaviour in pullout with that of the extensible geosynthetics. The specimen was a fully roughened aluminum sheet 1.5 mm thick, 0.5 m wide and placed to an embedment length of 0.965 m. The rough texture was achieved by gluing particles of the sand used in testing to its surface.

4.5 Direct Shear Tests on the Sand and Test Specimens

The same small scale laboratory shear box referred to in section 4.2.1.1 was used, with modifications to the bottom half, to study the behaviour of the sand-test specimen interface in direct shear. The objective was to obtain some data for comparison with results from the main program of pullout testing. Coupons of the test specimens were placed on an aluminum block in the lower half of the shear box. Sand was placed by air pluviation in the top half of the shear box. Normal stresses applied were in the range 5 to 20 kPa. The relationship between applied normal stress and the interface shear stress at large displacement is presented in Figure 4.10.

Similar values are obtained for both the sand-sand and sand-textured geomembrane interface (MT). The response is attributed to the shearing surface being transferred into the soil mass from the geosynthetic leading to shearing between sand particles. The interface friction angle for the sand-aluminum interface is 15° . A characteristic value for the arborite-sand, glass-sand, and smooth geomembrane-sand (MS) interfaces is 12.5° at large displacement.

Chapter 4. Material Properties

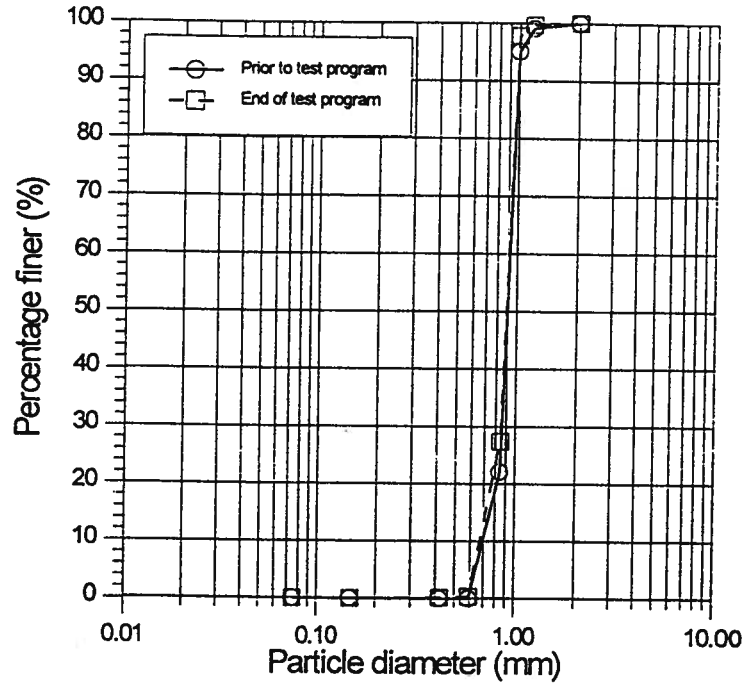


Figure 4.1: Grain size distribution curve of the sand before and after testing

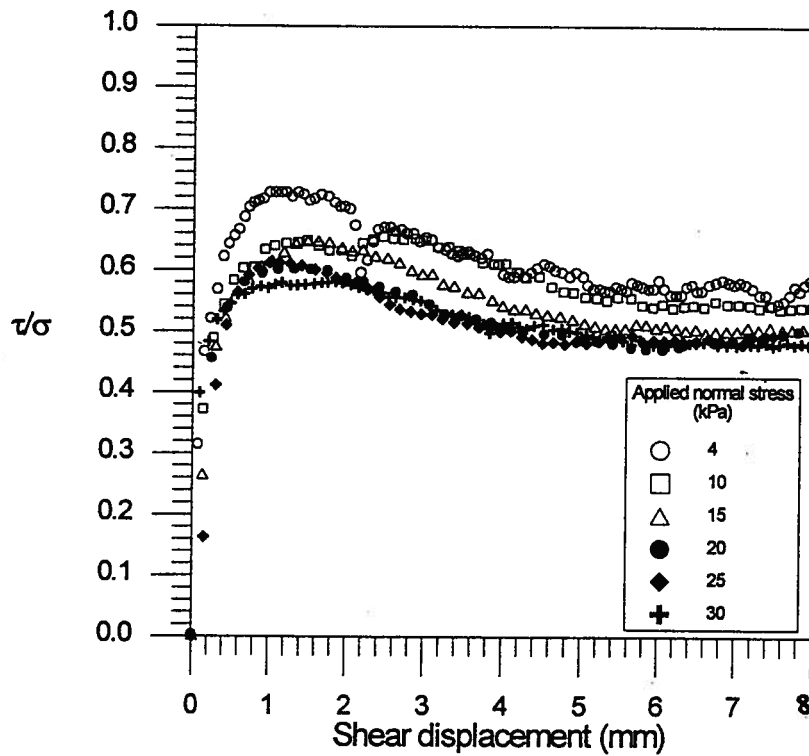


Figure 4.2: Normalized shear stress relationship with shear displacement for direct shear tests on the sand

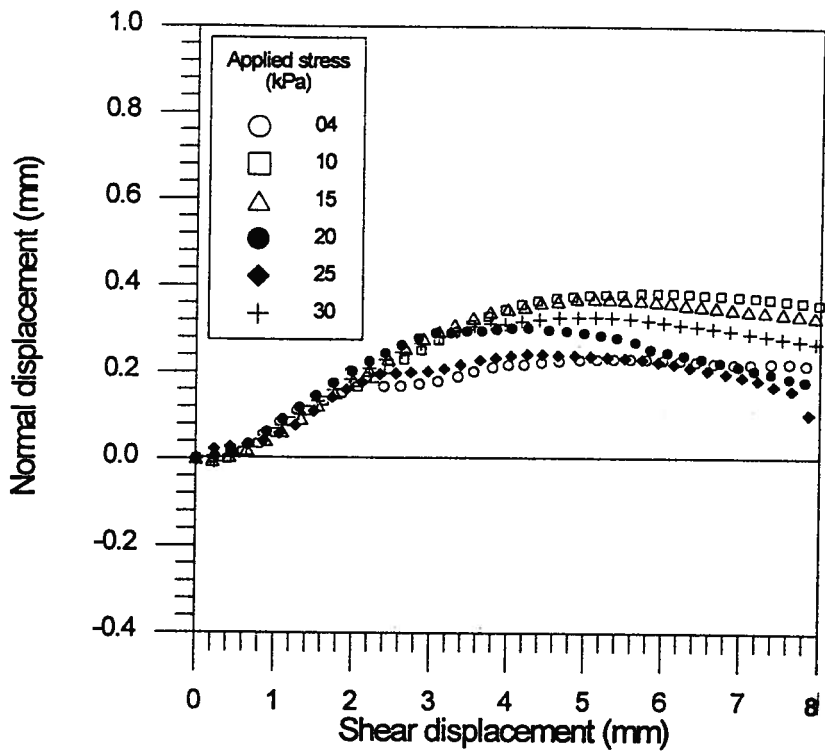


Figure 4.3: Relationship between normal displacement and shear displacement for the sand

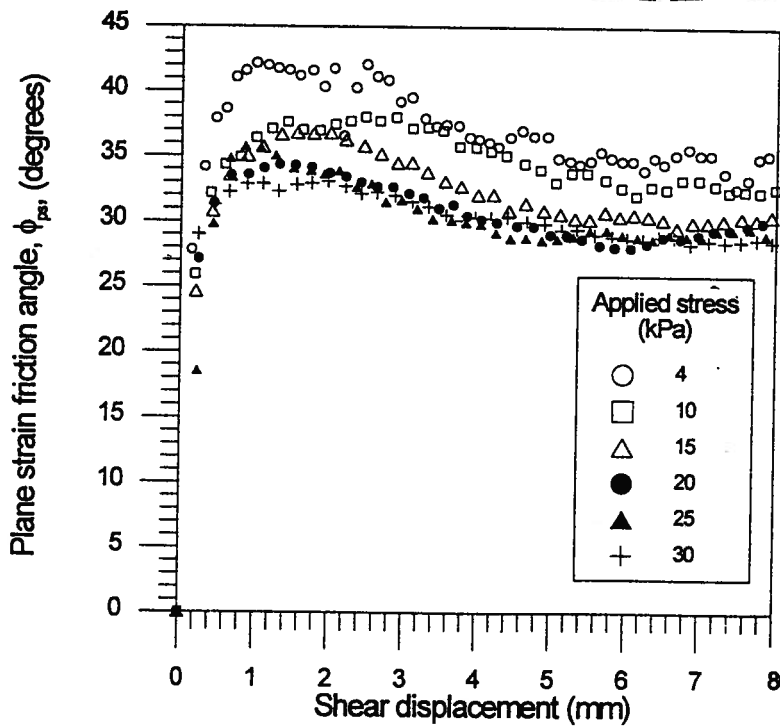


Figure 4.4: Plane strain friction angle for the sand

Chapter 4. Material Properties

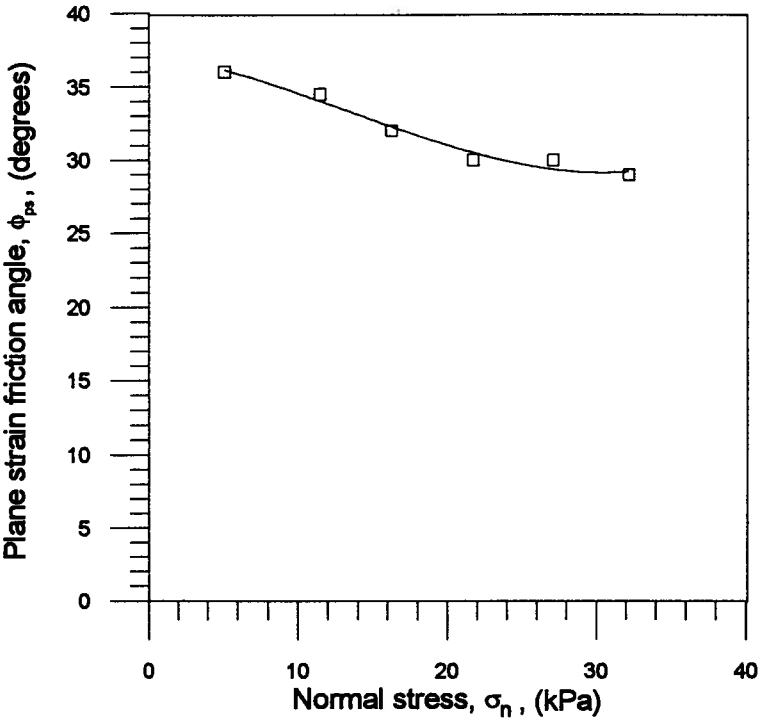


Figure 4.5: Variation of constant volume plane strain friction angle with normal stress

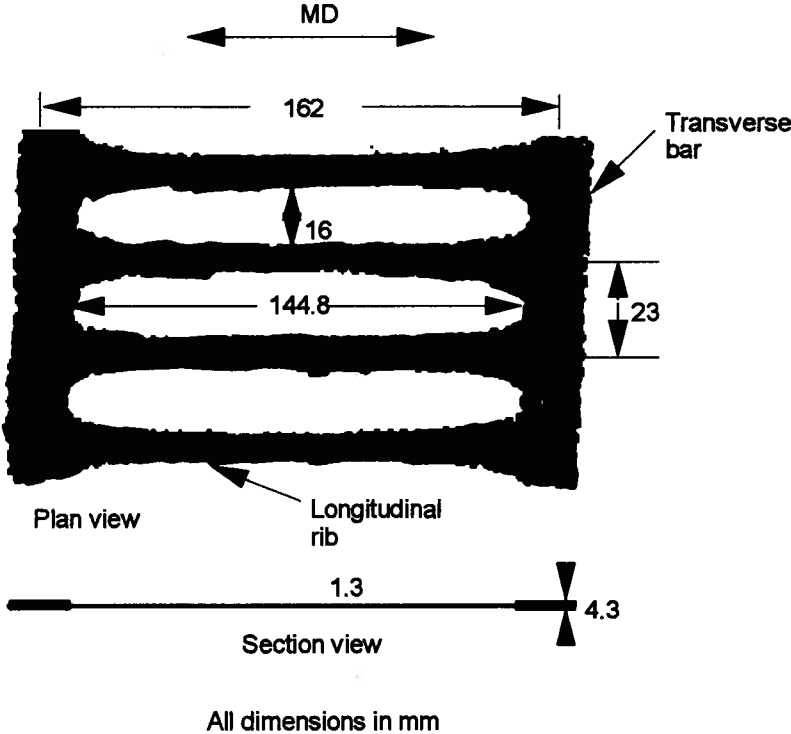


Figure 4.6: Measured dimensions of Tensar UX-1500

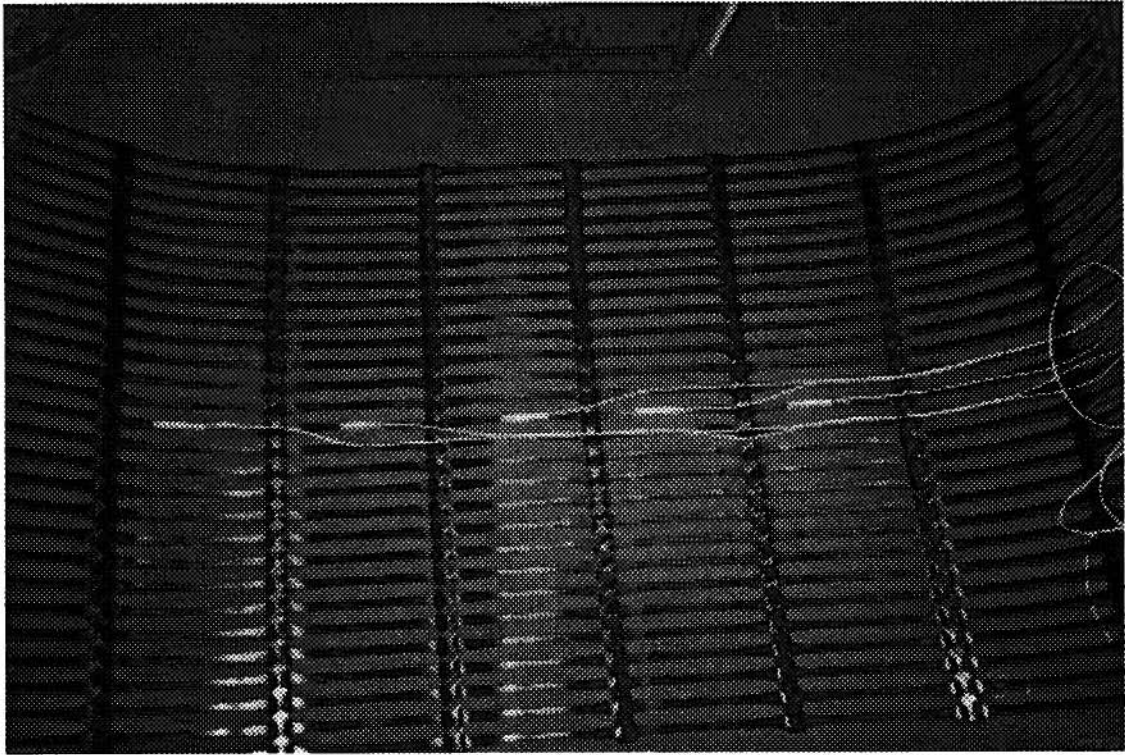


Figure 4.7: Instrumented Tensar UX-1500 test specimen with strain gauges

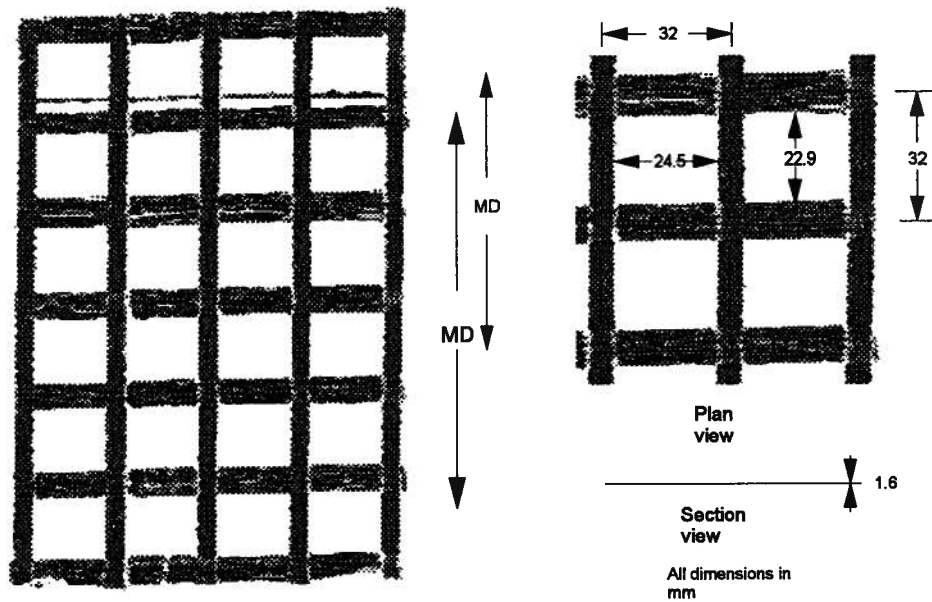


Figure 4.8: Photograph and measured dimensions of Miragrid 15T

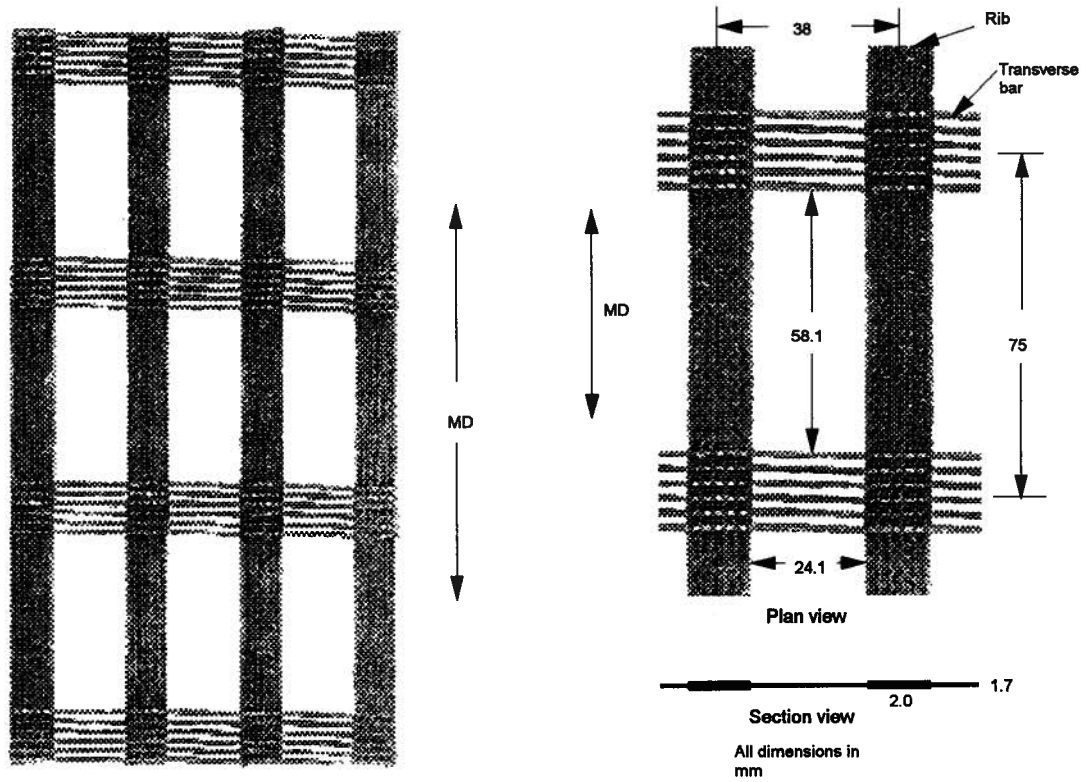


Figure 4.9: Photograph and measured dimensions of Stratagrid 700.

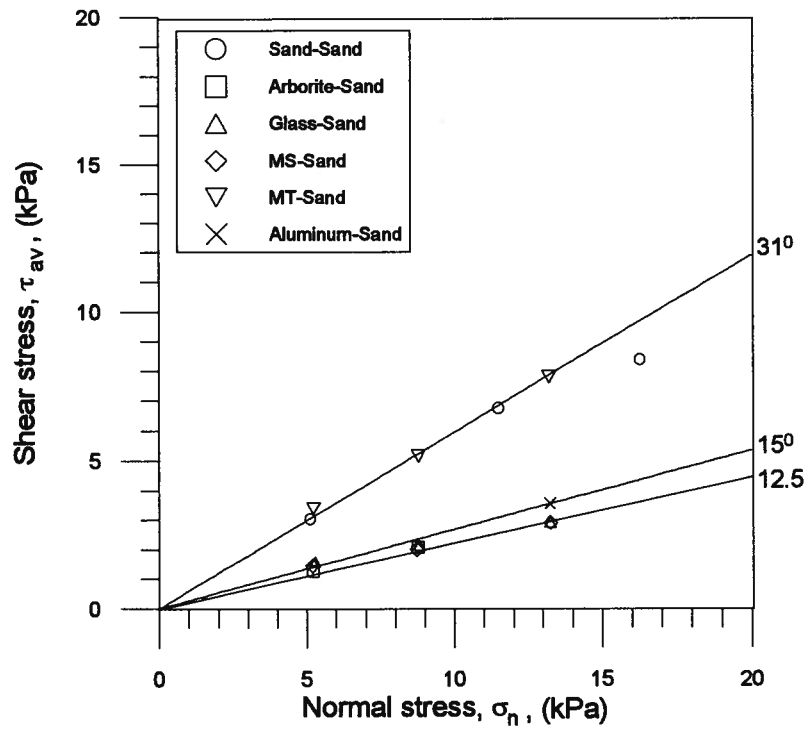


Figure 4.10: Shear stress and normal stress relationship for various interfaces from direct shear tests

CHAPTER 5

TEST PROCEDURE

5.1 Introduction and Test Program

In this chapter the procedure for performing a pullout test, including both preparation of the sand sample and the test specimen is described. The pullout resistance of extensible and inextensible specimens was studied using the large scale laboratory pullout test apparatus described in Chapter 3. Pullout resistance was mobilized in one of two modes of control - displacement or load. In a displacement controlled test, the test specimen was pulled at a constant rate of displacement (CRD) until the specimen exhibited tension failure or pullout failure defined as displacement in excess of 76 mm. The demand signal in the CRD test is a ramp function that varies linearly with time, see Figure 5.1: the rate of displacement (r_d) was typically 0.5 mm/min, although some tests were performed at $r_d = 0.25$ and 1.00 mm/min. The monotonic pullout resistance per unit width established in these tests is termed p_m .

In the second type of control, the test specimen was pulled out at a constant rate of loading (CRL) until a certain ratio of the monotonic pullout resistance (ap_m) was achieved, after which series of cyclic loading were imposed, see Figure 5.2: the rate of loading was 0.25 kN/m/min. The constant rate of loading (r_l) in the initial monotonic phase of loading is given by equation 5.1:

$$r_l = \frac{ap_m}{t_1} \quad (5.1)$$

where:

a is a constant,

Chapter 5. Test Procedure

t_1 is time, and

p_m is the maximum pullout resistance of the test specimen in the CRD test.

Several series of cyclic loading, in which the amplitude of loading (Δp_m) was increased with each series, were applied until the test specimen failed either in tension or pullout. Pullout failure of the specimen is defined as the condition corresponding to a substantial accumulation of displacements with little or no increase in pullout resistance. In each series of cyclic loading, the number of cycles ($N=10$) and frequency (f) are kept constant. Typically testing frequency was 0.01 Hz, although some tests were performed at 0.1 Hz. In contrast to the initial part of the test, the cyclic loading phase is characterised by a variable rate of loading (VRL). The behaviour in pullout, for both modes of testing, is interpreted from measurements of pullout resistance, displacement of the clamped and embedded ends of the test specimen, tensile strain along the specimen, lateral pressure on the front wall of the pullout box, and the surcharge pressure imposed on the sample.

5.2 Test Preparation

The preparation of each test involved air pluviation of the sand sample, placement of the test specimen and application of the surcharge pressure to the sand sample. Procedures followed in the preparation of each test are described in the following sections.

5.2.1 Preparation of the Test Apparatus

Prior to each test, the pullout box was thoroughly cleaned. The total pressure transducers were then connected to the data acquisition system and a series of baseline readings taken with the box empty before pluviation of the sand. The hopper was then lifted

Chapter 5. Test Procedure

and seated on the pullout box with the pneumatically controlled trap doors closed. The laboratory apparatus was then ready for sample preparation.

5.2.2 Preparation of the Test Specimen

Typically each geosynthetic specimen was cut to a width of 0.5 m and length 1.135 m, but some were also 0.5 and 0.65 m in length. The embedded length of a 1.135 m long specimen was 0.965 m leaving a protruding length of 0.17 m for clamping. Prior to placement in the box the test specimen was strain-gauged. The same routine, see Appendix-A, was used for fixing gauges to a geogrid and geomembrane. Five gauges were mounted, typically along the centreline of the specimen.

5.2.3 Placement of the Sand Sample and the Test Specimen

Sand was placed in several layers to a targeted relative density in excess of 85% by air pluviation from the hopper. The hopper was filled with sand from a storage drum that was lifted using an overhead crane. Using a straight edge, the sand in the hopper tray was levelled to form a loose layer, approximately 10 cm thick. A 10 cm layer in the hopper was found to give a finished thickness of 7 to 8 cm in the pullout box. The density variation of the sand sample in a layer was determined by placing small tins at six locations. Pluviation was initiated by the release of pressure to two pneumatic cylinders that support the trap doors on the hopper, causing them to retract, and the doors to open. A uniform thickness of loose sand in the hopper was found to give a uniform layer in the box.

Four pluviated layers brought the sand sample to the mid-height of the slot on the front wall of the apparatus. At this point the surface of the sand was levelled to receive the test specimen. Care was taken not to disturb the sand in any significant way. Excess material

Chapter 5. Test Procedure

at any location was removed carefully by hand, and any low pockets filled by manually pouring additional sand through the hopper.

The instrumented test specimen was placed on the surface of the sand with the gauges facing upwards. Three wires from each strain gauge were passed through a nylon tube (see Figure 4.7) that served two purposes: (1) protection of the wires, and (2) provision of unrestrained movement of the wire during the experiment. All wires were taken out of the box through a 16 mm hole in the back wall of the test apparatus and connected to a Wheatstone bridge circuit. A tell-tale cable attached to the rear end of the specimen was also taken out of the box in the same way and connected to the LVDT mounted outside the box.

Four more layers of sand were then placed following the procedure described previously. A determination of density was made from the mass of sand collected in tins placed at six locations on the sample before pluviation of the first and the penultimate layers. The local density thus measured establishes the spatial variation for each test. Following placement of the final layer of sand, the hopper was removed and the top surface levelled off as before, in preparation for surcharge loading.

5.2.4 Application of Surcharge Load

The sand sample was surcharge loaded using a pressurized PVC bag. It was placed empty, and care was required to avoid pinching it between the top plate and side frames of the box. The top plate and cross-beams were then positioned and bolted to the main reaction frame.

Chapter 5. Test Procedure

A reading of the total pressure transducers on the front wall of the apparatus was taken before filling the bag with water. The bag was then back-filled with water. The surcharge loading assembly and the pressurizing system are illustrated in Figure 3.8. For tests at low normal stress ($\sigma_n < 25$ kPa), a stand pipe was used to maintain a constant head, and therefore a uniform normal stress, on the test specimen. In tests at a higher normal stress, the water level in the air-water interface chamber was brought to mid-height; during this process the chamber was vented to atmosphere. The water pressure transducer that is mounted in alignment with the surcharging bag was then connected and an initial reading taken. At this point the venting hose was disconnected from the chamber, and surcharge pressure was applied with control from a pressure regulator on the laboratory air supply. A constant surcharge pressure was maintained during a test by manual adjustment of this regulator or by maintaining a constant head in the standpipe. This was necessary because of pressure changes caused by changes in volume of the sand sample during pullout.

5.2.5 Clamping of the Test Specimen

Following application of surcharge loading, the test specimen was attached to the pullout assembly. The lower jaw of the clamp was advanced to align with the test specimen, the clamp insert and upper jaw were placed on the test specimen, and the upper jaw was then bolted to the lower jaw. G-clamps placed on the clamp assembly at four locations to prevent the jaws from opening during pullout loading.

5.3 Test Procedure

The pullout test in a displacement-controlled (DC) mode or a load-controlled (LC) mode was carried out by specifying a demand signal as illustrated in Figures 5.1 and 5.2. A

Chapter 5. Test Procedure

test is started by sending a demand signal to the electro-hydraulic servo-controlled valve. The process of controlling displacement or load, and acquiring data is carried out entirely by software.

Fifteen channels of data were monitored during a test: six total pressure transducers on the front wall; five strain gauges on the test specimen; a load cell on the hydraulic actuator; two LVDTs on the clamp; a LVDT attached to embedded end of the test specimen; and a pressure transducer connected to the surcharge bag. The digital output of the A/D board is scanned continuously and stored at regular intervals throughout a test. Pressure in the surcharge bag is adjusted as necessary during testing by manually operating a pressure regulator or by maintaining a constant head in the stand pipe. Typically a displacement controlled test is continued to a displacement of 76 mm, which at a rate of displacement of 0.5 mm/min, takes 2 hours and 32 minutes. However, a load controlled test was continued until the test specimen failed in pullout or an accumulated displacement of 100 mm was recorded. The total duration of testing depends on several factors and typically ranged from 30 minutes to 3 hours.

5.4 Post-Test Procedure

At the end of the test the hydraulic supply was switched off, the data acquisition program stopped, the surcharge pressure released, and water allowed to drain out of the bag. All the instrumentation cables were disconnected from the data acquisition unit. The reaction frame was then dismantled, the top plate lifted off the box, and the surcharge bag removed. Sand was removed from the box using a modified vacuum cleaner. A measurement of the mass of the storage drums before and after emptying the box was used to determine the mass

Chapter 5. Test Procedure

of sand in the box, and hence calculate the mean density of the sample knowing the volume of the box.

A typical routine for testing was to clean the box and strain gauge a geosynthetic specimen on day 1. On day 2 the box was filled and instrumentation connections made. Surcharge load was applied and the test carried out on day 3. On day 4 the sand was removed from the box. Thus a typical testing routine requires 4 days of work for each test.

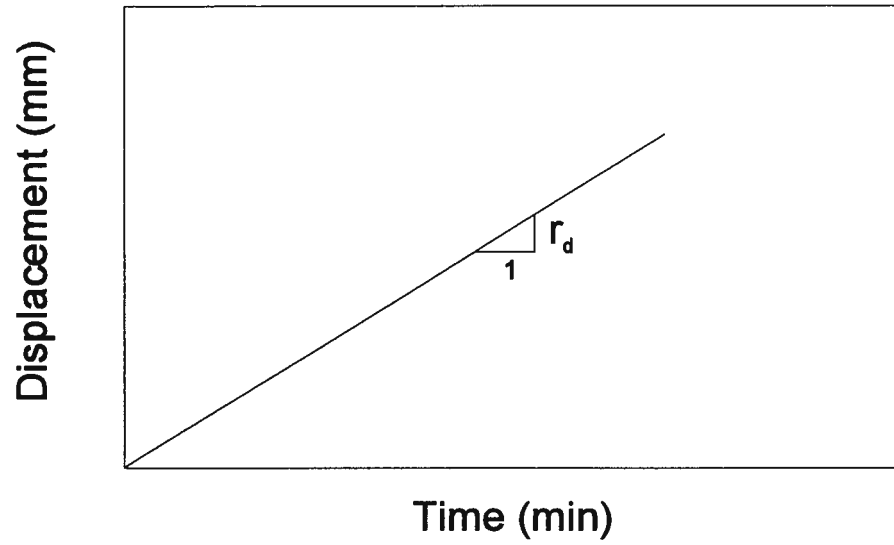


Figure 5.1: Demand signal in the displacement-controlled mode

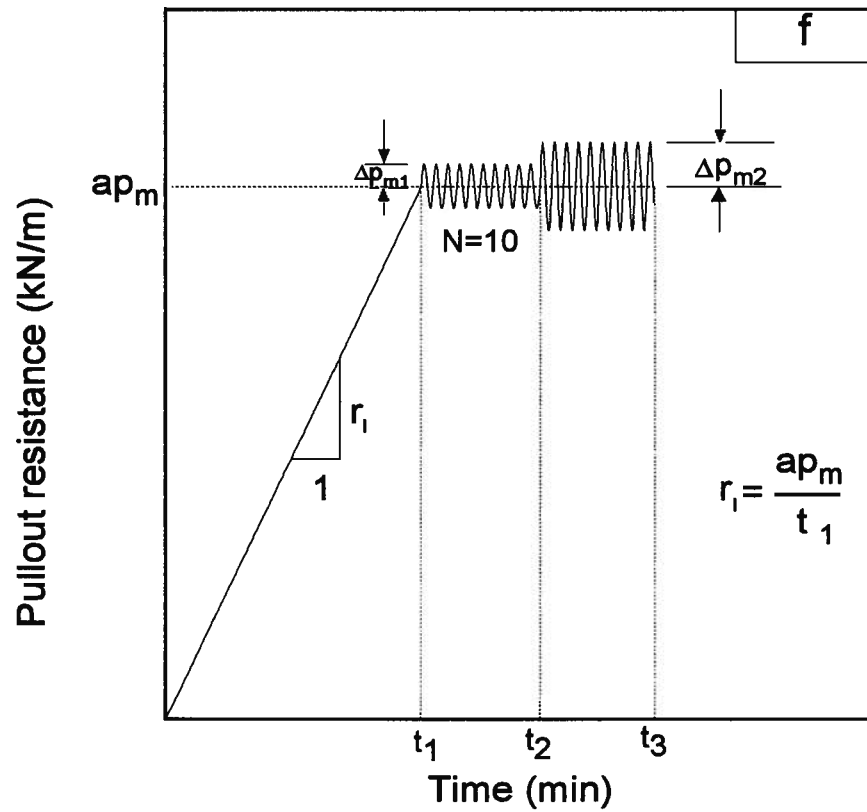


Figure 5.2: Demand signal in the load-controlled mode

CHAPTER 6

TEST RESULTS

6.1 Introduction

Results are presented for pullout tests on extensible and inextensible test specimens. Variables examined in the program of testing include: normal stress, geometry and stiffness of the test specimen, embedment length, roughness of the front wall of the pullout box and mode of testing. Most tests were performed on specimens 0.5 m wide and with an embedment length of 0.965 m: a shorter embedment length (0.5 m and 0.65 m) was used in a few tests. The testing mode was either displacement-control (DC) or load-control (LC). In the LC tests, a constant rate of loading (CRL) was applied to a targeted value and a variable rate of loading (VRL) then imposed that was dependent on the amplitude and frequency of loading. A reference code is used to identify each test configuration, see Figures 6.1 and 6.2. The fourth column is a suffix which identifies, for example, whether a test was repeated to assess the reproducibility of the results.

6.2 Displacement-Controlled Pullout Tests

The displacement-controlled tests were typically performed at a constant rate of displacement, $v_d=0.5$ mm/min. The applied normal stress (σ_n) at the interface of soil and test specimen was in the range 4 to 30 kPa, and was selected to promote development of a pullout failure. Test specimens evaluated in the monotonic series of tests are: (1) geogrids (Tensar grid, Stratagrid, and Miragrid), (2) geomembranes (smooth and textured) and (3) a rough aluminum sheet. The following section presents the results for these specimens of differing

Chapter 6. Test Results

geometry and stiffness. The influence of rate of displacement on the measured pullout resistance was examined by performing some tests on the Tensar grid at $r_d=0.25$ and 1.0 mm/min. Roughness of the front wall was examined in tests using an arborite surface fixed to the aluminum wall of the pullout box.

Characteristics of all displacement-controlled tests performed on geogrids are tabulated in Table 6.1 and in Table 6.2 for the geomembranes and aluminum sheets.

6.2.1 Influence of Front Boundary

To evaluate the influence of the front boundary, and more specifically the surface roughness of the front wall, on the measured pullout resistance, some tests were performed with two different front boundary materials. As fabricated, the front wall of the pullout box is made of aluminum, and most tests were performed with this arrangement. Direct shearbox tests gave a value of $\delta=15^\circ$ for the sand/aluminum at large displacement. However, in some tests an arborite sheet was fixed to the front wall to provide a lower friction boundary: direct shearbox tests for the sand/arborite gave $\delta=12.5^\circ$.

The variation of pullout resistance with displacement for the Tensar grid at $\sigma_n=10$ kPa (GT10) exhibits little difference at small displacement, see Figure 6.3. With increasing displacement and as the pullout resistance reached a maximum value, the test with the arborite surface gave a lower resistance. Finally, at large displacement, both curves appear to be converging. A very similar response is obtained with the textured geomembrane at $\sigma_n=8$ kPa (MT08), see Figure 6.4. The equivalent smooth geomembrane, test MS08, develops a peak pullout resistance that is slightly greater with the aluminum surface, and again, both curves converge at large displacement. It appears that tests with the arborite surface, which has a

Chapter 6. Test Results

relatively smaller value of interface friction with the sand, exhibit a maximum pullout resistance that is lower. The results imply the ideal front boundary that will give a lower bound to the pullout resistance is a smooth, frictionless material. Since the results with each material are not significantly different and there was a desire, in this study, to measure lateral pressures on the front wall of the pullout box, the aluminum surface was adopted for use in testing. All of the following data are presented for this configuration.

Table 6.1: Summary of displacement-controlled tests on geogrid specimens

Test code	Applied normal stress, σ_n (kPa)	Initial embedded length, L_{ei} (m)	Width (m)	Rate of displacement, r_d (mm/min)
GT04	3.9	0.965	0.50	0.50
GT10	10.0	0.965	0.50	0.50
GT10R	10.5	0.965	0.50	0.50
GT17	17.0	0.965	0.50	0.50
GT17R	17.0	0.965	0.50	0.50
GT20	19.9	0.965	0.50	0.50
GT20	19.8	0.965	0.50	0.25
GT20	20.9	0.965	0.50	1.00
GT25	25.0	0.650	0.50	0.50
GT25R	24.7	0.500	0.50	0.50
GT30	29.8	0.965	0.50	0.50
GT10S	10.5	0.965	0.50	0.50
GT04N	3.9	0.965	0.50	0.50
GT10N	10.0	0.965	0.50	0.50
GT18N	17.3	0.965	0.50	0.50
GS04	3.9	0.970	0.47	0.50
GS10	10.0	0.970	0.47	0.50
GS17	17.0	0.970	0.47	0.50
GM04	3.9	0.980	0.44	0.50
GM10	10.0	0.980	0.44	0.50
GM17	17.0	0.980	0.44	0.50
GM04C	3.9	0.965	0.47	0.50
GM04CR	3.9	0.965	0.47	0.50
GM10C	10.0	0.965	0.47	0.50
GM10CR	10.0	0.965	0.47	0.50
GM18C	18.0	0.965	0.47	0.50
GM18CR	18.0	0.965	0.47	0.50
GM10S	10.0	0.965	0.47	0.50
GM04N	3.9	0.965	0.47	0.50
GM10N	10.0	0.965	0.47	0.50

Chapter 6. Test Results

Table 6.2: Summary of displacement-controlled tests on the geomembrane and aluminum sheets

Test code	Applied normal stress, σ_n (kPa)	Initial embedment length, L_{ei} (m)	Width (m)	Rate of displacement, r_d (mm/min)
AR04	3.9	0.985	0.50	0.50
AR04R	3.9	0.945	0.50	0.50
AR08	8.0	0.948	0.50	0.50
AR12	12.0	0.960	0.50	0.50
AR12R	12.0	0.910	0.50	0.50
MS04	3.9	0.950	0.50	0.50
MS04R	3.9	0.950	0.50	0.50
MS08	8.0	0.950	0.50	0.50
MS08R	8.0	0.955	0.50	0.50
MS08S	7.5	0.950	0.50	0.50
MS12	11.8	0.950	0.50	0.50
MT04	3.9	0.950	0.50	0.50
MT08	8.0	0.950	0.50	0.50
MT08S	8.0	0.956	0.49	0.50
MT08RR	8.0	0.965	0.50	0.50
MT12	13.0	0.950	0.50	0.50

6.2.2 Influence of Rate of Displacement

Three tests were performed on Tensar grid specimens at $r_d=0.25$, 0.50, and 1.00 mm/min. A normal stress of approximately 20 kPa was applied to all specimens, i.e., 19.8, 19.9 and 20.9 kPa respectively. A similar response to loading is observed, especially at small to moderate displacements, suggesting that the mobilized pullout resistance of the grid is essentially independent of the rate of displacement at these relatively slow rates of displacement (see Figure 6.5). All of the tests subsequently reported were performed at a standard rate of 0.5 mm/min.

6.2.3 Aluminum Test Specimens

Displacement of the clamped end (d_c) and embedded end (d_e) of the specimens, and measured pullout resistance are used to describe the response to loading. The relationship between d_c and d_e for the rough aluminum sheet at different applied normal stresses is shown

Chapter 6. Test Results

in Figure 6.6. All tests show a value d_c equal to d_o : the response is attributed to the inextensible behaviour of the specimens. An important aspect of this inextensible behaviour is the development of a constant relative displacement between the soil and the test specimen along its embedded length, and therefore mobilization of a uniform shear stress with length.

6.2.3.1 Rough Aluminum Sheet

The variation of pullout resistance for the rough aluminum sheet, with $\sigma_n = 4$ to 12 kPa, is shown in Figure 6.7. Mobilized resistance increases with the applied normal stress. A peak value of resistance develops, and is followed by a strain softening behaviour. Three tests at $\sigma_n = 4$ kPa gave a similar response at large displacement: one test (AR04) was inadvertently disturbed during clamping of the specimen and is inconsistent at small displacement only. A staged test was performed with $\sigma_n = 8$ kPa, unloading loop, and $\sigma_n = 12$ kPa. The 12 kPa stage test exhibits a resistance similar to that of the corresponding AR12 test: the difference in pullout resistance for each test at large displacement is attributed to a shorter initial embedment length of the staged test. A unified interpretation of the data is presented in Chapter 7, where the pullout resistance is normalized with respect to the resisting area and normal stress.

6.2.4 Geosynthetic Test Specimens

The behaviour of the geogrids and geomembranes is described in general terms with reference to measured displacements d_c and d_o , prior to a separate description of the measurements of load and strain. Results for the Tensar grid with $\sigma_n = 4$ to 30 kPa, see Figure 6.8, show an initial displacement of the clamped end without any displacement of the

Chapter 6. Test Results

embedded end. The response is dependent on applied normal stress. At $\sigma_n=4$ kPa, $d_e>0$ when $d_c>5$ mm, and $d_c>10$ mm at $\sigma_n=17$ kPa. A non-linear relationship between d_c and d_e follows, and leads to a linear relationship for tests at $\sigma_n=4, 10$ and 17 kPa. The response of the test at $\sigma_n=30$ kPa is very different: displacement of the embedded end was not observed until $d_c>20$ mm, and thereafter $d_c>d_e$ throughout the test. A non-linear response, in which the embedded end displaces significantly less than the clamped end, is attributed to a markedly extensible behaviour of the test specimen.

A similar relationship between d_c and d_e is observed for the Stratagrid, see Figure 6.9, which shows an inextensible behaviour after 5 mm with increasing displacement at $\sigma_n=4$ kPa and greater non-linearity at $\sigma_n=17$ kPa. Again, the displacement of the clamped end that is necessary to mobilize an initial displacement at the embedded end is observed to increase with the applied normal stress. The general relationship is also true for tests on the Miragrid, see Figure 6.10

The characteristic response of the geosynthetic specimens is further illustrated in Figure 6.11, in which results for both the smooth and textured geomembrane with $\sigma_n=4$ to 12 kPa are presented. It is apparent that the smooth geomembrane (MS) exhibits a behaviour that is essentially inextensible at all values of normal stress after 4 mm. The response of the textured geomembrane (MT) at $\sigma_n=4$ kPa is similar to the smooth geomembrane, but not at $\sigma_n=12$ kPa where it is distinctly non-linear at small displacement and tends toward a linear behaviour at large displacement. A transition behaviour is observed in the test at $\sigma_n=8$ kPa.

Chapter 6. Test Results

It is clear from these test results that the response of the geosynthetic test specimen may be characterized as inextensible or extensible. The behaviour is dependent on applied normal stress. Pullout failure at constant strain must be associated with $d_c = d_e$, and an inextensible response. Details of the load and strain measurements for each geosynthetic test are presented below.

6.2.4.1 Geogrid

The detailed response of a geogrid to DC pullout testing is described from measurements of pullout resistance and mobilized strain with displacement of the clamped end. In this section the response of three geogrids (GT, GM and GS, see Table 6.1) is presented at different values of normal stress.

6.2.4.1.1 Pullout Resistance

Pullout resistance is seen to increase with displacement d_c for the GT test specimens at $\sigma_n=4$ to 30 kPa, see Figure 6.12. The characteristic response exhibits three zones: an initial linear relationship, a non-linear transition and a limiting resistance at large displacement. The slope of the linear zone is seen to increase with the magnitude of applied normal stress. The extent of the non-linear transition zone is also dependent on the applied normal stress. In GT04 test the non-linear transition zone occurs rapidly over a small range of displacement whereas the GT tests at 17 kPa illustrate the zone clearly. Tests with $\sigma_n=4$ to 17 kPa attain a constant limiting value of pullout resistance at a value of displacement d_c that also increases with applied normal stress, being 6 mm for $\sigma_n=4$ kPa and 30 mm for $\sigma_n=17$ kPa. Two tests were performed at $\sigma_n=17$ kPa to examine the repeatability of the testing routine. The

Chapter 6. Test Results

response of tests GT17 and GT17R are very similar and suggest an excellent repeatability (see Figure 6.12).

In contrast to the response at $\sigma_n=4$ kPa, that at $\sigma_n=30$ kPa shows a continued increase of pullout resistance with displacement of the clamped end. The non-linear transition zone predominates and no limiting value of resistance is attained. On continuation of the test, the specimen may fail in tension if the load per unit width exceeds the ultimate tensile strength of the specimen material, which is reported as 86 kN/m from wide width testing (see Table 4.1). In practice this places an upper limit to the applied normal stress for a given dimension of the test specimen if tensile failure of the specimen is to be avoided.

The pullout resistance of the GM geogrids, in the range $\sigma_n=4$ to 17 kPa, illustrates a slightly different initial response and a maximum value which again is dependent on stress level, see Figure 6.13. Displacement d_c required to attain the maximum value increases with the applied stress, as in the case of the GT tests. Although the response at large displacement for $\sigma_n=4$ kPa and 10 kPa shows a nearly constant pullout resistance, the response for $\sigma_n=17$ kPa is different in that there is a decrease as the displacement increases. After completion of the test, the sand was carefully removed to expose the specimen, and the displacement pattern of the transverse elements recorded. It showed that the deformed shape was parabolic in nature with a maximum displacement at the edges, see Figure 6.14. The behaviour could be due to yielding of the junctions: visual inspection of the specimen after the test revealed that the junctions were damaged.

To further examine the influence of grid orientation on measured pullout resistance, some tests were performed on the GM test specimens with the orientation changed to give the

Chapter 6. Test Results

direction of pullout in line with the cross-machine direction (weak) of the grid. The pullout resistance illustrates clearly the significance of the orientation, see Figure 6.15. In this orientation the transverse elements are stronger and the longitudinal elements weaker, therefore, the response is less stiff in the initial phase of the test when compared to that of the tests in machine direction (see Figure 6.13). The GM10C and GM17C test specimens were observed to fail in tension at large displacement of the clamped end. Tests performed on specimens without bearing elements (GM04CN and GM10CN) suggest that the pullout resistance mobilized by the friction component is 65 to 70% of the total pullout resistance.

The pullout resistance of the GS specimens exhibits a very similar response to GM specimens, see Figure 6.16. Although the initial response at all stress levels is similar, the value of limiting resistance is observed to be dependent on normal stress. At $\sigma_n=17$ kPa the response at large displacement exhibits a slight strain softening behaviour which is similar to the GM17 test. This behaviour is attributed to the surface characteristics of the grids.

6.2.4.1.2 Rib Strain

Strain gauges were mounted on the longitudinal ribs of a geogrid test specimen (see Figure 4.7). The variation of strain (ϵ_r) with displacement d_c for each geogrid at $\sigma_n=10$ kPa is presented in Figures 6.17, 6.18, and 6.19. The strain gauge location is reported as the distance (x) from the front wall of the apparatus (see Figure 3.10) normalized with respect to the initial embedment length (L_{ei}) of the specimen: values are shown in the legend, and a negative value is associated with a gauge mounted outside the pullout box on the specimen between the clamp and the front wall.

Chapter 6. Test Results

A general trend is observed, wherein the strain response exhibits three distinct phases as the displacement d_c increases. They are illustrated schematically in Figure 6.21. It is noted that the rate of strain at any gauge location can be deduced, knowing the strain (ϵ_r), displacement (d_c), and rate of displacement for the test (r_d). The behaviour at small displacement is characterised by a rate of strain which is essentially linear. This initial rate of strain decreases with distance from the clamped end of the specimen. The initial linear behaviour is followed by a second phase in which a transition occurs to the third phase in which variations in strain are typically small. Little or no variation in strain indicates that the specimen is failing in pullout at nearly constant strain. The magnitude of this constant strain decreases with distance from the clamped end. Therefore the distribution of strain along the length of the specimen is non-uniform, and different, at various stages of the test.

Consider the GT10 test, see Figure 6.17, in which the initial linear response at locations SG-1 to SG-3 shows a similar strain rate. The non-linear response is clearly exhibited at all strain gauge locations. The curves tend toward a constant limiting value at all locations except SG-3 and SG-5, where a small increment is observed at SG-3, and a moderate decrement at SG-5. A maximum strain is maintained constant throughout the test at other locations.

The response of the GS specimen is similar to that of the equivalent GT test in both shape and magnitude of the curves, see Figure 6.18. It should be noted the relative positions of the gauges (x/L_{ei}) are comparable, but not identical, due to the different size of the apertures in type of each grid. Again there is evidence of a small variation of strain at large displacements. The strain response of the GM specimen at $\sigma_a=10$ and 17 kPa is shown in

Chapter 6. Test Results

Figures 6.19 and 6.20. A typical linear response at small displacements is observed in both tests, where the linear strain rate again decreases with distance from the front wall of the apparatus.

A greater rate of strain occurs in the test at $\sigma_n=17$ kPa than at $\sigma_n=10$ kPa. A different behaviour is also observed in the non-linear transition behaviour of the test: the response at $\sigma_n=17$ kPa is marked by a much stronger non-linear transition. There is also evidence from SG-5, at this higher stress, of zero strain during early displacement (and straining) of the front of the specimen. At larger displacement d_c a constant limit strain is mobilized in both the tests.

The variation of the rate of displacement along the specimen during pullout testing is addressed by the tests at $r_d=0.25$, 0.50 and 1.00 mm/min on the GT grid at stress $\sigma_n=20$ kPa, see Figure 6.22. Strain measured on the longitudinal ribs at SG-1 ($x/L_{ei}=0.073$) and SG-5 (0.744) are presented for these tests. The results indicate that the strain rate at SG-1 is essentially independent of rate of pullout displacement, although a somewhat greater limiting strain is mobilized at $r_d=1.00$ mm/min. In contrast the strain rate at SG-5 appears to be dependent on the rate of pullout.

6.2.4.2 Geomembranes

The pullout resistance of the smooth and textured geomembrane are contrasted. Strain data are presented for the smooth geomembrane only, because of difficulties encountered in mounting the gauges on the textured geomembrane due to its surface characteristics.

Chapter 6. Test Results

6.2.4.2.1 Pullout Resistance

The pullout resistance of the smooth geomembrane at $\sigma_n=4$ to 12 kPa exhibits a stiff response, with small displacements in the range 1 to 4 mm sufficient to mobilize a marked peak value of pullout resistance, see Figure 6.23. Nevertheless, the displacement to reach the peak value increases with normal stress, as in the case for the geogrids. The post-peak response is typical of a strain softening behaviour and a nearly constant pullout resistance is mobilized at large displacement. The magnitude of peak pullout resistance increases with normal stress, but the values are very low in comparison to those for the grid specimens.

Again, the two tests performed at $\sigma_n=4$ kPa illustrate the repeatability of the testing procedure, see Figure 6.23.

The pullout resistance of the textured geomembrane is shown in Figure 6.24. The response of textured geomembrane is very different to that of smooth geomembrane. A significantly greater value of limiting pullout resistance is mobilized at similar normal stresses when compared to the smooth geomembrane, and there is no evidence of a strain softening behaviour. Comparison shows the limiting values exceed those obtained for the grids at comparable normal stresses. The displacement necessary to mobilise the limiting pullout resistance also increases with the increase in applied normal stress, from $d_c=6$ mm with $\sigma_n=4$ kPa to $d_c=35$ mm for $\sigma_n=12$ kPa.

6.2.4.2.2 Local Strain

Strains mobilized in the smooth geomembrane at $\sigma_n=4$ to 12 kPa are shown in Figures 6.25 to 6.27. The results indicate the magnitude of strain increases with increasing normal stress, and decreases with distance from the front wall of the apparatus. The strain

Chapter 6. Test Results

magnitudes are very small and fluctuate, particularly those at $\sigma_n=4$ kPa, a response which is attributed to small strain redistribution as a consequence of incremental displacement in pullout. Comparing the curves with the schematic response illustrated in Figure 6.21, a rapid transition is observed at all stress levels from a linear to non-linear behaviour. This is attributed to the distinct peak resistance mobilized in pullout. Deviations at large displacements are attributed to the relatively small magnitudes of strain (less than 0.4 %), and are considered uniform for all practical purposes.

6.3 Load-Controlled Tests

Cyclic pullout tests were performed on both geosynthetic and aluminum test specimens. Each test specimen was pulled at a constant rate of loading (CRL) to a targeted ratio of the CRD pullout resistance ($a\rho_m$), where $a<1$, after which cyclic loading was imposed, see Figure 5.2. The cyclic loading phase is characterised by a variable rate of loading (VRL). Several series of cyclic loading, with an amplitude of loading ($\Delta\rho_m$) that was increased with each series, were applied until the test specimen failed in pullout. Pullout failure of the specimen is defined as continued displacement with little or no increase in mobilized resistance. The number of cycles $N=10$ and frequency f of each series was kept constant.

A summary of all load-controlled pullout tests is given in Table 6.3. Variables examined in the program of testing are geometry of the specimen, normal stress and frequency. Most tests were performed at $f=0.01$ Hz and $\sigma_n<20$ kPa. Comparisons of pullout response in the displacement-controlled (DC) tests and load-controlled (LC) tests are made

Chapter 6. Test Results

based on measurements of tensile force, strain, and displacement of the clamped end and embedded end of the test specimen.

Table 6.3: Summary of load-controlled pullout tests

Test code	Applied normal stress, σ_n (kPa)	Test specimen length, L_{ei} (m)	Test specimen width (m)	Frequency of cyclic loading, f (Hz)
GT04	3.9	0.965	0.50	0.01
GT10	10.0	0.965	0.50	0.01
GT10	10.0	0.965	0.50	0.10
GT17	17.0	0.965	0.50	0.01
GS04	3.9	0.970	0.47	0.01
GS10	10.0	0.970	0.47	0.01
GS17	17.0	0.970	0.47	0.01
GM04	3.9	0.965	0.44	0.01
GM10	10.0	0.950	0.44	0.01
GM17	17.0	0.980	0.44	0.01
GM04C	3.9	0.965	0.44	0.01
GM10C	10.0	0.965	0.44	0.01
GM10C	10.0	0.965	0.47	0.10
GM18C	18.0	0.965	0.44	0.01
AR08	8.0	0.965	0.50	0.01
MS08	8.0	0.950	0.50	0.01
MS12	11.8	0.965	0.50	0.01
MT08	8.0	0.960	0.50	0.01
MT08	8.0	0.960	0.50	0.10
MT12	13.0	0.955	0.49	0.01

6.3.1 Aluminum Test Specimen

6.3.1.1 Pullout Resistance

One cyclic pullout test was performed on the rough aluminum sheet at $\sigma_n = 8$ kPa and a frequency of 0.01 Hz, for an embedment length identical to the equivalent displacement-controlled (DC) test (AR08). Initially the specimen was pulled at $r_f = 0.25$ kN/m/min to a targeted value corresponding to 60% ($a = 0.6$) of the pullout resistance in the DC test. In total the specimen was subjected to eight series of cyclic loading until it failed in pullout: the amplitude of loading was increased from one series to the next series, leading to imposed ratios of $a = 0.625$ for the first series and 0.65, 0.70, 0.80, 0.85, 0.90, 0.995 and 1.09

Chapter 6. Test Results

thereafter. The complete response to cyclic loading is shown in Figure 6.28 and the early response shown in further detail in Figure 6.29.

The maximum pullout resistance in each series of loading forms an envelope. The envelope is parallel to, and coincident with corresponding DC curve up to the peak resistance. Thereafter it remains parallel to, but greater than, the DC test. At lower amplitudes of cyclic loading the response is relatively stiff, with little or no measured displacement of the clamped end taking place during the ten load/unload cycles. When the load amplitude is high, such that the total load per unit width exceeds that mobilized in the DC test, a rapid accumulation of displacement takes place at the clamped end. After a few cycles of loading there is an accumulation of excessive displacement that results in the specimen being pulled out rapidly. Visual observations at that instant confirm that pullout was indeed very quick.

6.3.1.1.1 Displacement of the Embedded End

The relationship between displacements d_c and d_o is shown in Figure 6.30. Data are shown at equal time intervals of 2 secs and therefore the distribution indicates that most of the displacement was accumulated in the final few cycles of loading. The data lie on a line given by $d_c = d_o$, confirming the inextensible behaviour of the specimen.

6.3.2 Geosynthetic Test Specimens

Cyclic pullout test results for the geogrids and geomembranes are presented in this section.

Chapter 6. Test Results

6.3.2.1 Geogrids

6.3.2.1.1 Pullout Resistance

The variation in pullout resistance of the Tensar grid at $\sigma_n=4, 10$ and 17 kPa is shown in Figure 6.31 for both the DC tests and the LC tests at a frequency of 0.01 Hz. In the DC tests, the geogrid exhibits an increase in pullout resistance with displacement of the clamped end to a limiting value at large displacement. The initial, nearly linear relationship mobilized in a LC test is very similar to that of the corresponding DC test. An envelope describing the peak values of pullout resistance mobilized by cyclic loading illustrates the same smooth transition to a limiting value at large displacement. The limiting value tends to be greater in the load-controlled tests.

The incremental displacement that occurs with each cycle of load is seen to vary significantly with the amplitude, and therefore relative magnitude, of loading, being small at the lower amplitudes and larger at the higher amplitudes. The limiting value of pullout resistance increases with increasing normal stress in all tests, together with the displacement at which it is achieved. The shape of the curves leads to a nearly constant magnitude of pullout resistance under cyclic and monotonic loading, at large displacement.

The cyclic pullout resistance of the Miragrid, see Figure 6.32 and the Stratagrid, see Figure 6.33, is also compared with the corresponding DC test. At lower normal stresses, $\sigma_n=4$ and 10 kPa, the envelope of maximum cyclic pullout resistance coincides with the displacement-controlled pullout resistance. In contrast at $\sigma_n=17$ kPa the envelope to the cyclic pullout resistance of the Miragrid and Stratagrid (see Figure 6.34) is different: it lies below the corresponding DC test for the Miragrid but above for the Stratagrid. Nevertheless,

Chapter 6. Test Results

the envelope remains parallel to the corresponding DC test. The results indicate the mobilisation of pullout resistance of a geogrid in cyclic loading is dependent on the applied normal stress and stiffness of the grid. Comparison of the DC and LC results for each grid suggests the stiffer Tensar geogrid (see Table 4.1) tends to mobilize a higher pullout resistance in cyclic loading.

6.3.2.1.2 Influence of Loading Frequency

Tests were performed on the Tensar grid (GT) to examine the influence of loading frequency. The response at $\sigma_n = 10$ kPa and 0.1 Hz is shown in Figure 6.35. The response to the common initial constant rate of loading in both tests (0.25 kN/m/min), see Figures 6.31 and 6.35, is very similar in each case, and is considered indicative of the reproducibility of the tests. Thereafter the same generalized response to cyclic loading is evident from the curves, which exhibit a common envelope to the peak values of pullout resistance. The incremental displacements of each test specimen during cyclic loading vary a little: a slightly greater pullout displacement occurred during the series of load cycles up to a mobilized pullout resistance of 11 kN/m in the test at a lower frequency. The difference in behaviour is attributed to more displacement taking place between each series of cycles as the imposed load was increased at the lower frequency. However, for practical purposes the response is taken to be independent of loading frequency.

6.3.2.1.3 Rib Strain

The strain mobilized in each of the three types of geogrid during cyclic loading at $\sigma_n = 10$ kPa and $f = 0.01$ Hz is shown in Figures 6.36, 6.37 and 6.38. A comparison of the envelope to the cyclic strain, and the strain mobilized in the corresponding DC tests (Figures

Chapter 6. Test Results

6.17, 6.18 and 6.19), shows a similar trend and shape. In each case the strain rate decreases with the distance from the clamped end, and the magnitude of strain at the front is greater than that at the embedded end. The variation of strain with each load cycle is evident at gauge locations SG-1 and SG-2, which are near the clamped end: these changes are not seen at the gauge locations near the embedded end even when the load amplitude is sufficient to cause pullout failure.

At values of similar normal stress the Tensar geogrid mobilizes a maximum strain at relatively larger pullout displacements when compared to the strain response of the Miragrid (Figure 6.37) and Stratagrid (Figure 6.38). This difference in behaviour is attributed to the dominating mechanism in effect during pullout which is the relative contribution of friction and bearing resistance. Nevertheless, there is a tendency toward achieving a nearly constant strain at all strain gauge locations during pullout itself.

Again, a similar general response is observed in the geogrid tests at $\sigma_n=17$ kPa, see Figures 6.39, 6.40 and 6.41. The magnitude of strain at all locations is greater than that recorded in the LC tests at $\sigma_n=10$ kPa. The strain magnitude in the Tensar geogrid at the SG-1 location (outside the box) is higher than that at SG-2 (Figure 6.36) which is attributed to the difference between the unconfined and confined load-extension behaviour of the specimen. This effect is significant for the Miragrid at higher normal stress, see Figures 6.37 and 6.40, and the Stratagrid, see Figures 6.38 and 6.41. A similar comparison for the Tensar grid is not possible because the gauge at location SG-2 was inoperable during the GT17 test.

An important characteristic of the variation of strain with pullout displacement is observed at gauge locations closer to the embedded end of the specimen. The magnitude of

Chapter 6. Test Results

strain increase and decrease in response to cyclic loading is seen to be smaller: gauge locations SG-4 and SG-5 in all tests show an unload/reload loop that is essentially horizontal. The response is attributed to a “locking-in” of these small strains. In some cases, see for example location SG-4, in test GS17 (Figure 6.41) the behaviour changes as the test progresses and a pullout failure develops.

6.3.2.1.4 Displacement of the Embedded End

The relationship between displacement of the embedded end and the clamped end of the Tensor grid at $\sigma_n = 4, 10$ and 17 kPa is shown in Figure 6.42. At the lower normal stress, the behaviour is essentially inextensible, but at 17 kPa the response is markedly non-linear at small displacement and tends toward a linear behaviour as pullout occurs. The data were acquired at constant time intervals. The magnitude of incremental displacements is very small during the initial phase of the test, but accumulates rapidly during the final stage when the load amplitude is sufficiently high to cause the specimen to pull out of the box. This general behaviour is also observed with the Miragrid, see Figure 6.43 and with the Stratagrid, see Figure 6.44.

6.3.2.2 Geomembranes

6.3.2.2.1 Pullout Resistance

The response of the smooth geomembrane at $\sigma_n = 8$ kPa in the load-controlled pullout test at $f=0.01$ Hz is shown in Figure 6.45. An envelope to the peak values of pullout resistance under cyclic loading shows an abrupt transition to a limiting value of nearly 3.2 kN/m, and pullout failure occurs immediately. The failure is characterized by a brittle behaviour that is attributed to the strain-softening nature of the interface evident in the

Chapter 6. Test Results

corresponding DC test. Development of a significantly greater limiting value of pullout resistance in the load-controlled test is a result of the control system which, in seeking to achieve a peak demand load in the last cycle, pulled the specimen out of the soil in 8.3 secs at a mean rate of displacement that was approximately 360 mm/min.

A similar response is observed at $\sigma_n=12$ kPa: the pullout resistance beyond the peak value in the DC test again exhibits an instantaneous pullout. An envelope to the cyclic loading defines the pullout resistance in the DC test. The abrupt transition from a stable to unstable behaviour occurs at 4.3 kN/m which is the peak resistance value in the DC test.

The pullout resistance of the textured geomembrane at $\sigma_n=8$ and 12 kPa and $f=0.01$ Hz is shown in Figure 6.46. For clarity only half of the unload/reload loops is shown for the LC test at 12 kPa. The nearly instantaneous pullout failure of the smooth geomembrane contrasts markedly with the more ductile behaviour observed for the textured geomembrane. The same response is observed in the DC test and LC test during the constant rate of loading (CRL) phase prior to load cycling. The characteristic response to cyclic loading is generally similar for both tests. Again, a very similar response is seen in the CRL phase of the test at $\sigma_n=8$ kPa and $f=0.1$ Hz, see Figure 6.47. A frequency dependent response is observed in the incremental displacements during cyclic loading which is similar to that exhibited by the Tensar grid, with the test at a lower frequency experiencing greater displacement at a comparable cyclic pullout resistance.

For the test at $\sigma_n=8$ kPa and $f=0.01$ Hz, the envelope of pullout resistance is similar to that in the DC test. In contrast, the other two tests on the textured geomembrane exhibit an envelope to the cyclic pullout resistance curve that is greater than the corresponding DC test.

Chapter 6. Test Results

However, the trend is toward similar values of pullout resistance at large displacement, see Figure 6.46.

6.3.2.2.2 Local Strain

Strain mobilized in the smooth geomembrane during the load-controlled test at $\sigma_n=8$ and 12 kPa shows a decreasing strain magnitude with distance from the front wall, see Figures 6.48 and 6.49. At the instant of pullout, a uniform strain is mobilized at all gauge locations. Again, a characteristic horizontal strain loop is observed at SG-3, SG-4 and SG-5, an exception occurs at SG-4 in Figure 6.48, which is attributed to an improper electrical connection.

6.3.2.2.3 Displacement of the Embedded End

The relationship between d_c and d_e for the smooth geomembrane at $\sigma_n=8$ and 12 kPa is shown in Figure 6.50. For $d_c < 5$ mm, the displacement of the embedded end is zero. Thereafter a typical inextensible response is observed. The textured geomembrane, at $\sigma_n=8$ kPa and $f=0.01$ and 0.1 Hz, exhibits a similar response which is independent of frequency, see Figure 6.51, and in agreement with the general behaviour of the specimen observed in the displacement-controlled tests, see Figure 6.11.

Chapter 6. Test Results

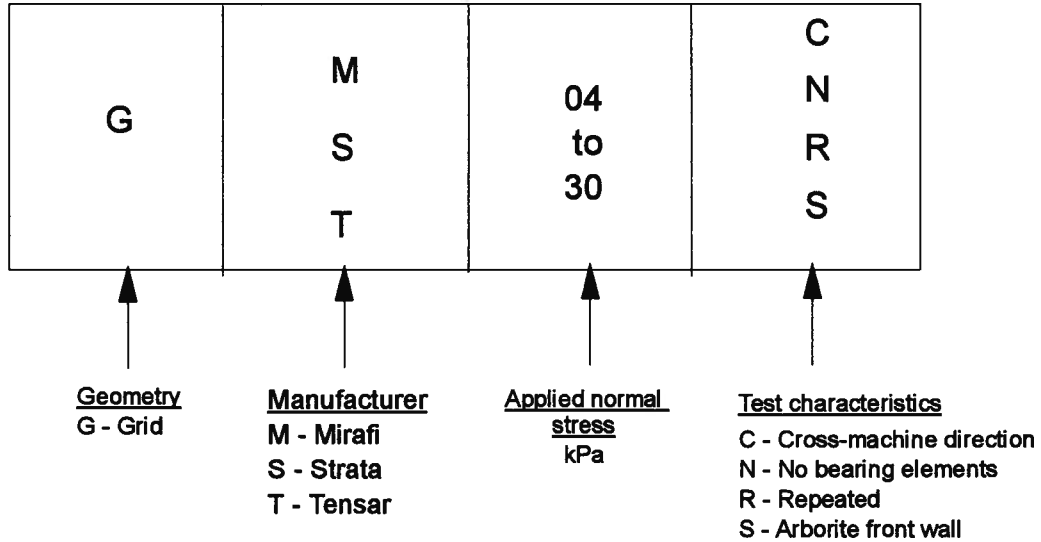


Figure 6.1: Reference code for tests on the geogrids

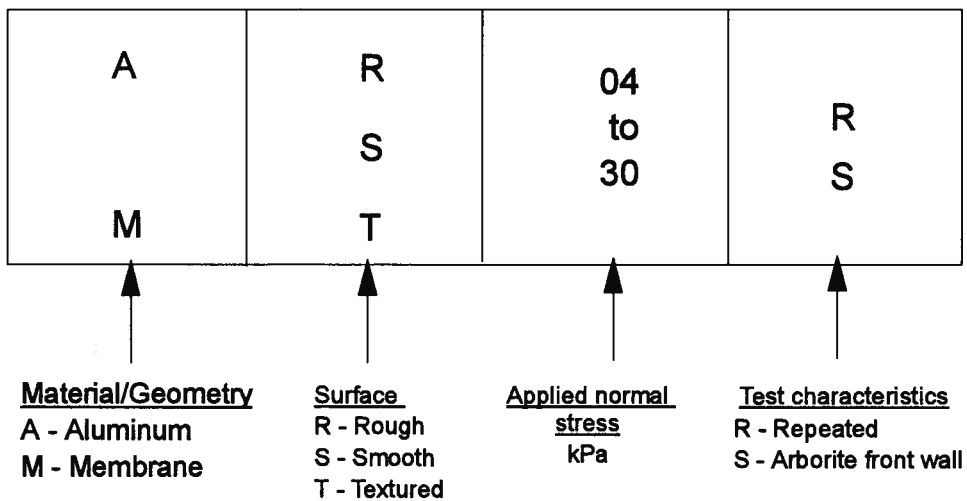


Figure 6.2: Reference code for tests on the geomembranes and aluminum sheets

Chapter 6. Test Results

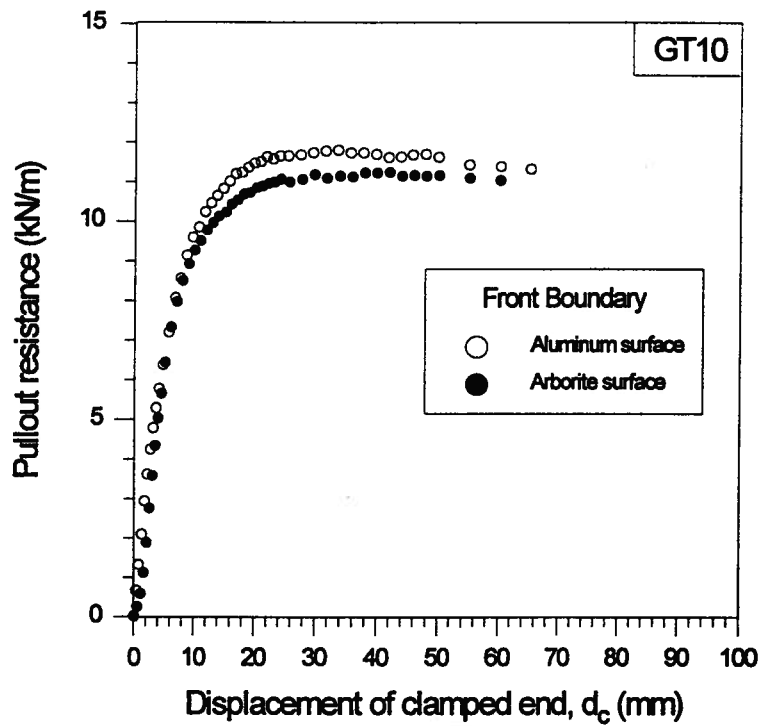


Figure 6.3: Pullout resistance of the Tensar grid with an aluminum or arborite surface on the front wall

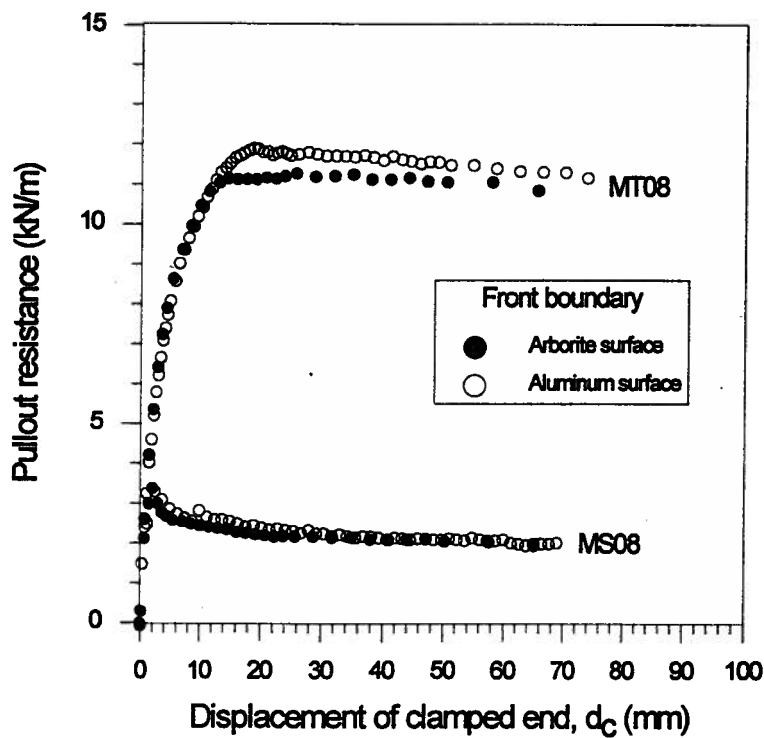


Figure 6.4: Pullout resistance of the smooth and textured geomembranes with an aluminum or arborite surface on the front wall

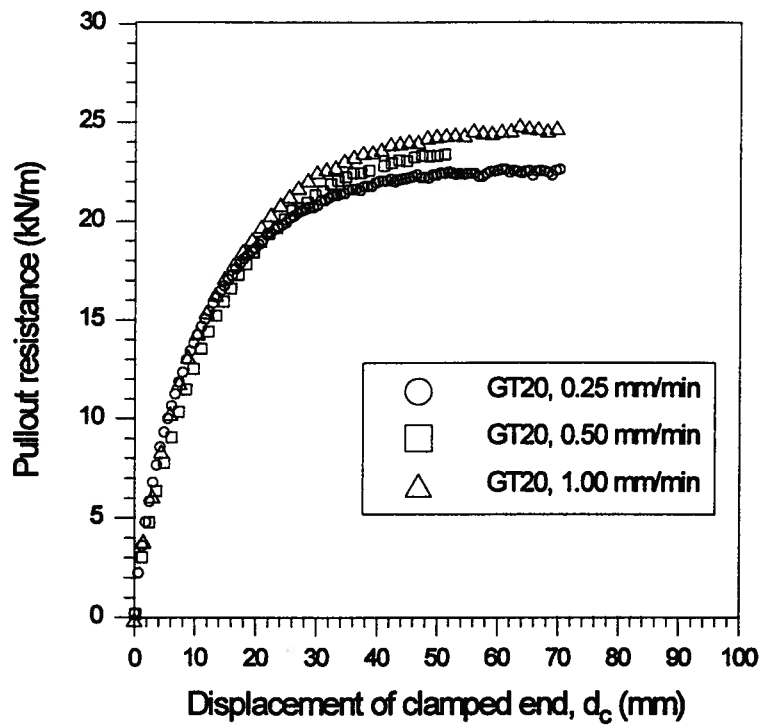


Figure 6.5: Influence of displacement rate on mobilized pullout resistance for the Tensar grid

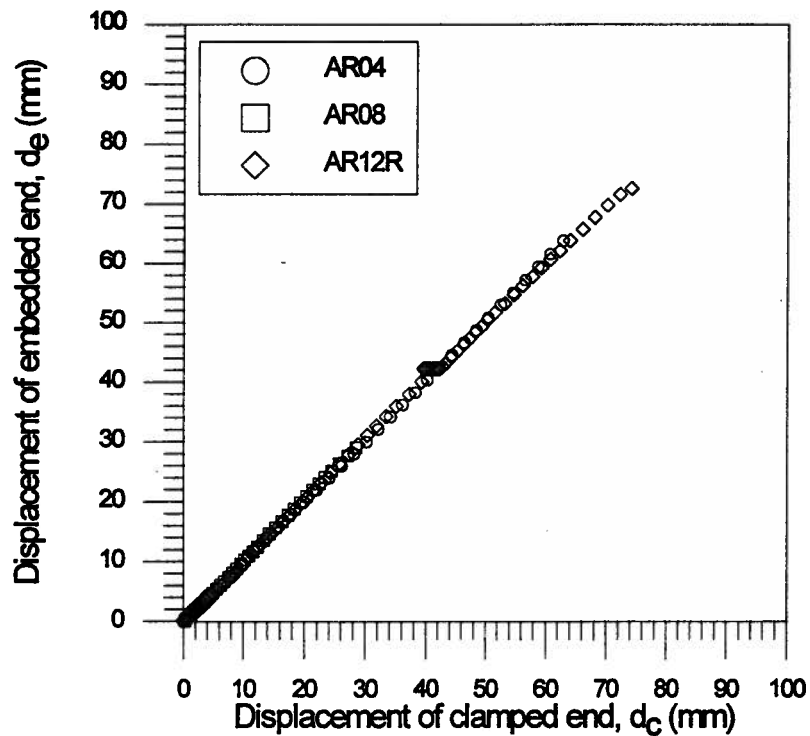


Figure 6.6: Relationship between d_c and d_e for the aluminum rough sheet

Chapter 6. Test Results

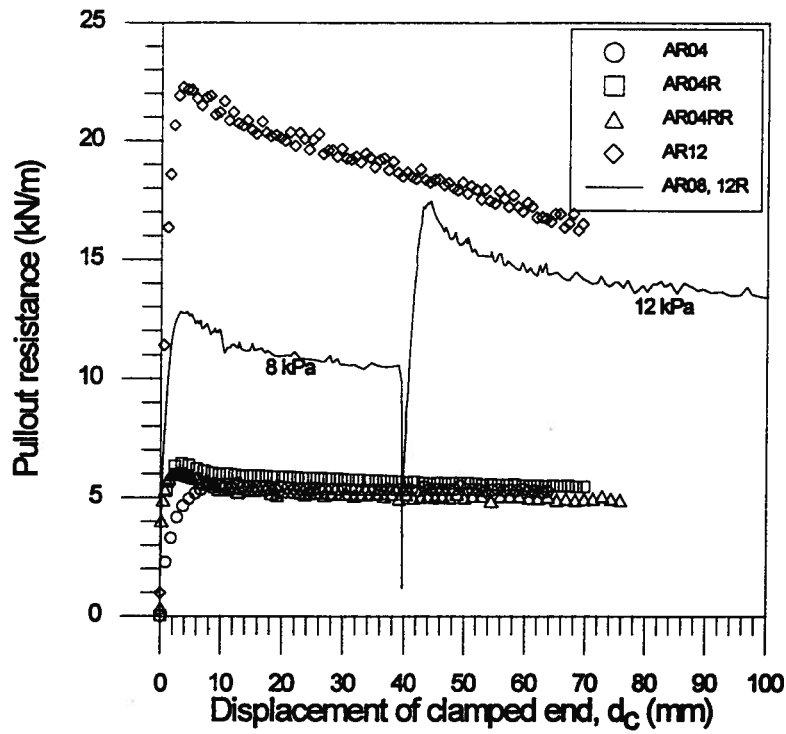


Figure 6.7: Pullout resistance of the aluminum rough sheet at $\sigma_n=4$ to 12 kPa

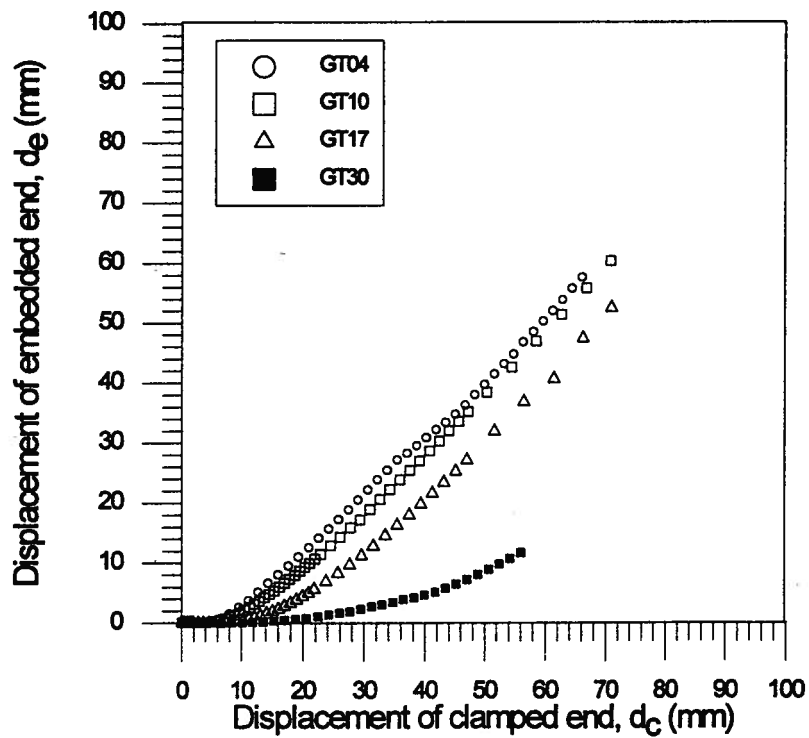


Figure 6.8: Relationship between d_c and d_e for the Tensar grid at $\sigma_n=4$ to 30 kPa

Chapter 6. Test Results

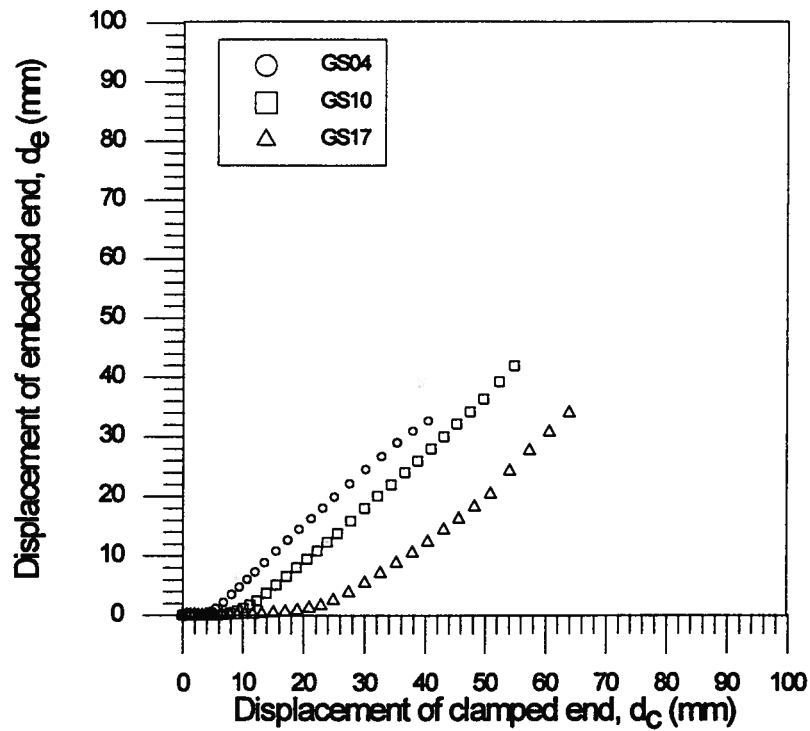


Figure 6.9: Relationship between d_c and d_e for the Stratagrid at $\sigma_n=4$ to 17 kPa

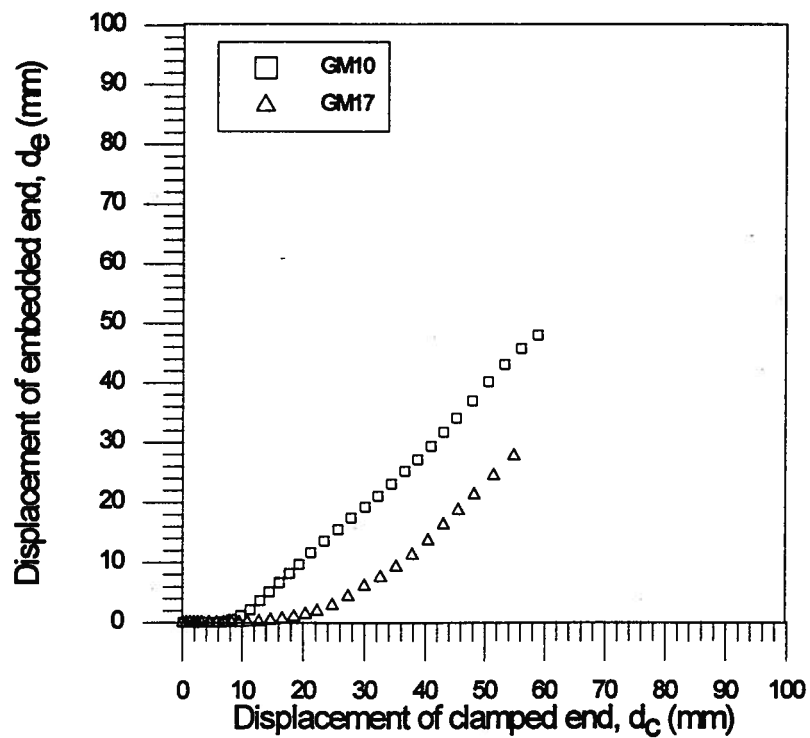


Figure 6.10: Relationship between d_c and d_e for the Miragrid at $\sigma_n=10$ and 17 kPa

Chapter 6. Test Results

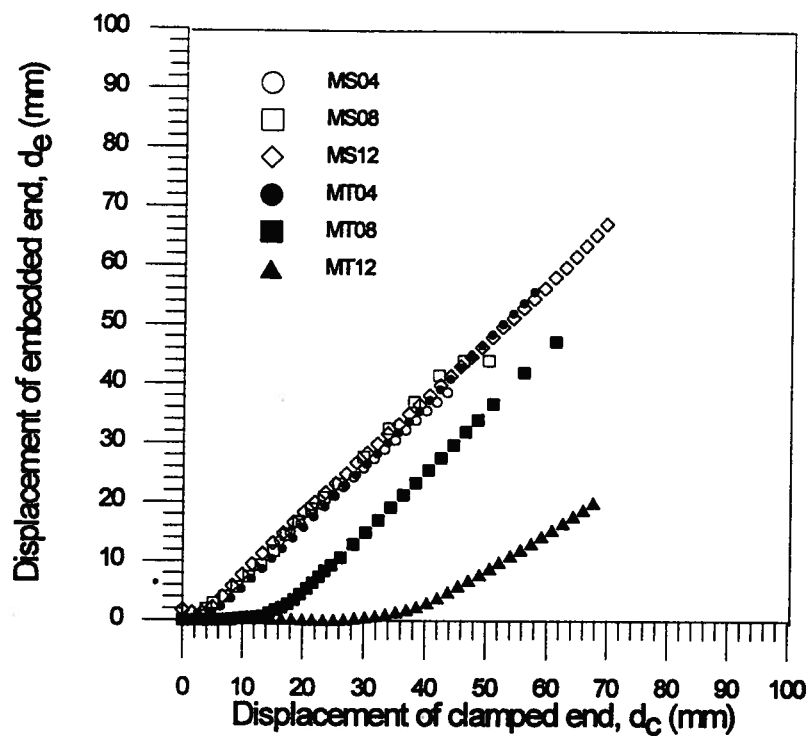


Figure 6.11: Relationship between d_c and d_e for the smooth and textured geomembrane at $\sigma_n=4$ to 12 kPa

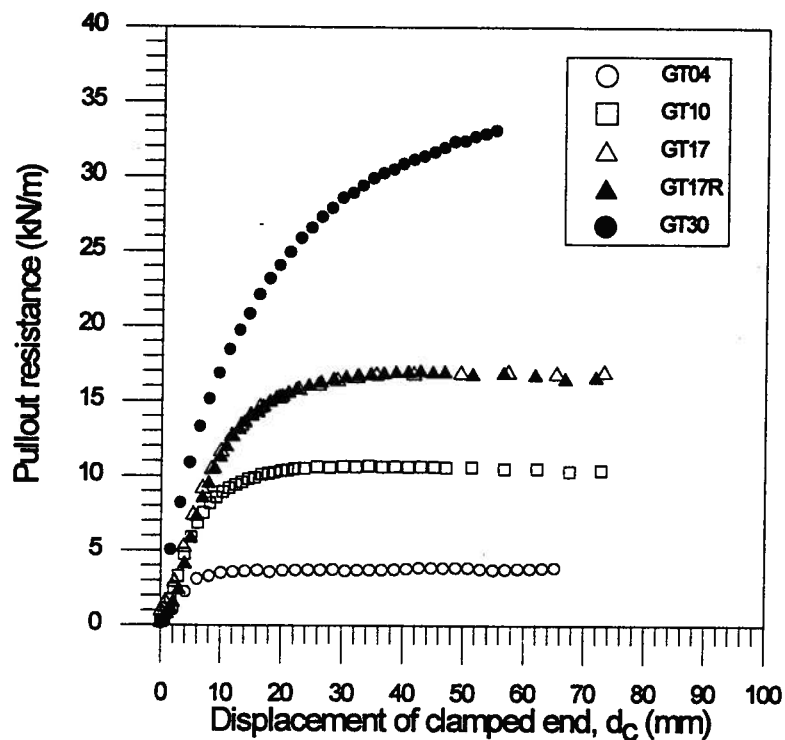


Figure 6.12: Pullout resistance of the Tensar grid at $\sigma_n=4$ to 30 kPa

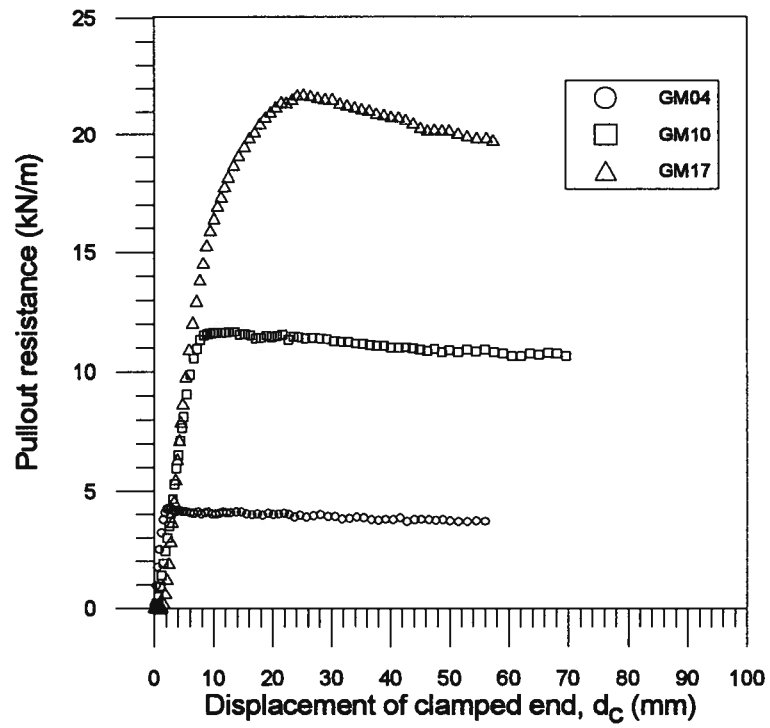


Figure 6.13: Pullout resistance of the Miragrid at $\sigma_n=4$ to 17 kPa



Clamped end

Embedded end

Figure 6.14: A photograph illustrating the displacement pattern of transverse elements for the Miragrid

Chapter 6. Test Results

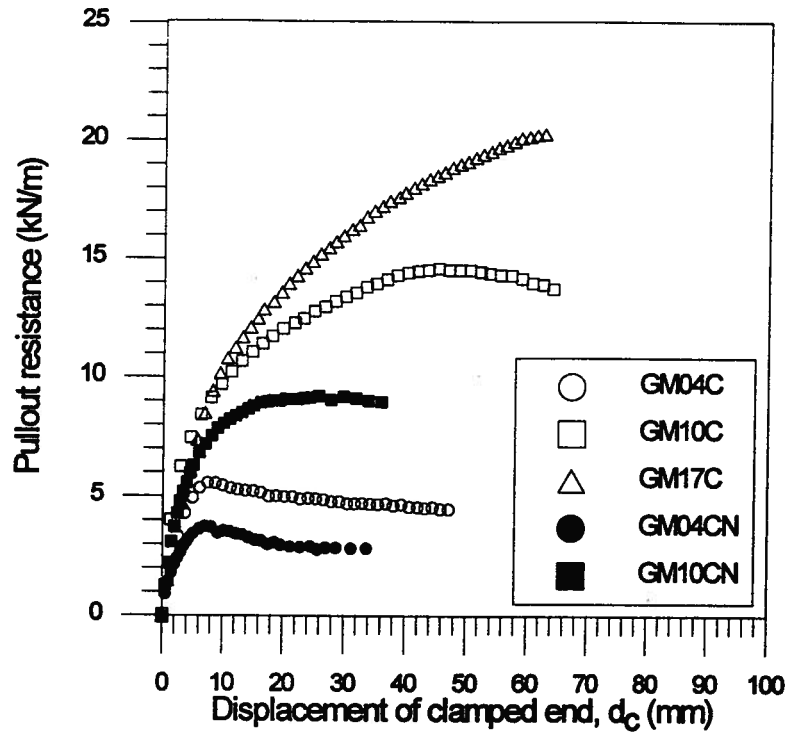


Figure 6.15: Pullout resistance of the Miragrid when tested in the cross-machine direction at $\sigma_n=4$ to 17 kPa

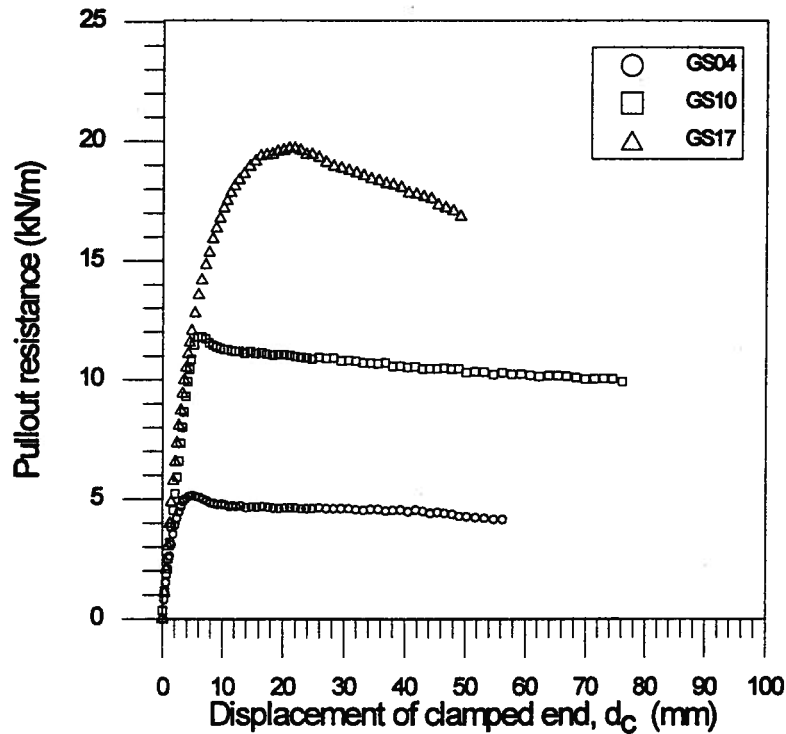


Figure 6.16: Pullout resistance of the Stratagrid at $\sigma_n=4$ to 17 kPa

Chapter 6. Test Results

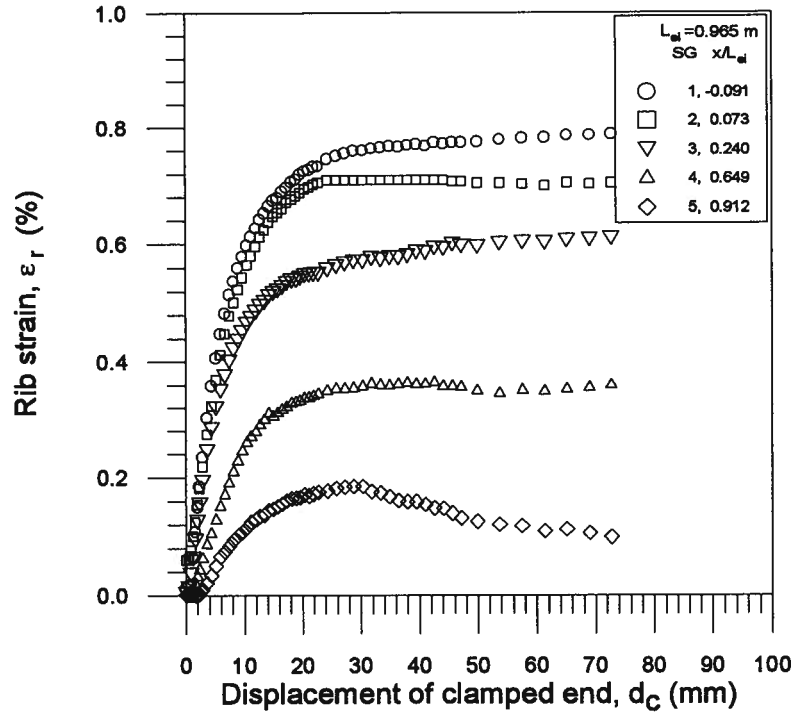


Figure 6.17: Mobilization of strain with d_c for the Tensar grid at $\sigma_n=10$ kPa

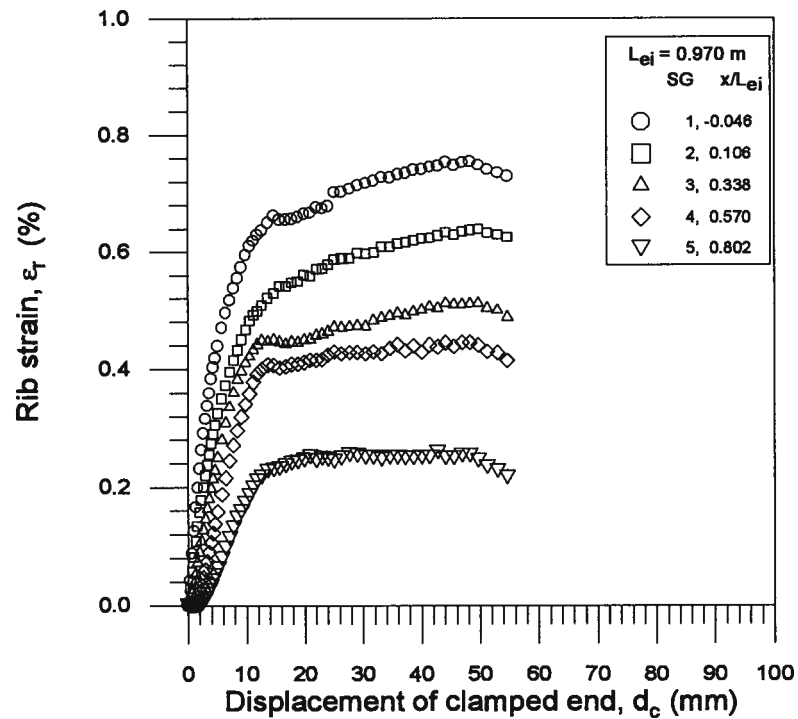


Figure 6.18: Mobilization of strain with d_c for the Stratagrid at $\sigma_n=10$ kPa

Chapter 6. Test Results

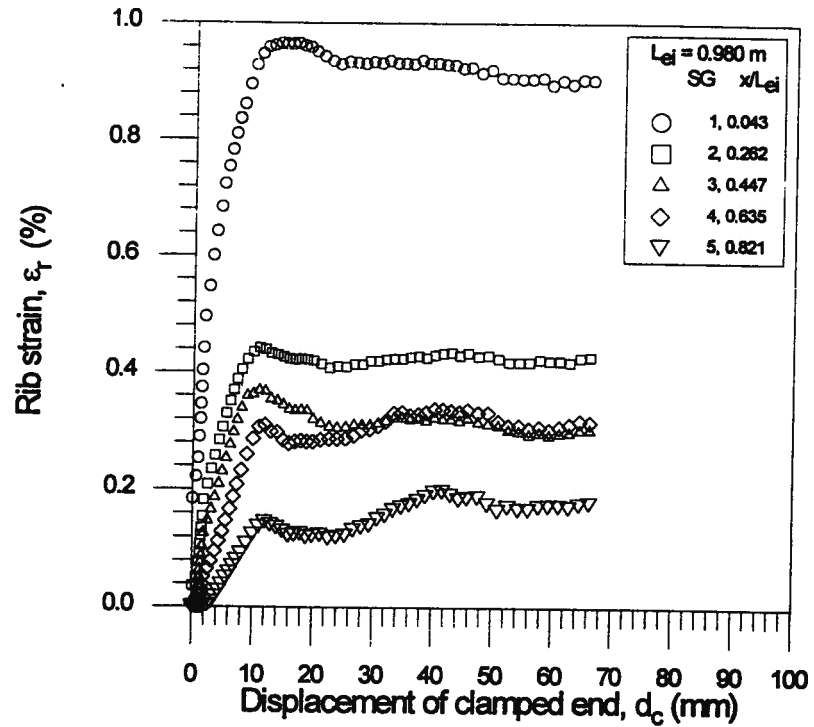


Figure 6.19: Mobilization of strain with d_c for the Miragrid at $\sigma_n = 10$ kPa

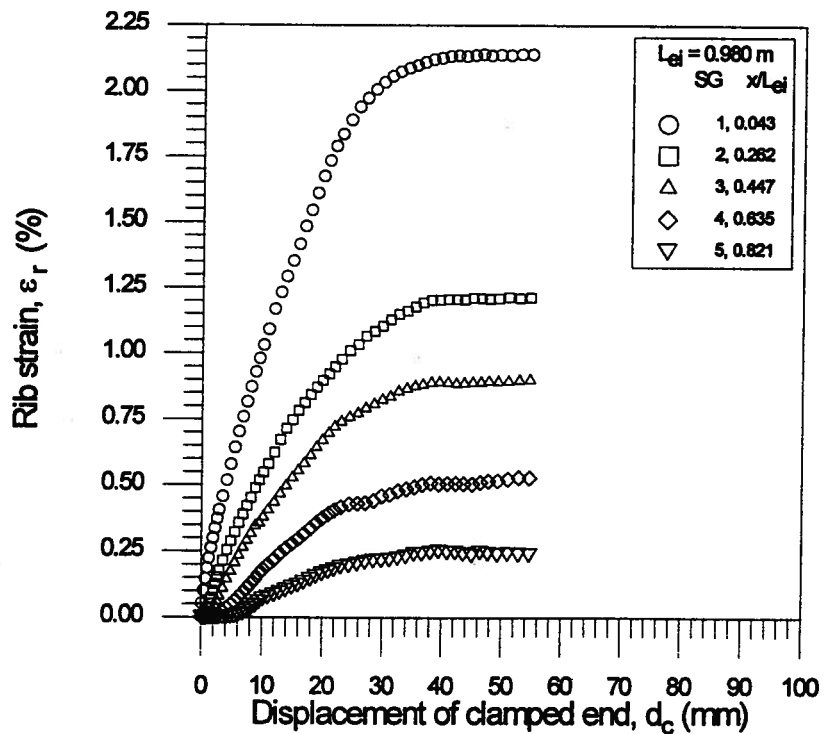


Figure 6.20: Mobilization of strain with d_c for the Miragrid at $\sigma_n = 17$ kPa

Chapter 6. Test Results

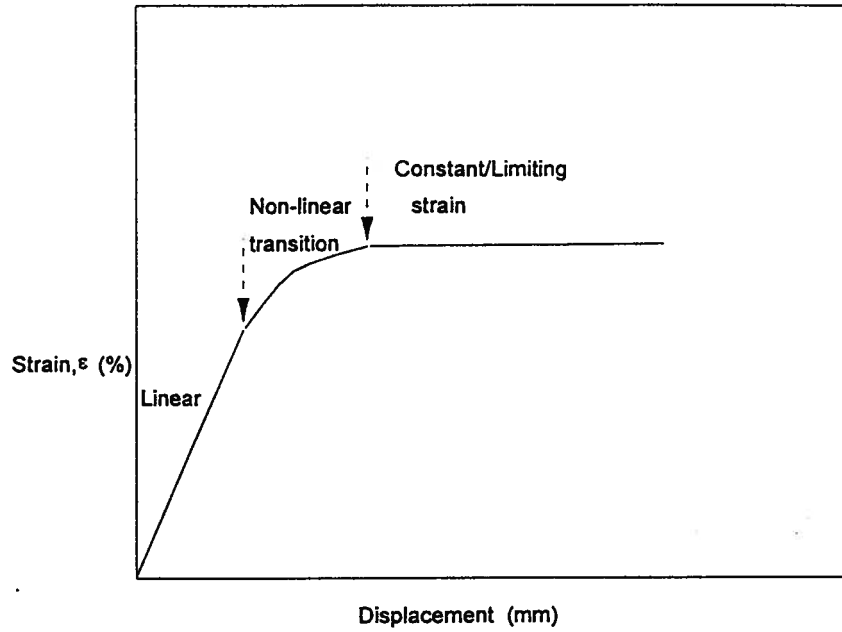


Figure 6.21: Characteristic variation of strain with displacement d_c

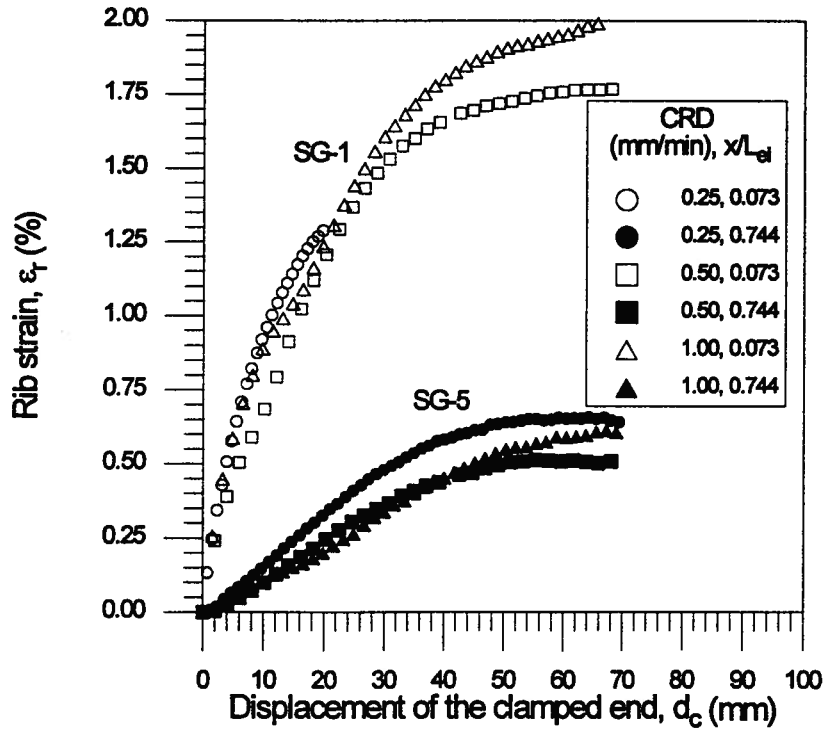


Figure 6.22: Variation of strain with rate of pullout for the Tensar grid at $\sigma_a = 20$ kPa

Chapter 6. Test Results

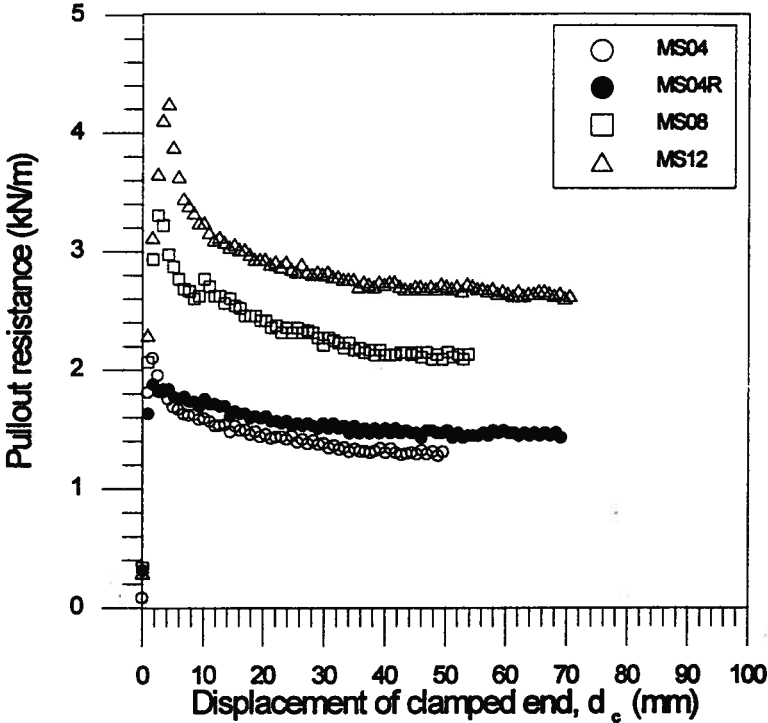


Figure 6.23: Pullout resistance of the smooth geomembrane at $\sigma_n=4$ to 12 kPa

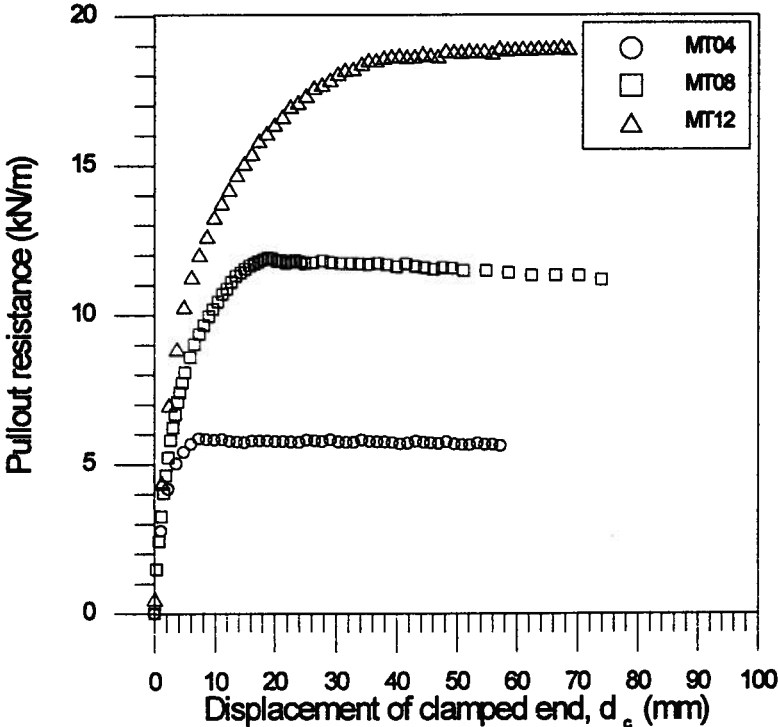


Figure 6.24: Pullout resistance of the textured geomembrane at $\sigma_n=4$ to 12 kPa

Chapter 6. Test Results

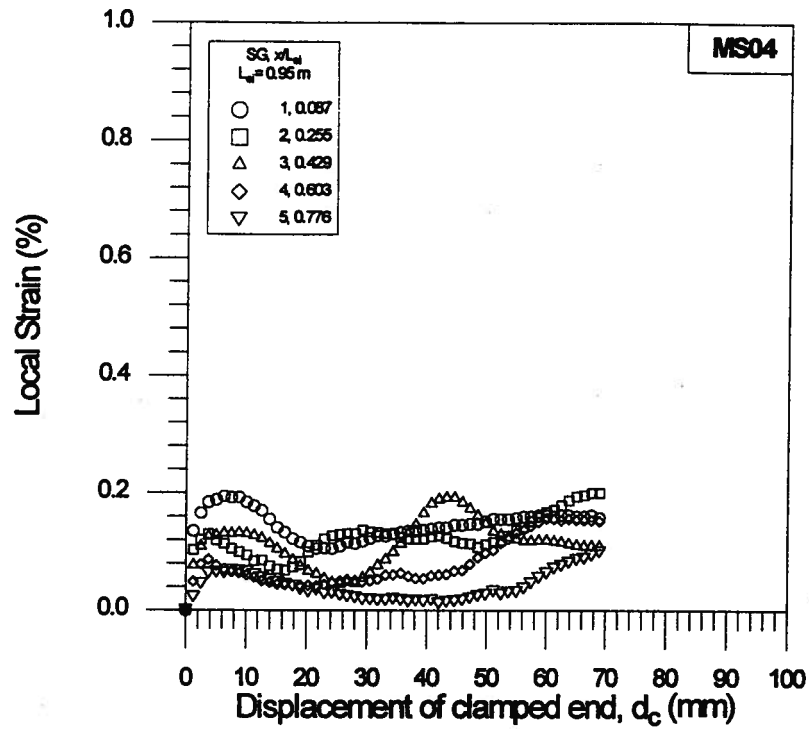


Figure 6.25: Mobilization of strain with d_c for the smooth geomembrane at $\sigma_n=4$ kPa

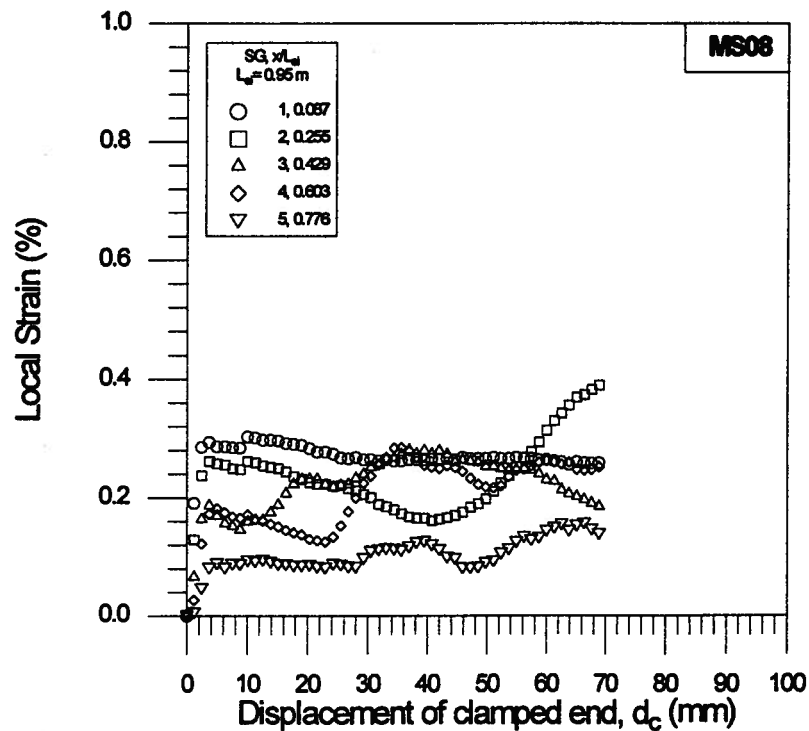


Figure 6.26: Mobilization of strain with d_c for the smooth geomembrane at $\sigma_n=8$ kPa

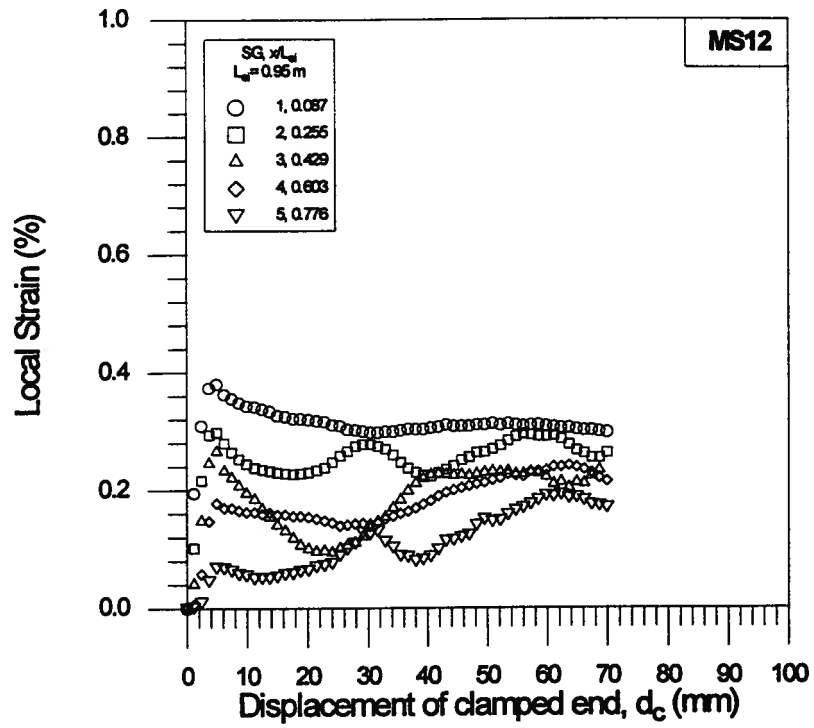


Figure 6.27: Mobilization of strain with d_c for the smooth geomembrane at $\sigma_n=12$ kPa

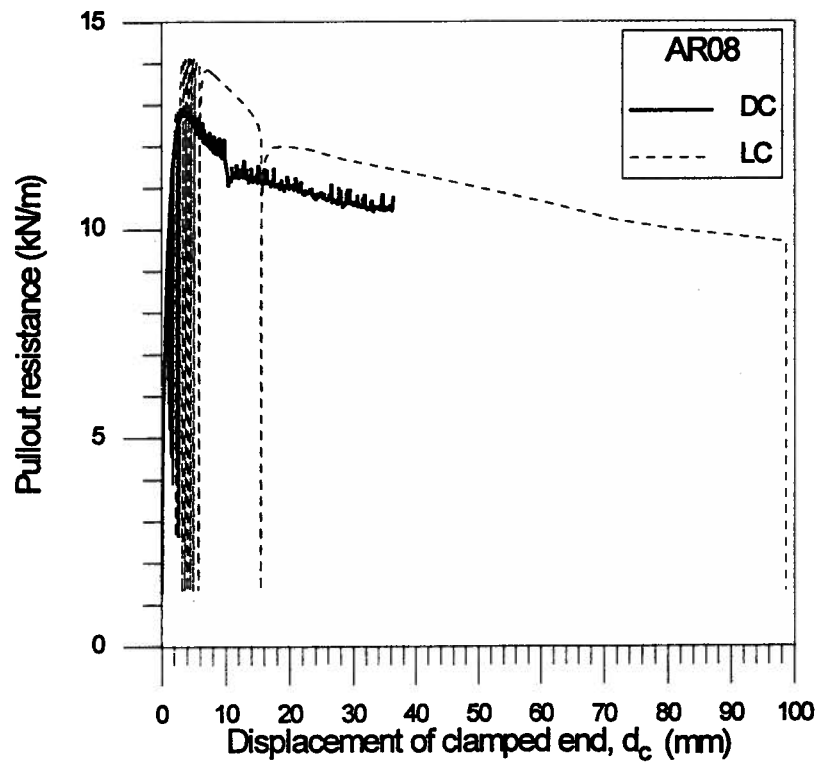


Figure 6.28: Pullout resistance of the rough aluminum sheet at $\sigma_n=8$ kPa and $f=0.01$ Hz

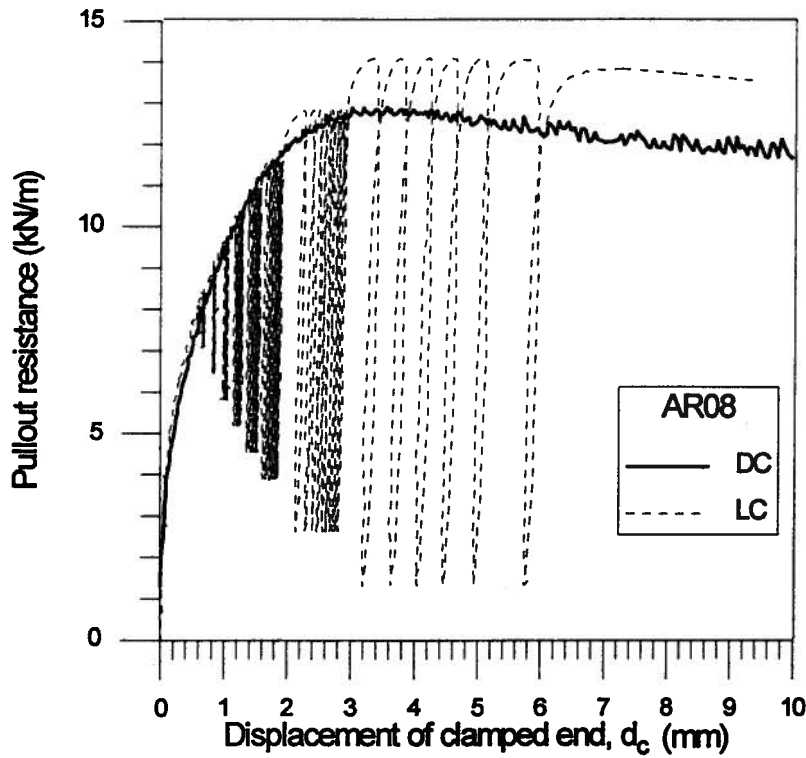


Figure 6.29: Detailed response at small displacement, from Figure 6.28

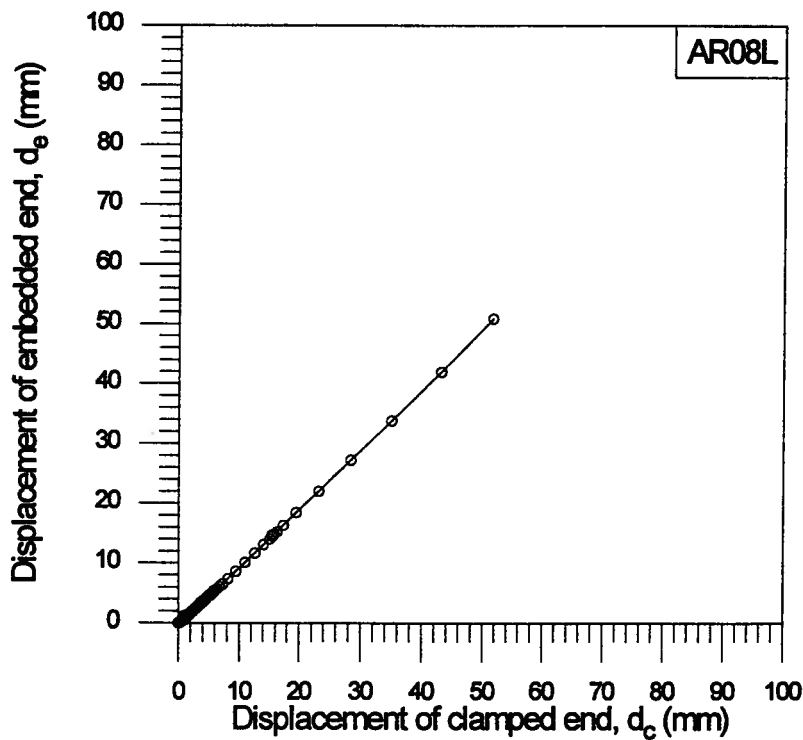


Figure 6.30: Relationship between d_c and d_e for the rough aluminum sheet in the LC tests at $\sigma_a=8$ kPa and $f=0.01$ Hz.

Chapter 6. Test Results

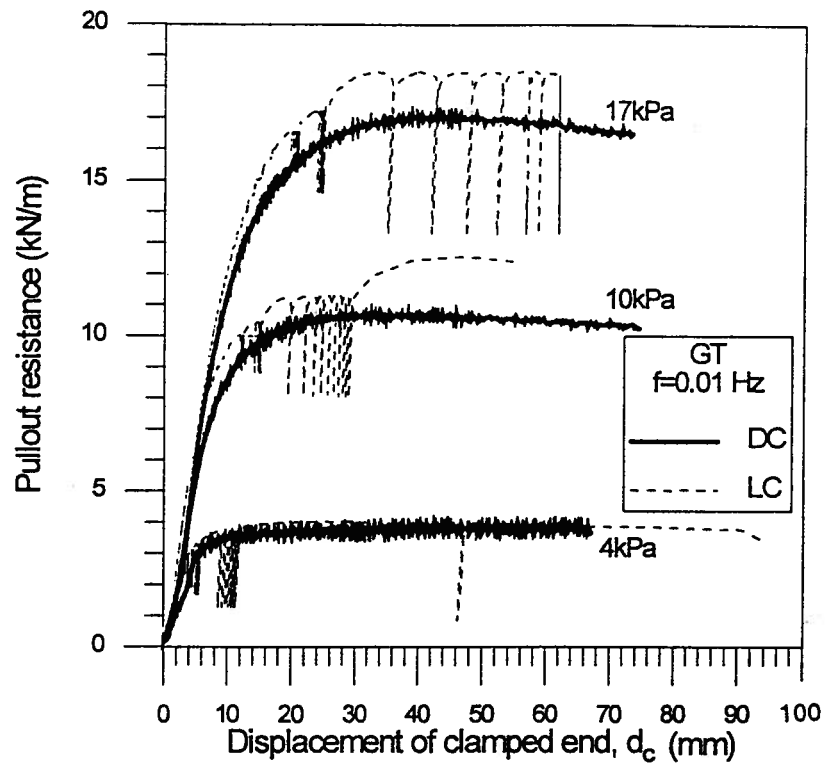


Figure 6.31: Pullout resistance of the Tensar grid in the DC and LC tests at $\sigma_a=4$ to 17 kPa and $f=0.01$ Hz

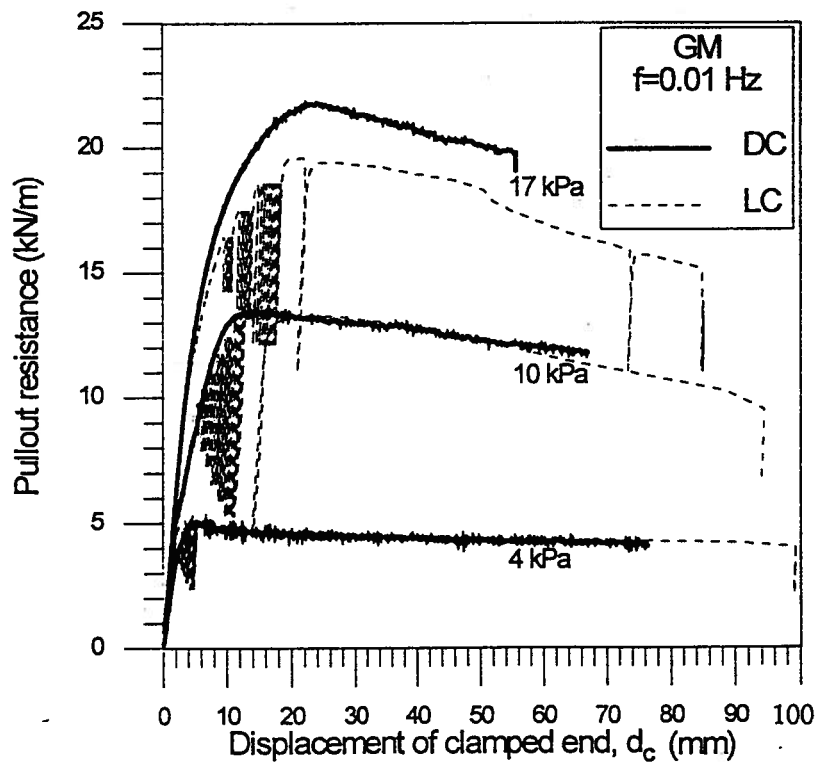


Figure 6.32: Pullout resistance of the Miragrid in the DC and LC tests at $\sigma_a=4$ to 17 kPa and $f=0.01$ Hz

Chapter 6. Test Results

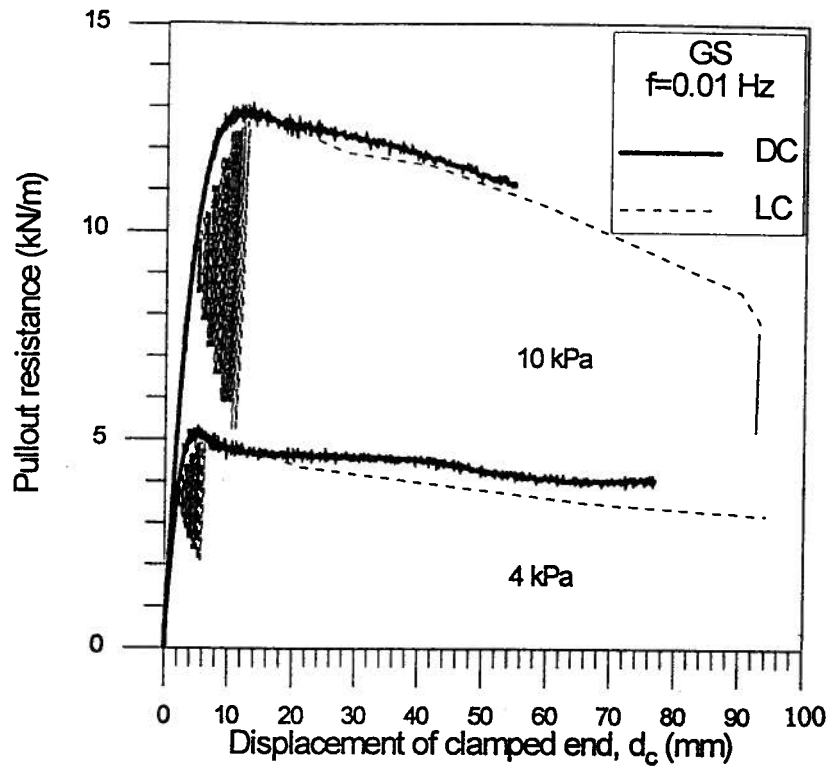


Figure 6.33: Pullout resistance of the Stratagrid in the DC and LC tests at $\sigma_n=10$ kPa and $f=0.01$ Hz

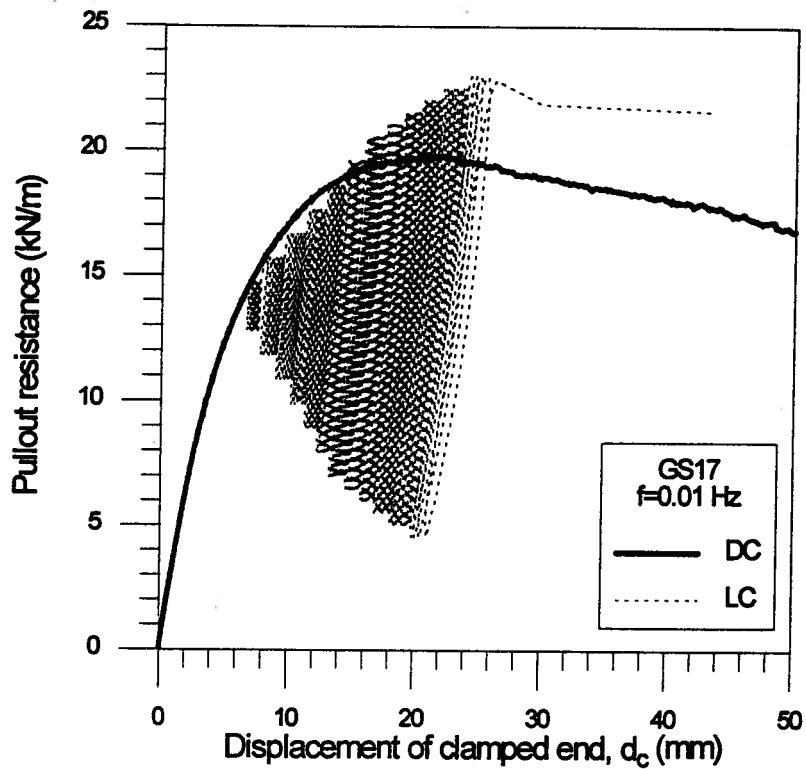


Figure 6.34: Pullout resistance of the Stratagrid in the DC and LC tests at $\sigma_n=17$ kPa and $f=0.01$ Hz

Chapter 6. Test Results

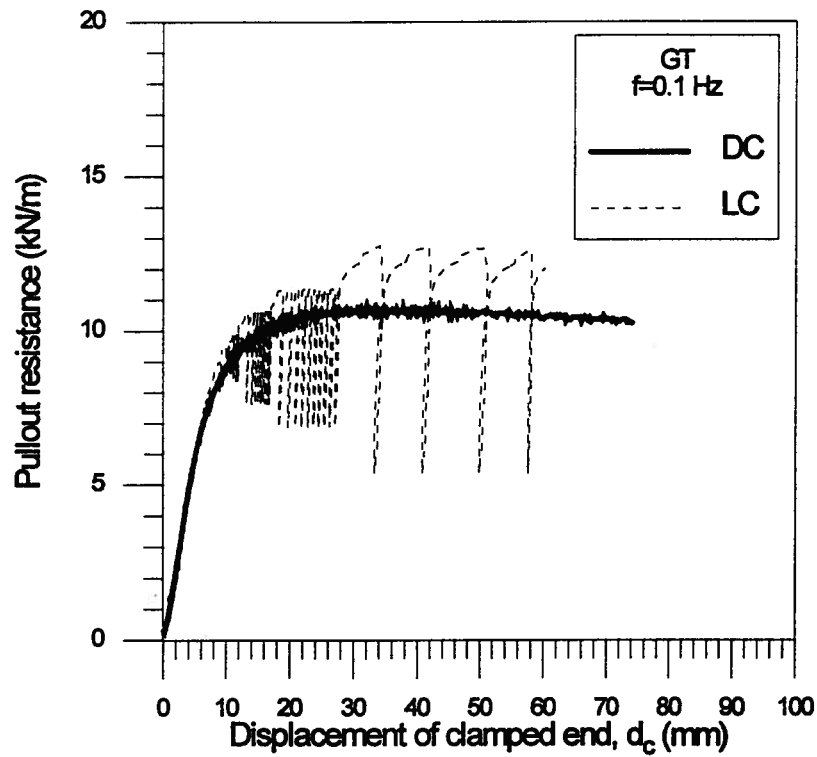


Figure 6.35: Pullout resistance of the Tensar grid in the DC and LC tests at $\sigma_v=10$ kPa and $f=0.1$ Hz

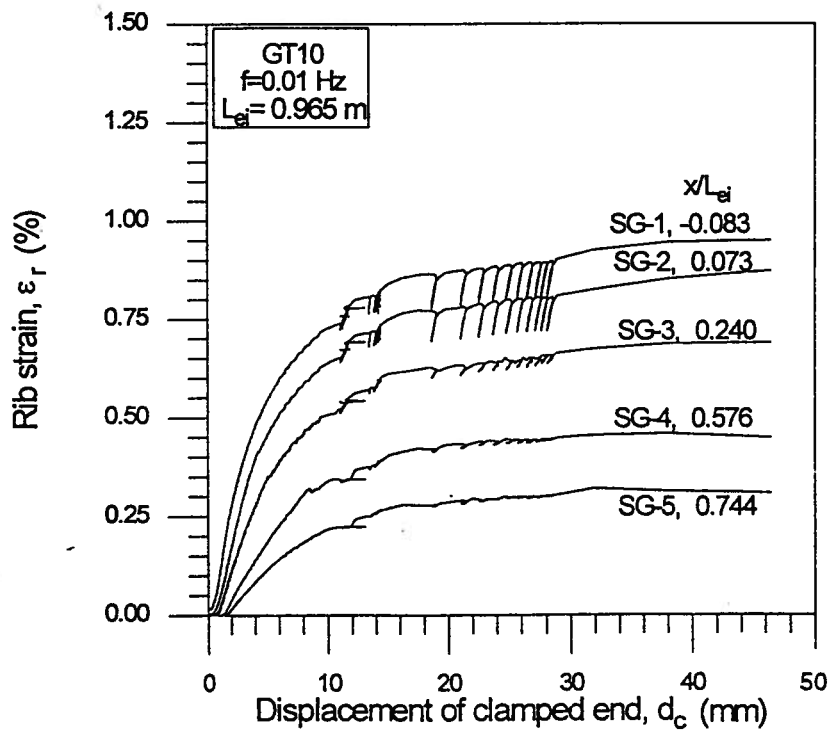


Figure 6.36: Mobilization of strain for the Tensar grid in the LC tests at $\sigma_v=10$ kPa and $f=0.01$ Hz

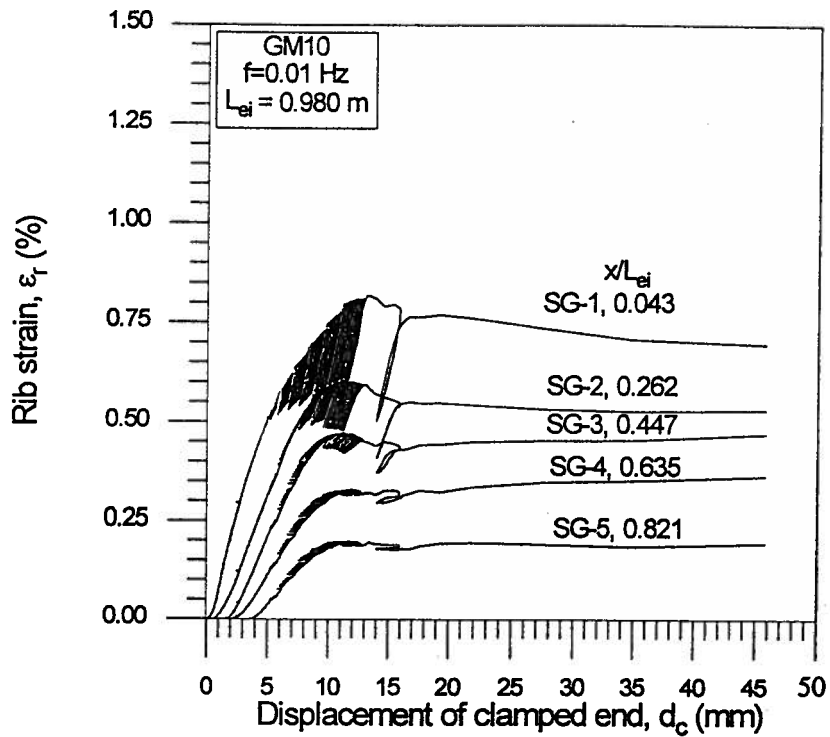


Figure 6.37: Mobilization of strain for the Miragrid in the LC test at $\sigma_n=10$ kPa and $f=0.01$ Hz

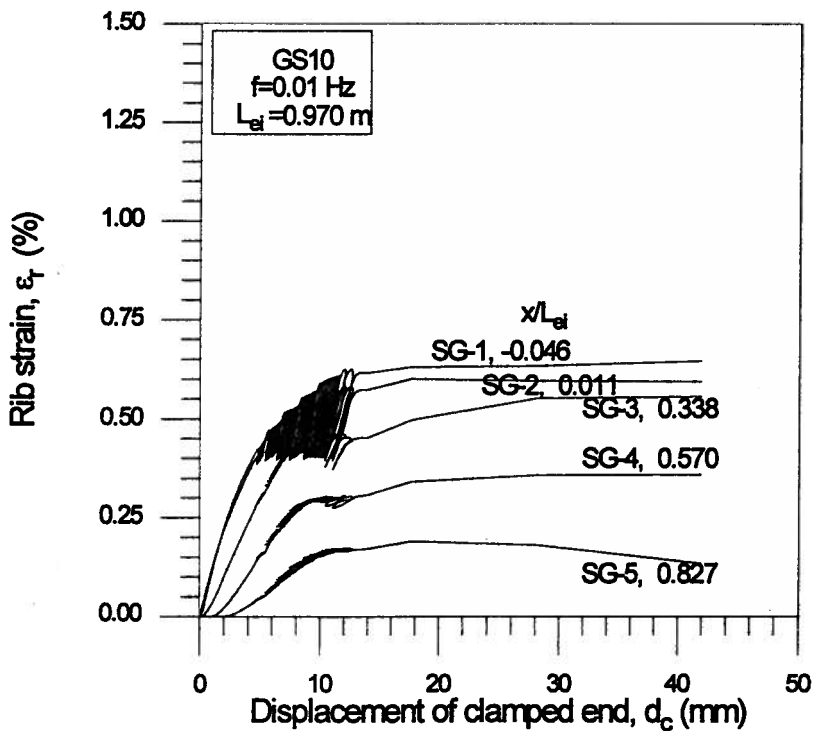


Figure 6.38: Mobilization of strain for the Stratagrid in the LC tests at $\sigma_n=10$ kPa and $f=0.01$ Hz

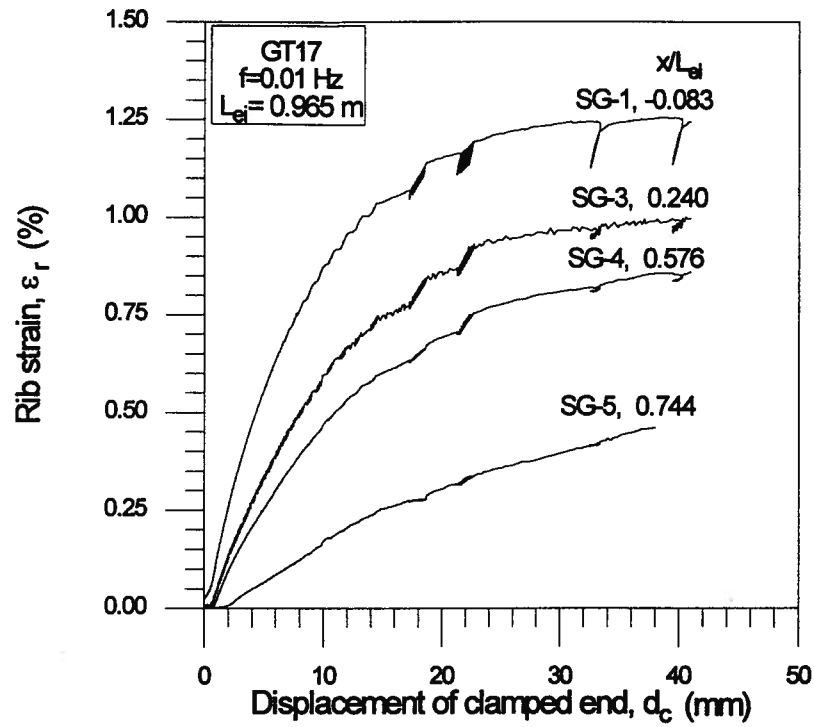


Figure 6.39: Mobilization of strain for the Tensar grid in the LC tests at $\sigma_n=17$ kPa and $f=0.01$ Hz

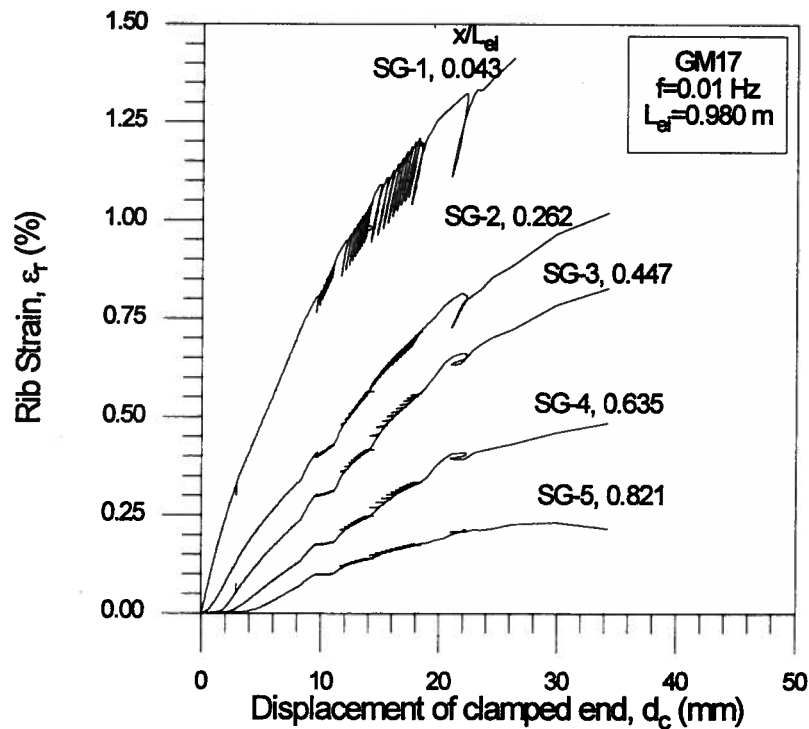


Figure 6.40: Mobilization of strain for the Miragrid in the LC tests at $\sigma_n=17$ kPa and $f=0.01$ Hz

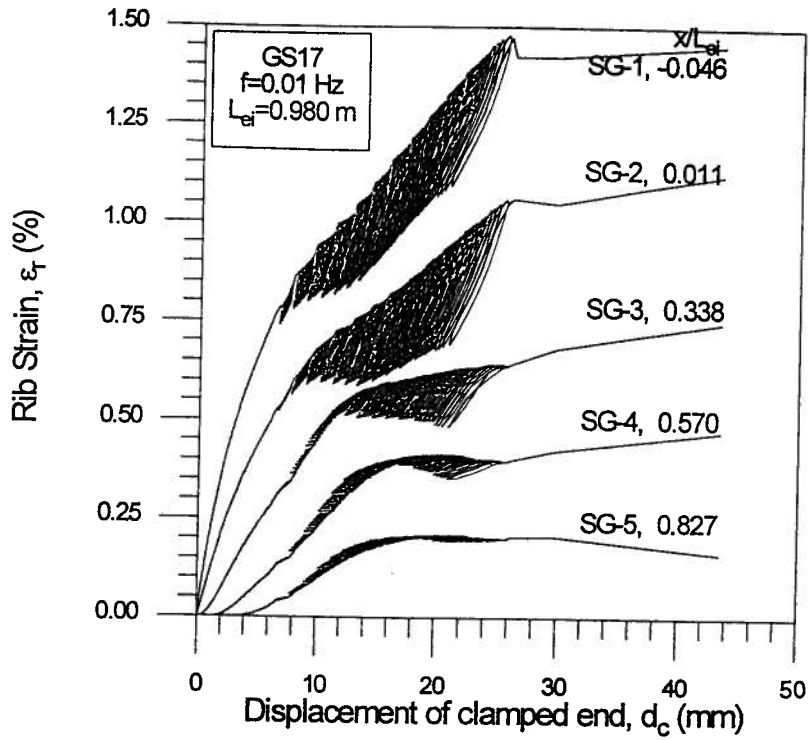


Figure 6.41: Mobilization of strain for the Stratagrid in the LC tests at $\sigma_n=17$ kPa and $f=0.01$ Hz

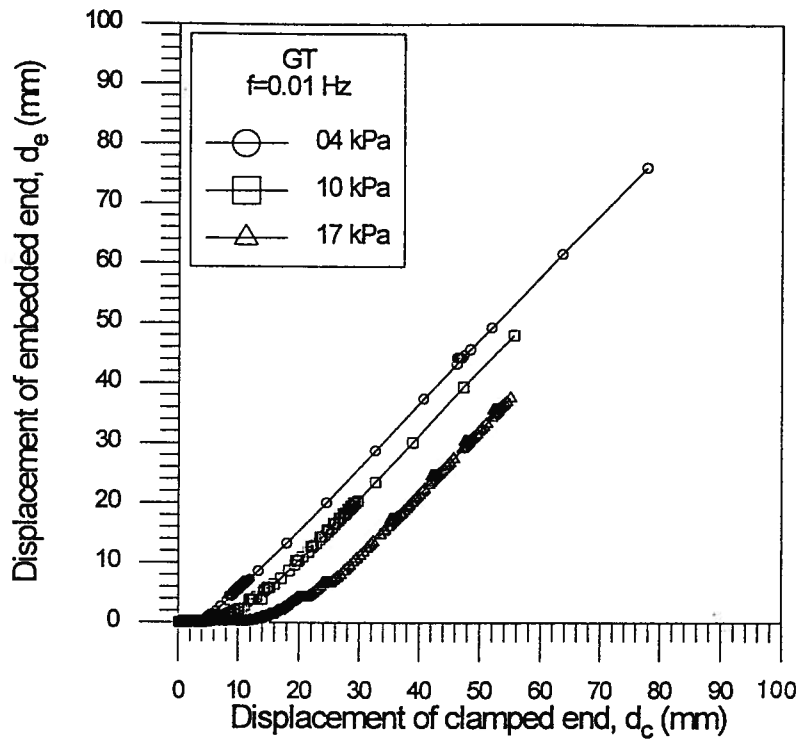


Figure 6.42: Relationship between d_c and d_e for the Tensar grid in the LC tests at $\sigma_n = 4, 10$ and 17 kPa

Chapter 6. Test Results

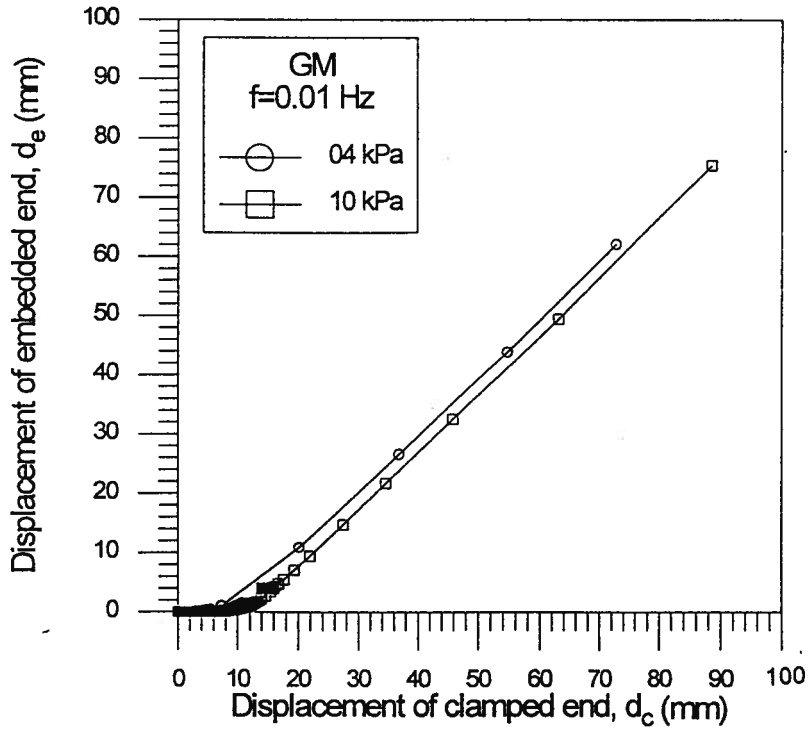


Figure 6.43: Relationship between d_c and d_e for the Miragrid in the LC tests at $\sigma_n = 4$ kPa and 10 kPa

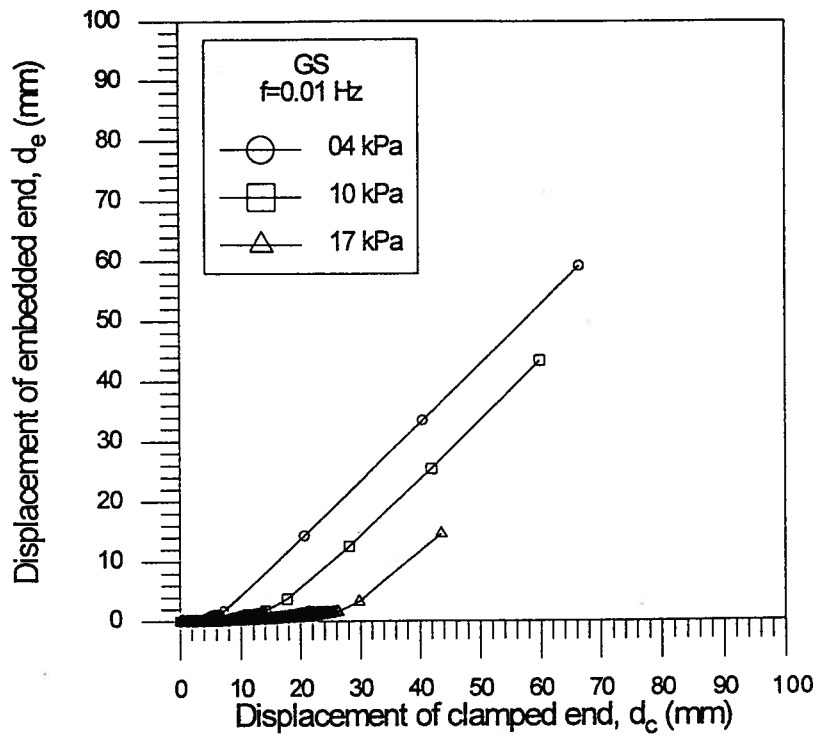


Figure 6.44: Relationship between d_c and d_e for the Stratagrid in the LC tests at $\sigma_n = 4, 10$ and 17 kPa

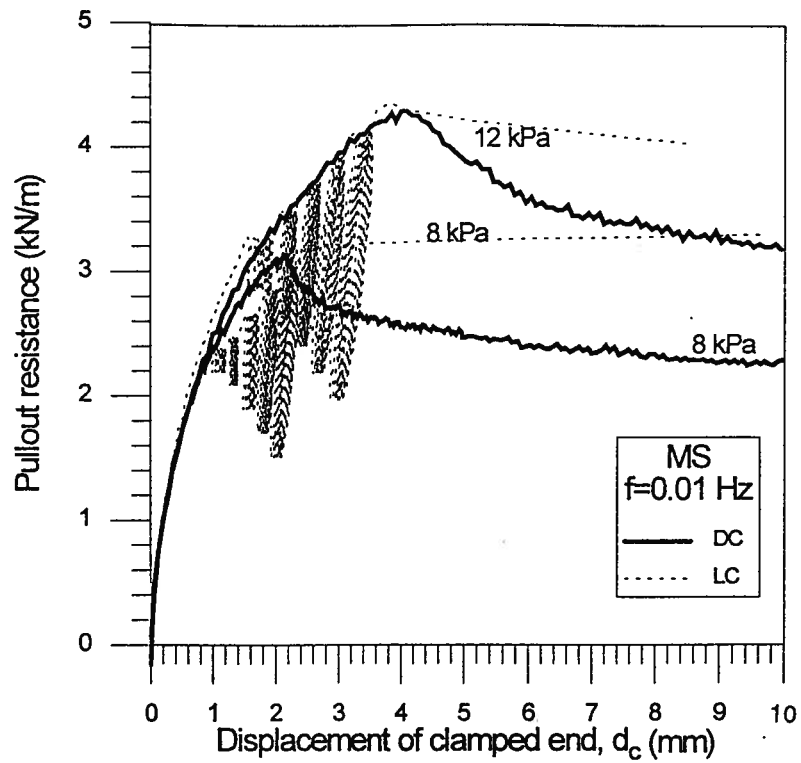


Figure 6.45: Pullout resistance of the smooth geomembrane in the DC and LC tests

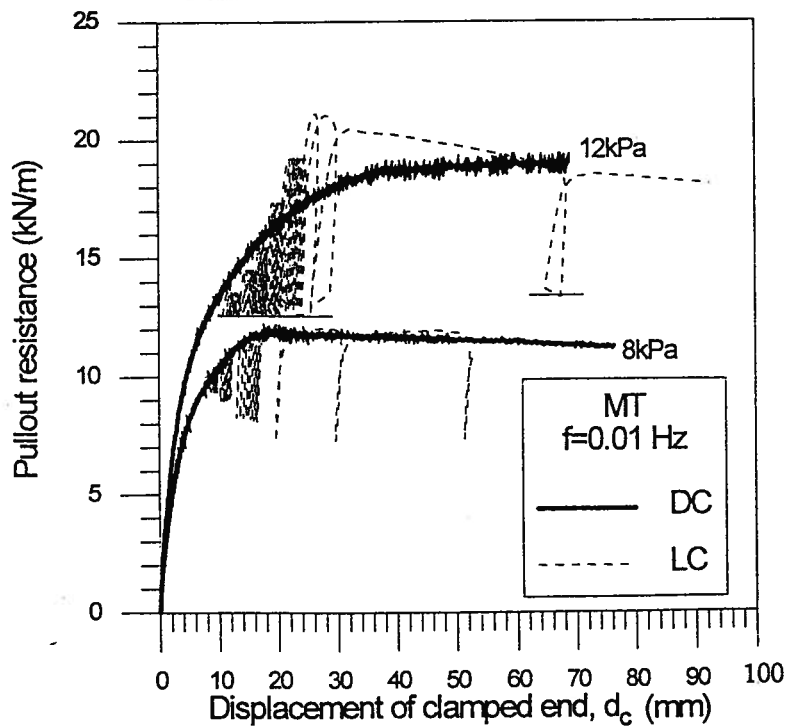


Figure 6.46: Pullout resistance of the textured geomembrane in the DC and LC test at $\sigma_n=8$ kPa and $f=0.01$ Hz

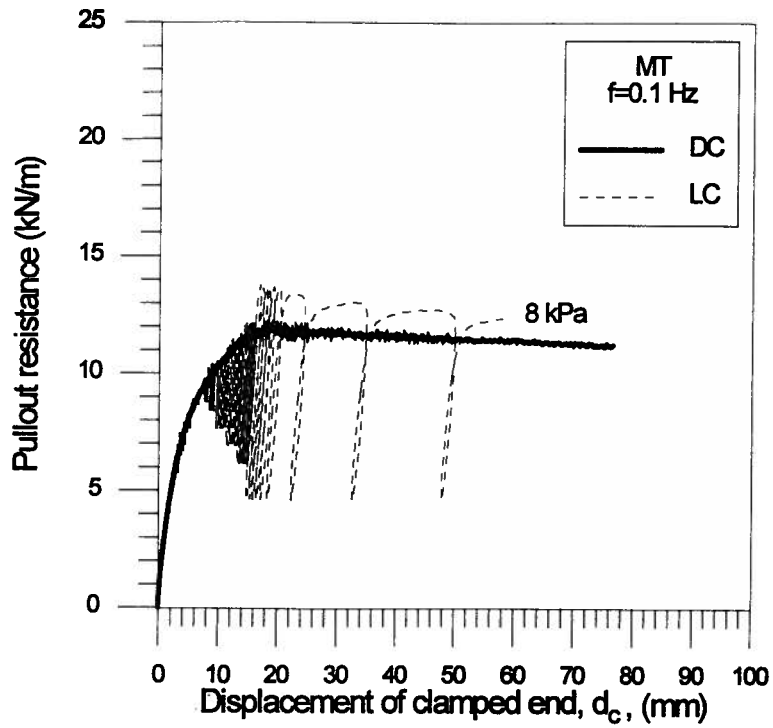


Figure 6.47: Pullout resistance of the textured geomembrane in the DC and LC tests at $\sigma_n=8$ kPa and $f=0.1$ Hz

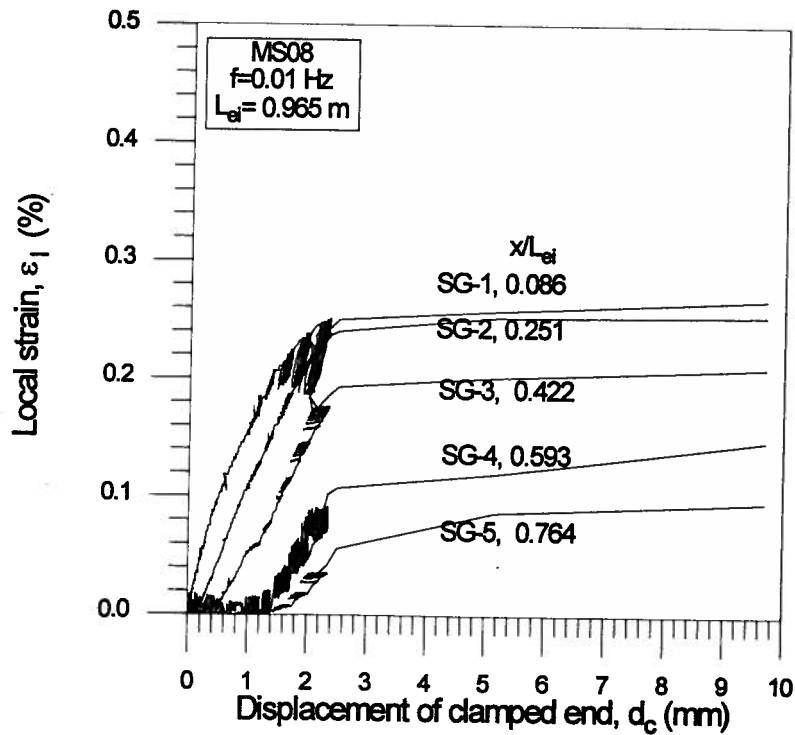


Figure 6.48: Mobilization of strain for the smooth geomembrane in the LC test at $\sigma_n=8$ kPa

Chapter 6. Test Results

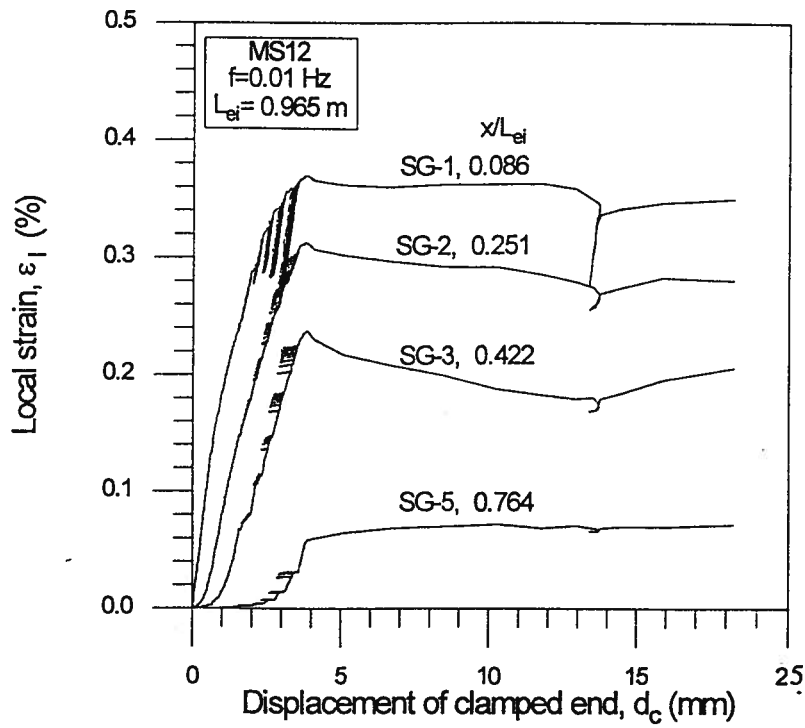


Figure 6.49: Mobilization of strain d_c for the smooth geomembrane in the LC test at $\sigma_n=12$ kPa

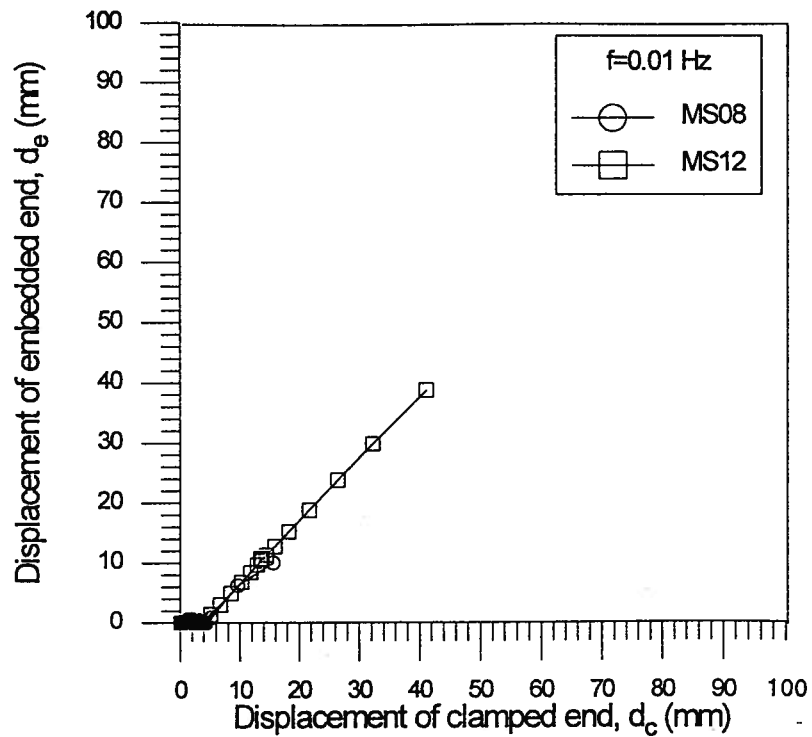


Figure 6.50: Relationship between d_c and d_e for the smooth geomembrane in the LC tests at $\sigma_n=8$ and 12 kPa

Chapter 6. Test Results

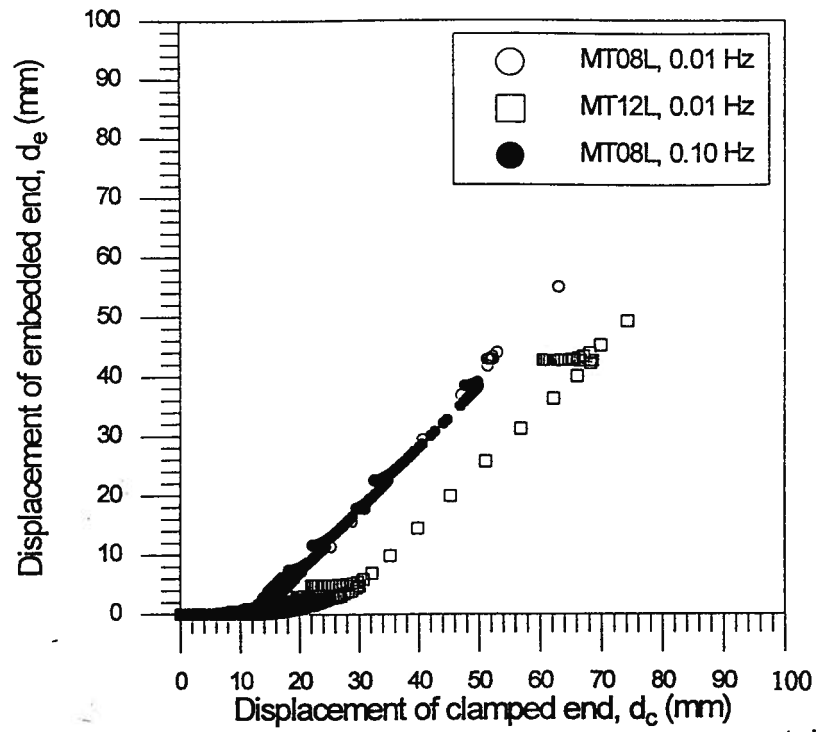


Figure 6.51: Relationship between d_c and d_e for the textured geomembrane in the LC tests at $\sigma_n=8$ and 12 kPa

CHAPTER 7

ANALYSIS OF TEST RESULTS

7.1 Introduction

In this chapter the test results are analyzed and an interpretation made to obtain soil-geosynthetic interaction factors for engineering design practice. The influence of the front boundary on the measured pullout resistance is discussed, and its implication for the interpretation of the results is outlined. A generalized method is proposed to interpret pullout test data that considers the extensibility of the test specimen. Several methods of interpreting monotonic pullout tests to obtain the interaction factors are reviewed, and are shown to be a special case of the proposed generalized method. Further, the rationale for choosing one method over the other is discussed with reference to test results for both grids and membranes.

The interaction factor from displacement-controlled tests is compared with results published by other researchers for both laboratory pullout tests and from instrumented field structures. Finally, the interaction factor in cyclic pullout loading is assessed with respect to the loading regime and characteristics of the specimen.

7.2 Displacement-Controlled Pullout Tests

The displacement-controlled pullout test results are interpreted to obtain an interaction factor for use in the design of reinforced soil structures and anchorage details for waste containment facilities. The interaction factor for design $F^*\alpha$ or $f_b \tan \phi$, see section 2.6.2, is defined as the ratio between the mobilized shear stress at the interface and the effective normal stress acting on that interface (τ/σ), where $F^*\alpha = f_b \tan \phi = \tau/\sigma$. In determining this

Chapter 7. Analysis of Test Results

interaction factor from pullout testing, it is necessary to know the distribution of shear stress along the embedded length of the test specimen at any displacement d_c .

The interpretation of a pullout test results is simple when the shear stress does not vary along the embedded length of the specimen. The distribution of shear stress is established from displacements at the clamped and embedded ends of the specimen, together with measurements of strain along the specimen. Since pullout resistance is influenced by the characteristics of the front wall of the apparatus, the following section presents data on the influence of the front wall on the test results.

7.2.1 Influence of the Front Boundary

Total pressure transducers (TPT) mounted on the front wall of the pullout apparatus, see Figure 3.9, record the distribution of lateral stress on the front wall. Measurements at locations TPT-1 and TPT-6 are used to determine a lateral earth pressure coefficient for the soil sample after application of the surcharge pressure to the sand sample but before clamping the specimen and application of pullout load. The relationship between lateral and normal stress at transducer locations TPT-1 and TPT-6 is shown for some tests in Figure 7.1. A best fit line for the data through the origin is also shown, for which the deduced lateral earth pressure coefficient is 0.415. Scatter in the data is attributed to the sensitivity of the transducers to the relatively low values of lateral stress at this stage in a test. Using Jaky's expression for K_o , the angle of friction for the sand for the relatively dense, undisturbed sand is computed to be 35.8° . For a soil deposit that is formed by layering, the lateral stress coefficient is found to vary between 0.4 to 0.5 (Lambe, 1979). Thus, the observed lateral

Chapter 7. Analysis of Test Results

earth pressure coefficient is in agreement with the expected values implying that the front wall behaves as a rigid boundary.

Mobilization of pullout resistance during testing induces additional lateral stresses on the front wall of the apparatus. The incremental lateral stress ($\Delta\sigma_h$) at any displacement due to pullout is the difference between the the current stress and that after surcharge loading. Values are reported with respect to a non-dimensional depth ratio, which is the distance of the TPT location (y) from the centre line of the slot normalized by the half height of the soil specimen (h), where $h=30$ cm. For locations above the slot the ratio y/h is positive, see Figure 3.12. All transducer locations are symmetrical about the slot except for TPT-6 which is slightly closer than TPT-1.

The lateral pressure at maximum or peak pullout resistance is selected for use in interpretation of results: the peak pullout resistance for those tests with strain softening behaviour, and the maximum resistance is for tests with a uniform resistance at large displacement. Note these values of lateral stress are not necessarily the maximum for the test: see for example Figure 7.2, where the maximum lateral stress at location TPT-3 is higher (70 kPa) than that measured at the mobilization of maximum pullout resistance (55 kPa). It is apparent that the magnitude of lateral stress is higher at locations TPT-3 and TPT-4, which are close to the slot on the front boundary. The values of lateral stress, and deduced coefficient of lateral earth pressure, confirm our understanding that the vertical stress acting on the test specimen can increase in the vicinity of the front slot. At locations TPT-1 and TPT-6 which are furthest away from the slot, the magnitude of lateral stress is significantly lower.

Chapter 7. Analysis of Test Results

Results for tests performed on the MS and the GT specimens at similar surcharge pressures are shown in Figure 7.3. A general trend is observed where the incremental lateral stress decreases at locations away from the slot: the distribution is asymmetric, with higher stresses above the slot than below it. This type of response is attributed to the different boundary conditions at the top and bottom boundary of the apparatus. Similar observations have been reported by Palmeira (1987), and Kharchafi and Dysli (1993). Further, the magnitude of lateral stress is significantly greater for the Tensar grid specimen than the smooth membrane.

The incremental lateral stress of Figure 7.3 is normalized with respect to the average shear stress mobilized on the test specimen and is illustrated in Figure 7.4. From the normalized behaviour the relationship appears to be unique with the stress ratio being independent of the type of specimen. Using this approach, the data for the other specimens are plotted at various normal stresses, see Figures 7.5 to 7.10.

The curves show the stress ratio tends to a unique relationship. Thus, for the front wall to exert a minimal influence on the measured pullout resistance the mobilized shear stress and hence normal stress used in tests should be relatively low.

7.2.2 Mobilization of Pullout Resistance

A unified description of the mobilization process in the displacement-controlled (DC) tests is illustrated first with reference to the GT10 test results. The relationship between the displacement of clamped (d_c) and embedded (d_e) ends is shown in Figure 7.11. It is distinguished by three zones. In zone I ($d_c = 0$ to 5 mm) there is no significant displacement of the embedded end, indicating the imposed displacement at the clamped end is not

Chapter 7. Analysis of Test Results

transferred along the entire length of the specimen, resulting in a non-uniform shear displacement. The response in zone II ($d_c = 5$ to 26 mm) shows the embedded end experiences some movement that increases with the displacement d_c . The behaviour in zones I and II is typical of an extensible element. In contrast, the relationship in zone III is linear and inclined at 45° , indicating $d_e = d_c$ and therefore increments of displacement are equal along the embedded length of the specimen.

To complement the above interpretation, the strain measurements at various displacements d_c are used to develop profiles of strain. The profiles are shown over the embedded length for the measured strains only: it is recognized that the strain at the embedded end is zero for all test specimens. Results for the Tensar grid at $\sigma_n = 10$ kPa are shown in Figure 7.12. At $d_c = 1$ mm, the strain profile indicates zero strain at a normalized distance of 0.60 from the front wall of the apparatus. As the test continues, the point of the zero strain moves progressively toward the embedded end, and the slope of the profile is observed to increase. Beyond $d_c = 30$ mm the strain profile appears to be unique and linear. This displacement corresponds to the onset of zone III in Figure 7.11, where $d_c = d_e$ and the test specimen behaves as an inextensible inclusion. Therefore, the condition of the test specimen during pullout at constant uniform strain is associated with a strain profile that is linear.

This concept of progressive strain mobilization is further illustrated by analysis of results for the Tensar grid test at $\sigma_n = 20$ and 30 kPa. Notwithstanding the absence of a zone III response in the GT30 test, see Figure 7.13, the strain profiles (Figure 7.14) show the position of zero strain again moving toward the embedded end although less conspicuously

Chapter 7. Analysis of Test Results

than seen in the GT10 test. The strain profile is non-linear, with the slope of the profile being greatest near the front wall and decreasing rapidly toward the embedded end. The slope of the profile increases rapidly with displacement d_c . A similar response is observed in the GT20 test, see Figure 7.15.

Results for the Stratagrid and Miragrid (Figures 7.16 to 7.20) confirm the general nature of the behaviour: inspection of the strain profiles for GT10 and GS10, and for GT20, GS17 and GM17, also reveal a characteristic nature in the magnitudes of strain and imply a response that is not overly dominated by differences in type or structure of the three grids.

The relationship between d_c and d_o for the MS08 test depicts a different behaviour, see Figure 7.21. The zones I and II are indistinct, and the relationship beyond $d_c = 3$ mm is typical of zone III. This fact is confirmed by considering the strain profiles of the test, see Figure 7.22. The position of zero strain on the specimen moves towards the embedded end for $d_c < 2$ mm. As the test continues further, the strain profile is defined by a unique line forming an upper bound to the measured strain. The observed scatter of data points for $d_c > 5$ mm is attributed to fluctuations in measurements at these small strain magnitudes.

In summary all tests illustrate a progressive mobilization of strain and describe a relationship between displacement of the clamped end, and relative displacement along the test specimen, that is non-linear. Interaction between the soil and test specimen is expressed in a non-dimensional form by normalizing the mobilized shear stress with respect to the applied normal stress. The following sections present and comment on various methodologies for determining interaction factors by experimental as well as theoretical methods.

Chapter 7. Analysis of Test Results

7.2.3 Experimental Interaction Factors

To determine the interaction factor experimentally, the most important parameter to be assessed is the mobilized shear stress at the soil-geosynthetic interface. Analysis of the results in the previous section has clearly demonstrated the variable tensile strain along the embedded length of the specimen. The response to pullout is one of progressive strain, with a behaviour that is either extensible or inextensible being dependent on the applied normal stress. This behaviour implies mobilization of a non-uniform shear stress along the embedded length of the specimen. Hence the shear stress distribution depends on the type of the specimen, its stiffness, and the magnitude of applied normal stress.

The mobilized shear stress and its variation along the length of the test specimen may be evaluated from the measurements of the pullout load at the clamped end if strain measurements are made along the length of the specimen. While interpreting the pullout test results, it is important that the part of the specimen contributing to the resistance be clearly delineated. Several researchers have addressed this aspect in different ways: the methods in use may be broadly classified into two categories, namely the average resistance and the mobilizing process methods.

7.2.3.1 Average Resistance Method

In this method the mobilized shear stress is assumed to be an average stress acting over a mobilized area of the test specimen. Depending on the definition of resisting area, several variations are used in practice: total area, effective area, and maximum slope methods. A schematic illustration in Figure 7.23 describes the definition of the resisting area. They are explained in following sections.

Chapter 7. Analysis of Test Results

7.2.3.1.1 Total Area

In this method, the average shear stress is calculated using the total initial embedded area of the specimen. The “area method” of Bonckewicz et al. (1986) and the “total area method” of Ochiai et al. (1992) are identical. An expression for average shear stress is given by:

$$\tau_{av} = \frac{P}{2L_{ei}W_r} \quad (7.1)$$

where:

P is the pullout resistance of the specimen,

τ_{av} is the average shear stress on the soil-specimen interface,

L_{ei} is the initial embedded length of the specimen, and

W_r is the width of the specimen

Thus, a measurement of pullout load is adequate to compute the average shear stress. This method would give a reasonable value when the specimen is pulled out with no significant elongation, as in the case of zone III (Figure 7.21). However, marked extension will lead to the resisting area being less than the initial, total embedded area, and an underestimation of the interaction factor. This method uses the total embedded length of the test specimen and hence is unsuitable for tests with relatively extensible specimens.

Chapter 7. Analysis of Test Results

An improvement to the total area method arises if displacement of the embedded end is measured, allowing the actual embedded length (L_{ea}) to be calculated throughout the test, where:

$$L_{ea} = (L_{ei} - d_e) \quad (7.2)$$

Replace L_{ei} by L_{ea} in equation 7.1 to compute a revised shear stress.

7.2.3.1.2 Effective Area

To consider only that part of the specimen resisting the pullout load, Bonczkiewicz et al., (1986) introduced the corrected area method in which mobilized length was determined by measurement of displacement along the specimen. Data are plotted in terms of measured pullout force and mobilized length. The mobilized length of the specimen is determined by assuming that movement at a gauge location indicates initiation of pullout at that point.

A more recent variation is the effective area of Ochiai et al., (1992) used when the distribution of pullout force along the embedded length of the specimen is known. The mobilized average shear stress in this method is given by

$$\tau_{av} = \frac{T_{max} - T_x}{2WL_x} \quad (7.3)$$

where:

T_{max} is the pullout force measured at the clamped end of the specimen,

T_x is the pullout force measured or estimated at a section x on the specimen

where the slope of the tensile force distribution changes direction (decreases), and

Chapter 7. Analysis of Test Results

L_x is the distance from the front wall to the section x .

The distribution of pullout force along the embedded length is obtained from measurements of displacement or strain. The constrained modulus of a specimen is required to facilitate the transformation. The point where the slope changes sign on the tensile force distribution curve is noted to obtain the effective distance (L_x) from the front wall of the box (Figure 7.23). This method ignores the resistance mobilized along the partial length of the specimen near the embedded end.

7.2.3.1.3 Maximum Slope

In this method the maximum slope of the pullout force profile is determined and this gives a maximum shear stress at the soil-specimen interface. This method will always give an upper bound to the interaction factor, Ochiai et al., (1992). The solution does not represent the actual interaction in any aspect, but will give an estimate of the possible maximum shear stress. When the strain or tensile force distribution is linear between the clamped end and the embedded end, the maximum slope method will predict an interaction factor that is identical to that calculated from the effective area method and the total area method.

7.2.3.1.4 Mobilizing Process Method

Ochiai et al., (1992) proposed a method to interpret pullout tests on geogrids only by assuming that the pullout resistance is transferred at the grid junctions in a concentrated manner. The shear stress acting on the specimen between consecutive junctions is obtained by dividing the difference in magnitude of pullout force per unit width by the spacing.

Chapter 7. Analysis of Test Results

Similarly, a method proposed by Juran et al., (1991) recognizes that the nodal displacement comprises two components. The first component is due to tensile strain of the element and the second due to relative movement or shear displacement of the node itself. The difference between consecutive nodal displacements is converted to shear strain for each element. Again using a confined modulus for the test specimen, the tensile force is computed at all nodes. From a consideration of static equilibrium, an equation for the distribution of shear stress along the specimen is then determined, and hence the interaction factor obtained.

7.2.3.2 Generalized Method

From the discussion in the previous section, it is evident that a method to evaluate the shear stress, and hence the interaction factor, at any point on the interface should account for the following:

- mobilized embedded length;
- the variation of pullout resistance along the mobilized embedded length; and
- decreasing embedment length, L_e , of the specimen with increasing displacement, d_c .

Based on experimental observations of load and strain with pullout displacement, a generalized method is proposed below which is applicable to various test specimens, and unifies the effective area and mobilizing process methods. A curve fitting technique is applied to define the tensile force distribution along the specimen length. The generalized method is described in following steps:

STEP 1: Discretizing the test specimen

Chapter 7. Analysis of Test Results

The test specimen is divided into a series of elements such that the strain gauge location is at the centre of each element. The boundary between elements is defined as a node. A schematic illustration of nodes and elements for grids and membranes is shown in Figure 7.24.

STEP 2: Relating measured local strain to element strain

The strain gauges record rib strain on a geogrid and local strain on the geomembrane specimen. The measured local strain is related to the global strain of the element by

$$\epsilon_{gl} = k_e \epsilon_{il} \quad (7.4)$$

where:

ϵ_{gl} is global strain of the element i ,

k_e is a constant, and

ϵ_{il} is the local strain in the element i .

Instron tensile tests (in-isolation) were performed in which the global strain was measured by mounting an LVDT between two consecutive nodes, and the local strain was measured with the strain gauge: the constant for the GT test specimen (Tensar UX-1500) was found to be $k_e=1.82$. Similar in-isolation tests on a stiffer Tensar UX-1600 specimens have been reported by Bathurst (1991) where the value of the constant was determined to be 1.25.

STEP 3: Relating measured local strain to the tensile force

The tensile force, T , in the specimen is related to the measured rib or local strain ϵ_{il} at the first embedded strain gauge by a polynomial expression of the form

$$T = a_1 + b_1 \epsilon_{il} + c_1 \epsilon_{il}^2 + d_1 \epsilon_{il}^3 + e_1 \epsilon_{il}^4 \quad (7.5)$$

Chapter 7. Analysis of Test Results

where:

a_1, b_1, c_1, d_1, e_1 are polynomial coefficients.

STEP 4: Calculation of the actual embedment length, L_{ea}

The position of the strain gauge changes with respect to the front wall of the box as the test progresses. At any instant, the position is calculated from the average displacement of each element using the measured local strains as follows:

The displacement of i th node is given by:

$$d_i = d_{i-1} - S\epsilon_{gi} \quad (7.6)$$

where:

d_i and d_{i-1} are the displacements of the i th node and $(i-1)$ th node respectively,

S is the spacing between i th and $(i-1)$ th node or length of the element, and

ϵ_{gi} is the global strain of i th element given by equation 7.4.

The average displacement of the element i , d_{ai} , bounded by nodes i and $i-1$ is given by equation 7.7

$$d_{ai} = \frac{(d_i + d_{i-1})}{2} \quad (7.7)$$

The distance between the new position of the i th gauge and the front wall, x_i , is given by equation 7.8

$$x_i = x_{oi} - d_{ai} \quad (7.8)$$

where:

x_{oi} is the initial distance of the i th gauge from the front wall of the apparatus.

Chapter 7. Analysis of Test Results

The actual embedded length of the test specimen, L_{ea} , is determined by

$$L_{ea} = L_{ei} - \sum_{i=1}^{i=n} d_{ai} \quad (7.9)$$

where $\sum_{i=1}^{i=n} d_{ai}$ is the summation of the average displacement of all elements.

STEP 5: Fitting a polynomial

Each strain gauge distance (x_i) is normalized with respect to the initial embedment length of the test specimen (L_{ei}). The deduced tensile force at each strain gauge location from step 3 is plotted with respect to the normalized distance of strain gauge locations from the front wall of the apparatus. A polynomial is fitted through the deduced data points. The distribution of tensile force along the specimen with distance from the front wall of the apparatus is expressed as

$$T_i = a_2 + b_2 \eta_i + c_2 \eta_i^2 + d_2 \eta_i^3 \quad (7.10)$$

where:

a_2, b_2, c_2, d_2 are polynomial coefficients and

η_i is the normalized distance of the strain gauge from the front wall of the apparatus.

STEP 6: Evaluation of shear stress at any point on the interface

The shear stress at any point on the interface is given by the slope of the pullout resistance profile. The pullout resistance profile is divided into n number of smaller segments and the shear stress for each segment is given by

$$\tau_i = \frac{T_i - T_{i+1}}{Ch_i} \quad (7.11)$$

Chapter 7. Analysis of Test Results

where:

T_i and T_{i+1} are the tensile forces at the i th and the $(i+1)$ interval respectively,

C is the perimeter of the test specimen, $C=2$ for sheets and grids,

h_i is the discretized interval of the polynomial which is $|x_{i+1}-x_i|$.

The shear stress distribution is obtained by substituting appropriate values in the above equations. Simpson's rule is used to find the area under the shear stress distribution curve, which is divided by the actual embedded length to determine the average shear stress.

STEP 7: Determination of interaction factor

The shear stress in each element from step 6 is normalized with respect to the applied stress (σ_n), to establish the variation of interaction factor along the length of the specimen. An average interaction factor is obtained by normalising the average shear stress with respect to the applied normal stress.

The above steps are incorporated in a data reduction program that is illustrated in Figure 7.25.

7.2.3.3 Application of the Generalized Method

The generalized method for interpreting pullout tests is illustrated by considering tests on all three geogrids and the smooth geomembrane. The method is not applied to the textured membrane because there were no strain measurements taken on these specimens. Application of the method is described with respect to (i) displacement of the embedded end, (ii) pullout resistance, (iii) shear stress and (iv) interaction factors.

Chapter 7. Analysis of Test Results

7.2.3.3.1 Displacement of the Embedded End

Since each specimen was instrumented with only five strain gauges, values of strain in elements without gauges were assigned by interpolation of the laboratory measurements. This was necessary to calculate the nodal displacement of the last node (node 7 for a GT grid and 0.965 m embedment length) and compare it with the measured displacement of the embedded end. Measured and back-calculated displacements of the embedded end of the GT specimen at $\sigma_n=10$ kPa are shown in Figure 7.26. The calculated displacement of the embedded end, based on rib strain, compares very well with the measured displacement using an LVDT attached to a tell-tale on the embedded end.

From these observations, it may be concluded that the generalized approach is capable of backcalculating the displacement of the embedded end when good strain measurements are available at all locations, and may be used in the absence of measured displacements of the embedded end.

7.2.3.3.2 Tensile Force

The variation of tensile force per unit width measured at the clamped end with measured rib strain at the first location inside the pullout box, for the Tensar grid, in DC tests at various normal stresses is shown in Figure 7.27. Included in the plot are data from in-isolation Instron tests (I1, I2 and I3) which exhibit a linear relationship in the given range of strain. Instron tests were performed in accordance with ASTM D4595, except for the imposed strain rate. The data from gauge location SG-1 ($x/L_{ei}=0.073$) in the pullout tests at displacement rates of 0.25, 0.50 and 1.0 mm/min all lie in a narrow band indicating that the relationship is essentially rate independent for the range of testing. The agreement confirms

Chapter 7. Analysis of Test Results

that confinement has little influence on the general force-strain response of the Tensar grid at these relatively low magnitudes of normal stress. In accordance with step 3 of the generalized method, polynomial coefficients were obtained for each test by relating the strain measured at the first embedded gauge to the measured tensile force. These coefficients were used to describe the variation of tensile force along the length of the specimen.

Similarly, the relationship between tensile force per unit width at the clamped end and strain measured at gauge location SG-2 ($x/L_{ei}=0.106$) for the Stratagrid at $\sigma_n=10$ and 17 kPa is shown in Figure 7.28. A stiffer response is observed in the displacement-controlled tests than the load-controlled tests at similar normal stress. The strain softening behaviour at large pullout displacements is clearly evident. The tensile force versus strain relationship for the Miragrid also exhibits a strain softening behaviour at large pullout displacements, see Figure 7.29. Measured local strain at gauge location SG-1 ($x/L_{ei}=0.043$) on the smooth geomembrane is plotted with respect to measured tensile force in tests at $\sigma_n=4, 8$ and 12 kPa, see Figure 7.30. An excellent relationship between force and strain is observed. Again, polynomial coefficients were obtained for each test by relating the measured force at the clamped end with the strain at first gauge location, and the resulting equation used to determine the variation of tensile force along the length of the specimen.

The deduced profile of tensile force/unit width for the Tensar grid, at various d_c for $\sigma_n=10$ kPa, is presented in Figure 7.31. Initially, at $d_c=1$ and 2 mm, the profile is non-linear and the mobilized normalized length of the specimen is 0.65 and 0.70 respectively. As the displacement increases further, the profiles of pullout resistance tend to become linear and simultaneously the slope of the profile increases. The entire length of the specimen is

Chapter 7. Analysis of Test Results

observed to have mobilized a resistance to pullout beyond $d_c = 5$ mm. The pullout resistance profile for the GT20 test (Figure 7.32) exhibits a response which is similar to the GT10 test. Again, at $d_c > 5$ mm resistance is mobilized over the entire length of the specimen. In contrast, the GT30 test specimen exhibits a profile where mobilization of the entire length occurs at $d_c > 15$ mm (Figure 7.33).

7.2.3.3.3 Shear Stress

The shear stress distribution obtained from the profile of tensile force in the GT10 test specimen is shown in Figure 7.34. The shape of the shear stress distribution is found to be very sensitive to the shape of the tensile force profile. Therefore an accurate measurement of strain along the specimen is necessary for determining a reasonable distribution of shear stress. A maximum shear stress is mobilized near the front wall of the apparatus and the magnitude of stress decreases with distance from the front wall. As pullout displacement increases, the slope of the shear stress profile tends toward a uniform value at large pullout displacement. This general trend is clearly illustrated by the shear stress profile for the GT20 test, see Figure 7.35. The shear stress varies at all values of pullout displacement except after 50 mm displacement when the shear stress distribution becomes uniform over the entire embedded length.

Contrary to the shear stress distribution shown in Figure 7.35, a different shape of distribution is obtained for the GT30 test, see Figure 7.36. The profile of tensile force in this test was found to be best defined by a polynomial of degree 3. The shape of the corresponding shear stress distribution is therefore non-linear, again with a maximum shear stress near the front wall, and rapidly decreasing values away from it. For $d_c < 5$ mm, the

Chapter 7. Analysis of Test Results

shear stress is observed to approach a zero or an insignificant value at a normalized distance of 0.5 to 0.7. This clearly demonstrates that the shear stress distribution is non-linear, and that only part of the specimen mobilized resistance to pullout. Although the point of zero shear stress shifts toward the embedded end as the displacement d_c increases, the shape of the distribution appears to remain non-linear.

The distribution of shear stress along the embedded length of the Stratagrid at $\sigma_n=10$ kPa is shown in Figure 7.37. The magnitude of shear stress increases with pullout displacement and attains a peak at $d_c=10$ mm. The post peak response shows that the shear stress decreases with increasing pullout displacement. The influence of an inextensible and an extensible behaviour on the distribution of shear stress is clearly illustrated by shear stress profiles for the Miragrid at $\sigma_n=17$ kPa, see Figure 7.38. At $d_c =2$ and 5 mm, the shear stress is mobilized over a normalized length of 0.55 and 0.85 respectively. Beyond 10 mm of displacement, the shear stress is mobilized over the total embedded length of the specimen although it is non-linear. A maximum shear stress is observed near the front wall at small displacements ($d_c < 10$ mm) but decreases with further displacement. The shear stress profile at $d_c =30$ and 50 mm is uniform and is indicative of an inextensible behaviour in the test specimen.

The shear stress distribution for the smooth geomembrane at $\sigma_n=8$ kPa is shown in Figure 7.39. A non-uniform profile of shear stress is observed at pullout displacements less than 2 mm, which corresponds with zones I and II illustrated in Figure 7.21. The inextensible behaviour beyond a pullout displacement of 3 mm manifests itself as a uniform shear stress profile, and is essentially constant as pullout failure occurs.

Chapter 7. Analysis of Test Results

From this discussion of shear stress, it follows that the profile of mobilized shear stress depends on whether the specimen behaves as an extensible or an inextensible inclusion. Shear stress has been deduced from values of force per unit width calculated from the measured strains. A consistent trend emerges where the variation of strain along the specimen is non-linear at small displacements, tending toward linear at large displacements. Therefore the shear stress distribution is non-linear at small displacements, being a maximum near the front wall and decreasing to a minimum value toward the embedded end. At large displacements a uniform shear stress is mobilized over the length of the specimen. If the specimen behaves as an extensible inclusion, an appropriate data analysis procedure is necessary to establish the shear stress distribution: the proposed generalized method has been shown to account for such extensibility.

7.2.3.3.4 Interaction Factors

The interaction factor in pullout, at any displacement d_c , is obtained by normalising the distribution of shear stress with respect to the applied normal stress, σ_n . Applied normal stress is maintained constant throughout the experiment, and hence the interaction factor varies along the embedded length of the test specimen in a manner similar to that of the shear stress. An average shear stress may be evaluated by considering the area under the shear stress profile. The area under the shear stress profile is determined using Simpson's 1/3rd rule, and divided by the mobilized length to obtain an average shear stress. The average shear stress so computed yields an average interaction factor at a particular pullout displacement and accounts for non-linear pullout resistance.

Chapter 7. Analysis of Test Results

The versatility of the generalized method is illustrated in Figure 7.40 where interaction factors determined using the corrected total area method (Bonczkiewicz, 1986) and proposed generalized methods are compared. The corrected area method gives a lower value of interaction factor than the generalized method. This is attributed to the extensibility of the test specimen.

The variation of interaction factor with pullout displacement for the Tensar grid at $\sigma_n=4$ to 30 kPa, from the generalized method is shown in Figure 7.41. The computed factors at small displacement are very similar in magnitude for all tests at $d_c < 5$ mm. This response gives an important insight to the mobilization of the pullout resistance: irrespective of the applied normal stress on an extensible inclusion, it is possible to obtain a unique interaction factor if an appropriate method is used for analysis of the test data.

Results for the Stratagrid and Miragrid at $\sigma_n=10$ and 17 kPa are shown in Figure 7.42. The general trend is similar to the Tensar grid where the values obtained by the total corrected area method are of lower magnitude. Although there is some scatter in the values obtained from the generalized method, again the interaction factors obtained are higher than the total corrected area method.

The generalized method is applied to the smooth geomembrane tests at $\sigma_n=8$ and 12 kPa, and the variation of interaction factors is shown in Figure 7.43. For the MS08 test, the interaction factor by both methods is similar because of a behaviour in pullout that was essentially inextensible, see Figure 7.21. However at 12 kPa the test specimen has a well-defined displacement response which exhibits some extensibility, and an interaction factor

Chapter 7. Analysis of Test Results

from the generalized method is in good agreement with that at $\sigma_n=8$ kPa. Again the interaction factor given by the generalized method is seen to be independent of applied normal stress.

7.2.3.3.4.1 Peak and Limiting Interaction Factors

The relationship between average shear stress and normal stress at maximum and limiting pullout resistance helps to establish an interaction factor for design purposes. Results for the geogrids are reported together with data from tests on the rough aluminum sheet. Since the rough surface of the aluminum is obtained by glueing sand to the surface of the sheet, the interface represents a sand-sand interface in the pullout test: a best fit line through the data points defines a peak ($\phi_{pps}=40.5^\circ$) and a large displacement angle of friction ($\phi_{lps}=34.5^\circ$) for the sand in a condition of plane strain, see Figure 7.44. Other tests on the sand in a small direct shear box at normal stresses between 4 and 10 kPa, see section 4.2.1, gave a deduced plane strain angle of friction at large shear displacements in the range 35° to 32° . This compares very well with the pullout test data. Further, the angle of friction in direct shear (ϕ_{ds}) and the constant volume angle of friction (ϕ_{cv}) are related to a plane strain friction angle (ϕ_{ps}) by the expression (Rowe, 1969):

$$\tan \phi_{ds} = \cos \phi_{cv} \tan \phi_{ps} \quad (7.12)$$

The above expression is valid for the measured values of $\phi_{ds}=31^\circ$, $\phi_{cv}=29^\circ$, and $\phi_{ps}=34.5^\circ$.

The maximum and limiting value of shear stress for the Tensar grid (GT) are identical. The angle of interface friction between the Tensar grid and sand is defined by a line which lies between $0.8 \tan \phi_{lps}$ to $0.9 \tan \phi_{lps}$. In contrast to this response, the Miragrid (GM) and the

Chapter 7. Analysis of Test Results

Stratagrid (GS) exhibit a noticeable peak value of shear stress at all normal stress levels. The maximum value of interface friction angle for these two grids is similar to the limiting angle of friction of the rough aluminum sheet, being in the range $1.0\tan \phi_{lps}$ to $0.9\tan \phi_{lps}$. It would appear that the Miragrid and Stratagrid are slightly more efficient than the Tensar grid at very low normal stresses.

To further study the influence of grid orientation, results from tests performed on the Miragrid in the cross-machine direction are considered, see Figure 7.45. A slightly higher interface friction is obtained at lower stresses for the cross-machine direction, however, the amount of displacement required to mobilize it is about 3 to 4 times that required in the machine direction (see Figure 6.15). At higher stresses a limiting interface friction of similar magnitude is observed. This behaviour is attributed to the similar S/B ratio in both the machine and cross-machine directions of the grid.

The peak and the limiting interface shear strength of the smooth and textured geomembrane are presented and compared with that of the rough aluminum sheet in Figure 7.46. Both the peak and limiting shear strength for the textured geomembrane are identical at all stress levels and correspond to a value between the peak and limiting shear strength obtained from rough aluminum sheet. It is believed the textured surface of the geomembrane transfers the shear surface into the soil mass above and below the specimen, thus resulting in shear between sand particles rather than at the specimen surface. The angle of interface friction for the textured geomembrane and sand is between the peak and limit values for the sand. Mobilization of a constant, maximum shearing resistance to the end of the test is

Chapter 7. Analysis of Test Results

attributed to dilation of sand at the interface as a result of the uneven surface characteristics of the geomembrane and progressive strain of the specimen.

In contrast to the textured geomembrane, the smooth geomembrane exhibits both a peak and limiting interface strength. A peak interface friction angle of 12° and a value at large displacement of 8° are obtained. The low interface friction angle realized in the pullout is due to the rounded to subrounded shape of the soil particles and the very low normal stresses.

7.2.4 Comparison of Interaction Factors With and Without Bearing Elements

Some tests were performed on the Tensar grid and Miragrid specimens with bearing elements removed to assess the contribution of bearing to the pullout resistance. In Figure 7.47 the interaction factors for the grids with and without transverse bearing elements are compared at different normal stresses. The limit interface strength for specimens without these bearing elements is lower, and is found to vary between 65% and 75% of the strength of the specimens with bearing elements.

The friction angle for the sand-smooth HDPE geomembrane interface from pullout testing is found to be 12° at peak and 8° at large displacement. Consider the Tensar grid: it exhibits a similar smooth HDPE surface and has a solid area of 57.3%. The friction component should account for the measured resistance of the specimen without transverse bearing elements, but this is not the case. The discrepancy is attributed to some component of bearing present due to the ribbed profile of the nodes of the Tensar grid, even with the transverse bearing elements removed.

Chapter 7. Analysis of Test Results

7.2.5 Comparison of Theoretical and Experimental Interaction Factors

Theoretical interaction factors are calculated based on the geometry of the specimen and the soil properties. Two methods are available for computing theoretical interaction factors (USFHWA, 1990, and Jewell et al., 1984). Both give an identical expression when the degree of interference, DI (equation 2.11) is zero. Relating equations 2.7 and 2.14, gives

$$F^* \alpha = f_b \tan \phi = \alpha_s \tan \delta + \frac{\alpha_b}{2} \frac{B}{S} \frac{\sigma_b}{\sigma_n} \quad (7.13)$$

The geometric characteristics of each geosynthetic test specimen and the corresponding interface friction angle for the materials are tabulated in Table 7.1. Values of $\tan \delta$ for the material are reported from the direct shear box tests. The interface friction angle of the Stratagrid and Miragrid is assumed to be that of the textured sheet in direct shear because of their surface texture.

The USFHWA design manual recommends that in the absence of test data a value of approximately 20 be assumed for the non-dimensional stress ratio σ_b/σ_n based on available pullout test results at that time. Deduced values of $F^* \alpha$ are tabulated in Table 7.2 along with the components due to friction and bearing.

The friction component of the interaction is maximum for the Stratagrid (73%) and minimum for the Tensar grid (36%). Farrag et al. (1993) report results on Conwed G-9027 geogrid without bearing elements and conclude that the predominant resistance is due to friction (up to 75% of total resistance). In contrast, the surface of the Tensar grid leads to a relatively small component derived from interface friction. The Miragrid exhibits a nearly

Chapter 7. Analysis of Test Results

equal component of friction and bearing: the higher component of bearing in the Miragrid compared to the Stratagrid is attributed to the smaller S/B ratio.

Table 7.1: Geometric and interface friction characteristics of the test specimens

Material	α_s	α_b	B (mm)	S (mm)	S/B	$\tan \delta$
Tensar UX-1500	0.573	0.520	4.32	162	37.5	0.22
Stratagrid 700	0.534	0.615	1.45	75.7	52.2	0.60
Miragrid 15T	0.453	0.780	1.10	32	29.1	0.60
Novex Smooth HDPE sheet	1	-	-	-	-	0.22
Gundle Textured sheet	1	-	-	-	-	0.60

Table 7.2: Theoretical interaction factor for the grid specimens, USFHWA guidance

Material	Friction ($\alpha_s \tan \delta$)	Bearing ($20 B \alpha_b / 2S$)	$F^* \alpha = f_b \tan \phi$
Tensar UX-1500	0.127	0.226	0.353
Stratagrid 700	0.320	0.118	0.438
Miragrid 15T	0.272	0.268	0.540

Chapter 7. Analysis of Test Results

In the method of Jewell et al. (1984) it is suggested that stress ratio σ_v/σ_n be measured directly in pullout tests. Experimentally the interaction factor is found to vary along the length of the embedded specimen with the displacement of the clamped end. The extent of interaction is dependent on relative shear displacement between the specimen and the soil. It has been shown that the normalized relationship of shear stress is unique for a specimen and independent of applied normal stress, see Figure 7.44. At large displacements the mobilization of shear stress corresponds to a limiting shear strength of the interface.

Using the experimentally observed interaction factor at large displacement, a value for the stress ratio is back-calculated for three geogrids and is tabulated in Table 7.3. For a soil friction angle of 31° in direct shear, the upper bound solution to the bearing capacity of a deep buried anchor gives a value of 20 (equation 2.6) and the lower bound a value of 6 (equation 2.5), see Figure 2.8. The tabulated values for the geogrids are slightly higher than the theoretical upper bound but are in reasonably good agreement.

Results from tests on the Tensar grid specimen without bearing elements suggests a higher friction component: this discrepancy is attributed to the geometric characteristics which impart additional bearing due to the profile of the nodes in the vertical direction. Considering an additional bearing component from a 3 mm thick node (node thickness - rib thickness=3mm), the stress ratio is computed to be 40. This is in the general expected range.

7.2.6 Comparison of Geogrid Interaction Factors with Other Laboratory and Field Data

Interaction factors from the present study are compared with laboratory pullout tests reported by Palmeira (1987) and Farrag et al., (1993), and with the performance of a field structure

Chapter 7. Analysis of Test Results

described by Fannin and Hermann, (1990) . Similar geogrids were used in the other two laboratory studies, a Netlon SR2 and Tensar SR2 respectively. Tensar UX-1200 is a direct equivalent of Tensar SR2. The reinforcement used in the field structure was Tensar SR55. The geogrid characteristics are given in Table 7.4: the notations used in Table 7.4 are illustrated in Figure 7.48. Soil properties used in the laboratory tests and the field structure are tabulated in Table 7.5.

Table 7.3: Stress ratio σ_v/σ_n from pullout tests on the geogrids

Material	Friction ($\alpha_s \tan \delta$)	Limiting interaction factor (see Figure 7.44)	$F_v=(\sigma_v/\sigma_n)$
Tensar UX-1500	0.127	0.588	40
Stratagrid 700	0.320	0.599	47
Miragrid 15T	0.272	0.644	27

The pullout test results of Palmeira (1987) on the Netlon SR2 geogrid performed at $\sigma_n=25$ kPa are converted to interaction factors using expression 7.13 and the reported constant volume friction angle of 35^0 for the Leighton Buzzard sand. Interaction factors for the Tensar grid from Farrag et al. (1993) and Palmeira (1987) are compared with the results from the present study, see Figure 7.49. The corrected total area method is used to calculate the interaction factors because appropriate strain measurements are unavailable. There is an excellent agreement between the curves given the variation in apparatus and test procedures, see Table 2.1. A detailed initial response is shown in Figure 7.50.

Chapter 7. Analysis of Test Results

Table 7.4: Typical properties of the geogrid specimens

Geogrid	Wide Width Strip Tensile, ASTM D4595-86, Ultimate strength (kN/m)	Dimension (mm)			
		l ₁	l ₂	l ₃	l ₄
Tensar SR55	NA	156	16	6.7	2.6
Netlon SR2/Tensar SR2	78	111	16.5	5.5	4.4
Tensar UX-1500	86	165	16	6.7	4.3

* dimensions are shown in Figure 7.48.

NA - Not available

Table 7.5: Properties of soil used in the laboratory studies and field structure

Researcher	Soil	D ₅₀ (mm)	C _u	Unit weight (kN/m ³)	Particle range (mm)	Particle shape	D _r (%)
Palmeira (1987)	Leighton Buzzard Sand 14/25	0.80	1.3	17	0.6 to 1.18	angular	87
Farrag et al., (1993)	Uniform blasting sand	0.26	---	16.5	0.1 to 1.18	----	----
Fannin and Hermann, (1990)	Uniform- medium coarse sand	0.28	2.5	17	0.02 to 10	sub- rounded	----
Present study	Uniform Silica sand	0.82	1.5	17.8	0.6 to 1.18	rounded	>85

The response of the Stratagrid is compared with the results for Conwed G-9027 reported by Farrag et al. (1993), see Figure 7.51, which is a similar grid. Although the initial response is softer for the Conwed geogrid, this is to be expected at higher normal stress, and

Chapter 7. Analysis of Test Results

the interaction factors at large displacement are observed to be comparable. The deduced strain profile from nodal displacements, see Figure 7.52, shows a similarity in shape with the observed strain profiles in the present study shown in Figure 7.18. The larger magnitude of strain is attributed to the greater normal stress (48.2 kPa) and the different location of strain measurement. At pullout displacements between 4 and 10 mm, shear stress is mobilized over the part of the embedded length of the specimen. On continuation of the test, the strain profile is observed to become linear at a pullout displacement of 26 mm.

Field observations of a sloped wall have been used to establish interaction factors mobilized by the grid reinforcement under “in-service” conditions (Fannin et al., 1994). These values are compared with the laboratory pullout test results. The characteristics of the field structure are illustrated in Figure 7.53. The 4.8 m high, slope (2V:1H) reinforced soil wall comprises two sections, each 10 m long and incorporating a different arrangement of geogrid reinforcement. The reinforcement attaches to lightweight modular facing units that are 0.6 m high. Primary reinforcement was a Tensar SR55, and intermediate reinforcement was a biaxially-oriented polymer grid. Instrumentation was used to measure force and strain in the reinforcement, soil strain, and temperature, and earth pressure. The structure has been subject to self-weight, a cycle of surcharge loading using water tanks, and finally a permanent surcharge loading of 49.2 kPa since October of 1987. Performance data, Fannin and Hermann (1990), show the measured forces in the reinforcement are in good agreement with predicted values of the coefficient of active earth pressure.

Global strain (ϵ_g) is deduced from the separation of pairs of Bison inductance coils that were fixed to the geogrid at the nodal junctions, see Figure 7.48, by a nylon screw that

Chapter 7. Analysis of Test Results

fitted through a central hole in the coil and a similar one drilled in the grid. Measurements were taken at three locations (A, B and C) on instrumented strips (Figure 7.54). A profile of mobilized strain in layer No. 7 of the structure located 1.2 m below the crest, see Figure 7.53, is illustrated in Figure 7.55 for each of the two sections. The mean value is that for all measurements taken during the 28 days of self-weight loading, and that for all measurements taken during the first 720 days of permanent surcharge loading. Largest strains are observed at the front face of the slope, decreasing non-linearly to zero at the embedded end. A nearly constant value of strain is observed at any point during self-weight loading.

Force in the reinforcement was measured using vibrating wire load cells connected directly to the geogrid at a distance 0.86 m from the face of the structure. The mean value of force in layer No. 7 during self-weight loading was 1.6 kN/m in section 'J' and 1.8 kN/m in section 'N'; during the designated period of permanent surcharge loading the values were 2.4 kN/m and 3.0 kN/m respectively. The vertical effective stress at this location is estimated to be 20 kPa during self-weight loading, and 70 kPa after permanent surcharge loading.

The mean value of interaction factor is determined knowing the embedded length, l , behind the point where load was measured at A, see Figure 7.54. Values of 0.02 and 0.03 represent section 'J' and 'N' respectively during self-weight loading, and 0.01 and 0.02 during the designated period of permanent surcharge loading. These values of interaction factors at working conditions correspond to a very small displacement in the pullout test (less than 1 mm), see Figure 7.50. The mean global strain mobilized under self-weight loading (20 kPa), was 0.52% in section 'N', and 0.33% in section 'J' (Fannin and Hermann, 1990): the

Chapter 7. Analysis of Test Results

corresponding rib strain measured in the pullout test was 0.2 (global strain 0.36%), see Figure 6.22.

In summary, displacement-controlled pullout tests on extensible inclusions should be analysed using appropriate interpretation methods to obtain interaction factors. A comparison of the results from the present study with those studies that used other pullout equipment shows good agreement. An excellent agreement is demonstrated between laboratory and field behaviour at small strain.

7.3 Load-Controlled Pullout Tests

A series of pullout tests were performed to study the effect of cyclic loading on mobilized interaction factors. The nature of the cyclic loading and control system are described in Chapter 5. The test results are discussed in the following sections with reference to displacement of the clamped (d_c) and embedded (d_e) ends, and strain measurements on specimens with gauges mounted on them. A unified method of interpretation is developed for the imposed cyclic loading.

Cyclic pullout tests were performed by loading the specimens monotonically at a constant rate of loading of 0.25 kN/m/min, to an initial targeted value (p_o) between 60 and 80% of the corresponding DC pullout resistance, and a series of load cycles then imposed (see Figure 5.2). The demand signal for cyclic loading was a sinusoidal wave form of constant frequency $f = 0.1$ or 0.01 Hz: each series comprised ten cycles, and the single amplitude (Δp_m) was increased between each series. A load ratio (LR) is defined in the load-controlled tests with respect to the maximum pullout resistance in a displacement-controlled test (p_m), by

$$LR = \frac{p_o + \Delta p_m}{p_m} \quad (7.14)$$

The load ratio increases with each series of load cycles. Each test was continued to a displacement greater than 60 mm or to failure by pullout.

7.3.1 Incremental Displacement Response

The cyclic pullout response is described by considering the incremental displacements of the clamped (Δd_c) and embedded (Δd_e) ends of the specimen. Incremental displacements are calculated relative to the displacement at the beginning of each series of cyclic loading. Incremental displacement of the clamped end is plotted below with respect to the number of cycles in a series, and the corresponding incremental displacement of the embedded end.

The response of the GT10 specimen at $f=0.01$ Hz, is found to be dependent on the value of load ratio, see Figure 7.56. At $LR=0.93$ and 0.97 , a small Δd_c is observed during the first few cycles but during subsequent cycles it remains constant and no further displacement takes place. It represents a stable behaviour. An increase in the LR leads to larger incremental displacements: at $LR=1.04$ the magnitude of Δd_c increases significantly during the first 6 cycles. However very little displacement accumulates during next 4 cycles, and the resulting shape of the curve is concave-upwards. On increasing the LR further to 1.16 the incremental displacement in less than 1 cycle was of such a magnitude that the specimen experienced an instantaneous pullout, see also Figure 6.31. It represents an unstable behaviour that was approached as the LR was increased. The relationship between incremental displacements shows that at lower load ratios the incremental displacements are small, but when $LR > 1$, the incremental displacements of both ends increase.

Chapter 7. Analysis of Test Results

The response observed in the GT10 test at $f=0.1$ Hz is very similar to that observed at $f=0.01$ Hz, see Figure 7.57. Again, when the $LR=1.19$, Δd_c increases with number of cycles and the shape of the relationship changes from a concave-upwards to a straight line. This corresponds to an unstable behaviour and is indicative of a pullout failure due to an accumulation of excessive incremental displacement.

The cyclic pullout response of the Stratagrid at $\sigma_n=10$ kPa (GS10) shows a very different behaviour, see Figure 7.58. Magnitudes of incremental displacement are small during most of the test. Although the response shows a stable behaviour during first few cycles of the final loading series at $LR=1.01$, there is a very abrupt change from a stable to unstable behaviour in the 4th cycle. At this stage of the test a rapid pullout of the test specimen was observed. An inextensible pullout behaviour is associated with this response, as indicated by the incremental displacements Δd_c and Δd_e .

A response similar to that of the GS10 test is observed for the Miragrid at $\sigma_n=17$ kPa, where again an abrupt change in behaviour occurs from a stable to an unstable response at $LR=0.90$, see Figure 7.59. The associated Δd_c versus Δd_e relationship shows zero displacement at the embedded end for first two cycles followed by an equal magnitude of displacements in the third cycle.

The response of the smooth and textured geomembranes at $\sigma_n=8$ kPa are shown in Figures 7.60 and 7.61. The response of the smooth geomembrane (MS08) at $LR < 1$ illustrates a stable behaviour but a rapid pullout failure occurs when the ratio exceeds 1. Although the textured membrane (MT08) exhibits a stable behaviour during first cycle when

Chapter 7. Analysis of Test Results

LR >1 the rate of accumulation of displacement increases rapidly thereafter toward a pullout failure.

All of the remaining cyclic pullout test data are plotted in a similar manner and reported in Appendix-B. From these results a general behaviour in cyclic pullout is observed. There appears to be a threshold load ratio beyond which the response moves from a stable to unstable behaviour with respect to pullout. The threshold ratio is around 1 for all types of specimens except for the GT specimens where a ratio greater than 1.1 was observed (see Figures 7.56 and 7.57).

Based on the results, a conceptual model is proposed in Figure 7.62 for the modes of behaviour observed in cyclic pullout testing. Curves 'oa' and 'ob' represent a stable behaviour (Figure 7.56), curve 'oc' a transition, and curves 'od', 'oe' and 'of' an unstable behaviour (Figure 7.61). Curve 'od' represents a catastrophic failure because the behaviour changes abruptly from being stable to unstable (Figure 7.58). The relationship between Δd_c and Δd_e is not unique for curves similar to 'oa', and the admissible range is bounded by oa_1 and oa_2 . However, the relationship is unique and lies along of_1 if pullout failure occurs without further tensile strain of the test specimen.

7.3.2 Strain Response

In this section the response to cyclic loading is described with reference to strain measurements. Based on the strain measurements in the displacement-controlled tests, it has been shown that tensile force varies along the embedded length of the specimen. Therefore,

Chapter 7. Analysis of Test Results

the mobilization of strain during cyclic loading is also valuable to gaining an understanding of the distribution of incremental loads along the specimen length.

Mobilization of rib strain, for the GT10 test at $f=0.01$ Hz, with number of cycles in each loading series is shown in Figure 7.63. As before, the strain gauge location is given in terms of the normalized distance (x/L_{ei}). As the load ratio increases, a marked increase in strain is recorded at all locations in the first cycle of loading. Mobilized strains at locations SG-1 to SG-3 indicate that the strain magnitude increases with the number of cycles. The rate of increase in strain decreases with the distance from the front wall, being greatest at location SG-1. At locations SG-4 and SG-5 the mobilized strain is observed to be essentially constant with number of cycles at a given load ratio.

The effect of cyclic loading on the strain profile for the same test is further illustrated in Figure 7.64. The strain profile at LR=0.89 represents the beginning of the cyclic loading. The increase of load ratio to 0.93 only increases strain at locations SG-2 and SG-3, and no change occurs at other locations. Therefore only a part of the specimen near the front wall mobilizes resistance to the relatively small applied cyclic load. As the LR was increased to 0.97 a nearly constant incremental strain was measured at all gauge locations. This type of behaviour was also observed when the LR was increased to 1.04.

The mobilization of strain (Figure 7.65) and the strain profile (Figure 7.66) with increasing load ratio and number of cycles for the GT17 test specimen are also observed to be of similar shape to the GT10 test specimen, though the magnitudes are greater. However a strain increase is measured for increased load ratios at all locations, irrespective of the distance from the front wall.

Chapter 7. Analysis of Test Results

The mobilization of strain with number of cycles and load ratio for the Miragrid at $\sigma_n = 10$ kPa is illustrated in Figure 7.67. The slope of the relationship indicates that the strain accumulates evenly between loading series and consecutive cycles. At $LR > 0.8$, strain accumulation has essentially ceased and the specimen tends toward a unique strain profile, see Figure 7.68. This behaviour is very similar to that in the DC tests. At $\sigma_n = 17$ kPa a strain increase is measured at locations near the front wall for smaller load ratios, and the embedded end experiences a smaller strain increase, see Figure 7.69. In contrast, the strain profile relationship tends to a highly non-linear shape, see Figure 7.70.

The same general response is also observed in the Stratagrid tests under cyclic loading, see Figures 7.71 and 7.73. In these tests the LR was increased in smaller intervals, and is seen to better define the mobilization of strain in a test specimen. The strain profiles at $\sigma_n = 10$ kPa, see Figure 7.72, indicate a fairly uniform increase of strain at all locations to a limiting envelope. In contrast, a markedly different response is observed at $\sigma_n = 17$ kPa where a similar uniform strain increase occurs up to $LR = 0.89$, and on further increase of the LR the response shows a significant strain increase at locations closer to the front wall, see Figure 7.74.

7.3.3 Interaction Factors for Cyclic Loading

A cyclic interaction factor may be determined by the generalized method for a test specimen with strain measurements. A comparison of the variation of interaction factor with displacement determined by the generalized method and the corrected total area method, for the GT10 test specimen illustrates an important aspect of the cyclic pullout response, see Figure 7.75. The corrected total area method uses the pullout load applied to the specimen to determine an interaction factor. Consequently, when the magnitude of the load decreases

Chapter 7. Analysis of Test Results

during unloading, a lower interaction factor is predicted. In the proposed generalized approach, the variation of pullout resistance along the embedded length of the specimen is determined from strain measurements. From the strain profile it was observed that even when the magnitude of cyclic loading was less than the mean load level, there was on occasion no strain reduction at some gauge locations inside the pullout apparatus. Therefore, the interaction factor determined by the generalized approach is larger than that computed by the corrected total area method. The unloading part of the cyclic loading sequence affects only a part of the specimen near the front wall, while most of the embedded portion remains loaded. A consequence of this phenomenon is that the test specimen experiences a 'locked in' stress due to cyclic loading.

7.4 Comparison of Interaction Factors from DC and LC Tests

The variation of interaction factor with pullout displacement in DC and LC tests is compared. For purposes of comparative analysis, the corrected total area method is used to obtain the interaction factors. While the generalized method is recognized as a more rigorous approach, the corrected total area method is selected for the comparisons in this section because not all DC and LC tests had a complete and adequate record of strain measurements. It should be noted that at low stresses and large displacement, when behaviour is predominantly inextensible, both methods give comparable results. Although a major limitation of the corrected total area method is that the interaction factor corresponding to the unloading phase of the cyclic test is not correct, since an envelope to the cyclic response is of prime interest, the use of the corrected area method for comparison purposes is not a

Chapter 7. Analysis of Test Results

limitation. Note, also that the ratio of interaction factor in the LC test to that in the DC test is independent of the method applied when a similar method is used.

Cyclic interaction factors for the Tensar grid are compared with those from monotonic displacement-controlled tests at $\sigma_n=4$ to 17 kPa (Figures 7.76 to 7.79). Also shown is the value recommended by USFHWA design manual for designing structures to resist dynamic loads, which is 80% of the interaction factor from a displacement-controlled test. For clarity only half of the unload/reload loops are shown. Although an envelope to the cyclic interaction factor is slightly higher than the corresponding DC test for small displacements in the test at $\sigma_n=4$ kPa, the large displacement values are very similar, see Figure 7.76. In contrast, for other tests on the Tensar grid a higher cyclic interaction factor is obtained, see Figures 7.77, 7.78, and 7.79. The envelope to cyclic interaction factors at $f=0.1$ Hz (Figure 7.78) is similar to that observed for $f=0.01$ Hz (Figure 7.77), and is indicative of frequency independent behaviour for the range used in testing.

The comparison of cyclic interaction factors for the Miragrid at $\sigma_n=4$ to 17 kPa is shown in Figures 7.80 to 7.82. Results indicate a response which is dependent on the magnitude of normal stress. At lower stresses, an envelope to the cyclic interaction factor is very similar to the monotonic DC test (Figures 7.80 and 7.81). A very different behaviour is observed at $\sigma_n=17$ kPa, where an envelope to the cyclic interaction factor indicates a lower value. The Stratagrid response at $\sigma_n=4$ and 10 kPa is very similar to the Miragrid response, see Figures 7.83 and 7.84. In contrast, at $\sigma_n=17$ kPa a higher interaction factor is mobilized in cyclic loading, see Figure 7.85.

Chapter 7. Analysis of Test Results

An envelope to the cyclic interaction factors for the smooth geomembrane at $\sigma_n=8$ kPa and 12 kPa coincides with the corresponding monotonic DC tests, see Figures 7.86 and 7.87. In both the tests a rapid pullout occurred during first cycle of the loading series when the interaction factor just exceeded the monotonic DC interaction factor.

An envelope to the cyclic interaction factors is seen to coincide with the corresponding DC interaction factors observed for the textured geomembrane at $\sigma_n=8$ kPa and $f=0.01$ Hz, see Figure 7.88. Although a test performed at a higher frequency ($f=0.1$ Hz) shows the same general response; the interaction factor is greater in magnitude, see Figure 7.89. At $\sigma_n=12$ kPa, the factor mobilized in cyclic loading tends to a value similar to that mobilized in monotonic DC test at large displacements, see Figure 7.90. Again the cyclic pullout interaction factor (τ/σ) is seen to meet or exceed that from the constant rate of displacement test.

In summary, the response of extensible specimens in cyclic pullout tests shows that the incremental loads are resisted by part of the embedded specimen closer to the front wall of the apparatus. As the loading regime approaches the limiting interaction factor from the displacement-controlled test, resistance to pullout is mobilized by the entire embedded length of the specimen. The limiting interaction factor in cyclic loading is found to be dependent on the specimen type but independent of the applied normal stress and the frequency in the range of frequency tested. Most of the results showed an interaction factor in cyclic loading to be equal to or higher than that of the interaction from the corresponding displacement-controlled loading.

Chapter 7. Analysis of Test Results

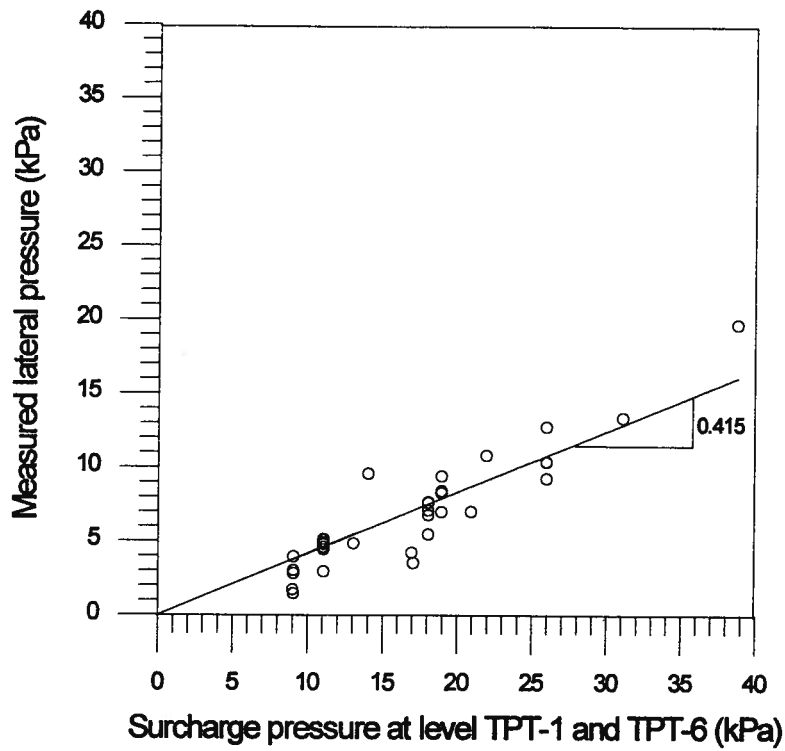


Figure 7.1: Measured lateral stress and applied normal stresses at TPT-1 and TPT-6 locations

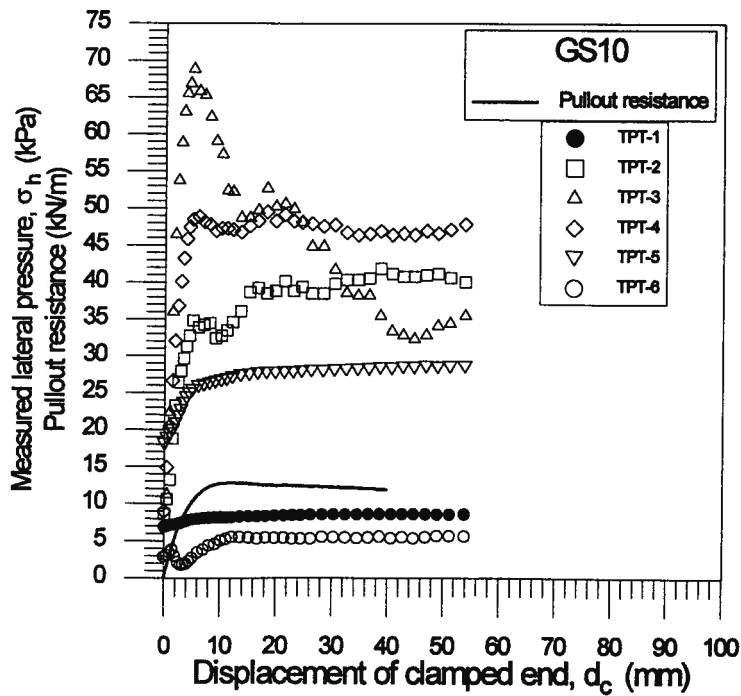


Figure 7.2: Measured lateral stress and pullout resistance for the Stratagrid at $\sigma_n=10$ kPa

Chapter 7. Analysis of Test Results

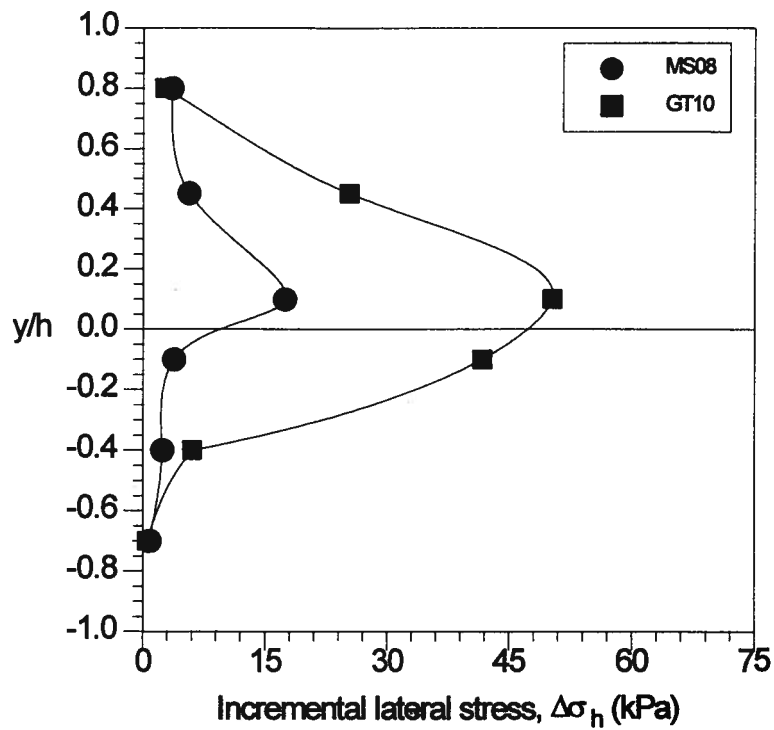


Figure 7.3: Incremental lateral stress on the front wall for the smooth geomembrane and Tensar grid at similar normal stress.

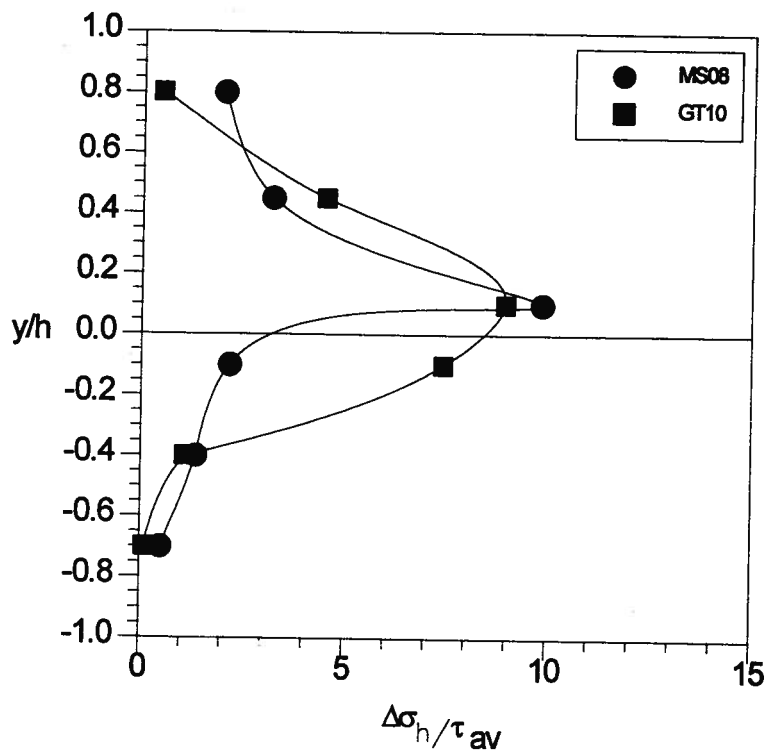


Figure 7.4: Variation of normalized lateral stress ratio with depth ratio for the smooth geomembrane and Tensar grid at similar normal stress

Chapter 7. Analysis of Test Results

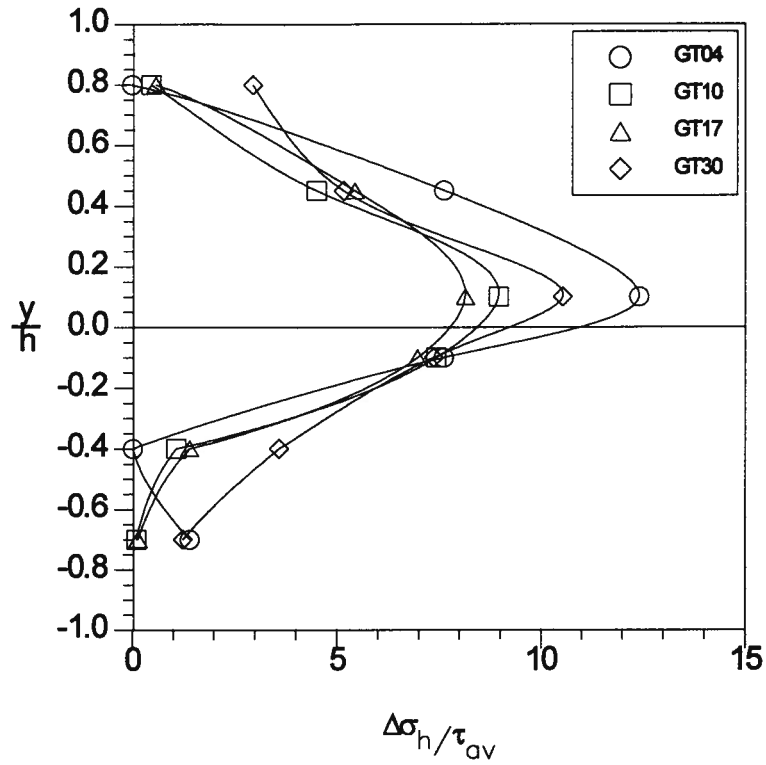


Figure 7.5: Variation of normalized lateral stress ratio with depth ratio for the Tensar grid at $\sigma_v=4$ to 30 kPa

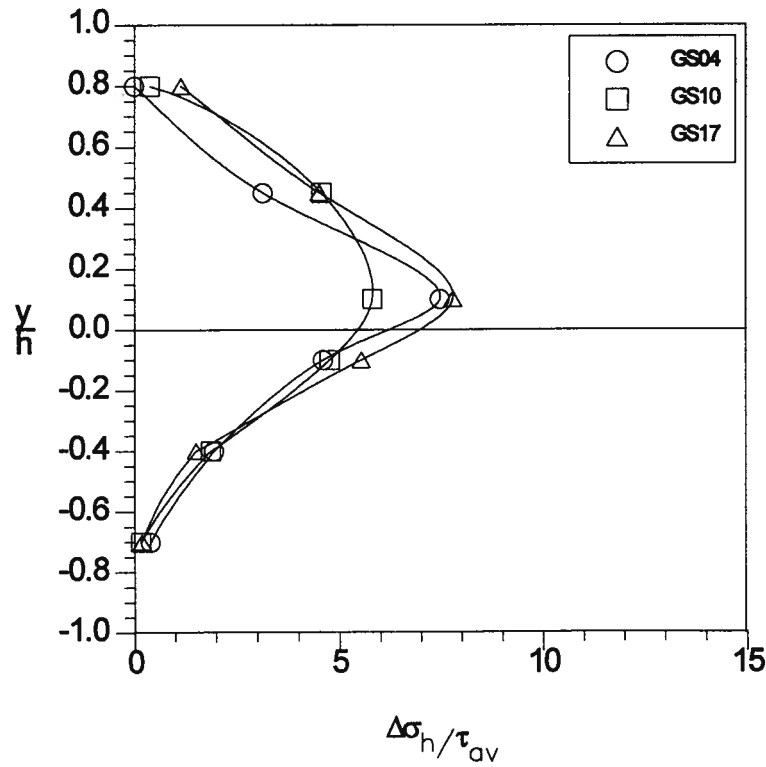


Figure 7.6: Variation of normalized lateral stress ratio with depth ratio for the Stratagrid at $\sigma_v=4$ to 17 kPa

Chapter 7. Analysis of Test Results

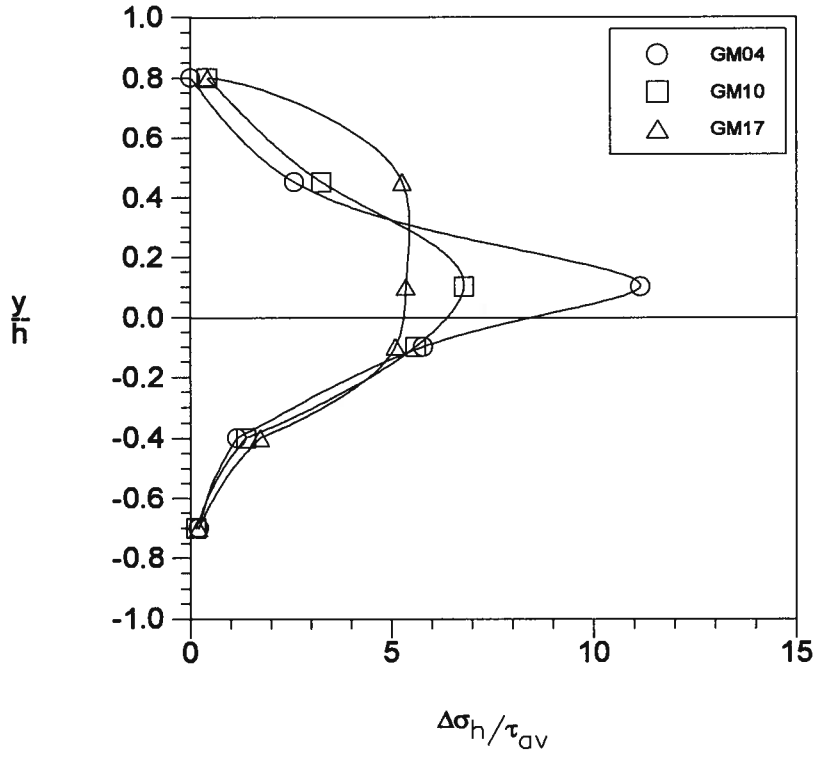


Figure 7.7: Variation of normalized lateral stress ratio with depth ratio for the Miragrid tested in the machine direction at $\sigma_v=4$ to 17 kPa

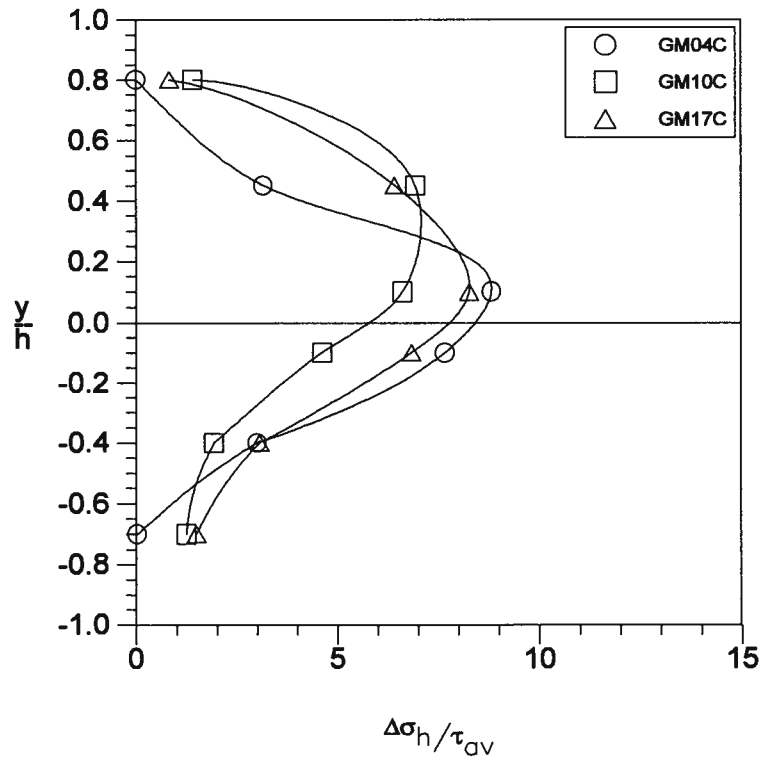


Figure 7.8: Variation of normalized lateral stress ratio with depth ratio for the Miragrid tested in the cross-machine direction at $\sigma_v=4$ to 17 kPa

Chapter 7. Analysis of Test Results

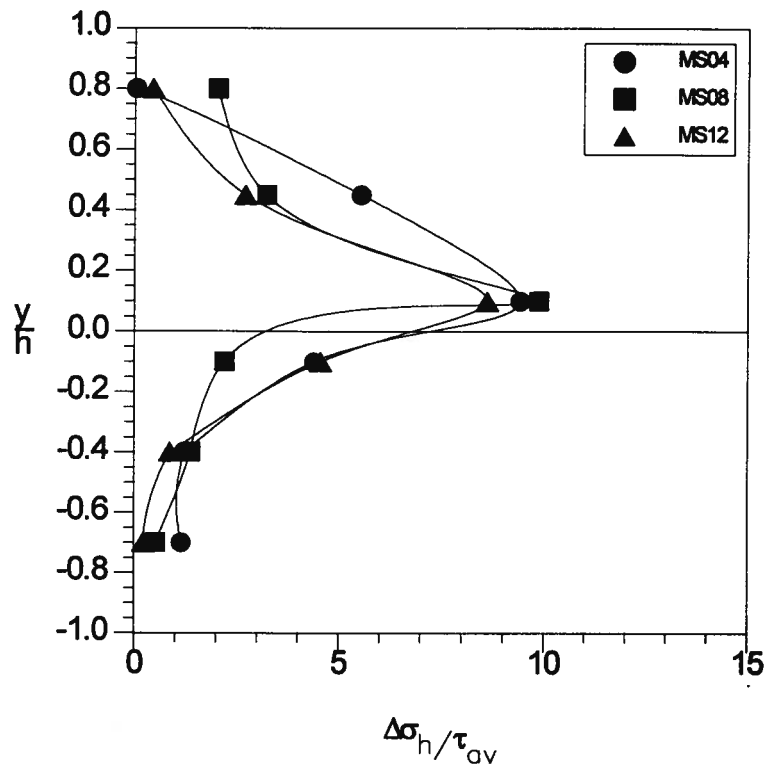


Figure 7.9: Variation of normalized lateral stress ratio with depth ratio for the smooth geomembrane at $\sigma_v=4$ to 12 kPa

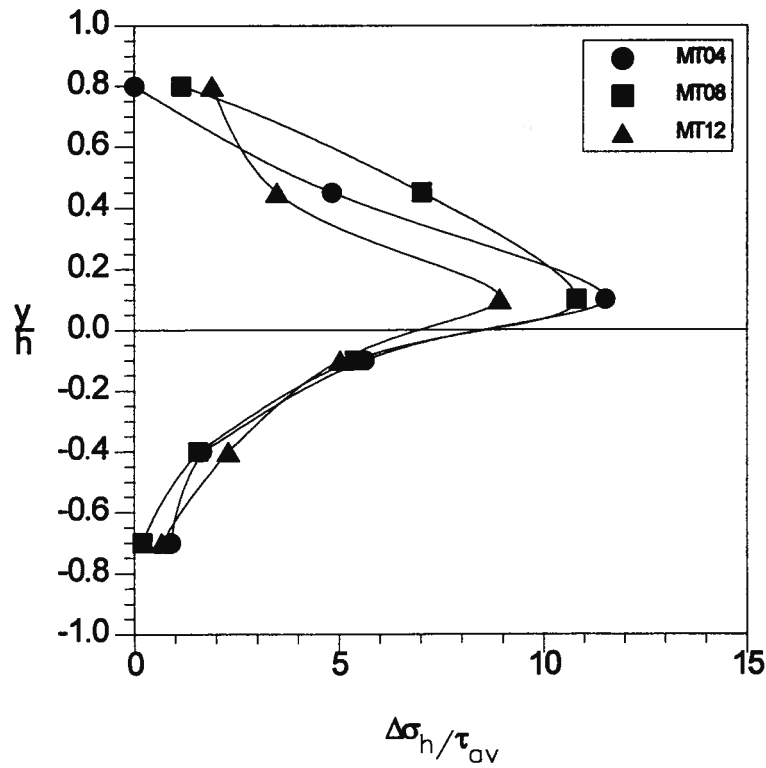


Figure 7.10: Variation of normalized lateral stress ratio with depth ratio for the textured geomembrane at $\sigma_v=4$ to 12 kPa

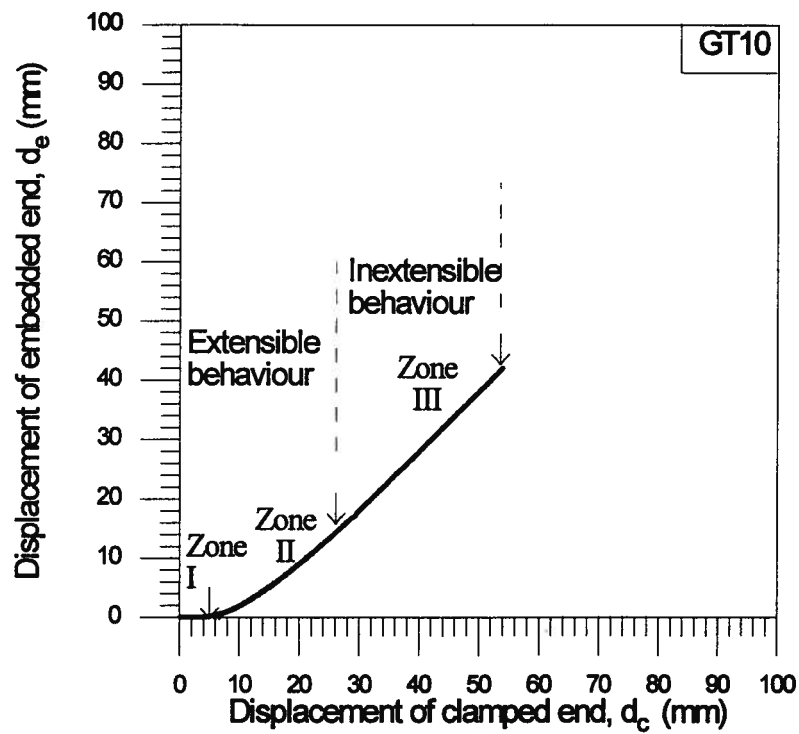


Figure 7.11: Relationship between d_c and d_e for the Tensar grid in the DC test at $\sigma_a=10$ kPa

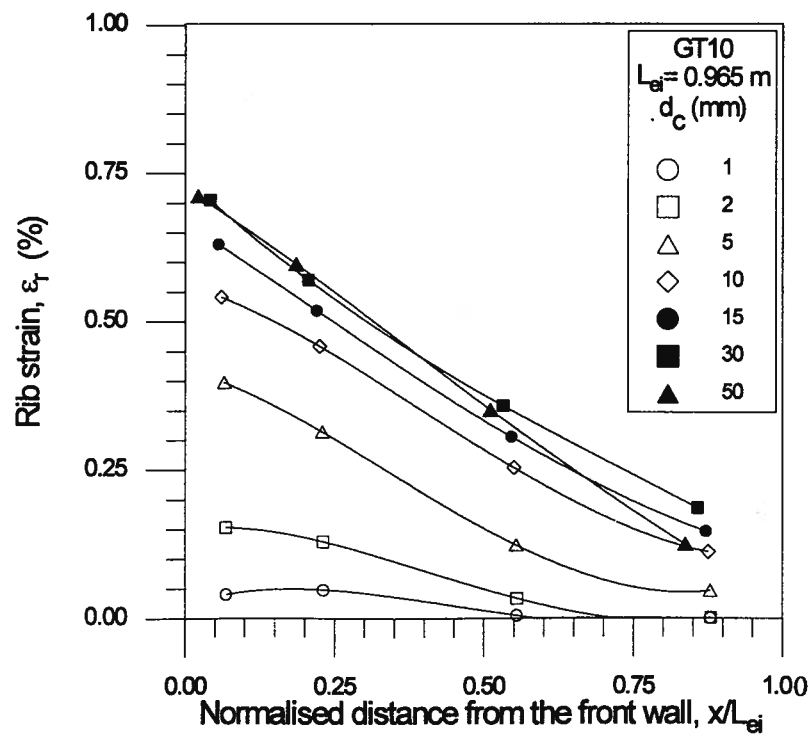


Figure 7.12: Strain profile for the Tensar grid in the DC test at $\sigma_a=10$ kPa

Chapter 7. Analysis of Test Results

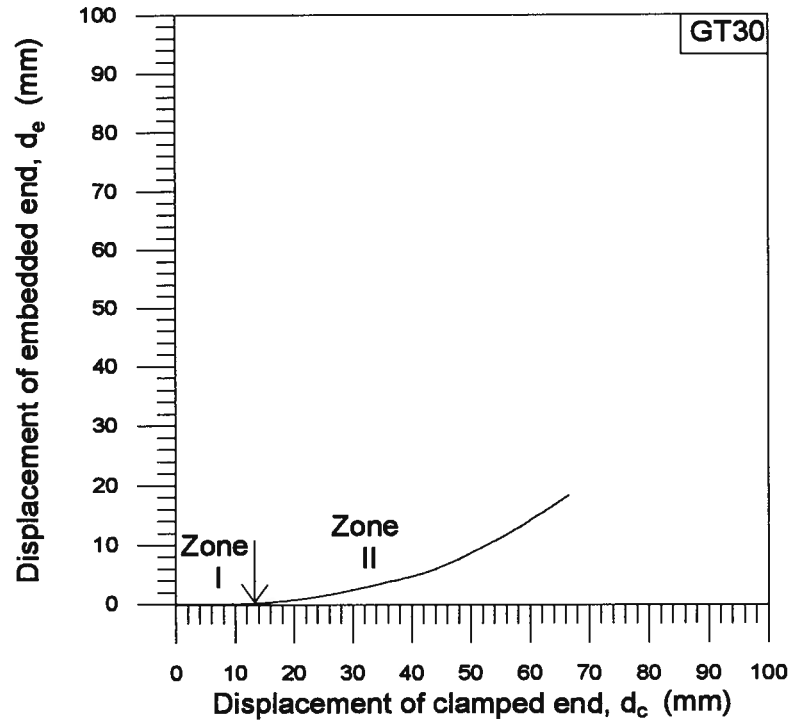


Figure 7.13: Relationship between d_c and d_e for the Tensar grid in the DC test at $\sigma_a=30$ kPa

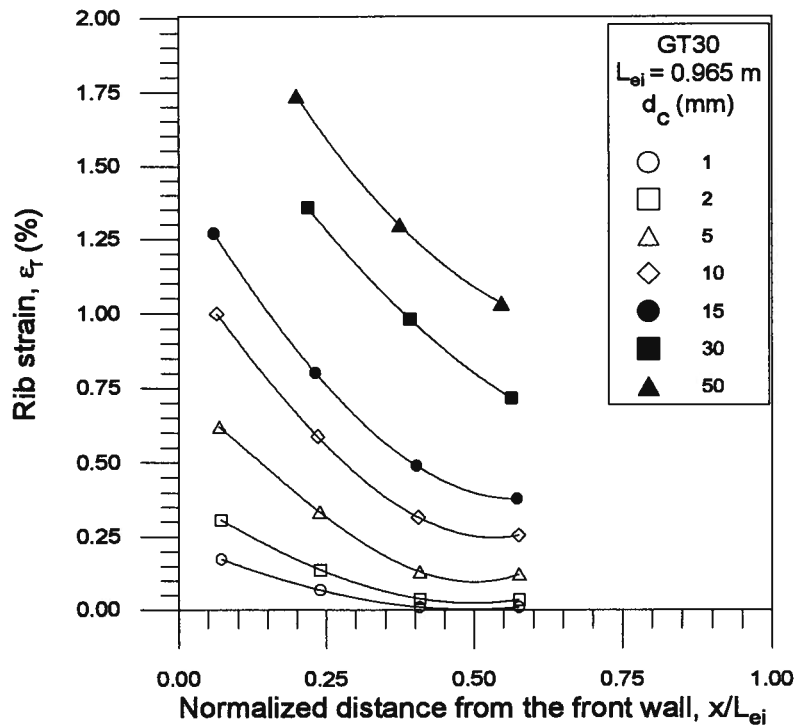


Figure 7.14: Strain profile for the Tensar grid in the DC test at $\sigma_a=30$ kPa

Chapter 7. Analysis of Test Results

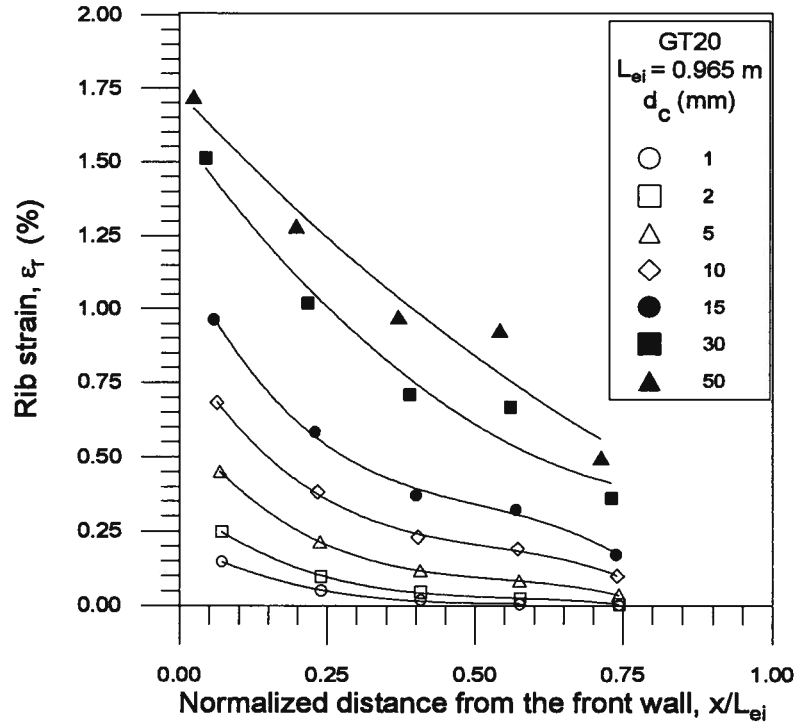


Figure 7.15: Strain profile for the Tensar grid in the DC test at $\sigma_n=20$ kPa and $r_d=0.50$ mm/min

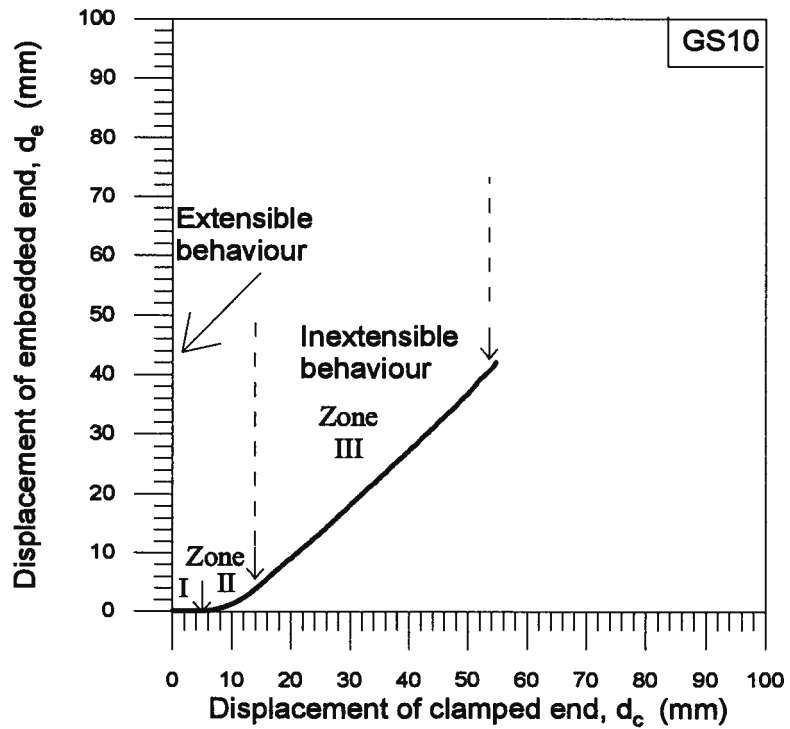


Figure 7.16: Relationship between d_c and d_e for the Stratagrid in the DC test at $\sigma_n=10$ kPa

Chapter 7. Analysis of Test Results

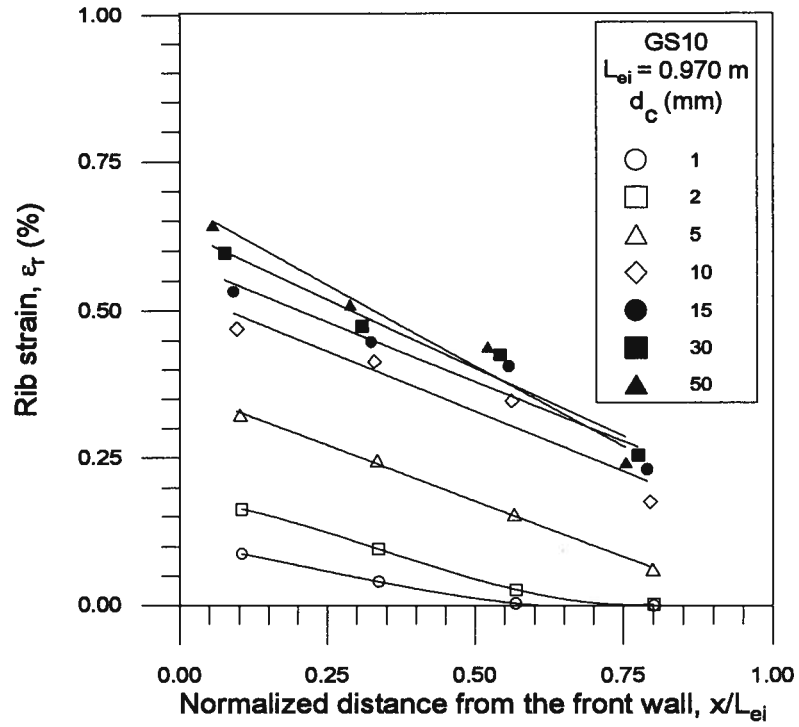


Figure 7.17: Strain profile for the Stratagrid in the DC test at $\sigma_n=10 \text{ kPa}$

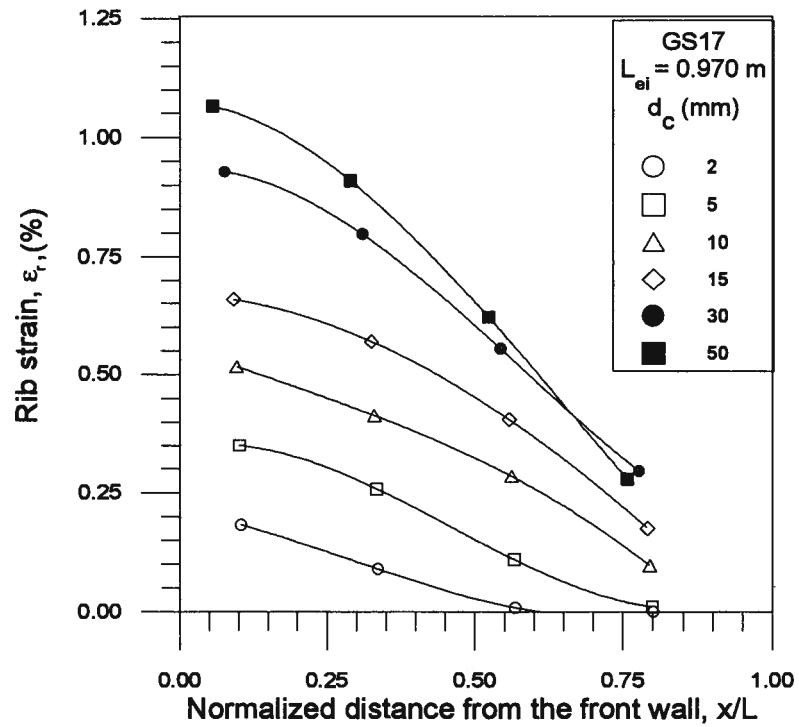


Figure 7.18: Strain profile for the Stratagrid in the DC test at $\sigma_n=17 \text{ kPa}$

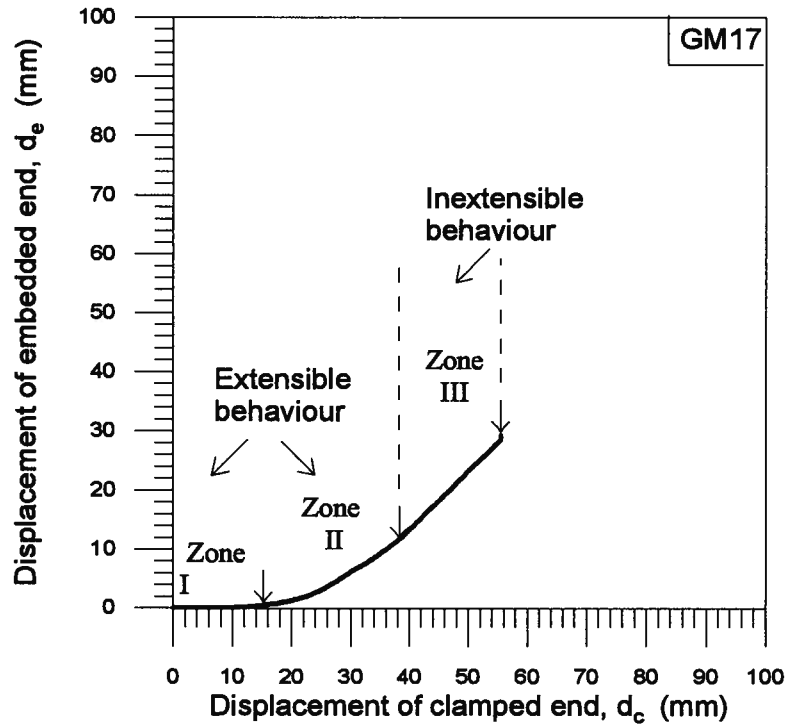


Figure 7.19: Relationship between d_c and d_e for the Miragrid in the DC test at $\sigma_x=17$ kPa

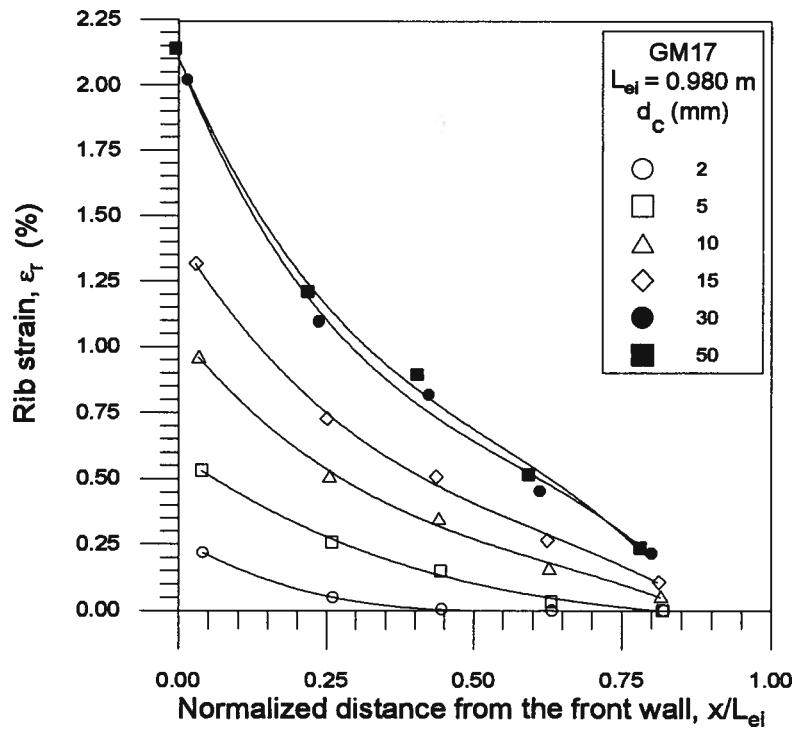


Figure 7.20: Strain profile for the Miragrid in the DC test at $\sigma_x=17$ kPa

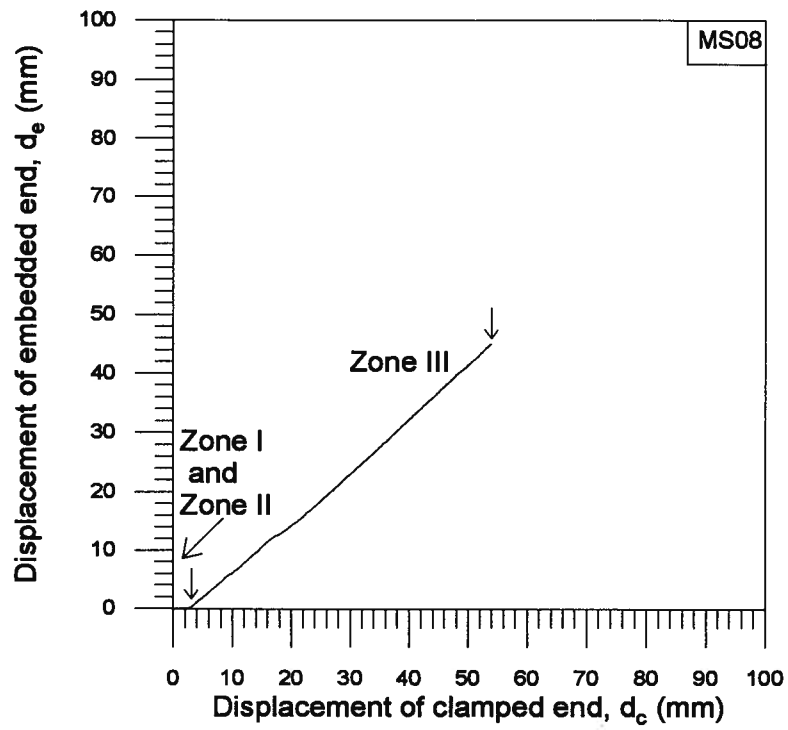


Figure 7.21: Relationship between d_c and d_e for the smooth geomembrane in the DC test at $\sigma_n=8$ kPa

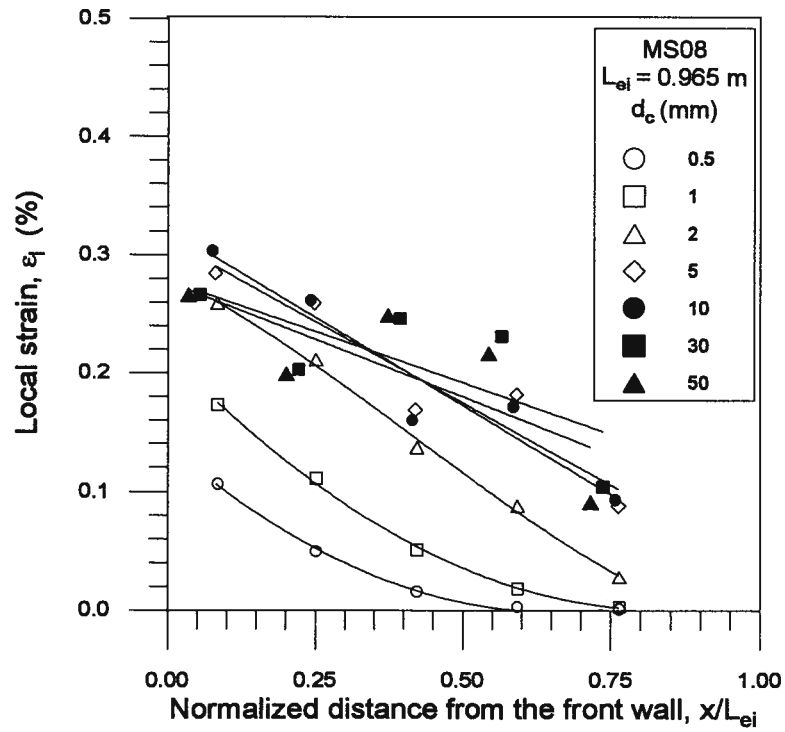


Figure 7.22: Strain profile for the smooth geomembrane in the DC test at $\sigma_n=8$ kPa

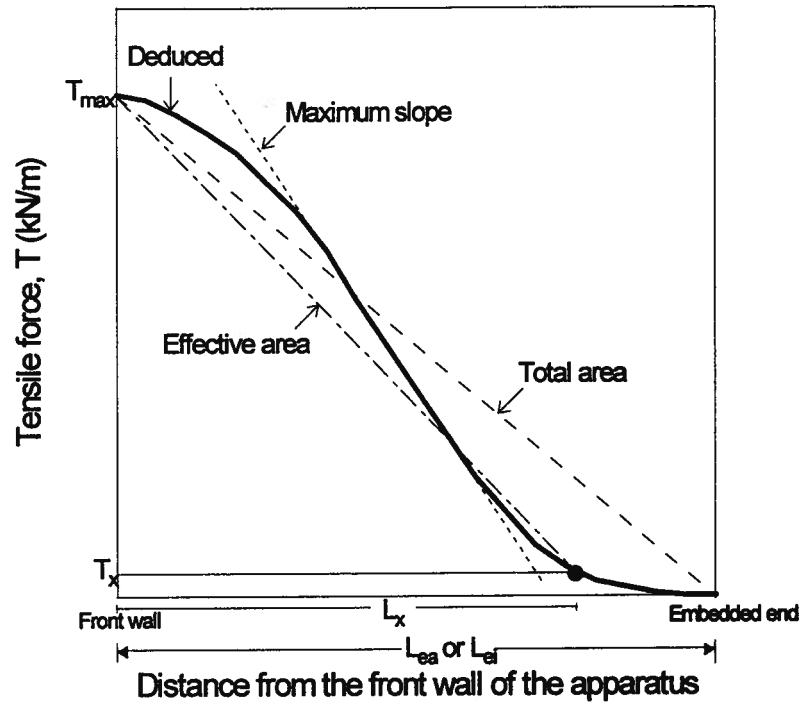


Figure 7.23: A schematic illustration of the interpretation of data by various resisting area methods (modified after Ochiai et al., 1992)

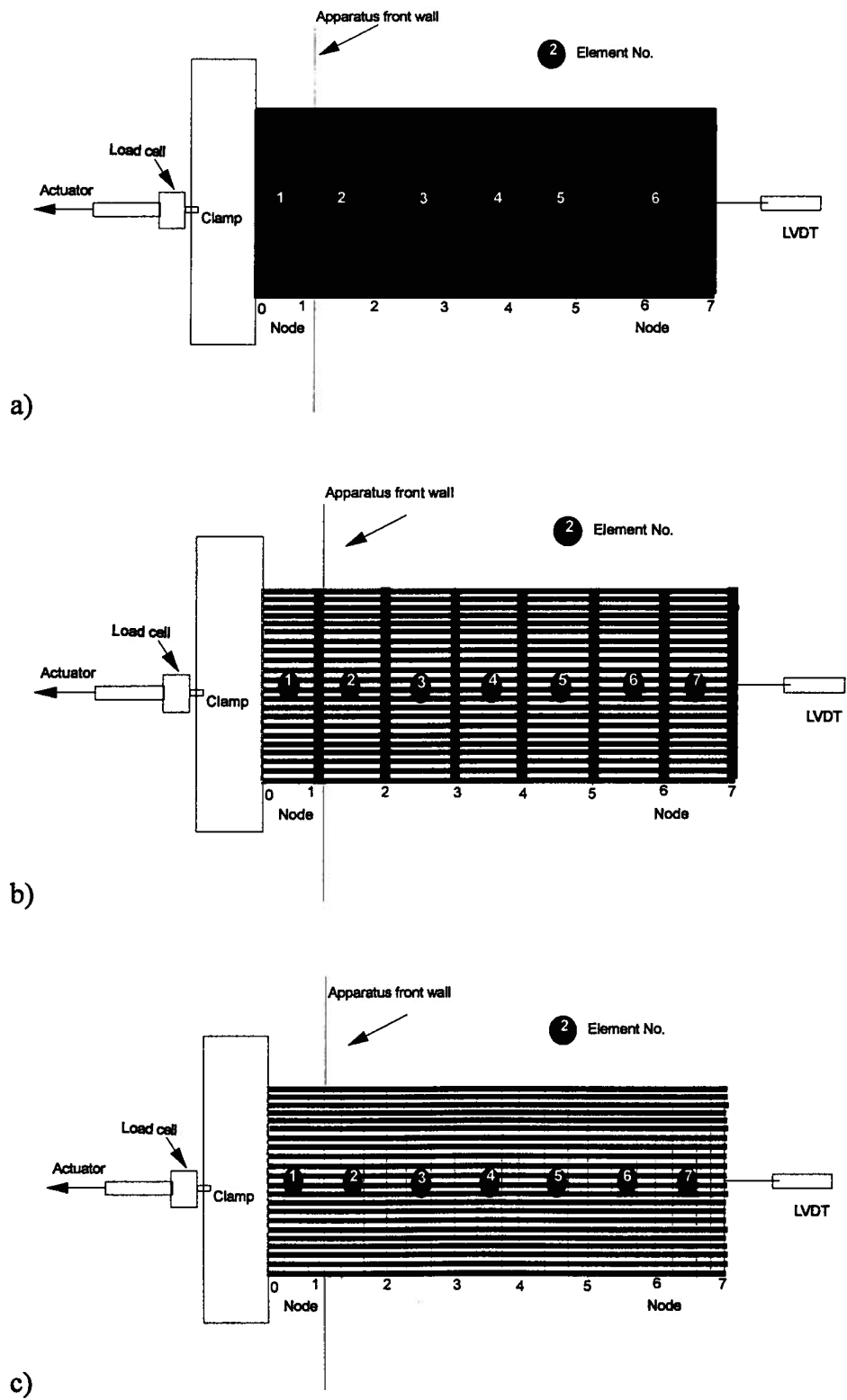


Figure 7.24: Schematic illustration of nodes and elements for a) smooth geomembrane, b) Tensar grid and c) Stratagrid and Miragrid

FLOW CHART OF THE GENERALIZED METHOD

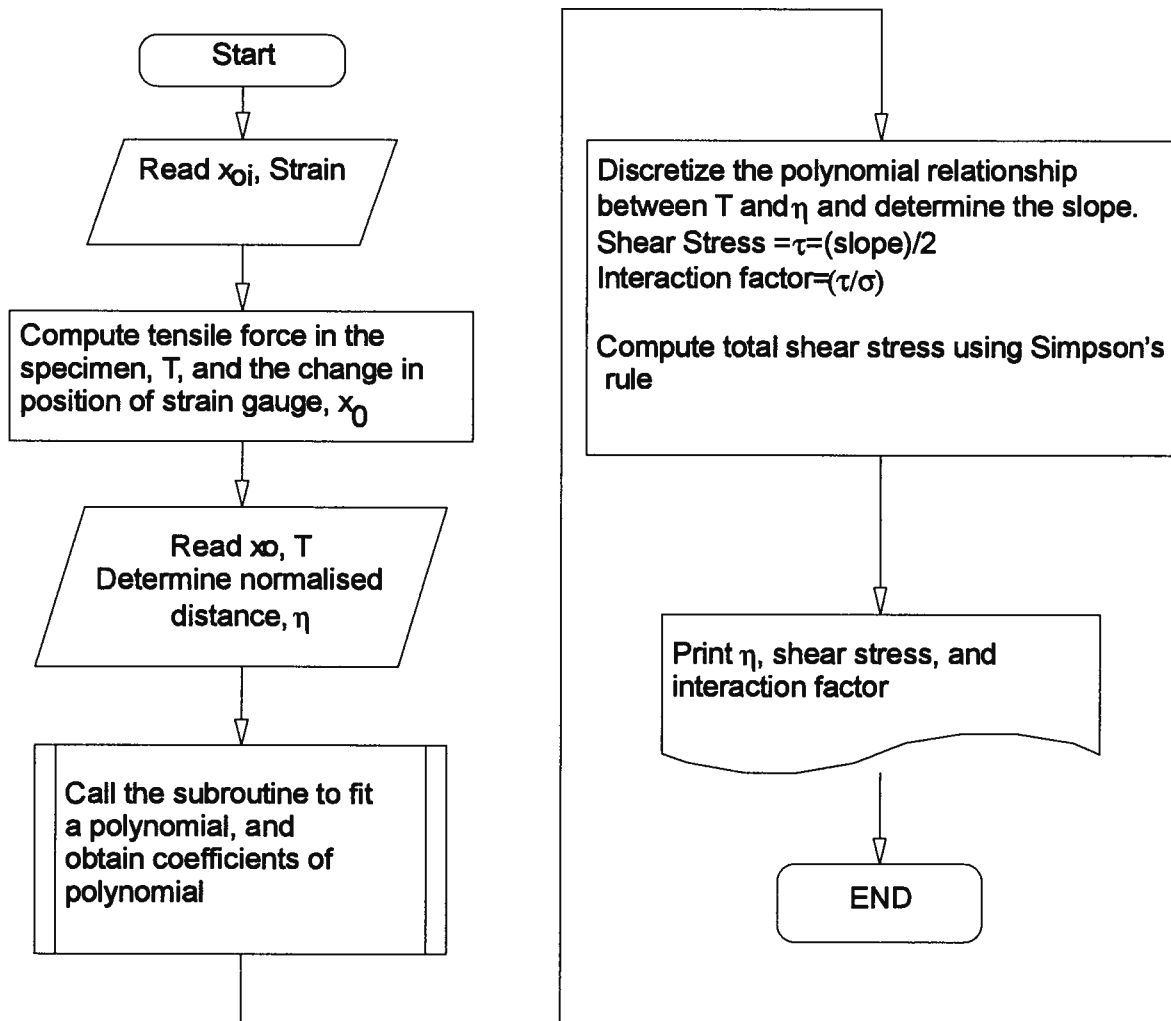


Figure 7.25: Flow chart of the generalized method for interpretation of a pullout test

Chapter 7. Analysis of Test Results

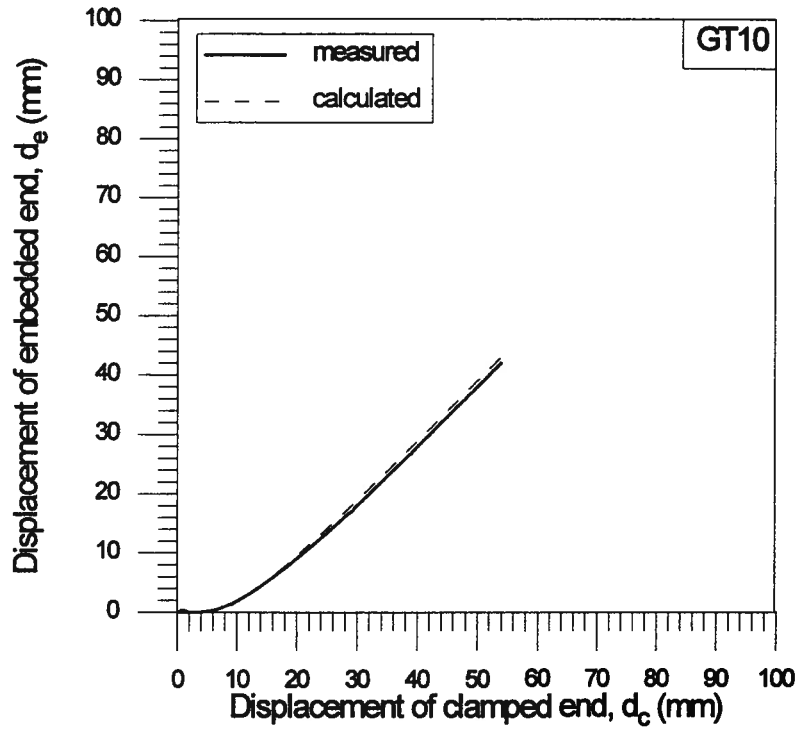


Figure 7.26: Comparison of measured and calculated displacements of the embedded end of the Tensor grid in the DC test at $\sigma_n=10$ kPa

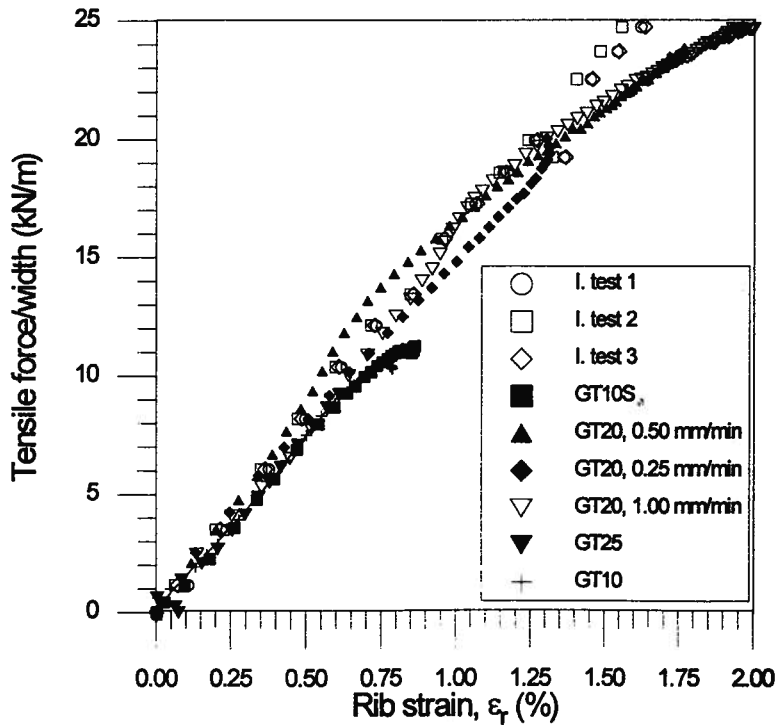


Figure 7.27: Relationship between strain and tensile force per unit width for the Tensor grid

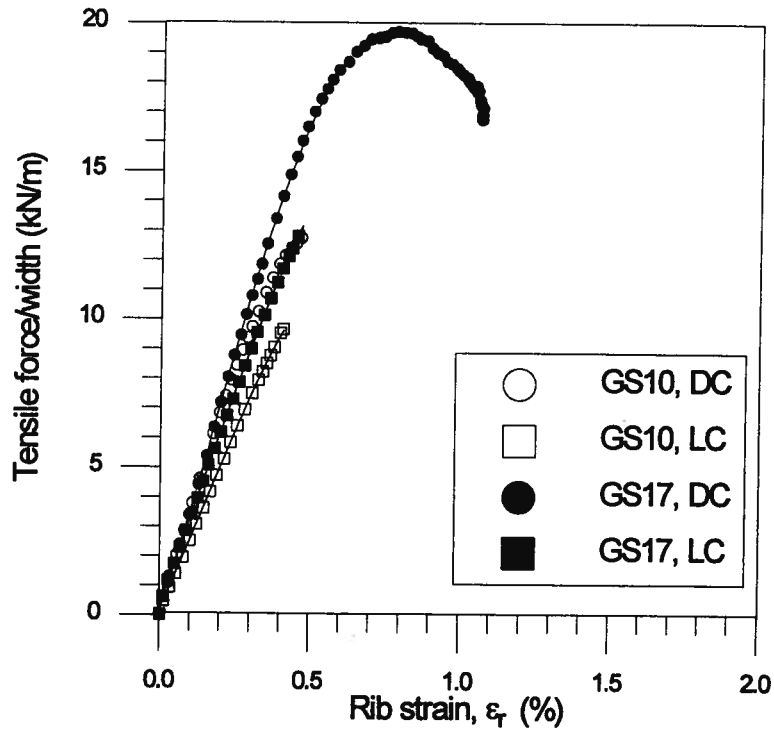


Figure 7.28: Relationship between tensile force at the clamped end and the measured strain at location SG-2 ($x/L_{a1}=0.106$) for the Stratagrid

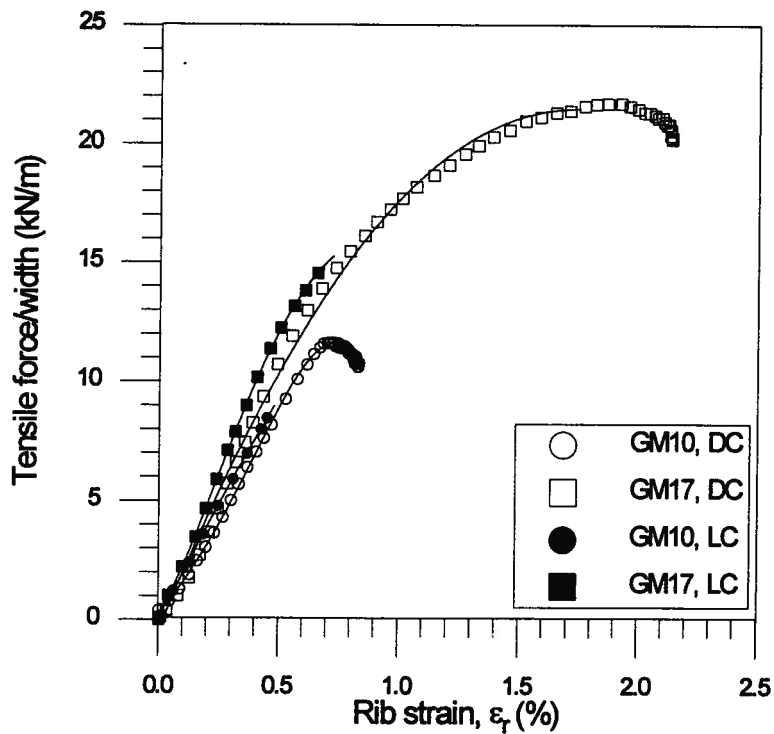


Figure 7.29: Relationship between tensile force at the clamped end and the measured strain at location SG-1 ($x/L_{a1}=0.043$) for the Miragrid

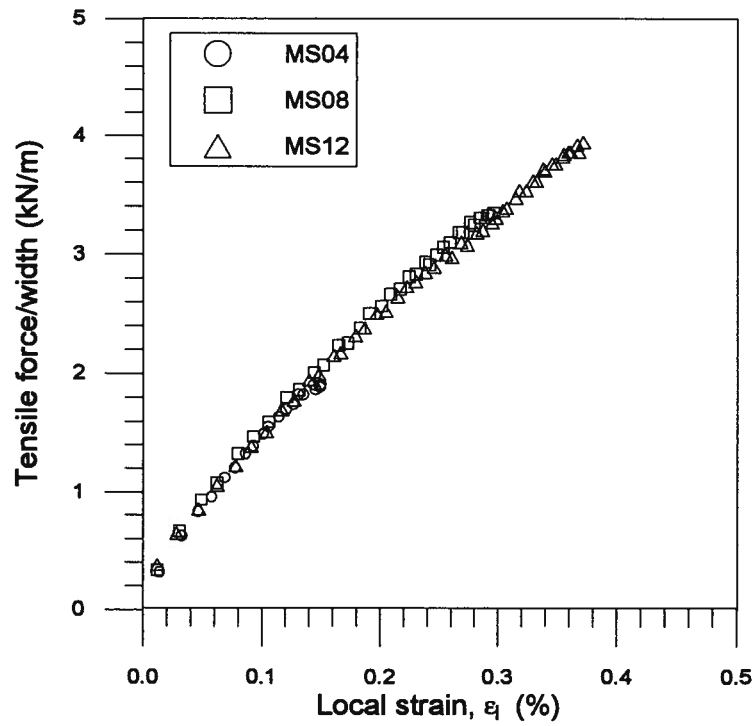


Figure 7.30: Relationship between tensile force at the clamped end and the measured strain at location SG-1 ($x/L_{ei}=0.074$) for the smooth geomembrane in the DC tests

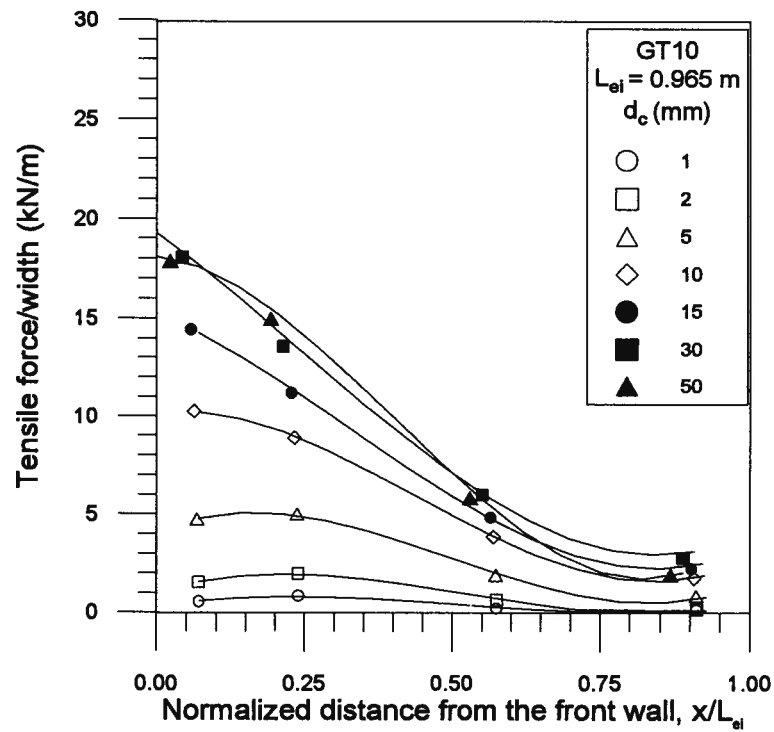


Figure 7.31: Profile of deduced tensile force/width and the generated polynomial fit for the Tensar grid at $\sigma_n=10$ kPa

Chapter 7. Analysis of Test Results

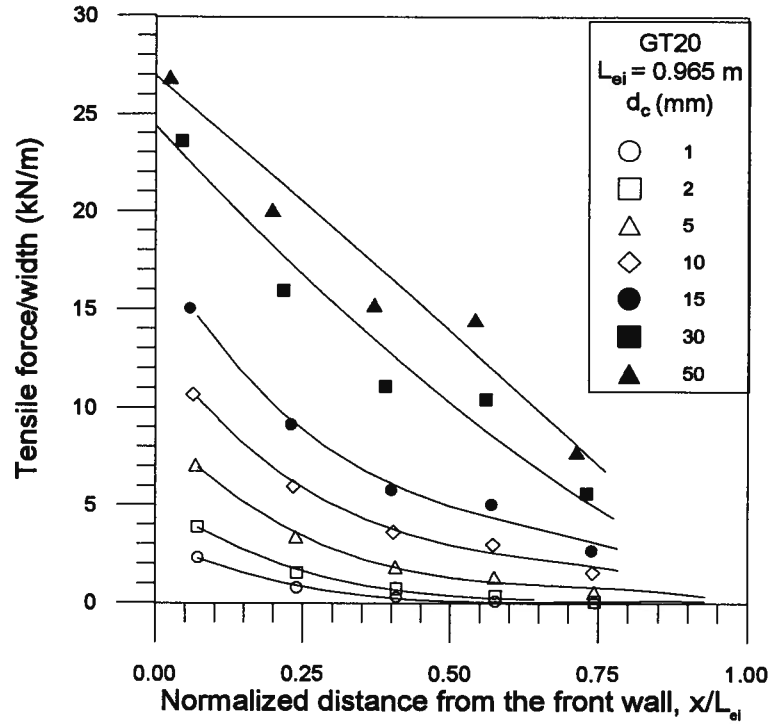


Figure 7.32: Profile of deduced tensile force/width and the generated polynomial fit for the Tensar grid at $\sigma_a=20 \text{ kPa}$ and $r_d=0.5 \text{ mm/min}$

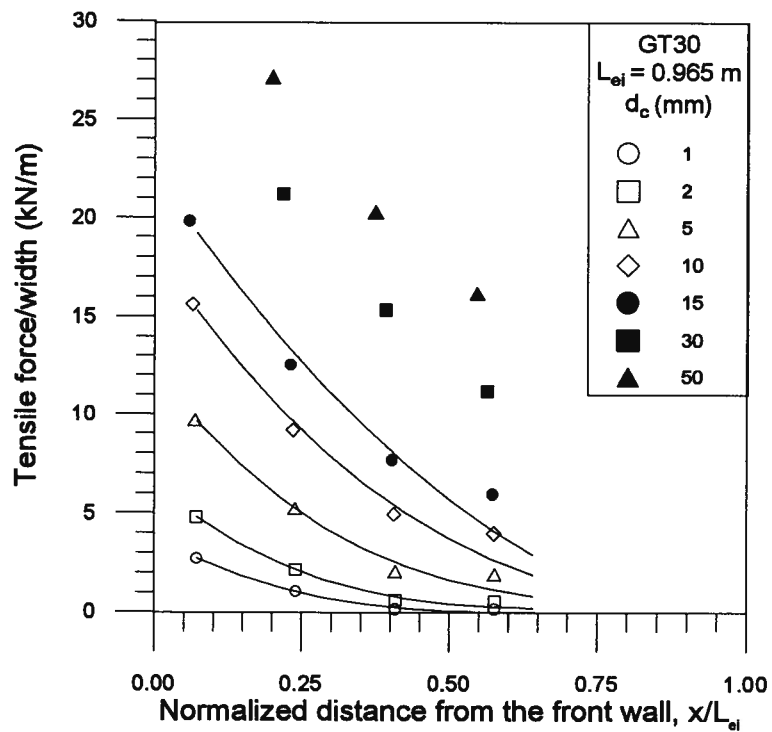


Figure 7.33: Profile of deduced tensile force/width and the generated polynomial fit for Tensar grid at $\sigma_a=30 \text{ kPa}$

Chapter 7. Analysis of Test Results

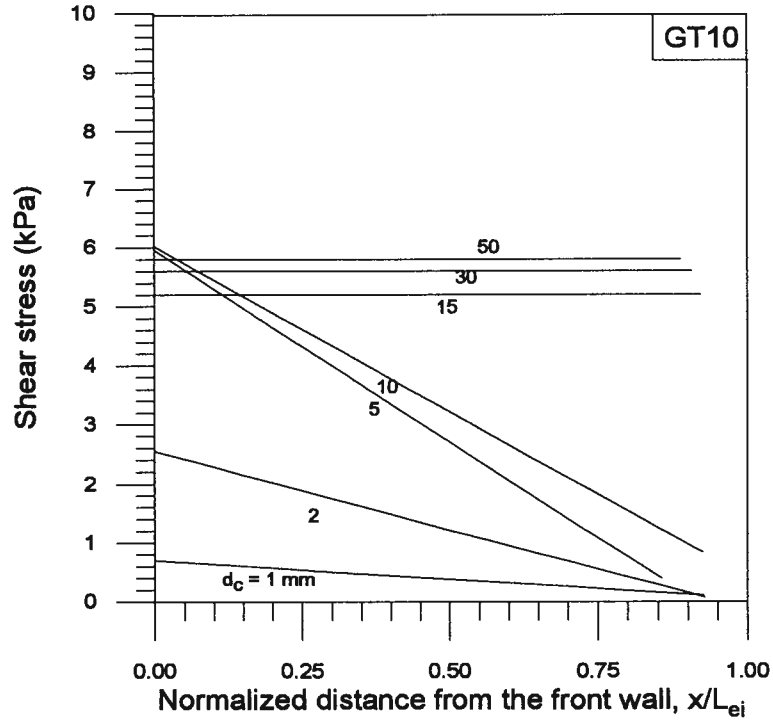


Figure 7.34: Shear stress variation along the embedded length of the Tensar grid at $\sigma_n=10$ kPa

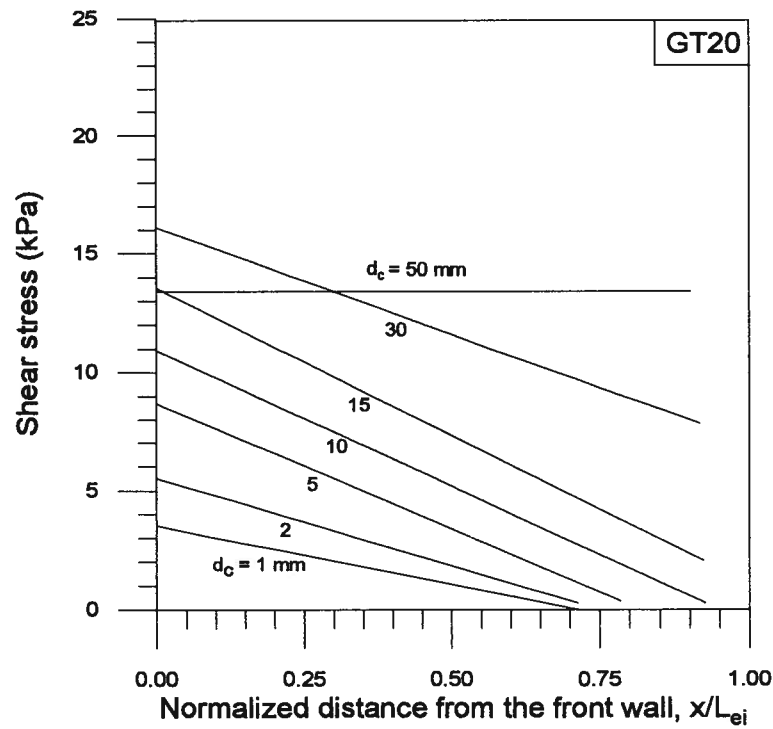


Figure 7.35: Shear stress variation along the embedded length of the Tensar grid at $\sigma_n=20$ kPa

Chapter 7. Analysis of Test Results

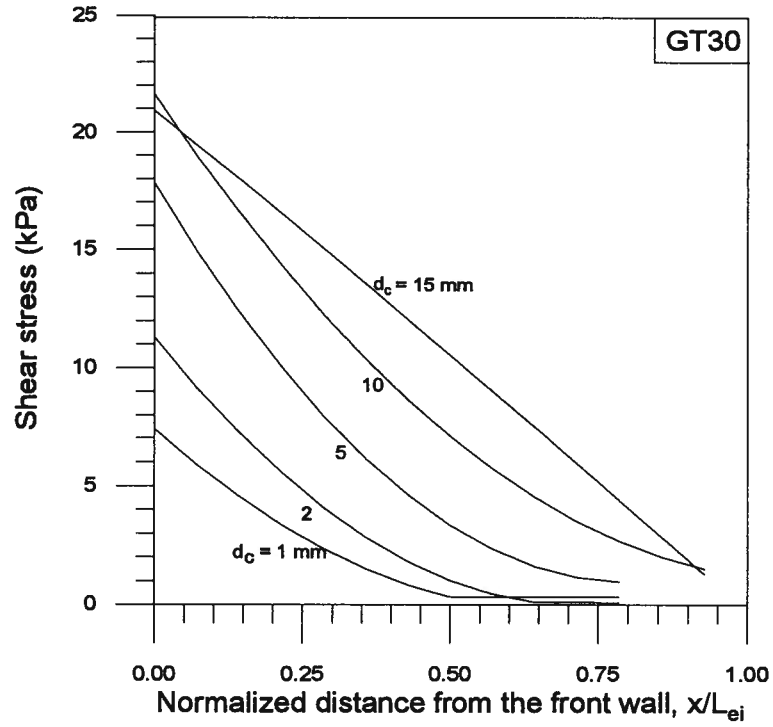


Figure 7.36: Shear stress variation along the embedded length of the Tensar grid at $\sigma_n=30$ kPa

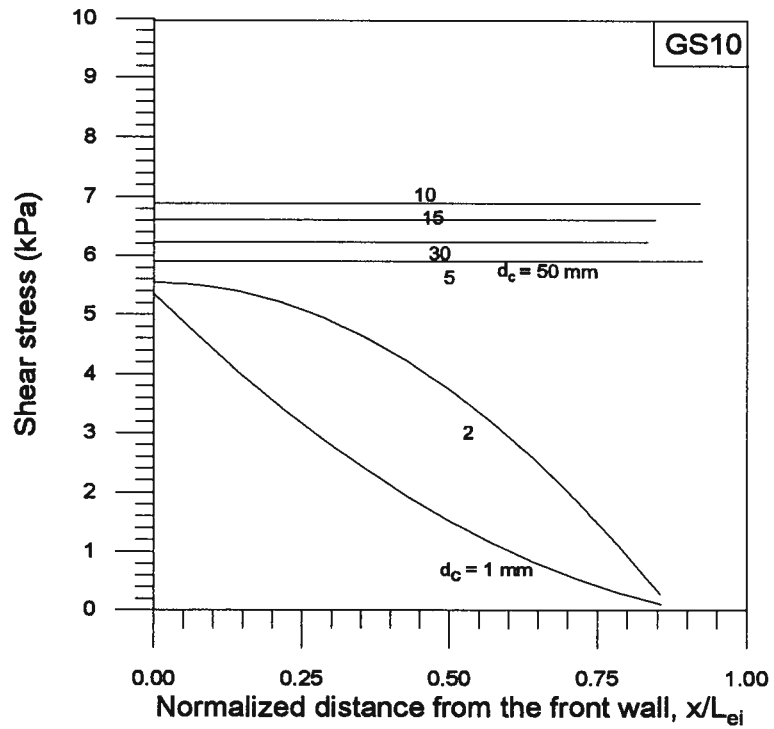


Figure 7.37: Shear stress variation along the embedded length of the Stratagrid at $\sigma_n=10$ kPa

Chapter 7. Analysis of Test Results

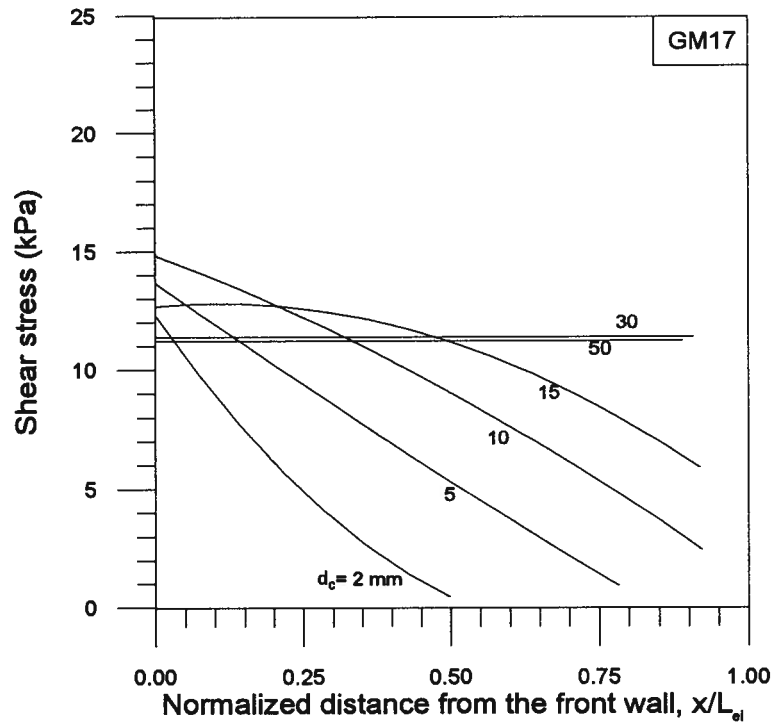


Figure 7.38: Shear stress variation along the embedded length of the Miragrid at $\sigma_n=17$ kPa

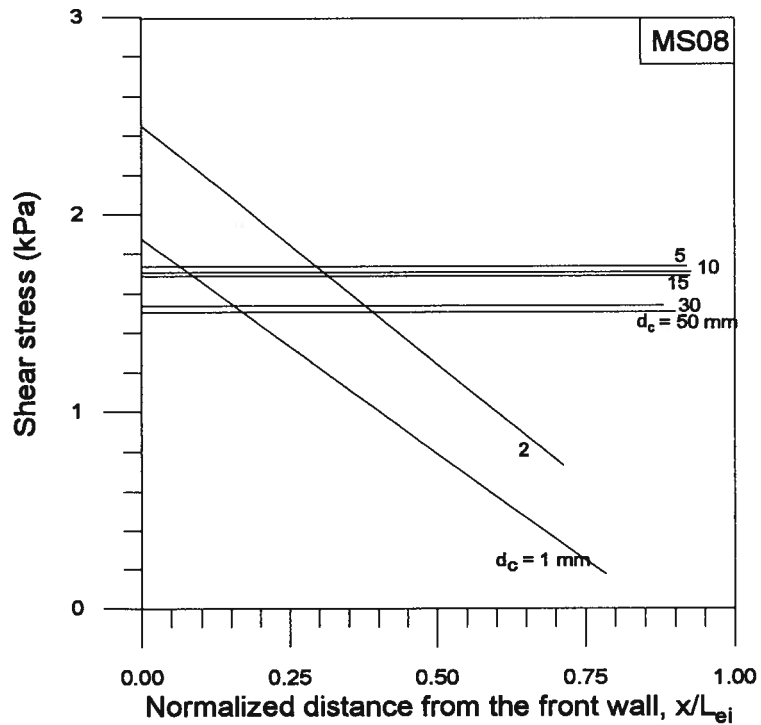


Figure 7.39: Shear stress variation along the embedded length of the smooth geomembrane at $\sigma_n=8$ kPa

Chapter 7. Analysis of Test Results

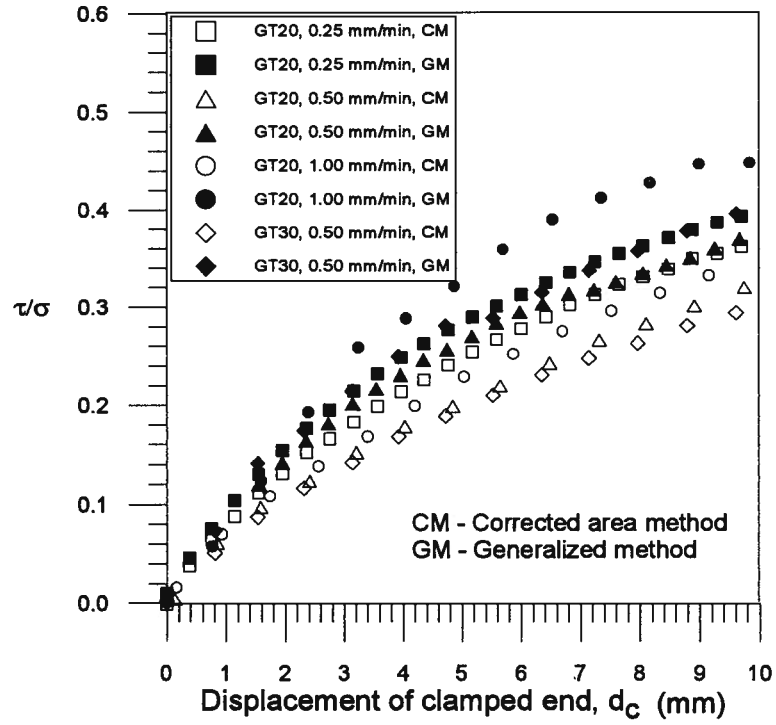


Figure 7.40: Interaction factors for the Tensar grid: corrected total area method and generalized method

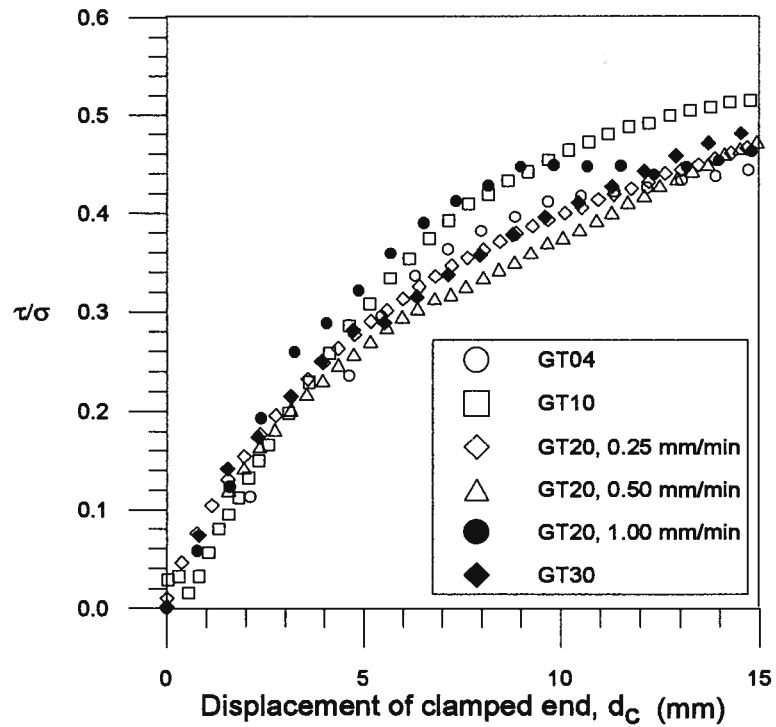


Figure 7.41: Interaction factors for the Tensar grid: generalized method

Chapter 7. Analysis of Test Results

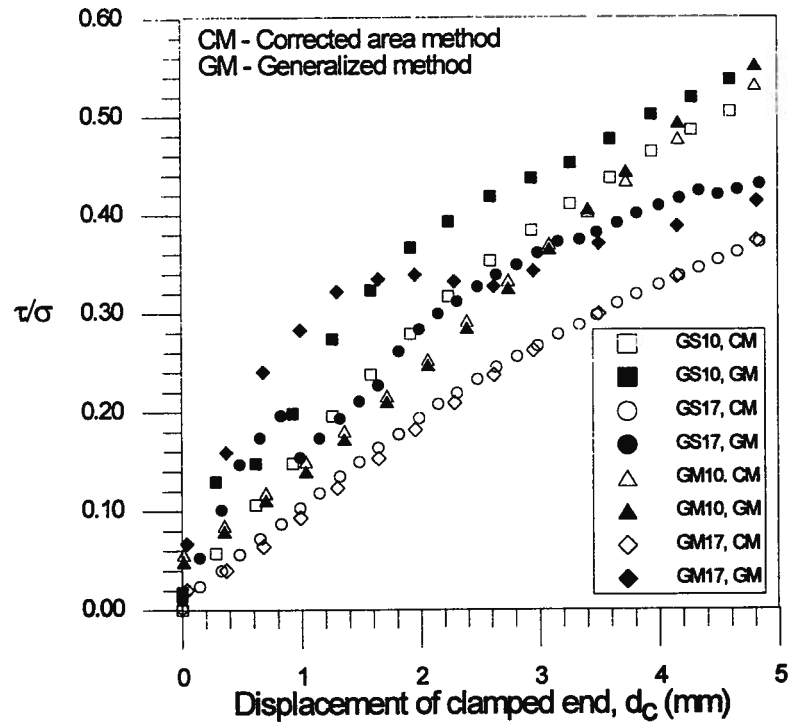


Figure 7.42: Interaction factor for the Stratagrid and Miragrid: corrected total area method and generalized method

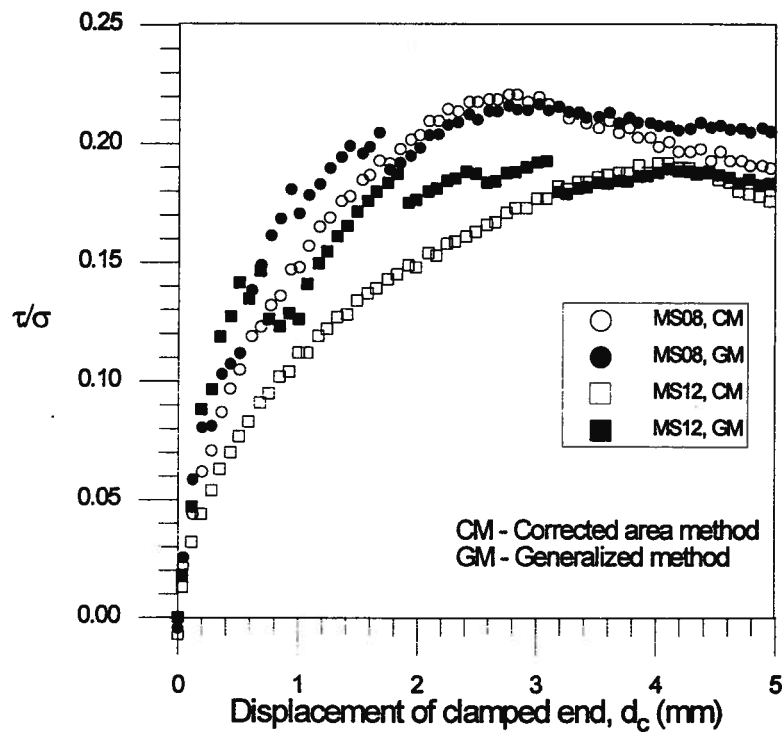


Figure 7.43: Interaction factor for smooth geomembrane using the corrected area and generalized method

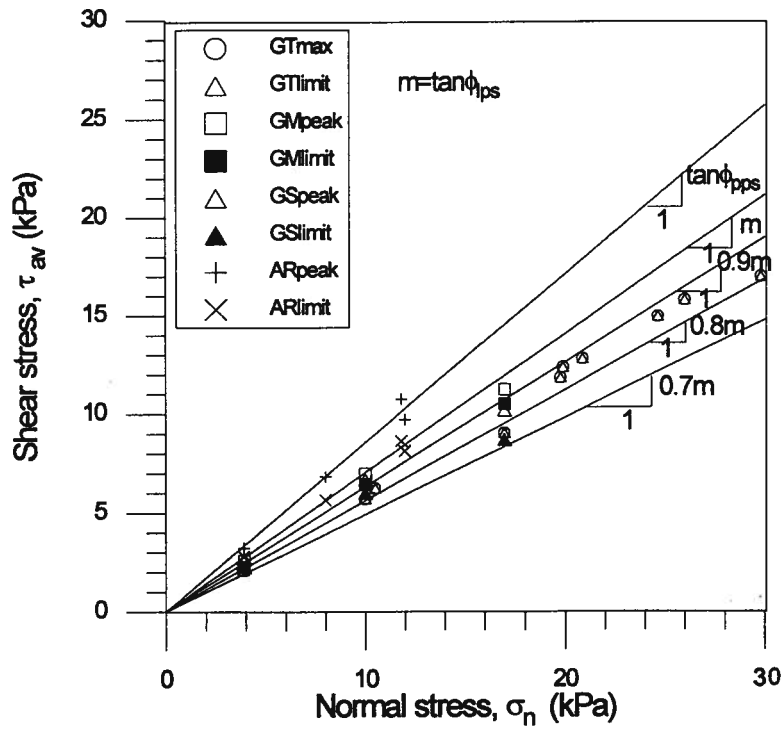


Figure 7.44: Relationship between average shear stress and normal stress for the grids and rough aluminum sheet

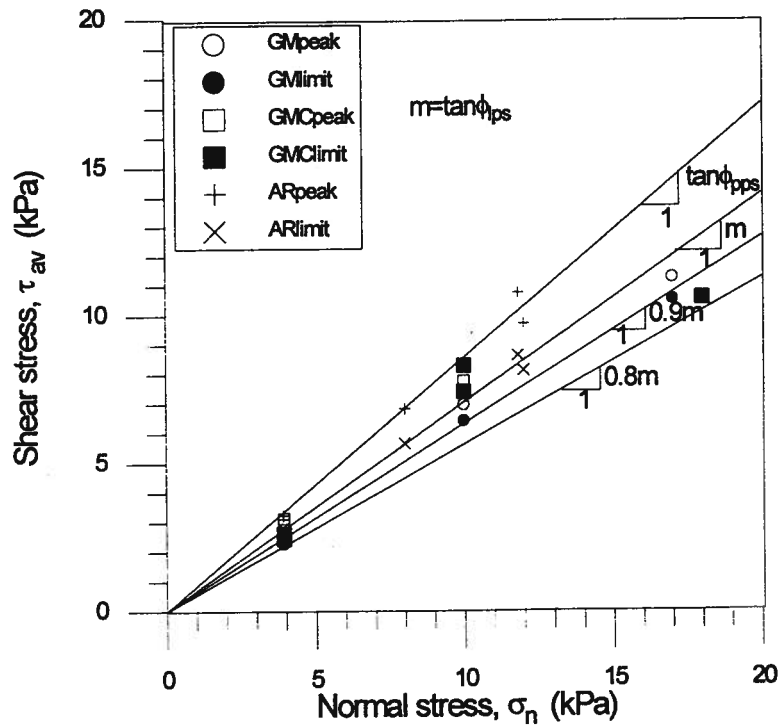


Figure 7.45: Influence of grid orientation on pullout behaviour of the Miragrid

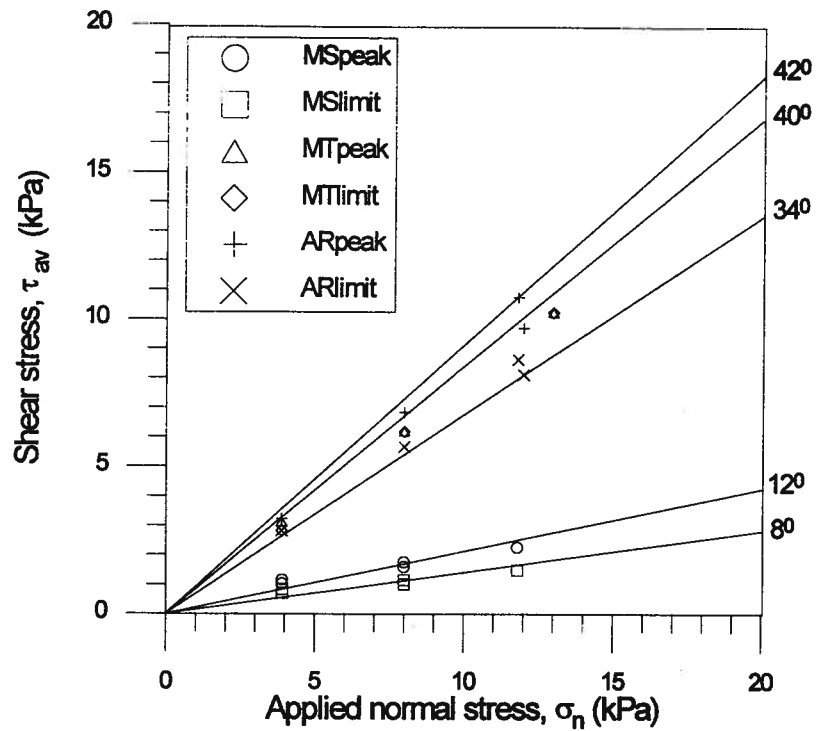


Figure 7.46: Relationship between average shear stress and normal stress for the geomembranes and rough aluminum sheet

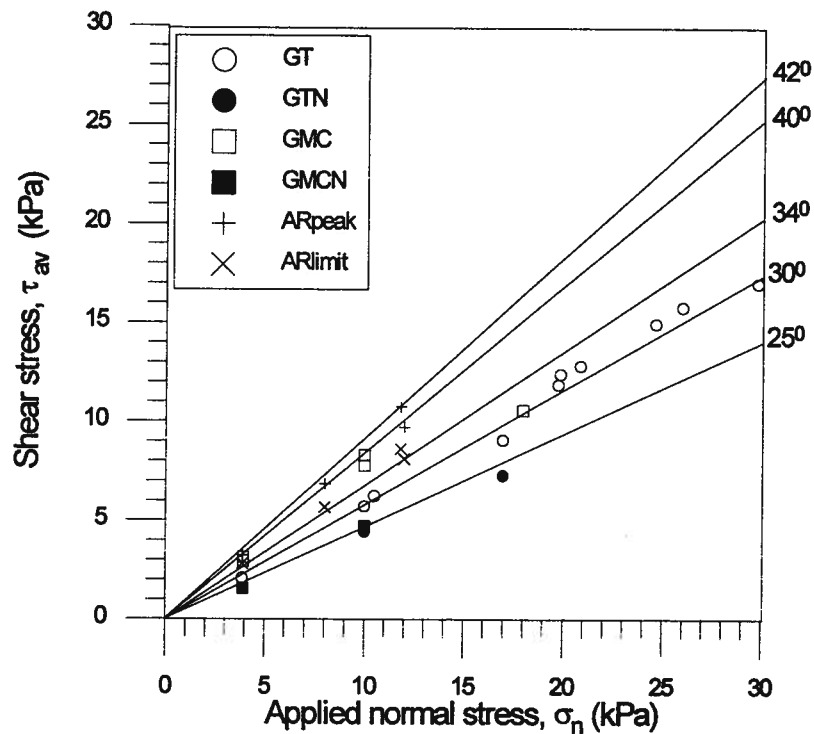


Figure 7.47: Relationship between average shear stress and normal stress for the Tensar grid and Miragrid with and without bearing elements

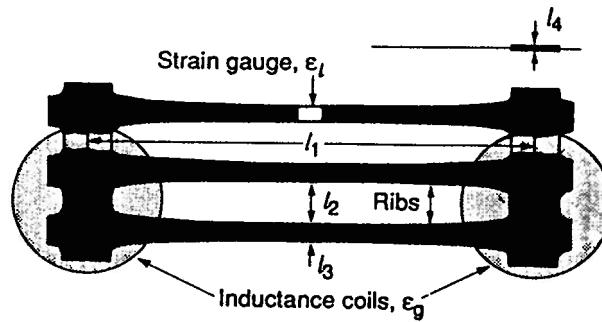


Figure 7.48: Details of the geogrid specimen (after Fannin et al. , 1994)

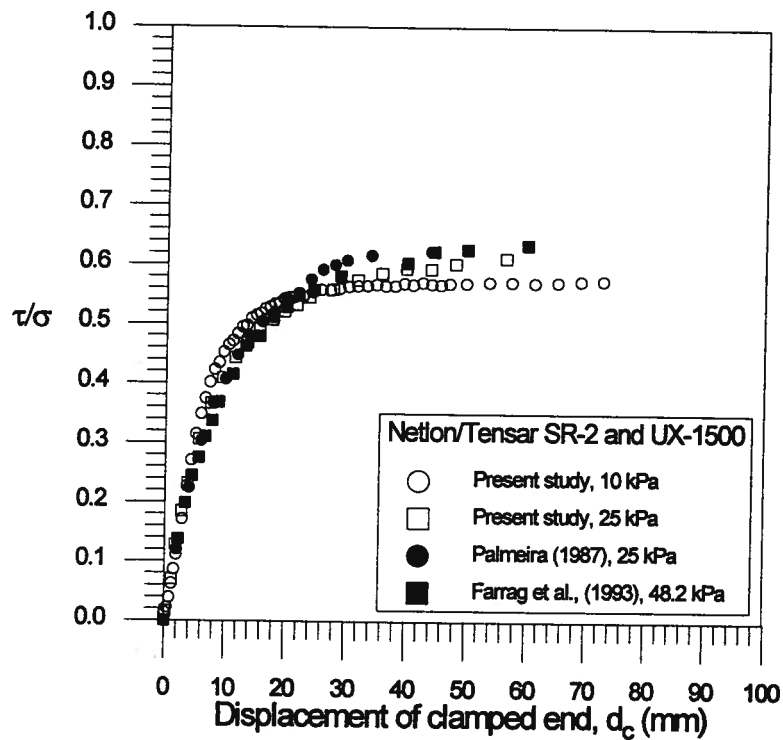


Figure 7.49: Comparison of Tensar grid interaction factors from laboratory pullout tests

Chapter 7. Analysis of Test Results

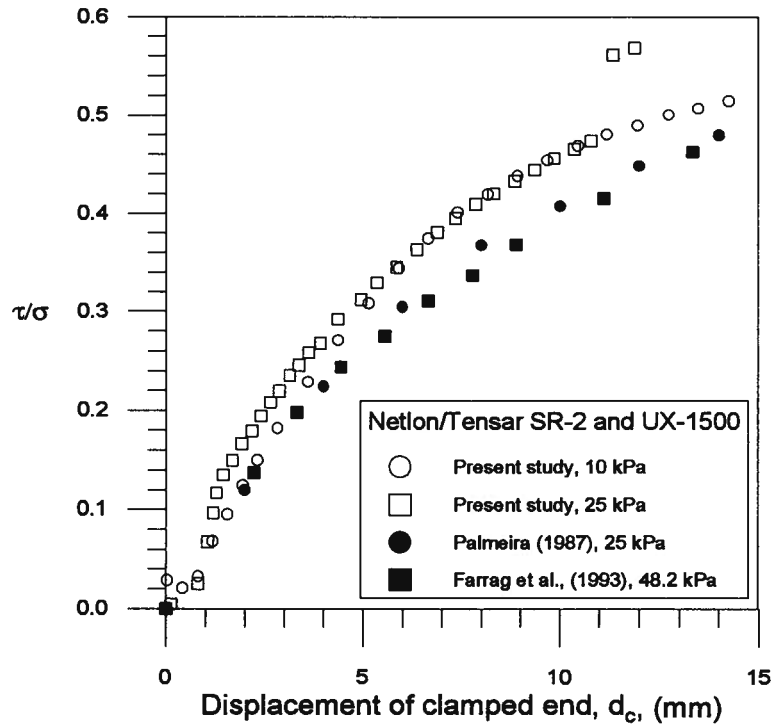


Figure 7.50: Comparison of interaction factors from Figure 7.49 for small displacement

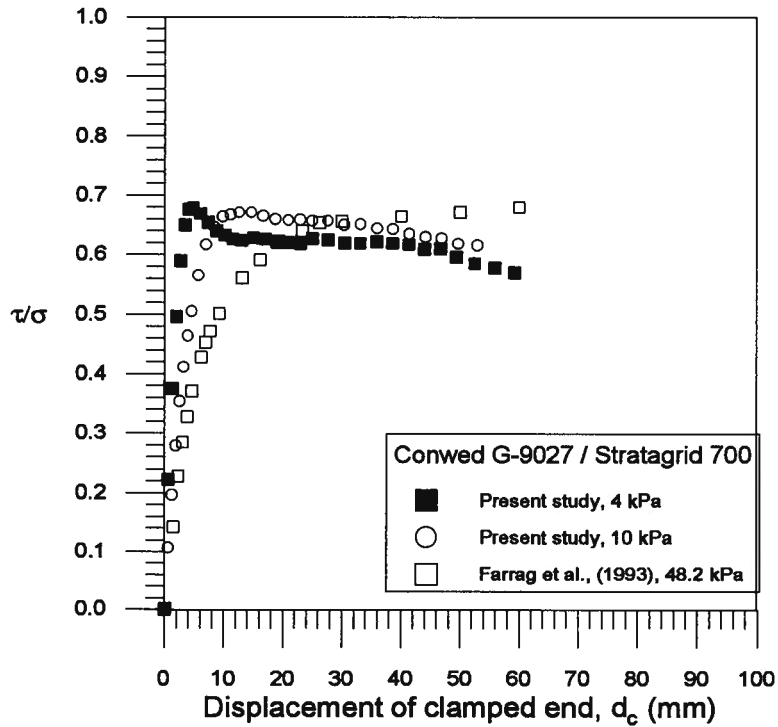


Figure 7.51: Comparison of interaction factor for Conwed G9027/Stratagrid 700

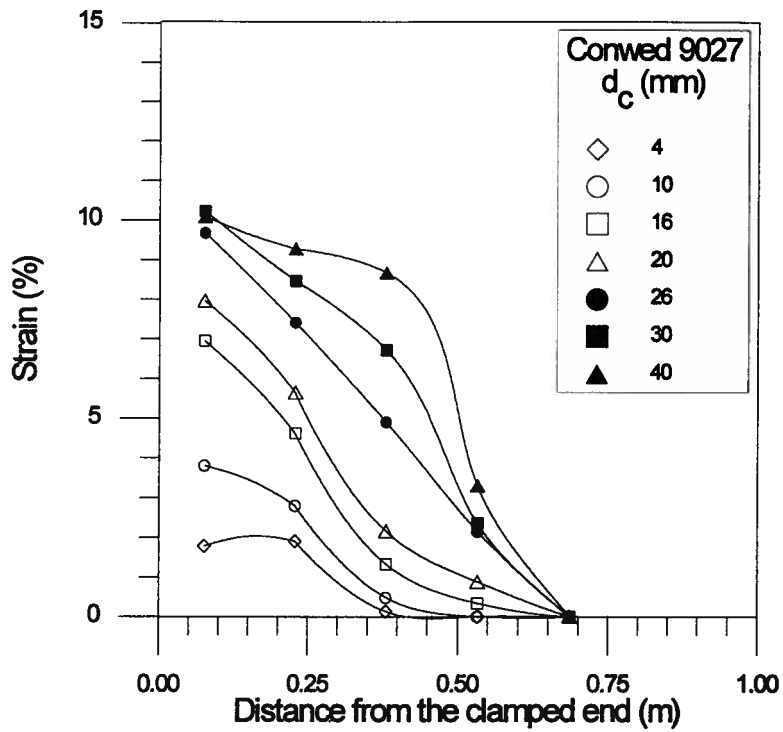


Figure 7.52: Strain profile deduced from the reported nodal displacements of Conwed grid at $\sigma_n=48.2$ kPa from Farrag et al. (1993)

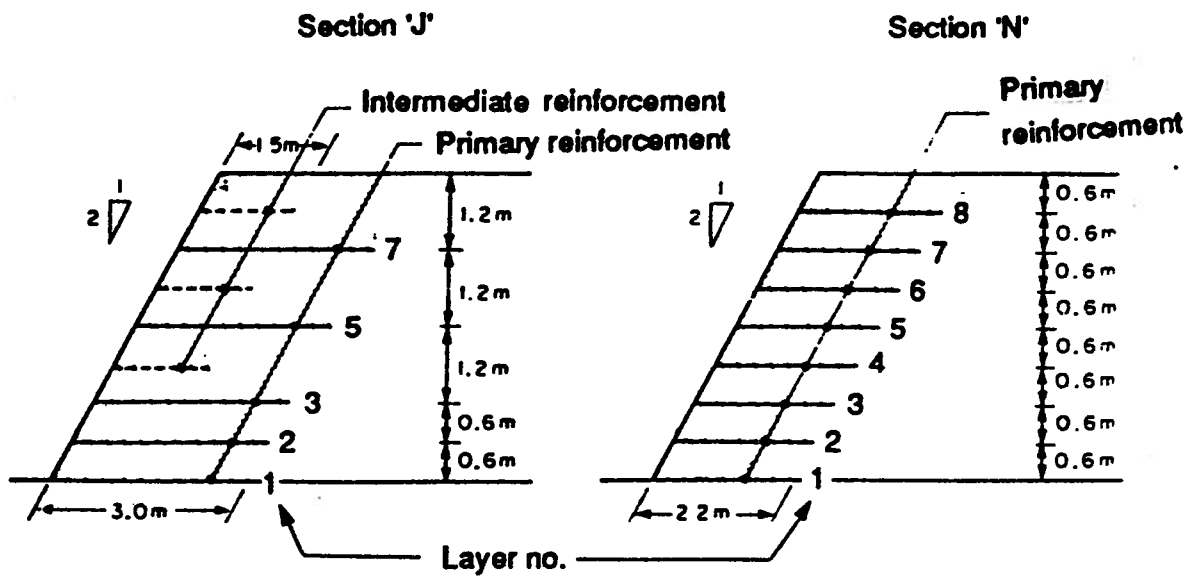


Figure 7.53: Reinforcement in the field structure (after Fannin et al., 1994)

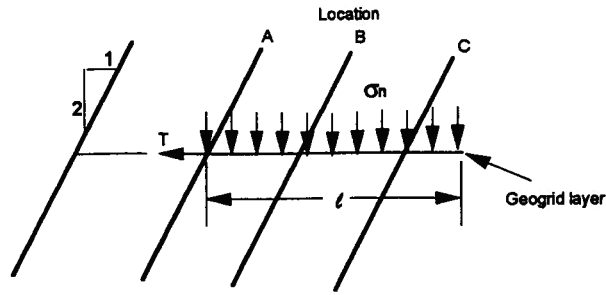
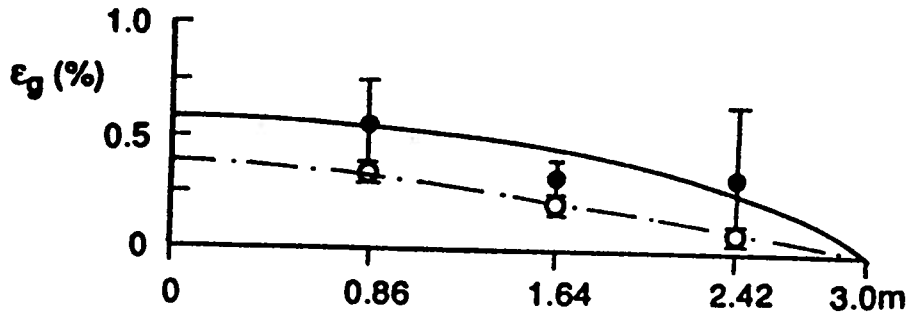
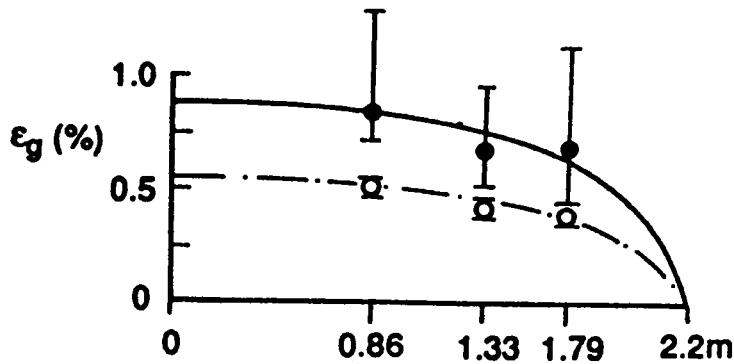


Figure 7.54: A schematic diagram showing strain gauge locations (after Fannin, 1990)

Section 'J'



Section 'N'



- Permanent surcharge loading ($\sigma_v = 70 \text{ kN/m}^2$)
- · - Self-weight loading ($\sigma_v = 20 \text{ kN/m}^2$)
- | | | |
|--|---|------|
| | } | max |
| | } | mean |
| | } | min |

Figure 7.55: Strain in layer No. 7 of the field structure (after Fannin and Hermann, 1990)

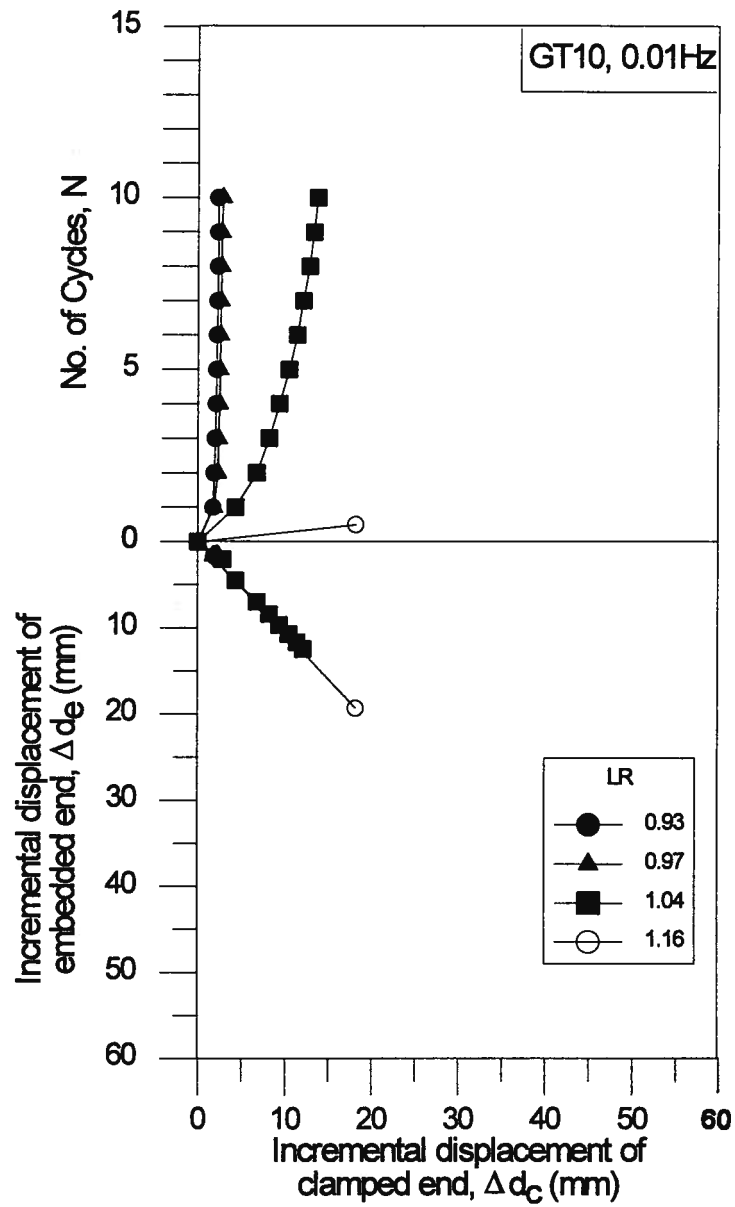


Figure 7.56: Relationship between Δd_c and Δd_e for the Tensar grid at $\sigma_n = 10$ kPa and $f = 0.01$ Hz

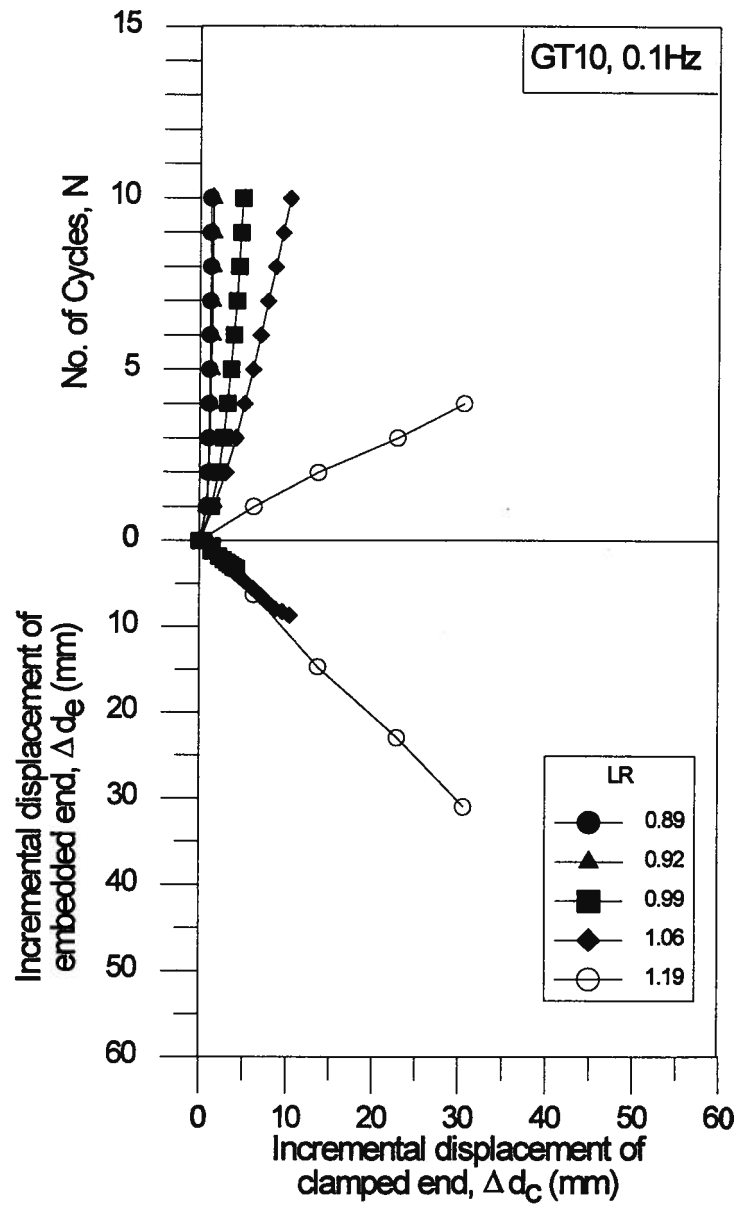


Figure 7.57: Relationship between Δd_c and Δd_e for the Tensar grid at $\sigma_v = 10$ kPa and $f = 0.1$ Hz

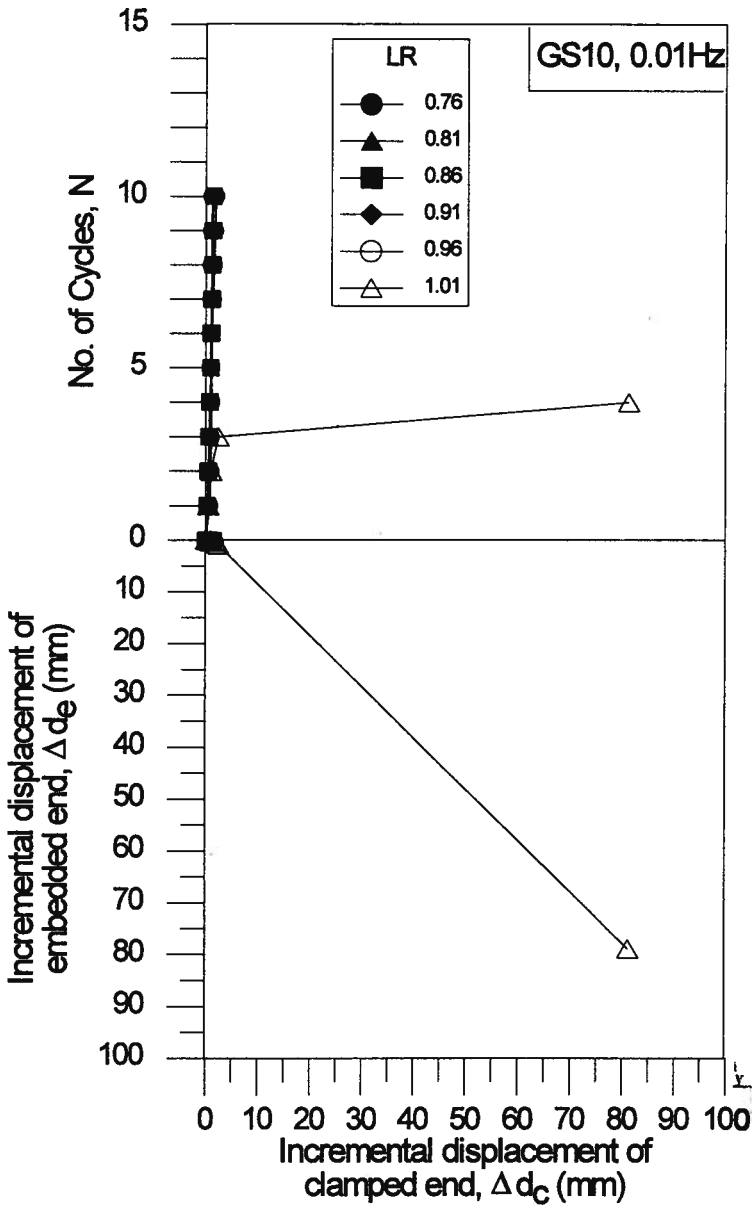


Figure 7.58: Relationship between Δd_c and Δd_e for the Stratagrid at $\sigma_n=10$ kPa and $f=0.01$ Hz

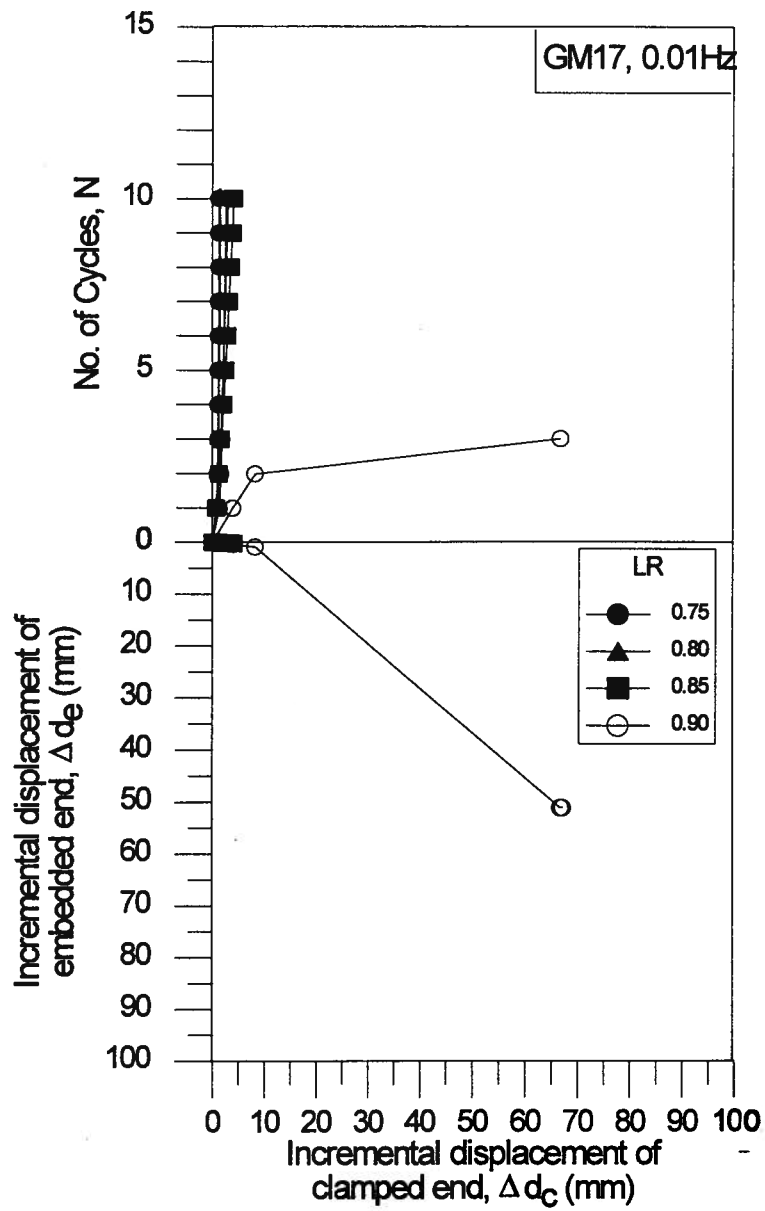


Figure 7.59: Relationship between Δd_c and Δd_e for the Miragrid at $\sigma_a=17$ kPa and $f=0.01$ Hz

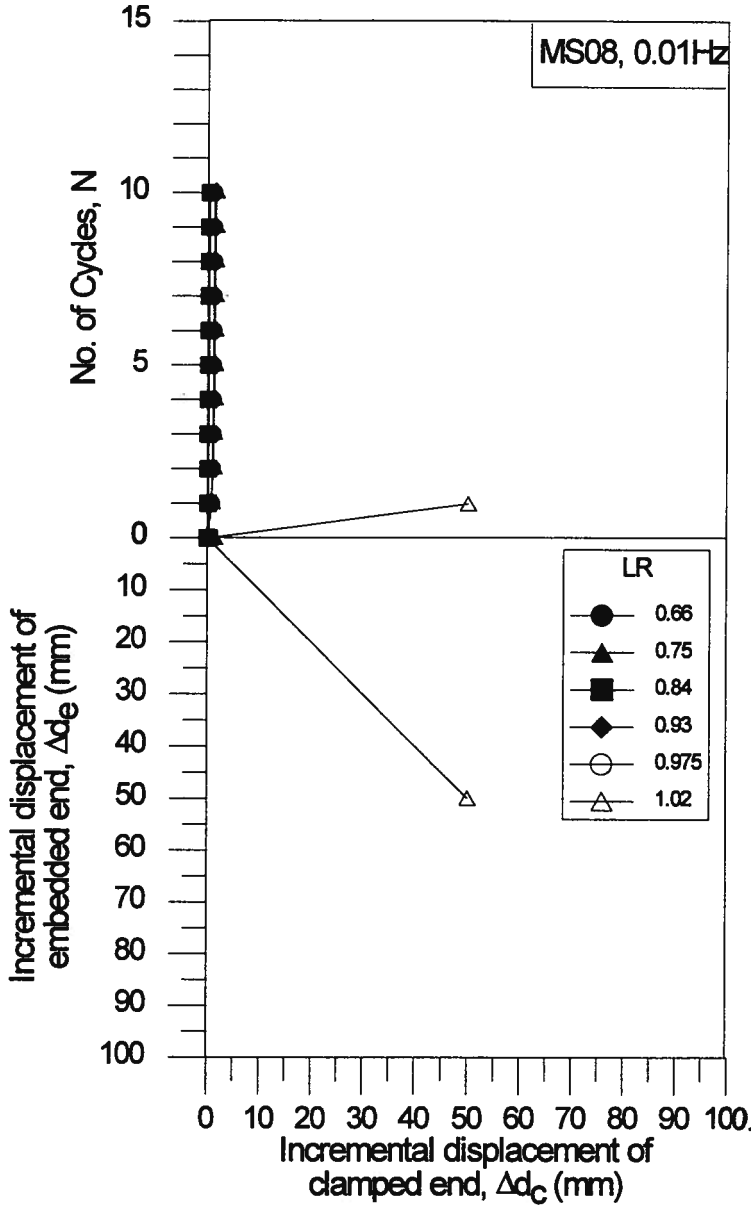


Figure 7.60: Relationship between Δd_c and Δd_e for the smooth geomembrane at $\sigma_v=8$ kPa and $f=0.01$ Hz

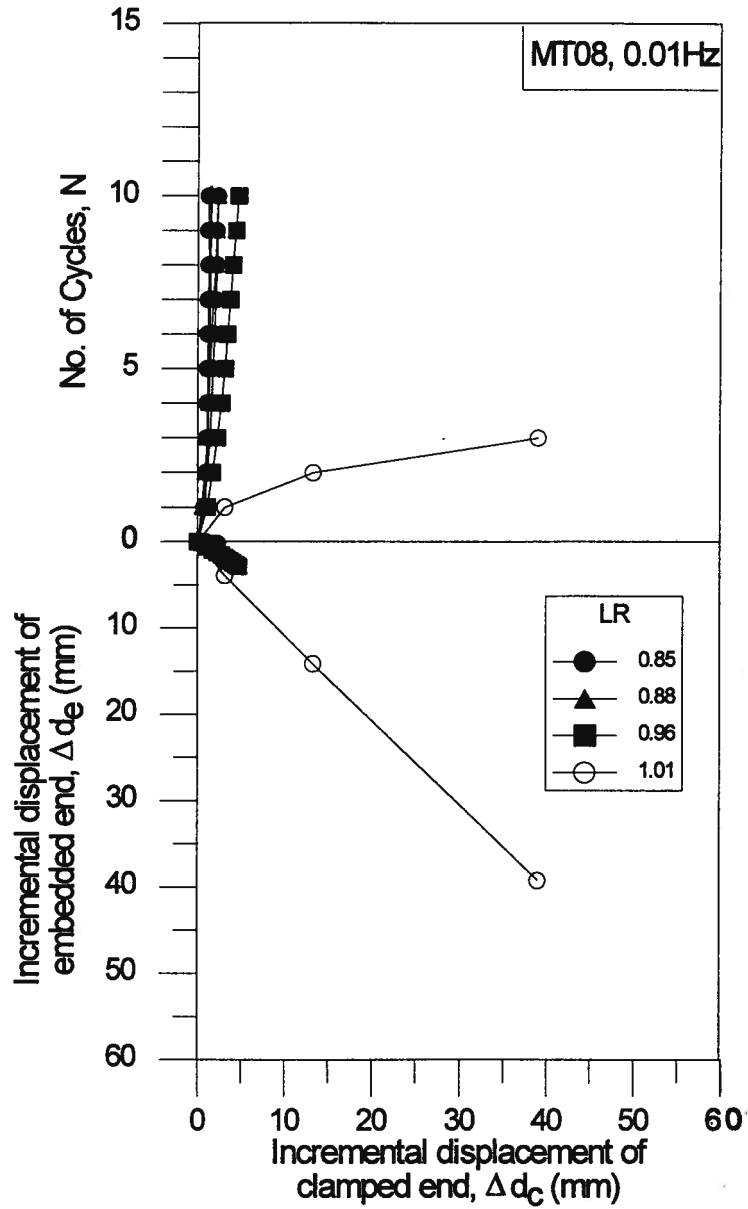


Figure 7.61: Relationship between Δd_c and Δd_e for the textured geomembrane at $\sigma_v = 8$ kPa and $f = 0.01$ Hz

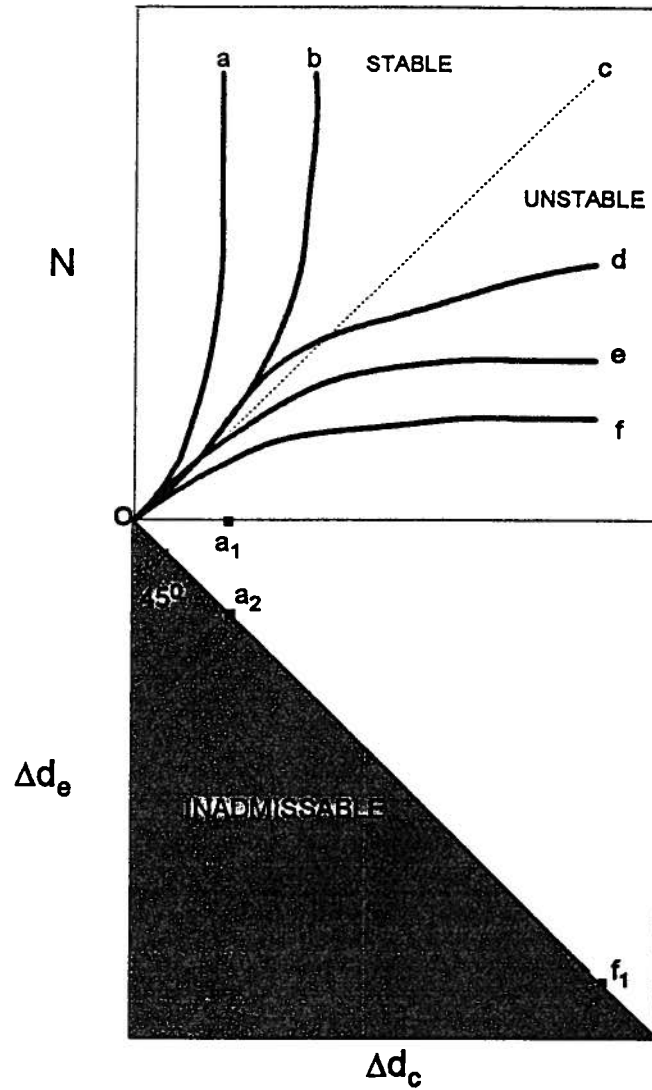


Figure 7.62: A conceptual model for the modes of behaviour observed in cyclic pullout testing

Chapter 7. Analysis of Test Results

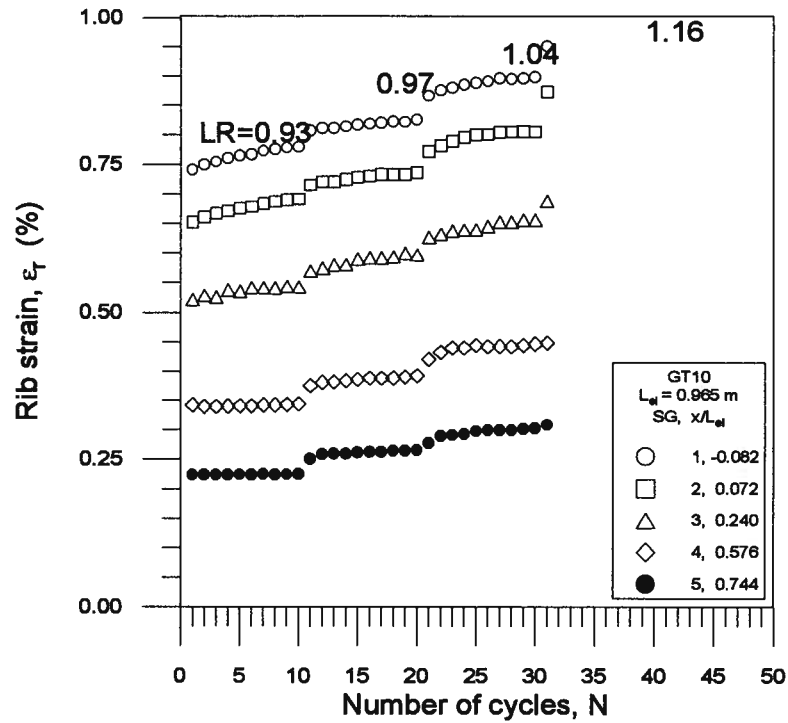


Figure 7.63: Mobilization of rib strain with number of cycles and increasing load ratio for the Tensar grid at $\sigma_v=10$ kPa and $f=0.01$ Hz

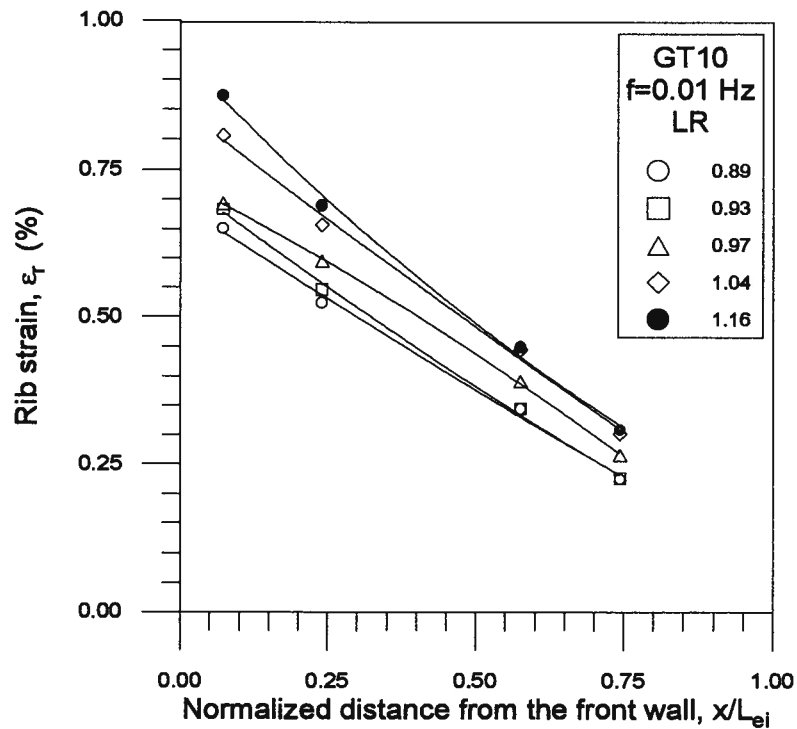


Figure 7.64: Strain profile with loading ratio at the end of the loading series for the Tensar grid at $\sigma_v=10$ kPa and $f=0.01$ Hz

Chapter 7. Analysis of Test Results

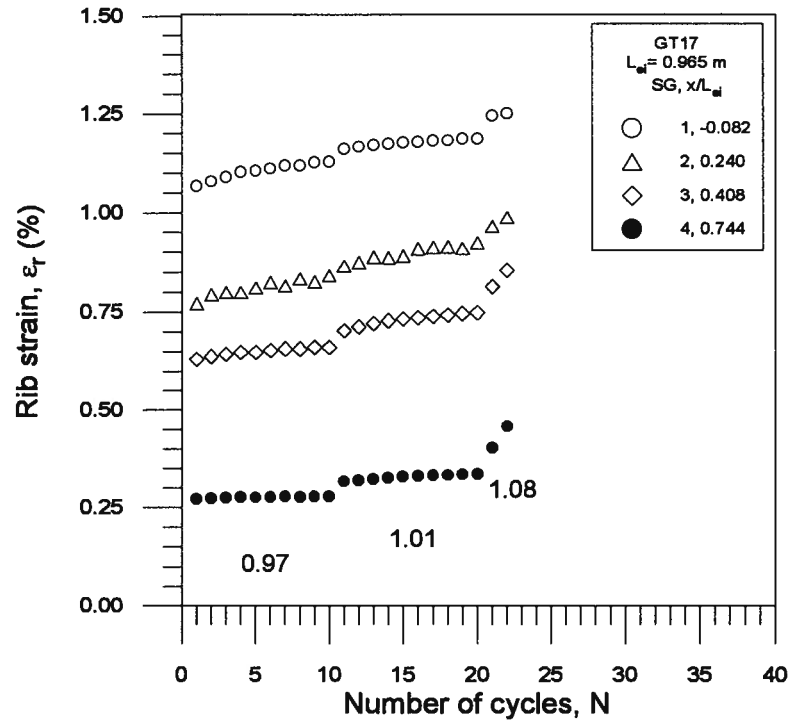


Figure 7.65: Mobilization of rib strain with number of cycles and increasing load ratio for the Tensor grid at $\sigma_n=17$ kPa and $f=0.01$ Hz

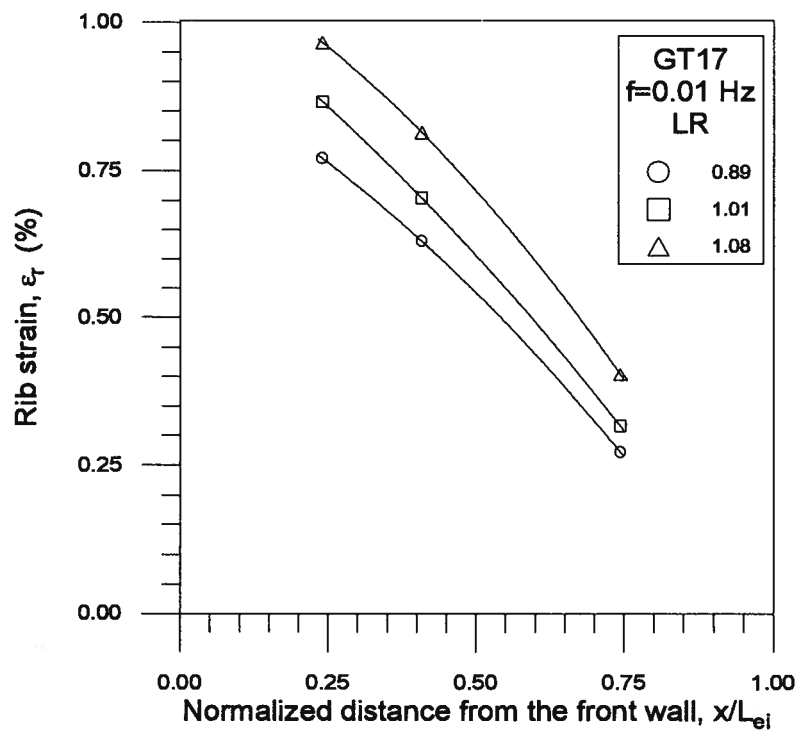


Figure 7.66: Strain profile with loading ratio at the end of the loading series for the Tensor grid at $\sigma_n=17$ kPa and $f=0.01$ Hz

Chapter 7. Analysis of Test Results

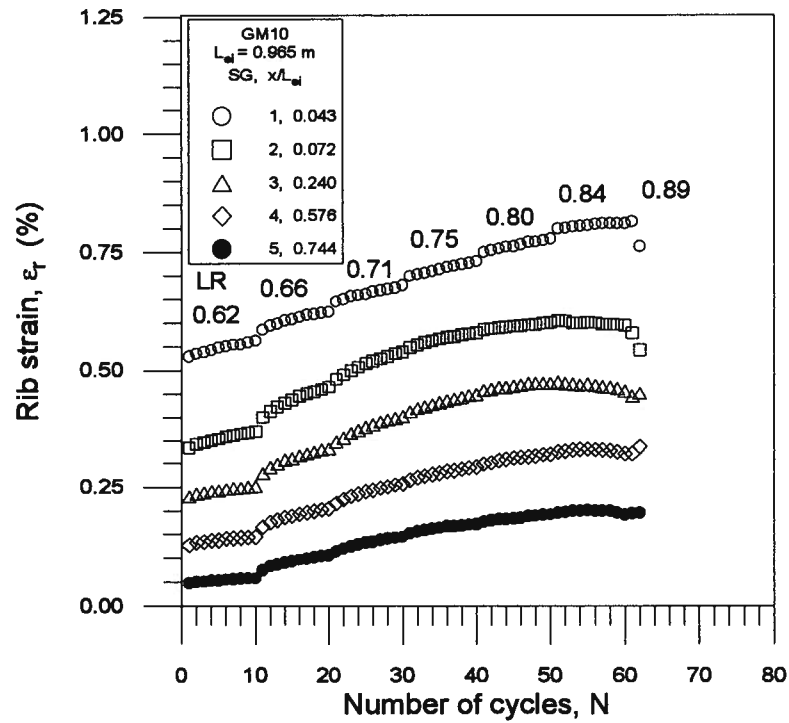


Figure 7.67: Mobilization of rib strain with number of cycles and increasing load ratio for the Miragrid at $\sigma_n=10$ kPa and $f=0.01$ Hz

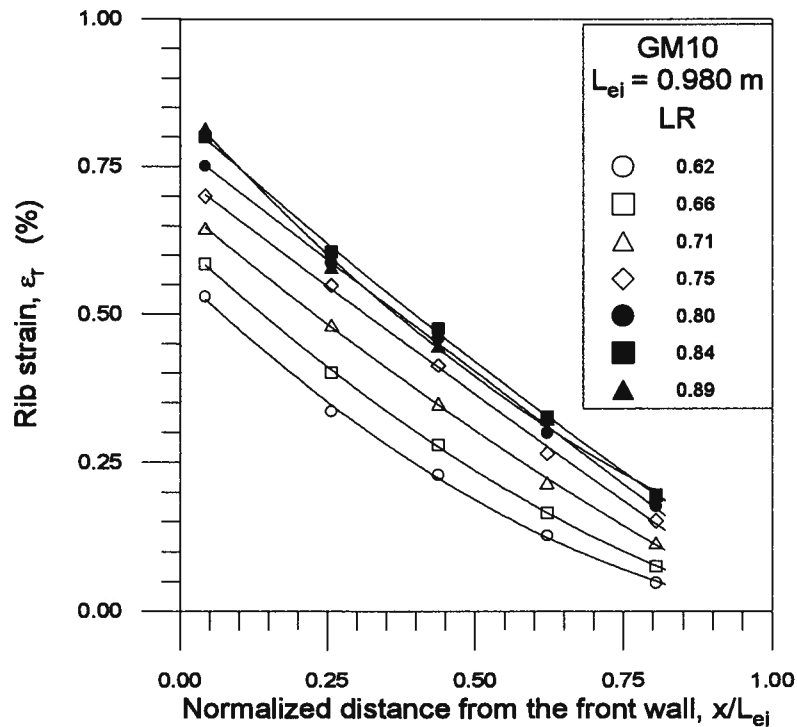


Figure 7.68: Strain profile with loading ratio at the end of the loading series for the Miragrid at $\sigma_n=10$ kPa and $f=0.01$ Hz

Chapter 7. Analysis of Test Results

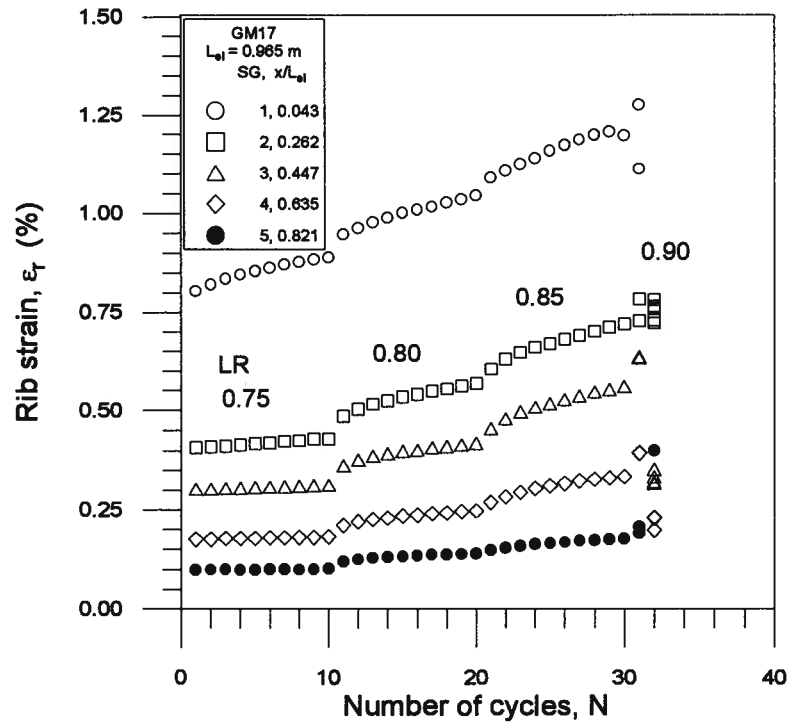


Figure 7.69: Mobilization of rib strain with number of cycles and increasing load ratio for the Miragrid at $\sigma_n=17 \text{ kPa}$ and $f=0.01 \text{ Hz}$

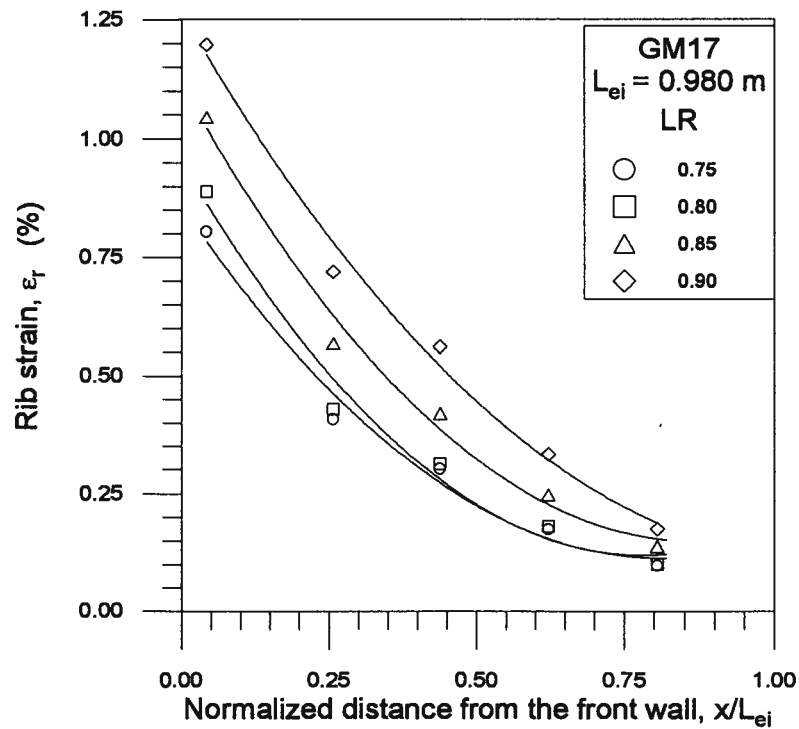


Figure 7.70: Strain profile with loading ratio at the end of the loading series for the Miragrid at $\sigma_n=17 \text{ kPa}$ and $f=0.01 \text{ Hz}$

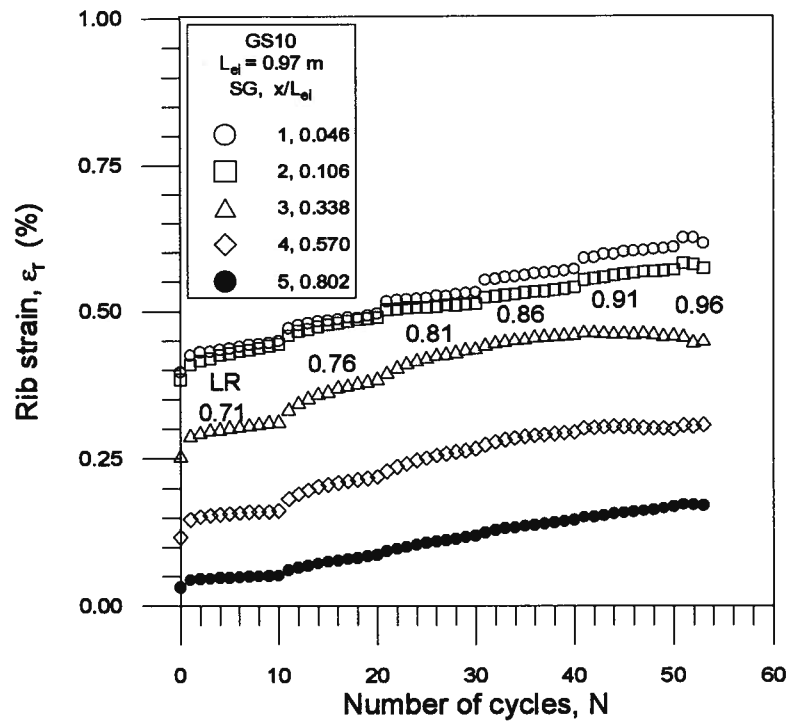


Figure 7.71: Mobilization of rib strain with number of cycles and increasing load ratio for the Stratagrid at $\sigma_n=10$ kPa and $f=0.01$ Hz

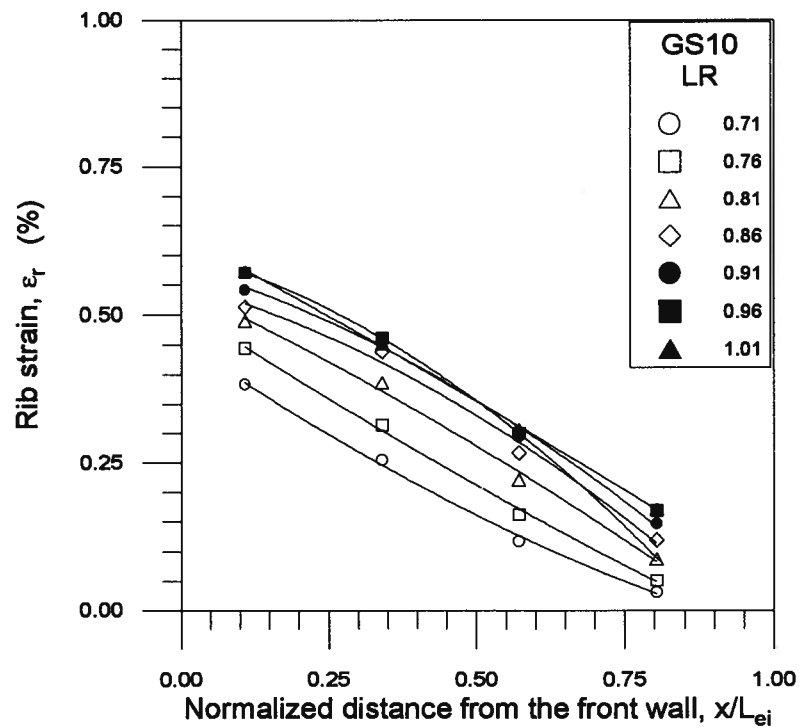


Figure 7.72: Strain profile with loading ratio at the end of the loading series for the Stratagrid at $\sigma_n=10$ kPa and $f=0.01$ Hz

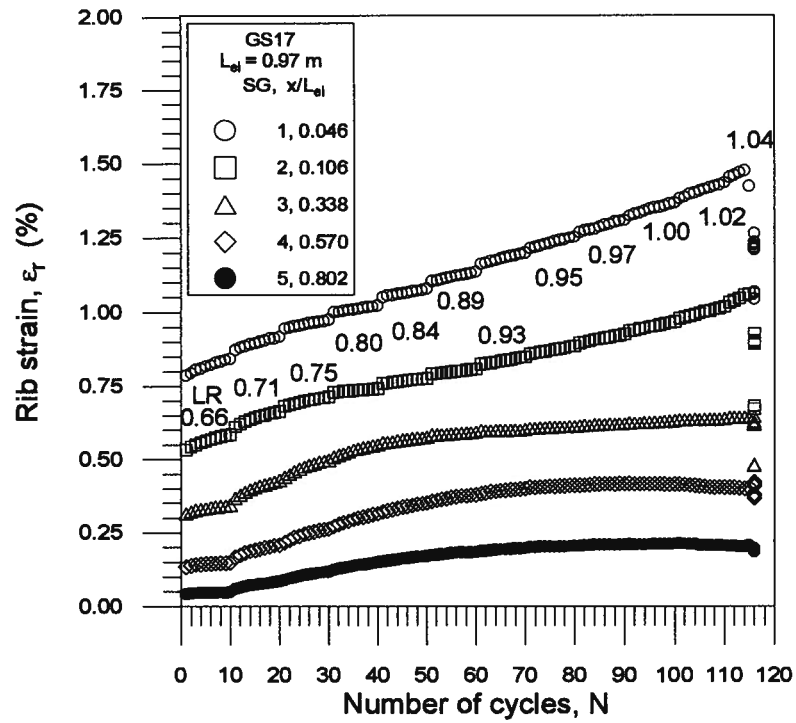


Figure 7.73: Mobilization of rib strain with number of cycles and increasing load ratio for the Stratagrid at $\sigma_n=17$ kPa and $f=0.01$ Hz

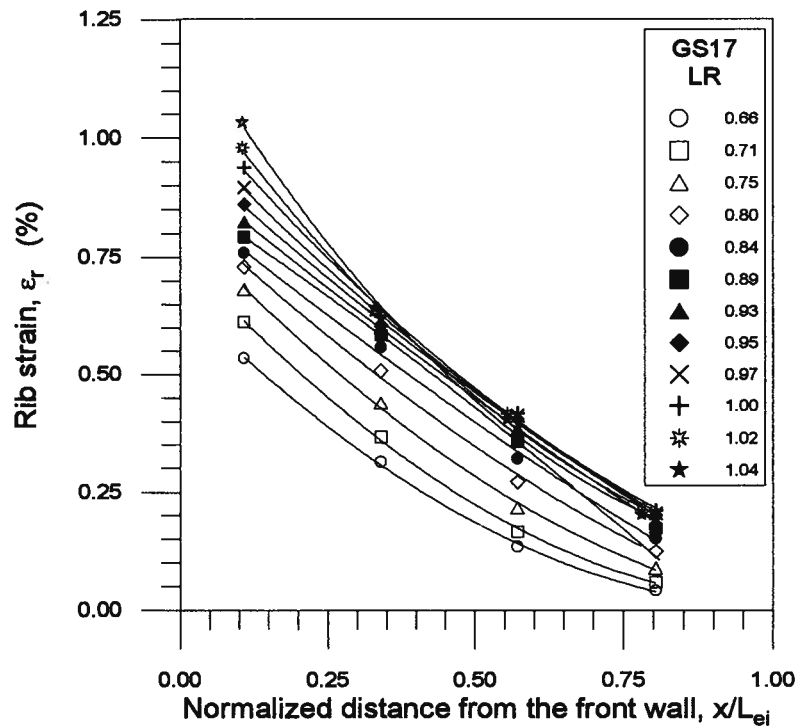


Figure 7.74: Strain profile with loading ratio at the end of the loading series for the Stratagrid at $\sigma_n=17$ kPa and $f=0.01$ Hz

Chapter 7. Analysis of Test Results

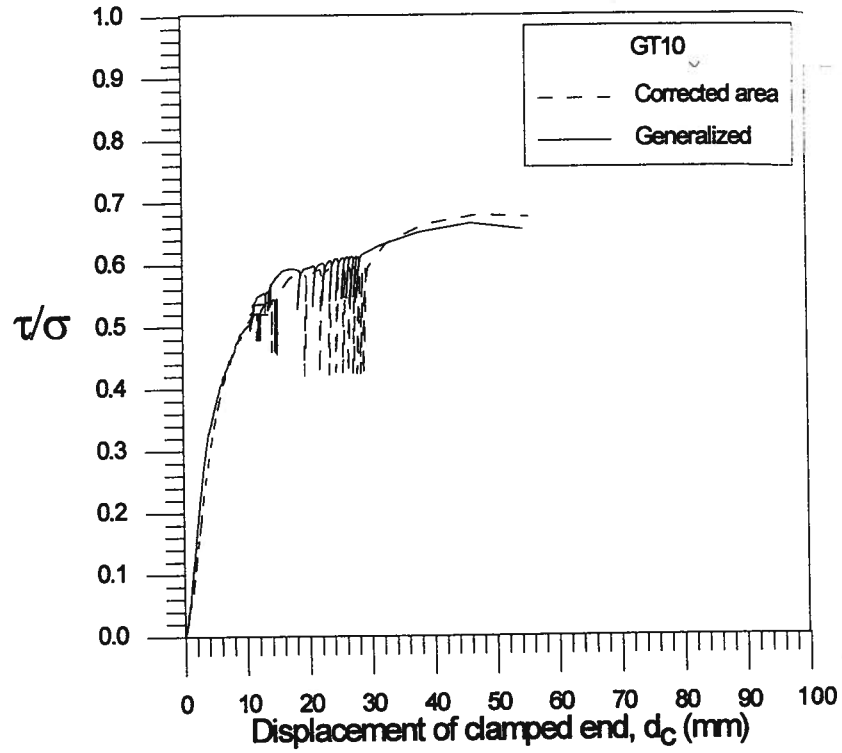


Figure 7.75: Cyclic pullout interaction factor from the generalized and corrected total area methods for the Tensar grid at $\sigma_v=10$ kPa and $f=0.01$ Hz

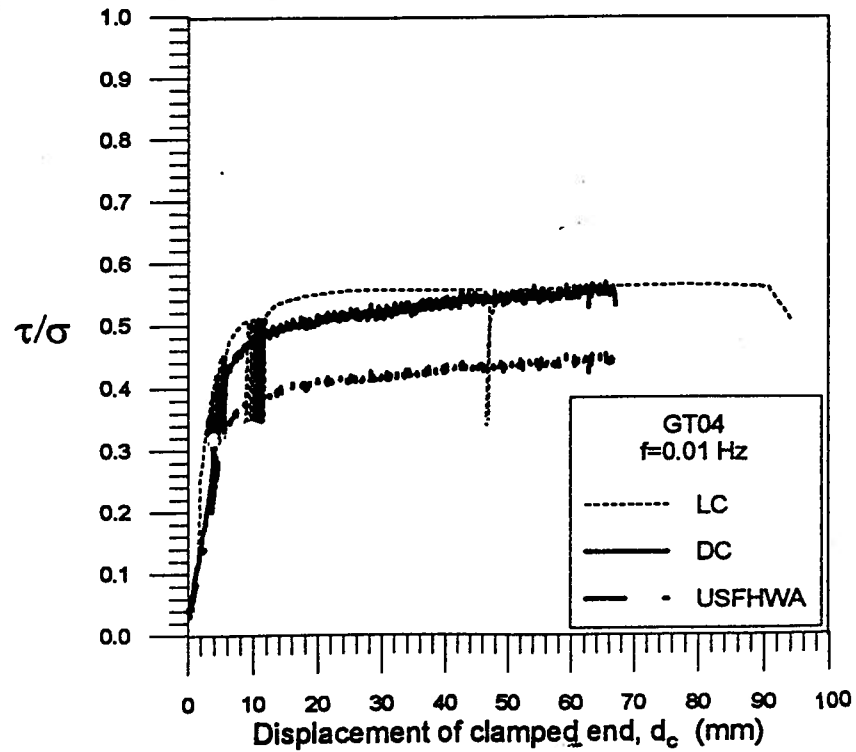


Figure 7.76: Comparison of interaction factors in the LC and DC tests for the Tensar grid at $\sigma_v=4$ kPa and $f=0.01$ Hz

Chapter 7. Analysis of Test Results

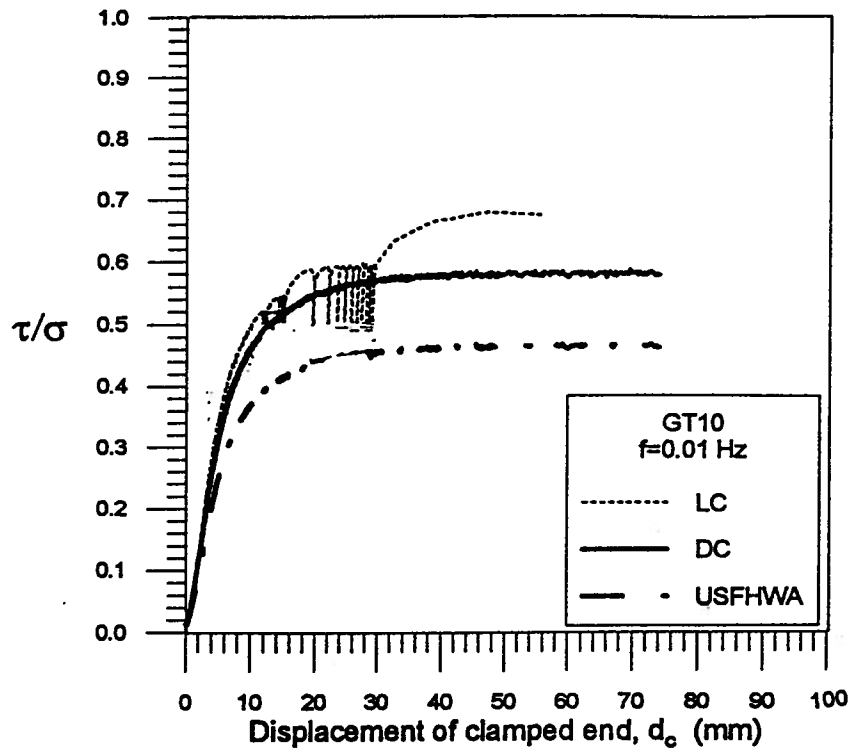


Figure 7.77: Comparison of interaction factors in LC and DC tests for the Tensar grid at $\sigma_v=10$ kPa and $f=0.01$ Hz

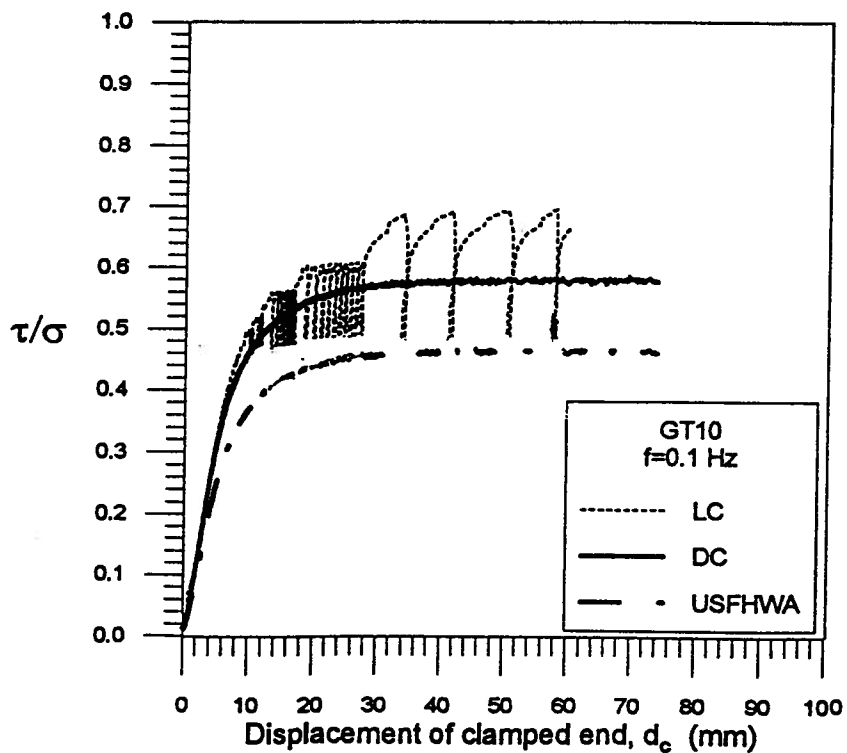


Figure 7.78: Comparison of interaction factors in the LC and DC tests for the Tensar grid at $\sigma_v=10$ kPa and $f=0.1$ Hz

Chapter 7. Analysis of Test Results

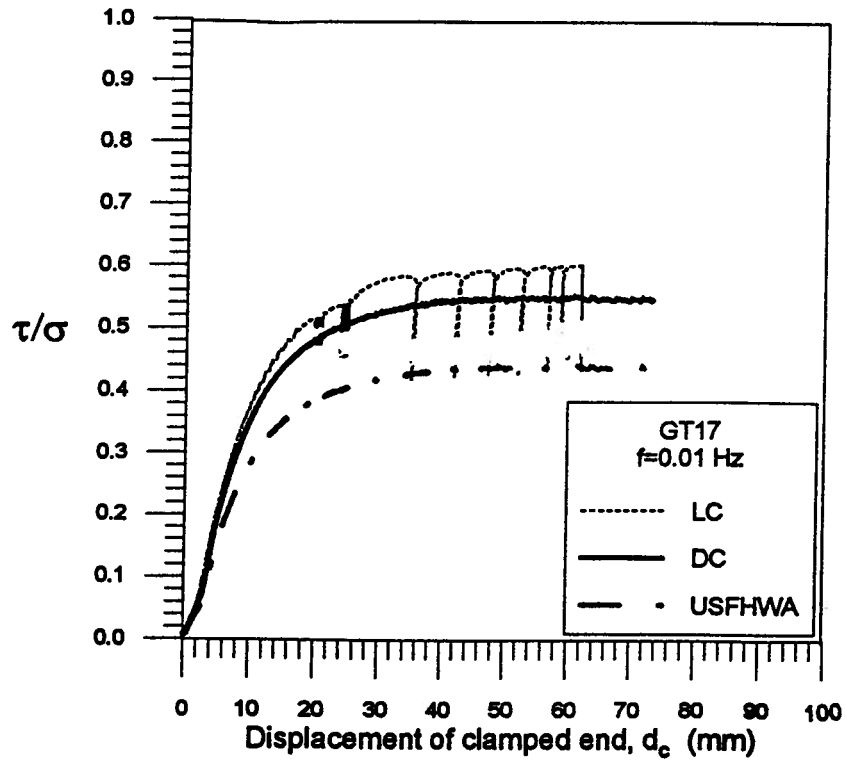


Figure 7.79: Comparison of interaction factors in the LC and DC tests for the Tensar grid at $\sigma_a=17$ kPa and $f=0.01$ Hz

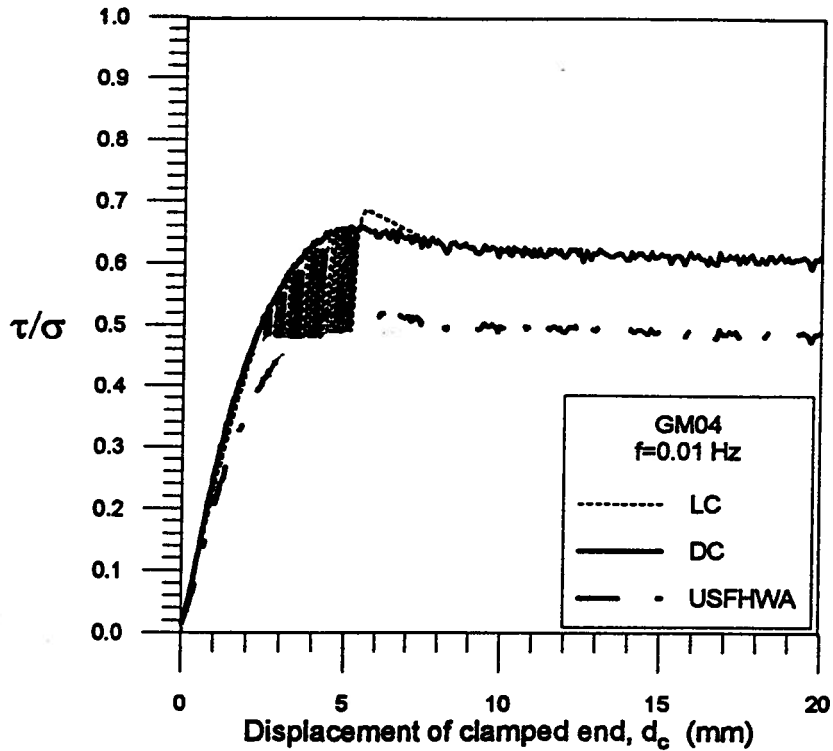


Figure 7.80: Comparison of interaction factors in the LC and DC tests for the Miragrid at $\sigma_a=4$ kPa and $f=0.01$ Hz

Chapter 7. Analysis of Test Results

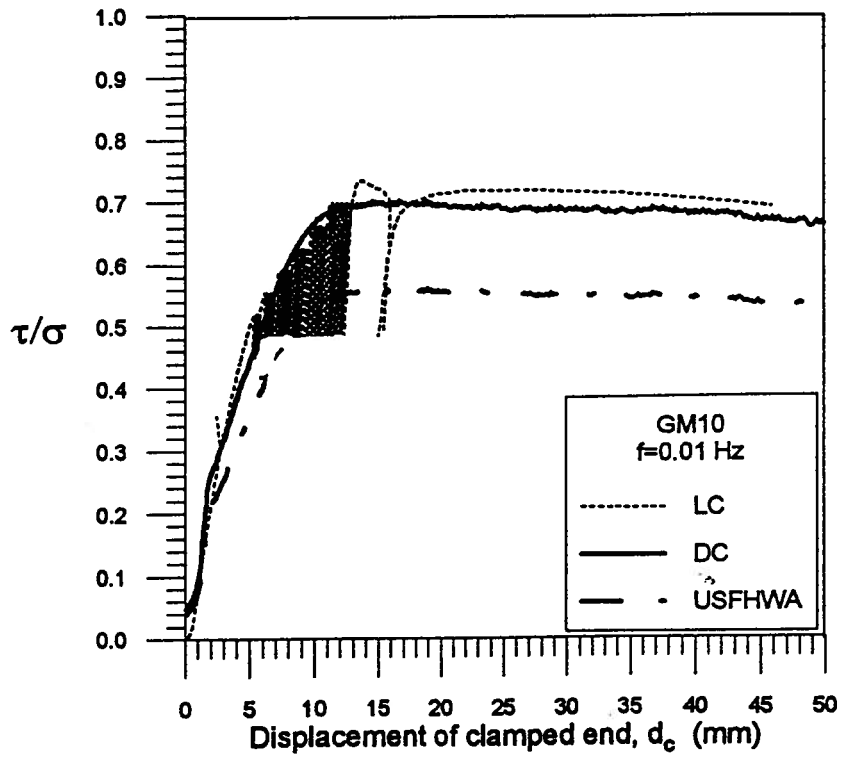


Figure 7.81: Comparison of interaction factors in the LC and DC tests for the Miragrid at $\sigma_n=10$ kPa and $f=0.01$ Hz

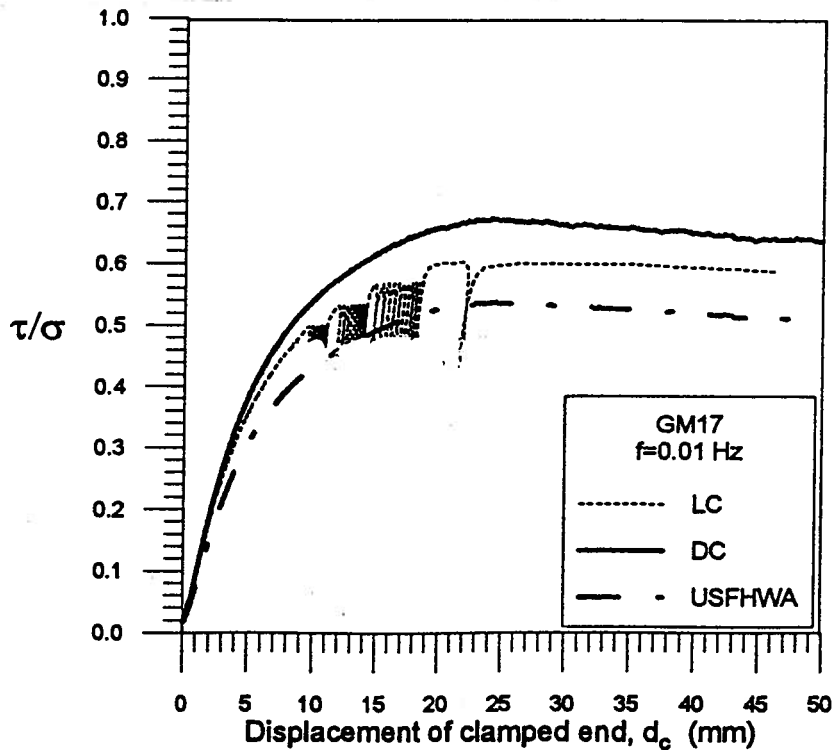


Figure 7.82: Comparison of interaction factors in the LC and DC tests for the Miragrid at $\sigma_n=17$ kPa and $f=0.01$ Hz

Chapter 7. Analysis of Test Results

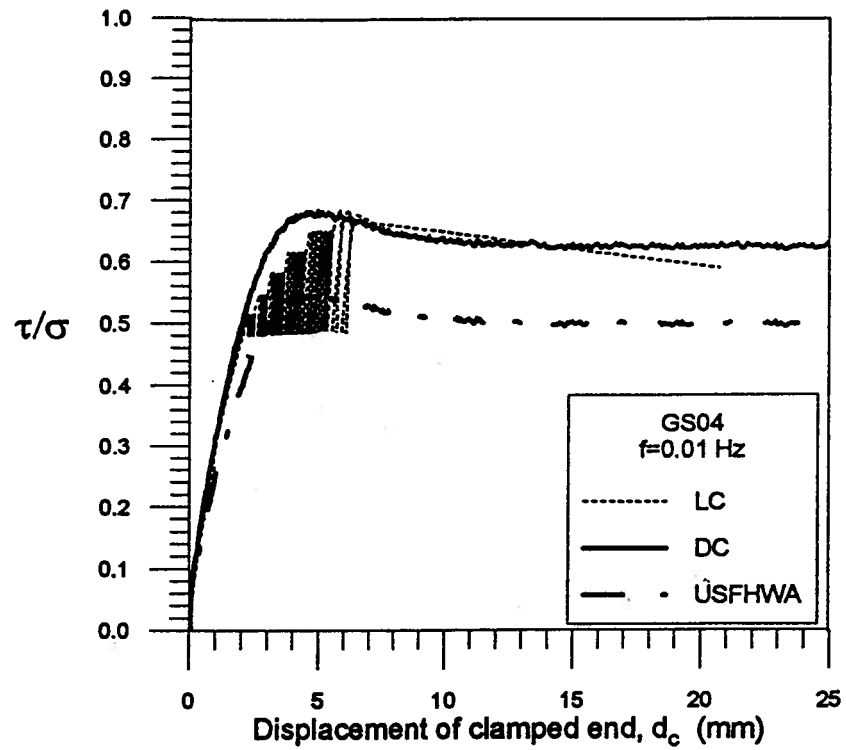


Figure 7.83: Comparison of interaction factors in the LC and DC tests for the Stratagrid at $\sigma_n=4$ kPa and $f=0.01$ Hz

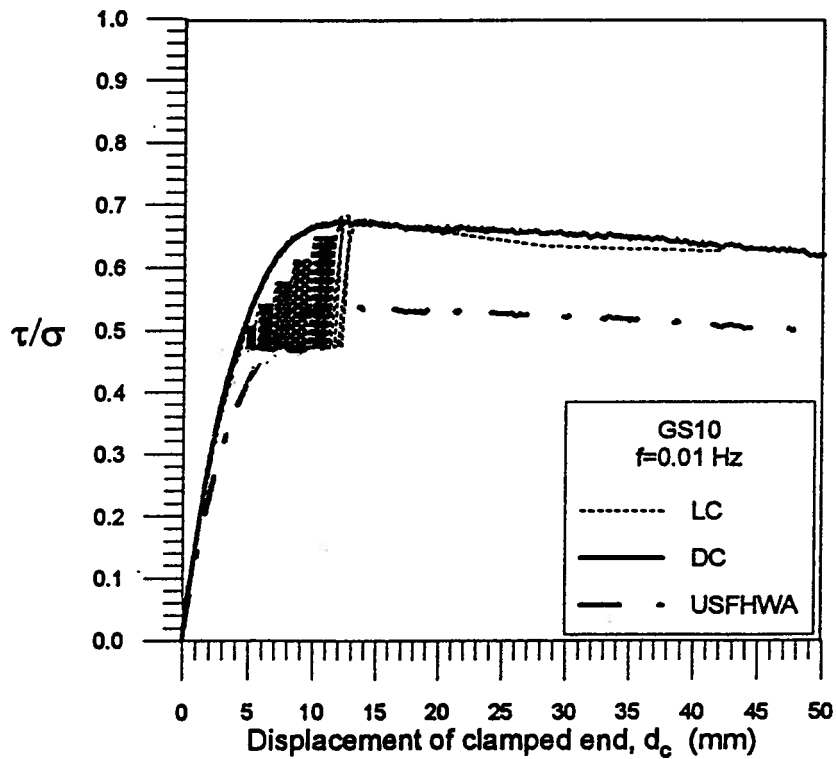


Figure 7.84: Comparison of interaction factors in the LC and DC tests for the Stratagrid at $\sigma_n=10$ kPa and $f=0.01$ Hz

Chapter 7. Analysis of Test Results

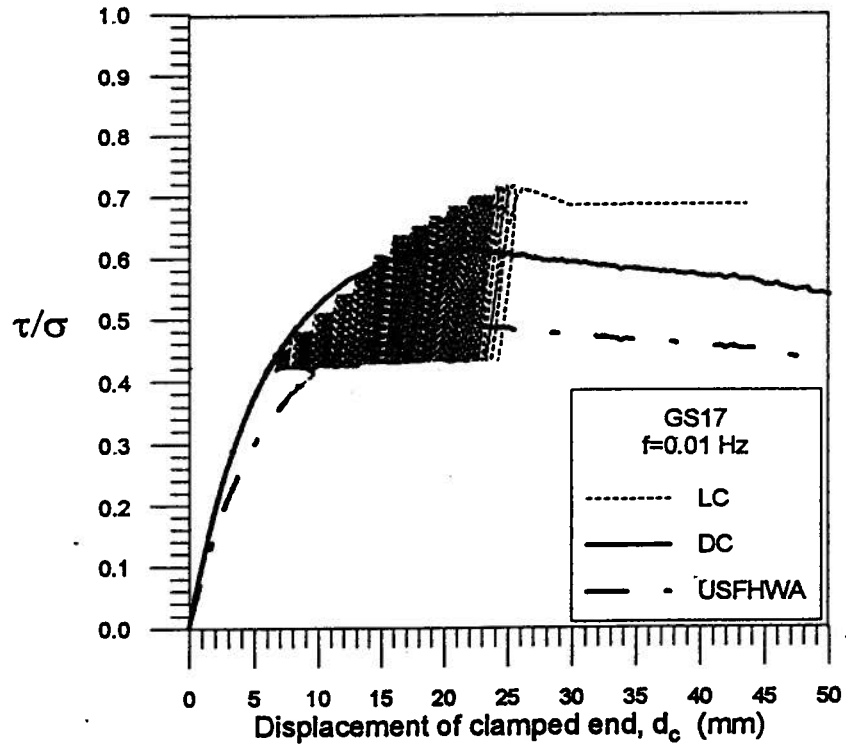


Figure 7.85: Comparison of interaction factors in the LC and DC tests for the Stratagrid at $\sigma_n=17$ kPa and $f=0.01$ Hz

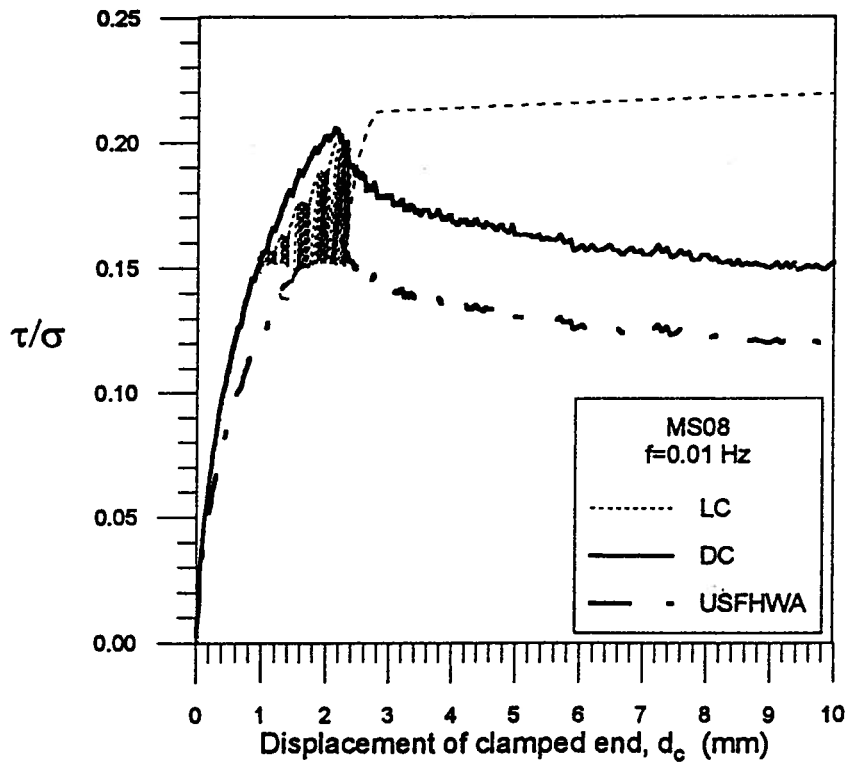


Figure 7.86: Comparison of interaction factors in the LC and DC tests for the smooth geomembrane at $\sigma_n=8$ kPa and $f=0.01$ Hz

Chapter 7. Analysis of Test Results

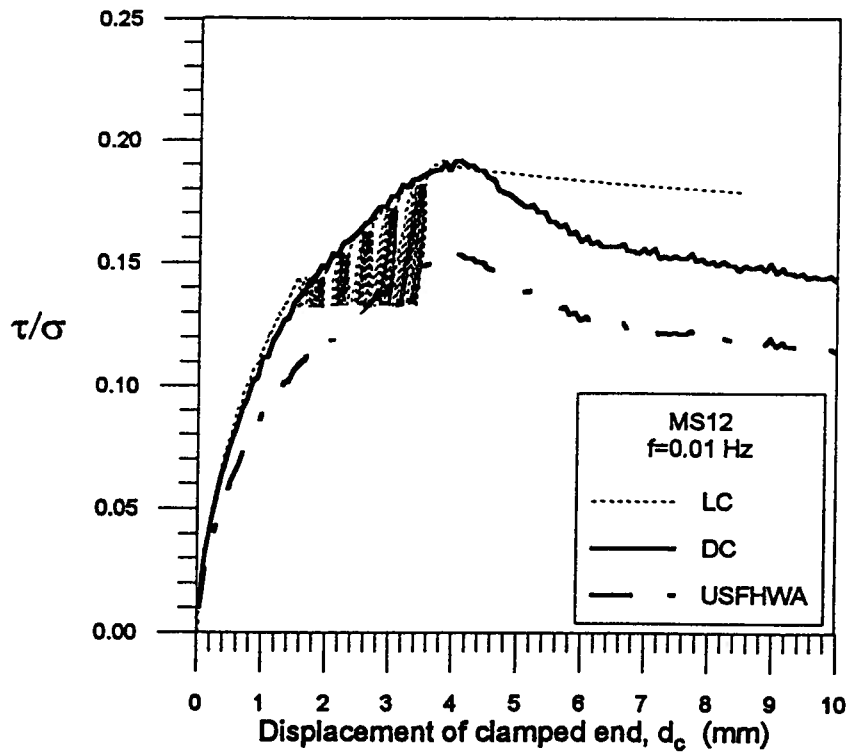


Figure 7.87: Comparison of interaction factors in the LC and DC tests for the smooth geomembrane at $\sigma_n=12$ kPa and $f=0.01$ Hz

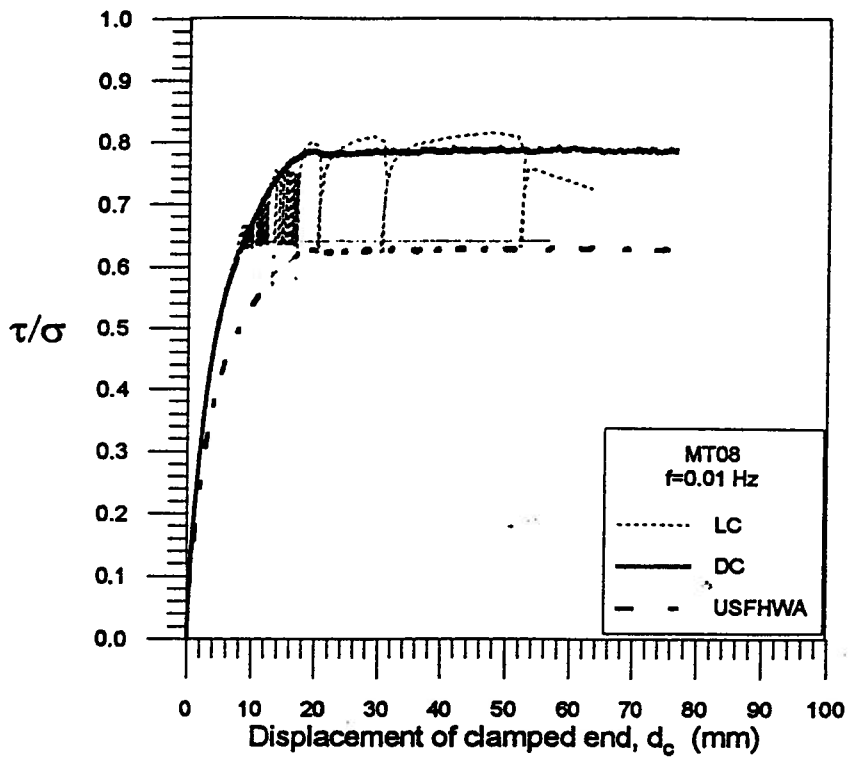


Figure 7.88: Comparison of interaction factors in the LC and DC tests for the textured geomembrane at $\sigma_n=8$ kPa and $f=0.01$ Hz

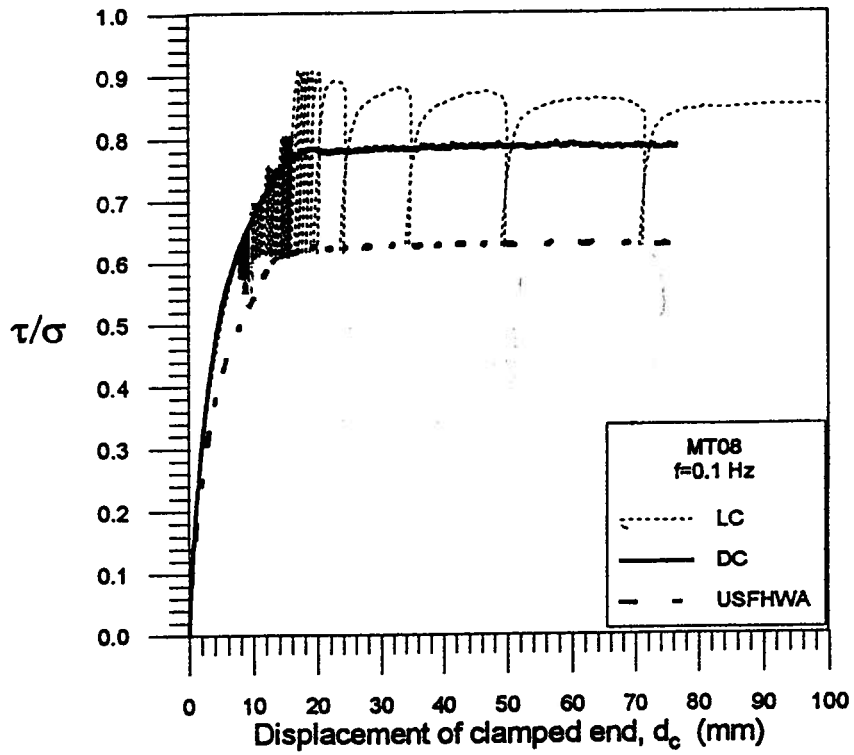


Figure 7.89: Comparison of interaction factors in the LC and DC tests for the textured geomembrane at $\sigma_v=8$ kPa and $f=0.1$ Hz

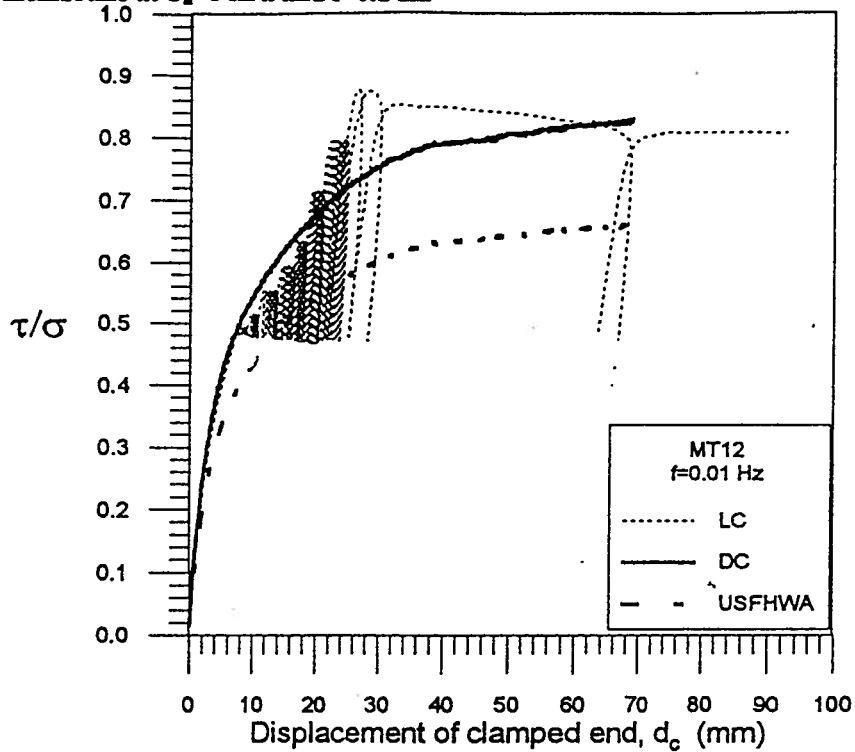


Figure 7.90: Comparison of interaction factors in the LC and DC tests for the textured geomembrane at $\sigma_v=12$ kPa and $f=0.01$ Hz

CHAPTER 8

SUMMARY AND CONCLUSIONS

8.1 Summary

The emphasis of this thesis was placed on the pullout testing of geosynthetic test specimens in monotonic and cyclic pullout modes. The intent is to better understand the interpretation of pullout test data for viscoelastic materials, and to evaluate current approaches used to characterize soil-geosynthetic interaction factors for design of anchorage details.

Specifically the objectives of the thesis were as follows:

- Design and commission a large pullout test apparatus, and associated controls to perform pullout tests under displacement-control and load-control;
- Develop a routine for cyclic loading of test specimens, taking into account the current method for monotonic loading in pullout tests;
- Comprehensively describe the development of pullout resistance from instrumentation on the test specimen and on the test apparatus;
- Establish a method of interpretation for the response of the test specimen based on measurements of pullout load, and strain along the embedded length, that accounts for the extensible behaviour of geosynthetic test specimens;
- Compare and contrast behaviour of grid and sheet specimens;
- Contrast the results of this work with the limited experimental database for laboratory testing;
- Assess experimental and theoretical interaction factors for geosynthetics;

Chapter 8. Summary and Conclusions

- Compare the behaviour in pullout testing with that for “in-service” conditions; and
- Contrast values of interaction factor for static and dynamic loading, within the context of the current approach used in design for selection of an interaction factor.

A program of experimental research was undertaken to meet these objectives. A summary of the findings is presented below that addresses the apparatus and instrumentation, the test procedure and the interpretation of the tests. In concluding, the implications for design practice are discussed and some recommendations are made for the direction of future studies.

8.2 On the Pullout Test

8.2.1 Apparatus and Instrumentation

A large pullout apparatus was designed and fabricated to accommodate a sand sample of length 130 cm, width 64 cm, and height 60 cm. Pullout tests were performed on test specimens 0.5 m wide.

Important features of the apparatus and instrumentation scheme are summarized below:

- The pullout apparatus has rigid boundaries, with exception of the top where a stress controlled boundary is used to apply normal stress to the sand sample. The front wall incorporates a slot, through which the test specimen is pulled.
- A sophisticated electro-hydraulic servo-controlled system was developed for controlling either displacement or load imposed on the pullout test specimen.

Chapter 8. Summary and Conclusions

- Instrumentation was used to measure normal stress, pullout force, displacement and strain along the length of the test specimen; and lateral stress on the front wall of the apparatus.
- A vertical array of pressure transducers on the centerline of the front wall revealed a distribution of lateral stress ($\Delta\sigma_h$) that was asymmetric about the slot. A normalised stress ratio ($\Delta\sigma_h/\tau_{av}$) is developed that is independent of specimen type and normal stress.
- A procedure for strain gauging the polymeric test specimens was adapted from Bathurst (1990): a two part epoxy coating was used on the Stratagrid and Miragrid to allow mounting of gauges on a plane surface.
- The consistency of sample preparation and test routine is evident from the reproducibility of results of tests that were repeated.

8.2.2 Materials and Test Procedure

- An air-pluviation technique was used to place the uniformly-graded, medium sand samples to relative density between 85 to 90%.
- Pullout tests were performed on geosynthetic test specimens, and the results compared with the response of a rigid, fully rough sheet. The geosynthetic test specimens comprised three types of geogrids, a smooth geomembrane and a textured geomembrane.

Chapter 8. Summary and Conclusions

- Tests were performed in one of two modes. Displacement-controlled (DC) tests were performed at a constant rate of displacement (r_d). Typically DC tests were performed at $r_d=0.5$ mm/min. No significant variation in pullout resistance was observed for $0.25 < r_d < 1.0$ mm/min. Load-controlled tests were performed at a constant rate of loading to a targeted value between 60 and 80% of the resistance measured in the corresponding DC test. Thereafter a sinusoidal variation of load was applied as a loading series comprising 10 cycles of constant amplitude and constant frequency. The amplitude of loading was increased with each series of loading.

8.2.3 Test Results and Interpretation

- Independent measurements of pullout force, and strain along the length of the geosynthetic test specimen, reveal a response that is characterized by a varying extent of progressive strain. It is important to the interpretation of a pullout test results that a distinction be made between an extensible and inextensible behaviour of the test specimen. It has been shown that the extensible and inextensible behaviour of a geosynthetic specimen is dependent on the magnitude of normal stress. This has implications for use of a particular method of interpretation to deduce a value of interaction factor.
- Progressive mobilization of pullout is described with respect to displacements characterized by three zones ($d_c > 0, d_e = 0; d_c > 0, d_c \neq d_e; d_c > 0, d_c = d_e$).

Chapter 8. Summary and Conclusions

- A review of the present state of practice for interpretation of pullout test data has indicated the total area method is applicable to an inextensible response only. Although the effective area method is better it fails to address the non-linear distribution of tensile force that may develop in the test specimen. However, both methods give a similar value when the tensile force distribution is linear, which is the case at large pullout displacement. The mobilizing process method (Ochiai et al., 1992; Juran et al., 1991) accounts for a non-linear distribution of tensile force along the specimen during pullout. A generalized method is proposed, that unifies aspects of the mobilizing process method and effective area method, and is tested against the laboratory data.
- Geogrids are seen to develop a relationship between pullout resistance and displacement that is very similar in shape to that for the textured geomembrane, but not the smooth geomembrane, with no distinct peak value of pullout resistance. The relationship between average shear stress and normal stress shows all three geogrids to be less efficient than the equivalent fully rough sheet.
- Good agreement is observed when the variation of interaction factor with displacement for the Tensar grid and Stratagrid is compared with results published by Palmeira (1987) and Farrag et al. (1993). The comparison suggests the configuration of the apparatus does not influence significantly the measured pullout resistance at relatively low values of normal stresses. Further, the relationship between interaction factor and angle of friction is seen to compare well with upper bound values reported for various studies on grid specimens.

Chapter 8. Summary and Conclusions

A conceptual model is proposed that links a load ratio to stable and unstable behaviour in cyclic pullout, and identifies a threshold load ratio above which an unstable behaviour results.

8.3 Implications for Selection of a Pullout Interaction Factor in Design

- Values of interaction factor for the three geogrids deduced from pullout testing were compared with theoretical values. In all cases values of the stress ratio (σ_v/σ_n) inferred by the laboratory pullout data exceed the default value of $\sigma_v/\sigma_n = 20$ recommended by USFHWA for use in the absence of specific test data. It would appear the USFHWA approach is conservative but not overly so.
- Comparison of the laboratory data with field data from an instrumented sloped reinforced soil wall indicate mobilized values of interaction factor in the field structure which correspond to a value mobilized in the pullout test at very small displacements, $d_c < 1$ mm. This value at small displacement is associated with very small strains, less than 0.5%, which lie within acceptable limits of existing codes of practice incorporating permissible strains.
- In design of a structure to resist dynamic loads the USFHWA approach (Christopher et al., 1990) recommends the interaction factor be taken as 80% of that used for static design. Results of the cyclic pullout tests performed in this study would suggest the interaction factor is higher than or equal to the interaction factor from corresponding displacement-controlled tests. This implies

Chapter 8. Summary and Conclusions

that using a reduced value of interaction factor for dynamic loads is inappropriate, in that it does not properly describe the mobilized response.

- A seismic event is associated with both horizontal and vertical accelerations. Vertical acceleration leads to the normal stress at the interface increasing and decreasing in a cyclic manner during the event, which may adversely influence the behaviour of a reinforced soil structure. The effect of a decrease in normal stress and simultaneous increase in horizontal thrust is to promote a pullout type of failure. Therefore, in design it would be more appropriate to use a reduced normal stress to account for the variation of imposed loading during the seismic event.

8.4 Recommendations for Future Studies

Specifications are being developed for the pullout test apparatus and a standardized test method which will govern tests performed at a constant rate of displacement. The following issues pertain to this ongoing development, and to the interpretation of pullout test data.

- To further evaluate the influence of a rigid front wall on measured pullout resistance, tests should be performed with a stress-controlled boundary on the front wall of the apparatus.
- Direct measurement of the normal stress acting at the soil-specimen interface, using pressure cells embedded in the soil sample, is desirable to assess any influence of boundary friction.

Chapter 8. Summary and Conclusions

- The mechanism of pullout resistance involved in grids will vary with particle size. Use of different soils to study the influence of particle size and soil gradation, and interlocking within the grids, is important to describe the behaviour of soils used in construction.
- Direct measurement of load at sections along the test specimen using profile-type load cells will define more accurately the shape of the tensile force distribution. In conjunction with the load measurement, measurement of strain will provide specific values for confined stress-strain properties of extensible test specimens.
- In cyclic loading, the selection of loading rate is important to obtain a comparable response in initial phase of load-controlled test. Test specimens should be loaded monotonically to a desired level before applying any series of cyclic loads, and the amplitude of loading should be selected to narrowly bound the pullout resistance established from displacement-controlled test.

BIBLIOGRAPHY

- Al-Ashou, M. O., and Hanna, T. H. (1990), "Deterioration of Reinforced Earth Elements under cyclic loading," *Performance of reinforced soil structures: Proceedings of the International Reinforced Soil Conference*, edited by A. McGown, K. Yeo and K. Z. Andrawes, pp. 303-307, published by the British Geotechnical Society, 1990.
- ASTM D4253-93. Standard Test Methods for Maximum Index Density and Unit Weight of Soils Using a Vibratory Table. *1993 Annual book of ASTM Standards*. Vol. 04.08, pp. 661-673.
- ASTM D4254-91. Standard Test Method for Minimum Index Density and Unit Weight of Soils and Calculation of Relative Density. *1993 Annual book of ASTM Standards*. Vol. 04.08, pp. 674-681.
- ASTM D5321-92. Standard Test Method for Determining the Coefficient of Soil and Geosynthetic or Geosynthetic and Geosynthetic Friction by the Direct Shear Method. *1993 Annual book of ASTM Standards*. Vol. 04.08, pp. 1380-1384.
- Bathurst, R. J. (1990), "Instrumentation of Geogrid Reinforced Soil Walls," *Private Communication*.
- Bathurst, R. J. (1991), "Case Study of a Monitored Propped Panel Wall," *Proceedings of the International Symposium on Geosynthetic Reinforced Soil Retaining Walls, held at Denver, Colorado, 8-9 August 1991*, edited by J. T. H. Wu, published by A. A. Balkema, Rotterdam, 1992.
- Bathurst, R. J., and Simac, M. R. (1993), "Two Computer Programs for the Design and Analysis of Geosynthetic-Reinforced Soil-Retaining Walls," *Geotextiles and Geomembranes*, Elsevier, Vol. 12, pp. 381-396.
- Bauer, G. E., Halim A. O. A., and Shang, Q. (1991), "Large Scale Pullout Tests: Assessment of Procedure and Results," *Proceedings of the Geosynthetics '91*, Atlanta, Georgia, Industrial Fabrics Association International, February 1991, Vol. 2, pp. 615-627.
- Bergado, D. T., Bukkanasuta, A., and Balasubramaniam, A. S. (1987), "Laboratory Pull Out Tests Using Bamboo and Polymer Geogrids Including a Case Study," *Geotextiles and Geomembranes*, Elsevier, Vol. 5, No. 3, pp.153-189.
- Bergado, D. T., Lo, K. H., Chai, J. C., Shivashankar, R., Alfaro, M. C., and Anderson, L. R. (1992), "Pullout Tests Using Steel Grid Reinforcements with Low-quality Backfill," *Journal of Geotechnical Engineering*, ASCE, Vol. 118, No. 7, pp. 1047-1063.

Bibliography

- Bolton, M. D. (1990), "Reinforced Soil: Laboratory Testing and Modelling," *Performance of Reinforced Soil Structures: Proceedings of the International Reinforced Soil Conference*, edited by A. McGown, K. Yeo and K. Z. Andrawes, pp. 287-298, published by the British Geotechnical Society, 1990.
- Bolton, M. D. (1986), "The Strength and Dilatancy of Sands," *Geotechnique*, Vol. 36, No.1, pp. 65-78
- Bonaparte, R., Schmertmann, G. R., and Williams, N. D. (1986), "Seismic Design of Slopes Reinforced with Geogrids and Geotextiles," *Proceedings of the 3rd International Conference on Geotextiles*, Vienna, Austria, International Geotextile Society, Vol. 1, pp. 273-278.
- Bonaparte, R., Holtz, R. D., and Giroud, J. P. (1987), "Soil Reinforcement Design Using Geotextiles and Geogrids," *Geotextile Testing and the Design Engineer, ASTM STP 952*, ed. J. E. Fluet, Jr. American Society for Testing and Materials, Philadelphia, PA, pp. 69-116.
- Bonczkiewicz, C., Christopher, B. R., and Atmazidis, D. K. (1986), "Evaluation of Soil-Reinforcement Interaction by Large-Scale Pull-out Tests," *Transportation Research Record 1188*, Washington, D.C., pp. 1-18.
- Bonczkiewicz, C., Christopher, B. R., and Simac M. (1991), "Load Distribution in Geogrids With Low Junction Efficiency," *Proceedings of the Geosynthetics '91*, Atlanta, Georgia, Industrial Fabrics Association International, February 1991, Vol. 2, pp. 643-652.
- Brown I. E. W., and Rochester, T. A., (1979), "Reinforced Earth - Technical Guidance Provided by the Department of Transport, England," *Proceedings of the Internatinal Conference on Soil Reinforcement*, Paris, Vol. 2, pp. 423-430.
- C.G.S., (1992). Canadian Foundation Engineering Manual. Third edition. Canadian Geotechnical Society, Technical Committee on Foundations. BiTech Publishers Ltd, Richmond, B.C., 512p.
- Chalaturnyk, R. J., Scott, J. D., Chan, D. H. K., and Richards, E. A. (1990). "Stresses and Deformations in a Reinforced Soil Slope." *Canadian Geotechnical Journal*, Vol. 27, pp. 224-234 .
- Chan, D. H., Yi, C. T., and Scott, J. D. (1993), "An Interpretation of the Pull-out Test, " *Proceedings of the '93 Geosynthetics Conference*, Vancouver, Canada, Industrial Fabrics Association International, April 93, Vol. 2, pp. 593-604.

Bibliography

- Chang, J. C., Hannon, J. B., and Forsyth, R. A. (1977), "Pull-out Resistance and Interaction of Earthwork Reinforcement and Soil," *Transportation Research Record 640*, Washington, D.C., pp. 1-7.
- Christopher, B. R., Gill, S. A., Giroud, J. P., Juran, I., Mitchell, J. K., Schlosser, F. and Dunnicliff, J., (1990), "Design and Construction Guidelines for Reinforced Soil Structures - Volume I," and "Summary of Research - Volume II," *Report No. FHWA-RD-89-043*, Federal Highway Administration, U.S Department of Transportation.
- Claybourn, A. F., and Wu, J. T. H. (1993), "Geosynthetic-Reinforced Soil Wall Design," *Geotextiles and Geomembranes*, Elsevier, Vol. 12, 707-724.
- Collin, J. G., Chouery-Curtis, V. E., and Berg, R. R. (1992), "Field observations of reinforced soil structures under seismic loading." *Proceedings of the International Geotechnical Symposium on Earth Reinforcement Practice*, edited by Ochiai, Hayashi & Otani, Balkema, Rotterdam, pp. 223-228.
- Costalonga M. A. R. (1988), "Geogrid Pull-out Tests in Clay," *The University of Alberta, thesis submitted in partial fulfillment for the degree of M.Sc.*
- Cowell, M. J., and Sprague, C. J. (1993), "Comparison of Pull-out Performance of Geogrids and Geotextiles," *Proceedings of the Geosynthetics '93*, Vancouver, Canada, Industrial Fabrics Association International, April 93, Vol. 2, pp. 579-591.
- Deutsch Jr. W. L. (1993), "Strain Compatibility Considerations and Tensioning Analysis for Geosynthetic Lining Systems," *Proceedings of the Geosynthetics '93*, Vancouver, Canada, Industrial Fabrics Association International, April 93, Vol 2, 703-718.
- Eigenbrod, K. D., and Locker, J. G. (1987), "Determination of Friction Values for the Design of Side Slopes Lined or Protected With Geosynthetics," *Canadian Geotechnical Journal*, Vol. 24, pp. 509-519.
- Eigenbrod, K. D., Burak, J. P., and Locker, J. G. (1990), "Differential Shear Movements at Soil-Geotextile Interfaces," *Canadian Geotechnical Journal*, Vol. 27, pp.520-526.
- Fannin, R. J., and Hermann, S. (1990), "Performance data for a Sloped Reinforced Soil Wall," *Canadian Geotechnical Journal*, Vol. 27, pp. 676-686.
- Fannin, R. J. (1990), "Geosynthetics for Containment of Special Waste," *Proceedings of the 5th Annual Symposium: Geotechnical Aspects of Contaminated sites*, Vancouver, The Vancouver Geotechnical Society, May 25th 1990.

Bibliography

- Fannin, R. J., and Raju, D. M. (1991), "Pullout Resistance of Geosynthetics," Proceedings 44th Canadian Geotechnical Conference, Calgary, Vol. 2, October, 1991.
- Fannin, R. J., and Raju, D. M. (1993), "Large Scale Pull-Out Test Results on Geosynthetics," *Proceedings of the Geosynthetics '93*, Vancouver, Industrial Fabrics Association International, March 1993, Vol. 2, pp. 633-643.
- Fannin, R. J., and Raju, D. M. (1993), "On the Pullout Resistance of Geosynthetics," *Canadian Geotechnical Journal*, Vol. 30, June 1993.
- Fannin, R. J., Hermann, S., Vaslestad, J., and Raju, D. M. (1994), "Coefficients of Interface Bond in Reinforced Soil Structures." *Proceedings of the 13th International Conference on Soil Mechanics and Foundation Engineering*, New Delhi, India.
- Farrag, K. H., Acar, Y. A., and Juran, I. (1993), "Pullout Testing of Geogrids," *Geotextiles and Geomembranes*, Elsevier, Vol. 12, pp. 132-158.
- Hanna, T. H., Sivapalan, E. and Senturk, A. (1978), "The Behaviour of Dead Anchors Subjected to Repeated and Alternating loads," *Ground Engineering*, Vol. 11, No. 3, pp. 28-34.
- Hanna, T. H., and Touhamia, M., (1991), "Comparative Behaviour of Metal and Tensar Geogrid Strips Under Static and Repeated Loading, " *Proceedings of the Geosynthetics '91*, Atlanta, Georgia, Industrial Fabrics Association International, February 1991, Vol. 2, pp. 575-585.
- Handel, E., Schweiger, H. F., and Yeo, K. C. (1990), "A Simple Thin-layer Element to Model Soil-Geotextile Interaction, " *Performance of reinforced soil structures: Proceedings of the International Reinforced Soil Conference*, edited by Alan McGown, Khen Yeo and K. Z. Andrawes, pp. 317-321, published by the British Geotechnical Society, 1990.
- Hryciw, R. D. and Irsyam, M. (1993), "Behaviour of Sand Particles Around Rigid Ribbed Inclusions During Shear," *Soils and Foundations*, Vol. 33, No. 3, pp. 1-13.
- Jewell, R. A., Milligan, G. W. E., Sarsby, R. W. and Dubois, D. D. (1984), "Interaction Between Soil and Geogrids," *Proceedings from the Symposium on Polymer Grid reinforcement in civil engineering*, pp. 18-30, London, England, Thomas Telford.
- Jewell, R. A. (1985), "Material Properties for the Design of Geotextile Reinforced Slopes," *Geotextiles and Geomembranes*, Elsevier, Vol. 4, No. 2, pp. 83-109.
- Jewell, R. A., and Wroth, C. P. (1987), "Direct Shear Tests on Reinforced Sand," *Geotechnique*, Vol. 37, No.1, pp. 53-68.

Bibliography

- Jewell, R. A., and Greenwood, J. H. (1988), "Long Term Strength and Safety in Steep Soil Slopes Reinforced by Polymer Materials," *Geotextiles and Geomembranes*, Elsevier, Vol. 7, No. 1, pp. 81-118.
- Jewell, R. A. (1990), "Reinforcement Bond Capacity," *Technical note, Geotechnique*, Vol. 40, No.3, 513-518.
- Johnston, R. S. (1985), "Pullout Testing of Tensar Geogrids," *University of California at Davis, California, thesis submitted in partial fulfillment of M.S degree.*
- Juran, I., and Chen, C. L. (1987), "Soil-geotextile Pullout Interaction Properties: Testing and Interpretation," *Transportation Research Record 1188*, Washington, D.C., pp. 37-47.
- Juran, I., Knochenmus, G., Acar, Y. B., and Arman, A. (1988), "Pull-out Response of Geotextiles and Geogrids (Synthesis of Available Experimental Data)," *Proceedings of the Symposium on Geosynthetics for Soil Improvement, Tennessee, May 1988; (edited by R. D. Holtz.)*, ASCE, pp. 92-111.
- Juran, I., Ider, H. M. and Farrag, K. H. (1990), "Strain Compatibility Analysis for Geosynthetics Reinforced Soil Walls," *Journal of Geotechnical Engineering*, ASCE, Vol. 116, No. 2, pp. 312-329.
- Juran, I., Farrag, K. H., and Richmond, L. (1991), "Short and Long Term Performance of Polymeric Geogrids," *Proceedings of the Geosynthetics '91*, Industrial Fabrics Association International, Atlanta, Georgia, February 1991, Vol. 2, pp. 587-599.
- Kharchafi, M. and Dysli, M. (1993), "Study of Soil-Geotextile Interaction by an X-Ray Method," *Geotextiles and Geomembranes*, Elsevier, Vol. 12, pp. 307-325.
- Koerner, R. M., Hsuan, Y., and Lord Jr., A. E. (1993), "Remaining Technical Barriers to Obtaining General Acceptance of Geosynthetics," *Geotextiles and Geomembranes*, Elsevier, Vol. 12, pp. 1-52.
- Kutara, K., Aoyama, N., Yasunaga, H., and Kato, T. (1988), "Long-term Pull-out Tests of Polymer grids in Sand," *International Geotechnical Symposium on Theory and Practice of Earth Reinforcement*, Fukoka, Japan, 5-7 October, Balkema, Rotterdam, pp. 117-122.
- Lentz, R. W., and Pyatt, J. N. (1987), "Pull-out Resistance of Geogrids in Sand," *Transportation Research Record 1188*, Washington, D.C., pp. 48-55.

Bibliography

- Leschchinsky, D., and Perry, E. B. (1987), "A Design Procedure for Geotextile-Reinforced walls," *Proceedings of the Geosynthetics '87*, New Orleans, Industrial Fabrics Association International, Vol. 1, pp. 95-107.
- Martin, J. P., Koerner, R. M., and Whitty, J. E. (1984), "Experimental Friction Evaluation of Slippage Between Geomembranes, Geotextiles and Soils," *International Conference on Geomembranes*, Denver, U.S.A. pp. 191-196.
- McGown, A., Andrawes, K. Z., and Al Hasani, M. M. (1978), "Effect of Inclusion Properties on the Behaviour of Sands," *Geotechnique*, Vol. 28, No. 3, pp. 327-346.
- McGown, A., Andrawes, K. Z., Yeo, K. C., and Dubois, D. (1984) "The Load-Strain-Time behaviour of Tensar Geogrids," *Proceedings from the Symposium on Polymer Grid reinforcement in civil engineering*, London, England, Thomas Telford.
- McGown, A., Yeo, K. C., and Yogarajah, I. (1990). "Identification of a Dynamic Interlock Mechanism," *Performance of reinforced soil structures: Proceedings of the International Reinforced Soil Conference*, edited by A. McGown, K. Yeo and K. Z. Andrawes, published by the British Geotechnical Society, 1990.
- McGown, A., Yogarajah, I., and Yeo, K. C. (1992), "The instrumentation and measurement performance of synthetic polymers in reinforced soil structures," *Proceedings of the International Geotechnical Symposium on Earth Reinforcement Practice*, edited by Ochiai, Hayashi and Otani, Balkema, Rotterdam, pp. 115-120.
- Milligan, G. W. E., and Palmeira, E. P. (1987), "Prediction of Bond between Soil and Reinforcement," *Prediction and Performance in Geotechnical Engineering*, Calgary, June 1987, pp. 147-153.
- Mitchell R. A., and Mitchell J. K. (1992), "Stability Analysis of Waste Landfills," *Proc. ASCE Specialty Conference on Stability and Performance of Slopes and Embankments-II, Geotechnical Special Publication*, No.31, edited by R. B. Seed and R. W. Boulanger, pp. 1152-1187.
- Murray, R. T., and Bolden, J. B. (1979), "Reinforced Earth Wall Constructed with Cohesive Fill," *Proceedings of the 3rd International Conference on Geotextiles*, Vienna, International Geotextile Society, Vol. 3, pp. 701-706.
- Murray, R. T., Carder, D. R., and Krawczyk, J. V. (1980), "Pullout Tests on Reinforcement Embedded in Uniformly Graded Sand Subject to Vibration," *Proceedings of the 7th European Conference on Soil Mechanics and Foundation Engineering*, Brighton, Vol. 3, pp. 115-120.

Bibliography

- Negussey, D., Wijewickreme, W. K. D., and Vaid, Y. P., (1989), "Geomembrane Interface Friction," *Canadian Geotechnical Journal*, Vol. 26, pp. 165-169.
- Nimmegern, M., and Bush, D. (1991), "The Effect of Repeated Traffic Loading on Geosynthetic Reinforcement Anchorage Resistance," *Proceedings of the Geosynthetics '91*, Atlanta, Georgia, Industrial Fabrics Association International, Vol. 2, pp. 665-672.
- Ochiai, H., Hayashi, S., Otani, J., Umezaki, T., and Ogisako, E. (1988), "Evaluation of Pull-Out Resistance of Geogrid Reinforced Soils," *Proceedings of the International Geotechnical Symposium on Theory and Practice of Earth Reinforcement*, Kyushu, Balkema, Rotterdam, pp. 577-582.
- Ochiai, H., Hayashi, S., Otani, J., and Hirai, T. (1992), "Evaluation of pull-out resistance of geogrid reinforced soils," *Proceedings of the International Geotechnical Symposium on Earth Reinforcement Practice*, edited by Ochiai, Hayashi and Otani, Balkema, Rotterdam, pp. 141-146.
- O'Rourke, T. D., Druschel, S. J., and Netravali, A. N. (1990), "Shear Strength Characteristics of Sand-Polymer Interfaces," *Journal of Geotechnical Engineering*, ASCE, Vol. 116, No. 3, pp. 451-469.
- Palmeira, E. M. (1987), "The Study of Soil-Reinforcement Interaction by means of Large Scale Laboratory Tests," *University of Oxford, thesis submitted in partial fulfillment for the Ph.D. degree.*
- Palmeira, E. M., and Milligan, G. W. E. (1989), "Scale and Other Factors Affecting the Results of Pull-out Tests of Grids Buried in Sand," *Geotechnique*, Vol. 39, No. 3, pp. 511-524.
- Raju, D. M. (1991), "Large Scale Pullout Testing of Geosynthetics," *The University of British Columbia, thesis submitted in partial fulfilment of requirements for M.A.Sc degree.*
- Richardson, G. N., and Lee, K. L. (1975), "Seismic Design of Reinforced Earth Walls," *Journal of Geotechnical Engineering*, ASCE, Vol. 101, No. GT2, pp. 167-187.
- Richardson, G. N., Feger, D., Fong, A., and Lee, K. (1977), "Seismic Testing of Reinforced Earth Walls," *Journal of Geotechnical Engineering Division*, ASCE, Vol. 103, GT11, pp. 1-17.
- Richards Jr. R., and Elms, D. G. (1979), "Seismic Behaviour of Gravity Retaining Walls," *Journal of Geotechnical Engineering*, ASCE, Vol. 105, No.4, pp. 449-464.

Bibliography

- Richards Jr. R., and Elms, D. G. (1992), "Seismic Passive Resistance of Tied-back Walls," *Journal of Geotechnical Engineering*, ASCE Vol.118. No. 7, pp. 996-1011.
- Rinne, N. (1989), "Evaluation of Interface Friction Between Cohesionless Soil and Common Construction Materials," *The University of British Columbia, thesis submitted in partial fulfilment of requirements for M.A.Sc degree.*
- Schlosser, F., (1978), "History, Current and Future Developments of Reinforced Earth," *Proceedings of the Symposium on Soil Reinforcing and Stabilising Techniques*, N.S.W. Institute of Technology, pp. 5-28.
- Schmertmann, G. R., Chourey-curtis, V. E., Johnson, R. D., and Bonaparte, R. (1987), "Design charts for geogrid-reinforced soil slopes," *Proceedings of the Geosynthetics '87*, New Orleans, Industrial Fabrics Association International, Vol. 1, pp. 108-120.
- Schneider, H. R., and Holtz, R. D. (1986), "Design of Slopes Reinforced with Geotextiles and Geogrids," *Geotextiles and Geomembranes*, Elsevier, Vol. 4, pp. 29-51.
- Seed, R. B., Mitchell, J. K., and Seed, H. B. (1990), "Kettleman Hills Waste Landfill Slope Failure. II: Stability Analyses," *Journal of Geotechnical Engineering*, ASCE, Vol. 116, No.4, pp. 686-693.
- Segrestin, P., and Bastick, M. (1988), "Seismic design of Reinforced Earth retaining walls-The contribution of finite element analysis," *Proceedings of the International Geotechnical Symposium on Theory and Practice of Earth Reinforcement*, Kyushu, Balkema, Rotterdam, pp. 577-582.
- Sluimer, G., and Risseeuw, P. (1982), "A Strain Gauge Technique for Measuring Deformations in Geotextiles," *Proceedings of the 2nd International Conference on Geotextiles*, Las Vegas, U.S.A, International Geotextile Society, Vol. 3, pp. 835-838.
- Sommers and Wolfe, (1984), "Earthquake Induced Responses of Model Retaining Walls," *Proceedings of the 8th World Conference on Earthquake Engineering*, San Francisco, Vol. 3, pp. 517-524.
- Srinivasa Murthy, B. R., Sridharan, A., and Bindumadhava. (1993), "Evaluation of Interfacial Frictional Resistance," *Geotextiles and Geomembranes*, Elsevier, Vol. 12, pp. 235-253.
- Sweeney, B. P., and Clough, G. W. (1990), "Design of a Large Calibration Chamber," *Geotechnical Testing Journal*, ASTM, Vol. 13, No.1, pp. 36-44.

Bibliography

- Swinianski, J., and Sawicki, A. (1991), "A Model of Soil-Pile Interaction Owing to Cyclic Loading." *Canadian Geotechnical Journal*, Vol. 28, pp. 11-19.
- Takasumi, D. L., Green, K. R., and Holtz, R. D. (1991), "Soil-Geosynthetic Interface Strength Characteristics: A Review of State-of-the Art Testing Procedures," *Proceedings of the Geosynthetics '91*, Atlanta, Georgia, Industrial Fabrics Association International, February 1991, Vol. 1, pp. 87-100.
- Turner, J. P., and Kulhawy, F. H. (1990), "Drained Uplift Capacity of Drilled Shafts Under Repeated Axial Loading," *Journal of the Geotechnical Engineering*, ASCE, Vol. 116, No. 3, pp. 470-491.
- Udwari, J., and Kittridge, J. (1986), "Designing of Double Lined Impoundments-Lessons Learned," *Proceedings of the 3rd International Conference on Geotextiles*, Vienna, Austria, International Geotextile Society, Vol. 3, pp. 929-934.
- UK Department of Transport (1988), "Performance of A Reinforced Earth Bridge Abutment At Stirling," *Transport And Road Research Laboratory*, Research Report No. 128.
- U. S. EPA Report No. 530-SW-85-014, 1985. Minimum technology guidance on double liner systems for landfills and surface impoundments-design, construction and installation. Washington, DC.
- Vaid, Y. P., and Negussey, D. (1988), "Preparation of Reconstituted Sand Specimens," *Advanced Triaxial Testing of Soil and Rock*, ASTM STP 977, American Society for Testing and Materials, Philadelphia, pp. 405-417.
- Vesic, A. S., Banks, D. C., and Woodward, J. M. (1965), "An Experimental Study of Dynamic Bearing Capacity of Footings on Sand," *Proceedings of the 6th International Conference on Soil Mechanics and Foundation Engineering*, Vol. 1, pp.209-249.
- White, D. M., and Holtz, R. D. (1992), "Seismic Analysis of Reinforced Slopes - A Review." *International geotechnical symposium on Earth Reinforcement Practice*, edited by Ochiai, Hayashi & Otani, Balkema, Rotterdam, pp. 311-316.
- Weiler, W. A., and Kulhawy, F. H. (1982), "Factors Affecting Stress Cell Measurements in Soil," *Journal of the Geotechnical Engineering Division*, ASCE, Vol. 108, No. GT12. pp. 1529-1548.
- Wilson-Fahmy, R. F., and Koerner, R. M. (1993), "Finite Element Modelling of Soil-Geogrid Interaction with Application to the Behaviour of Geogrids in a Pullout Loading Condition," *Geotextiles and Geomembranes*, Elsevier, Vol. 12, pp. 479-501.

Bibliography

- Wilson-Fahmy, R. F., and Koerner, R. M., and Sansone, L. J. (1994), "Experimental Behaviour of Polymeric Geogrids in Pullout," *Journal of the Geotechnical Engineering Division*, ASCE, Vol. 120, No. 4, pp. 661-667.
- Yasuda, S., Nagase, H., and Marui, H. (1992), "Cyclic Pull-out Tests of Geogrids in Soils." *International Geotechnical Symposium on Earth Reinforcement Practice*, edited by Ochiai, Hayashi & Otani, Balkema, Rotterdam, pp. 185-190.
- Yegian, M. K., and Lahlaf, A. M. (1991), "Discussion on Kettleman Hills Waste Landfill Slope Failure. I: Liner-System Properties," *Journal of Geotechnical Engineering*, ASCE, Vol. 117, pp. 643-645.
- Yegian, M. K., and Lahlaf, A. M. (1992), "Dynamic interface shear strength properties of geomembranes and geotextiles." *Journal of Geotechnical Engineering*, ASCE, Vol.118, No.(5), pp. 760-779.
- Yogarajah, I., Yeo K. C. (1994), "Finite Element Modelling of Pull-Out Tests with Load and Strain Measurements," *Geotextiles and Geomembranes*, Elsevier, Vol. 13, pp. 43-54.
- Yogendrakumar, M., Bathurst, R. J., and Finn, W. D. L. (1992), "Dynamic Response Analysis of Reinforced-Soil Retaining Wall." *Journal of Geotechnical Engineering*, ASCE, Vol.118, No. 2, pp. 1158-1167.

APPENDIX A

TECHNIQUE OF STRAIN GAUGING PLASTICS

A.1 Introduction

The development of a strain gauging technique for plastics requires that consideration be given to the mechanical, thermal and chemical properties of these polymeric materials. With regard to mechanical properties, plastics have a relatively low modulus of elasticity in comparison to metals. Consequently there is potential for large strain magnitudes, which places a demand on the capacity for elongation of a strain gauge, the adhesive, and the wiring procedures. In addition, any tendency of the strain gauge to impart an effect of local reinforcement to the test specimen must be recognized. With regard to thermal properties, polymeric materials have thermal coefficients approximately 5-10 times greater than those of metals and concrete. The thermal conductivity of plastics influences both the selection of gauge size and excitation voltage to achieve an acceptable power dissipation per unit of grid area; it also increases the difficulty of maintaining an active and dummy strain gauge at the same temperature in a variable thermal environment. With regard to chemical properties, care must be taken to avoid any reaction between the geosynthetic test specimen and those chemicals used as cleaning solvents, adhesives, and protective coatings for the gauges.

Consideration of these factors is important to the selection of a high-elongation strain gauge for measuring relatively large strains, a suitable surface preparation technique for the test specimen, compatible solvents and cleaning agents, and an adhesive to achieve a good bond within an acceptable curing time.

Appendix A

A.2 Characteristics of the Strain Gauge

The strain gauge selected for the program of laboratory testing is type EP-08-250BF-350 Option E, manufactured by the Micro-Measurements Division of Measurements Group Inc. It is selected for the following reasons:

- the EP series gauges are made of a special annealed constantan foil with a tough high elongation polyimide backing that offers high elongation capacity;
- the geometry of the gauge, defined by the gauge pattern designation 250BF and reported in Table A-1.1, fits well on the ribs of the geogrid test specimens;
- a high resistance gauge minimizes heat dissipation, for which the 350 ohm is selected;
- encapsulation of the gauge, the option E, protects the gauge circuit from damage by abrasion with the backfill sand.

Table A-1.1: Dimensions of the strain gauge

Gauge length (mm)	Overall length (mm)	Grid width (mm)	Overall width (mm)	Matrix size (mm) (L x W)
6.35	9.53	3.18	3.18	13.2 x 5.6

A.3 Strain Gauging Procedure

A.3.1 Chemicals for Surface Preparation

A 1-1-1 Trichloro-ethylene solvent is used to degrease the surface of the test specimen because of its inertness to polyethylene. The degreaser prevents embedment of contaminants in the surface of the geosynthetic specimen. A No. 400 grit paper is used to roughen the

Appendix A

surface for bonding. It is an important factor in getting a good bond between the polyamide backing of the strain gauge and the polyethylene material. The surface is then neutralized with a mild ammonia solution, which leaves it with a slightly alkaline pH. Gauge installation is performed within a few minutes of completing the surface conditioning.

A.3.2 Adhesive Selection and Preparation

M-Bond AE 10/15 adhesive was selected to obtain a high elongation capability. Resin AE (10 gram unit) with Curing Agent 10 will cure in 6 hours giving approximately 6% elongation capabilities. By extending the curing time from 24 to 48 hours at 24⁰ C, a higher elongation capability of 10% may be obtained.

A.3.3 Geosynthetic Surface Preparation

Supplies required: 1-1-1 Trichloro-ethylene degreaser, No. 400 grit sand paper, gauze sponge, compressed air, cotton swab, and M-Prep neutralizer 5.

Steps involved in surface preparation are:

1. Trim the geosynthetic test specimen to the required dimensions. Secure it on clean flat surface and mark the gauge locations. Precise alignment of the gauge with the direction of loading is important for meaningful data. (For the Stratagrid and Miragrid specimens, an additional step was used to obtain a flat surface: the strain gauge location was coated with two part 5 minute epoxy).
2. Spray the gauge location with 1-1-1 Trichloro-ethylene degreaser and wipe clean using a gauze sponge.

Appendix A

3. Use No. 400 grit sand paper to roughen up the surface, sanding first at a 45° angle to the direction of testing and then at right angles to get a pattern of cross hatches. Approximately 4 minutes of sanding is required.
4. Using compressed air, clean the gauge location to remove any small particles.
5. Neutralize the surface by wiping the location with M-Prep Neutralizer 5, a mild ammonia solution, which leaves it with an alkaline pH.
6. The gauge should be applied within 2 or 3 minutes of completing the surface preparation.

A.3.4 Gauge Preparation

Supplies required: Plexiglas frame (rectangular hollow), 1-1-1 Trichloro-ethylene degreaser, tweezers, eraser, MGJ-2 tape, and strain gauges.

Steps involved in the preparation are:

1. Clean the plexiglas frame with the 1-1-1 Trichloro-ethylene degreaser, wiping with a gauze sponge.
2. Take a small length of MJG-2 tape and tape it down on the plexiglas frame causing the tape to be exposed at the hollow portion.
3. Remove the strain gauge from its package, ensuring it is held on the edge using tweezers.

Appendix A

4. Place the gauge on to the exposed tape, aligning it parallel with the edge of the tape. Low air pressure from the compressed air supply is used to affix it firmly.
5. The gauge is now ready for transfer to the geosynthetic test specimen.

A.3.5 Application of the Gauge

Supplies required: AE 10/15 adhesive kit, gauze sponge, TFE-1 sheet, silicone pad, aluminum block, and MJG-2 tape.

Steps involved in the adhesive preparation are:

1. To prepare the adhesive mix, fill one of the calibrated droppers with Curing Agent 10 exactly to the number 10 and dispense the contents into the jar of Resin AE. Immediately cap the bottle of Curing Agent to avoid moisture absorption.
2. Thoroughly mix for 5 minutes using plastic stirring rods.
3. The pot life or working time after mixing is 15 to 20 minutes. Perform application of the gauge within the working time.
4. Discard the dropper, stirring rod and the adhesive mix after the gauge application.

Steps involved in gauge application are:

1. Lift the tape off the plexiglas frame along with the gauge and attach it to the geosynthetic at the desired gauge location, aligning the gauge in the testing direction. The tape on the side of the terminal should not be pressed firmly, but the opposite side should be.

Appendix A

2. Peel back the tape from the terminal side at an acute angle so that the tape lifts off with the gauge. Pull back the tape 3 mm further than the edge of the gauge.
3. Apply two drops of prepared adhesive (M Bond AE 10) to the geosynthetic test specimen at the gauge location and quickly lower the gauge to make contact.
4. Using the gauze sponge, apply a uniform pressure to the gauge.
5. Overlay the gauge with TFE-1 film, a silicone pad, and an aluminum block, and apply pressure using a dead weight to obtain a clamping pressure in the range 35 to 135 kPa.
6. Maintain the clamping pressure for 15 to 20 hours to obtain a reasonable elongation capability.
7. Carefully peel off the tape from the terminal side, pulling back at an angle of more than 150°.
8. The gauge is ready for soldering.

A.3.6 Gauge Soldering

Supplies required: Rosin solvent, 3-strand wires, and soldering accessories

The steps involved are:

1. Cut the 3-strand wire into desired lengths, and pass it through the stiff plastic tubing that is used to protect the wire from damage by the sand grains.
2. Solder the ends of the wires and trim to leave 2mm exposed.

Appendix A

3. Tape down the stiff tubing to the geosynthetic test specimen forming a loop of excess wire adjacent to the gauge.
4. Brush the gauge surface with rosin solvent to remove dust particles.
5. Using flux and solder, and taking care not to apply excess heat that will damage the test specimen, quickly place solder on the tabs of the gauge.
6. Solder the prepared wires to the solder on the gauge tabs.
7. Check the resistance of the gauge and its connection using an ohm-meter.
8. Clean the surface with rosin solvent to remove flux.
9. The gauge assembly is now ready for protecting.

A.3.7 Gauge Protection

Supplies required: Cellophane tape, M-coat A, TFE-1 and MJG-2tape.

The steps involved are:

1. Coat the gauge assembly with M-coat A, a polyurethane coating, placing three coats at an interval of 30 minutes.
2. Coat the exposed wires between the gauge and protective tubing as well.
3. Cover the gauge assembly with TFE-1 film, a Teflon film, and tape it down firmly using cellophane tape or MJG-2 tape.

Appendix A

A.3.8 Analysis of Strain Data

Corrections which are to be applied to the measured data are: transverse sensitivity; thermal output; gauge factor variation with temperature; Wheatstone bridge non-linearity; and gauge factor variation with strains. Considering all these factors, the measured percentage strain in a full bridge circuit is related to the change in electrical output recorded, by the following expression:

$$\% \epsilon = \left[\frac{4E_o * 100}{(F + \epsilon)E - 2 * E_o (F + \epsilon)} \right] \quad (\text{A.1})$$

where:

E_o is the output of the bridge in mV,

E is the input to the bridge in mV, =5000 mV,

F is the gauge factor supplied by the manufacturer.

APPENDIX B

Raw Data of Pullout Resistance and Strain

In this appendix, the data of pullout resistance and measured strain with pullout displacement for some monotonic displacement-controlled tests are presented.

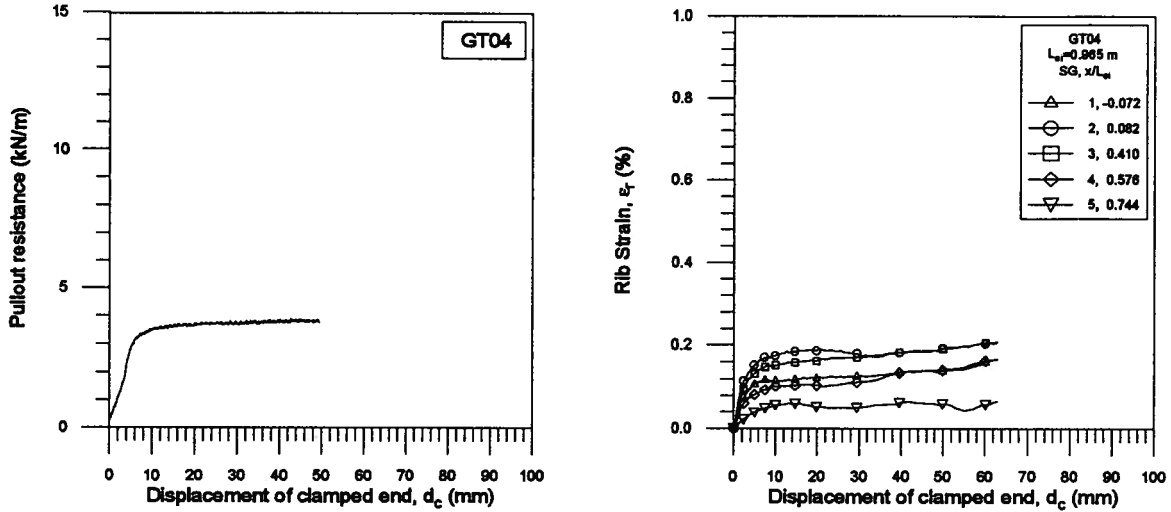


Figure B.1: Mobilization of pullout resistance and strain with pullout displacement for the Tensar grid at $\sigma_a=4$ kPa

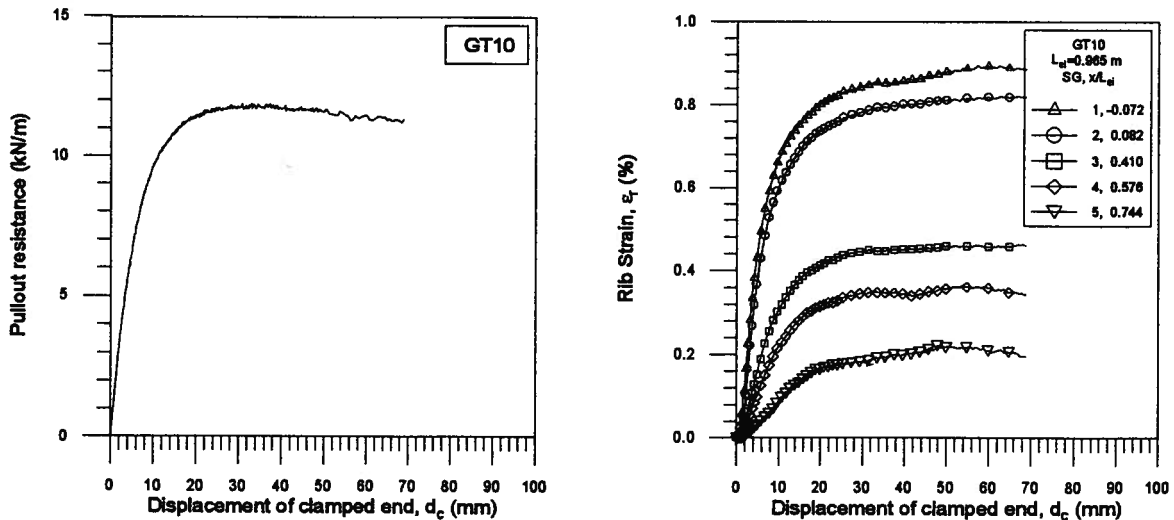


Figure B.2: Mobilization of pullout resistance and strain with pullout displacement for the Tensar grid at $\sigma_a=10$ kPa

Appendix B

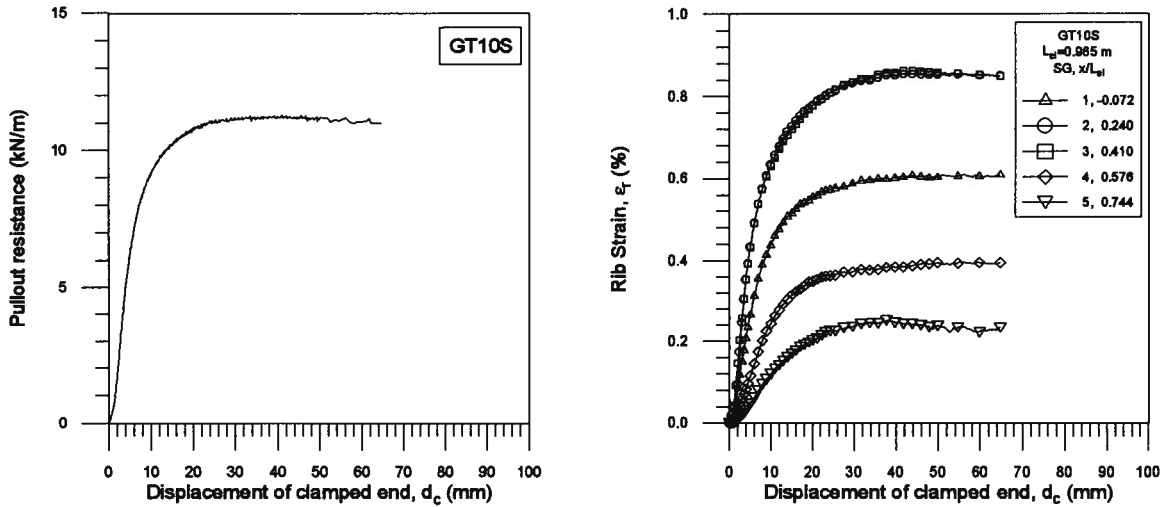


Figure B.3: Mobilization of pullout resistance and strain with pullout displacement for the Tensar grid at $\sigma_n=10$ kPa: smooth arborite front boundary

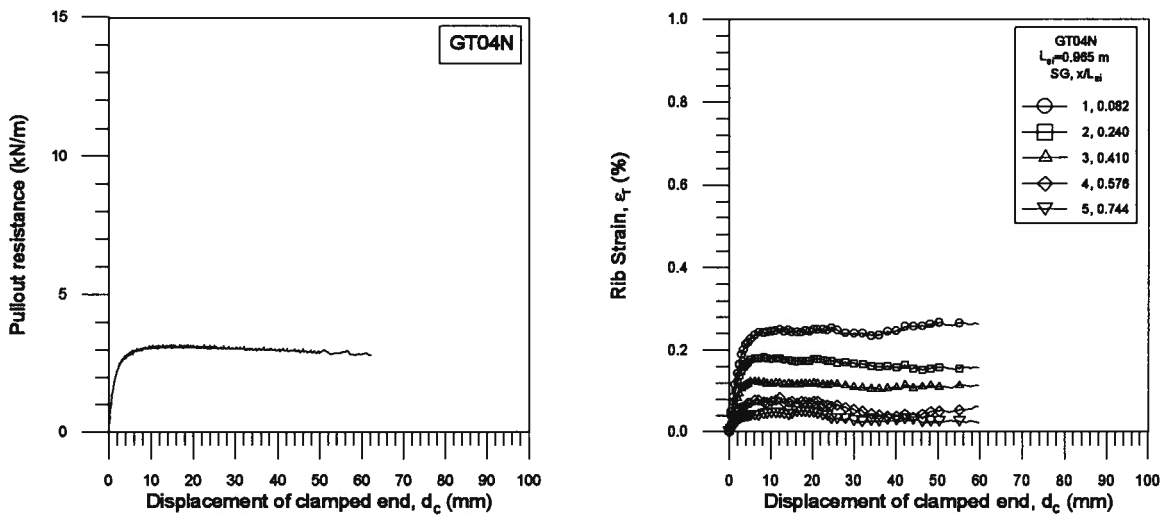


Figure B.4: Mobilisation of pullout resistance and strain with pullout displacement for the Tensar grid without bearing elements at $\sigma_n=4$ kPa

Appendix B

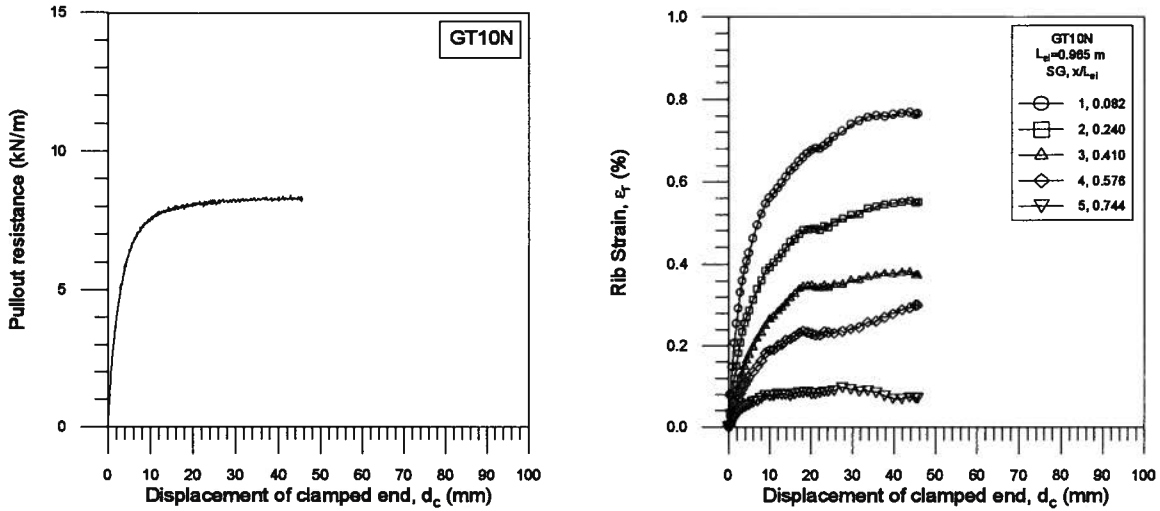


Figure B.5: Mobilisation of pullout resistance and strain with pullout displacement for the Tensar grid without bearing elements at $\sigma_n=10$ kPa

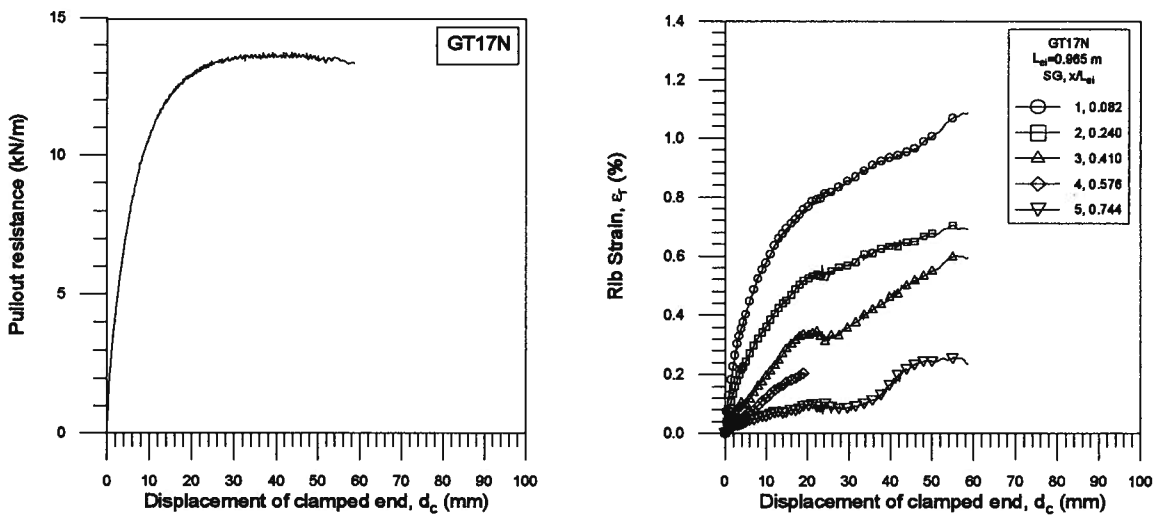


Figure B.6: Mobilisation of pullout resistance and strain with pullout displacement for the Tensar grid without bearing elements at $\sigma_n=17$ kPa

Appendix B

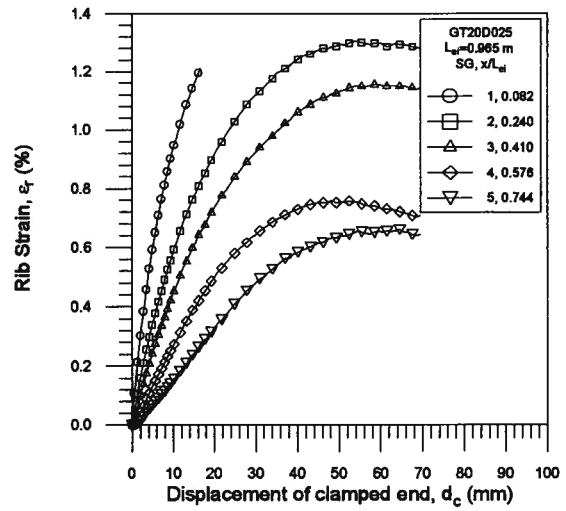
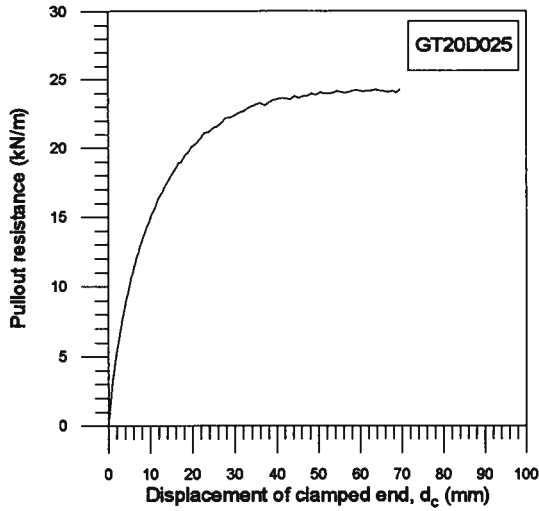


Figure B.7: Mobilisation of pullout resistance and strain with pullout displacement for the Tensar grid without bearing elements at $\sigma_v=20$ kPa and $r_d=0.25$ mm/min

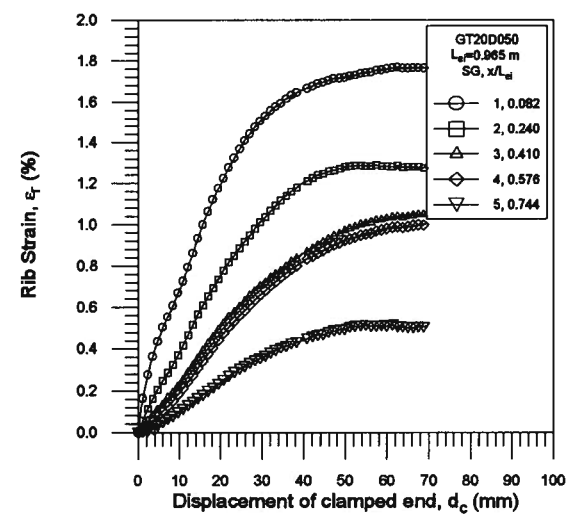
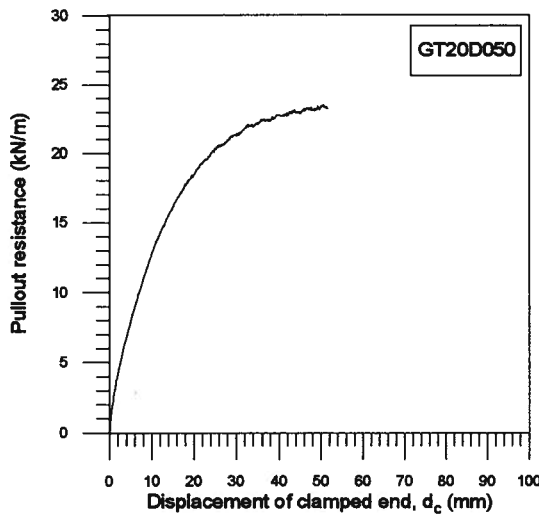


Figure B.8: Mobilisation of pullout resistance and strain with pullout displacement for the Tensar grid without bearing elements at $\sigma_v=20$ kPa and $r_d=0.50$ mm/min

Appendix B

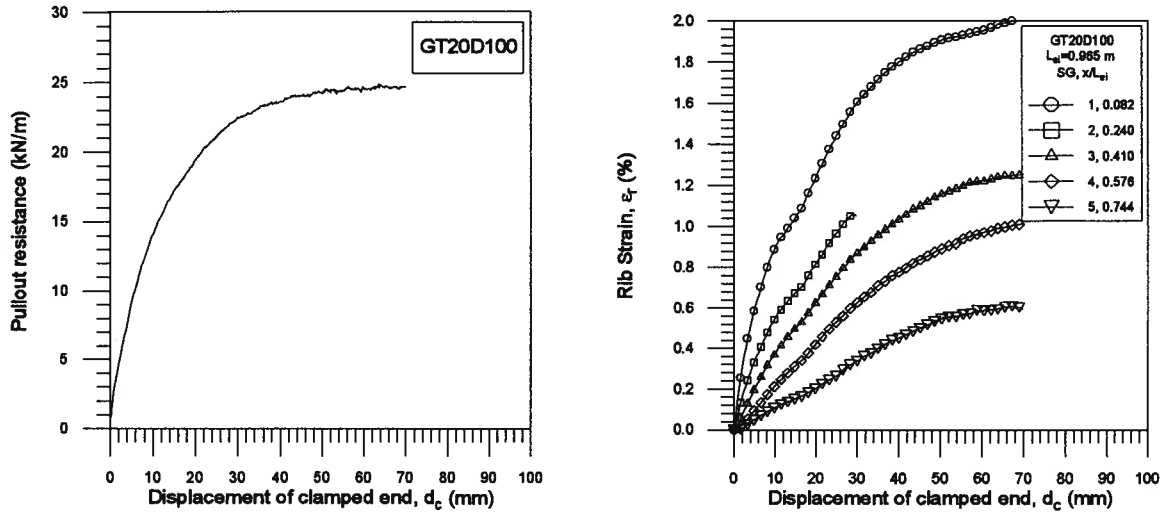


Figure B.9: Mobilisation of pullout resistance and strain with pullout displacement for the Tensar grid without bearing elements at $\sigma_v=20$ kPa and $r_d=1.00$ mm/min

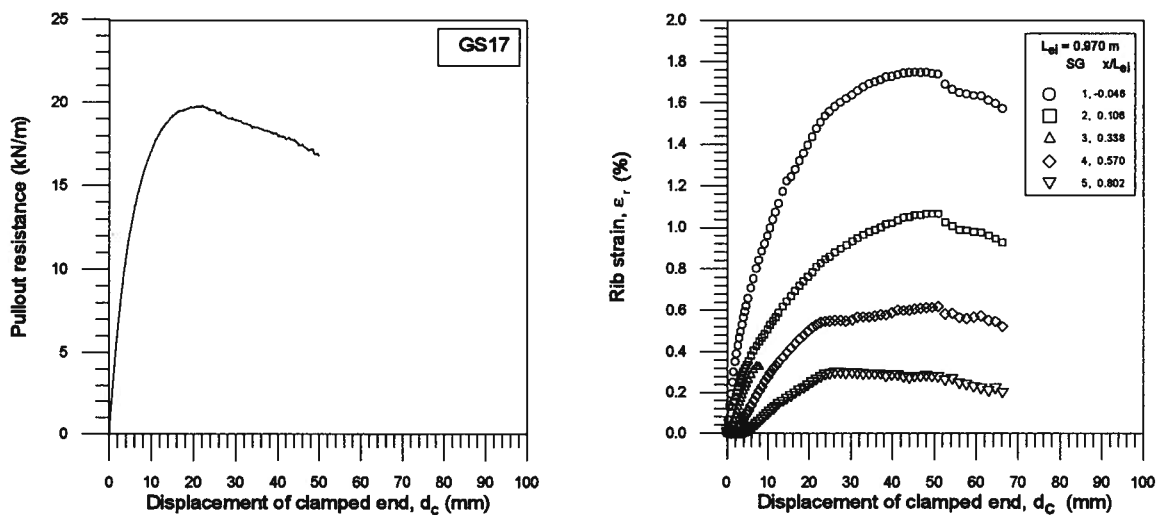


Figure B.10: Mobilisation of pullout resistance and strain with pullout displacement for the Stratagrid without bearing elements at $\sigma_v=17$ kPa

The displacement response of cyclic pullout tests which are not shown in the main body of the thesis are presented below.

Appendix B

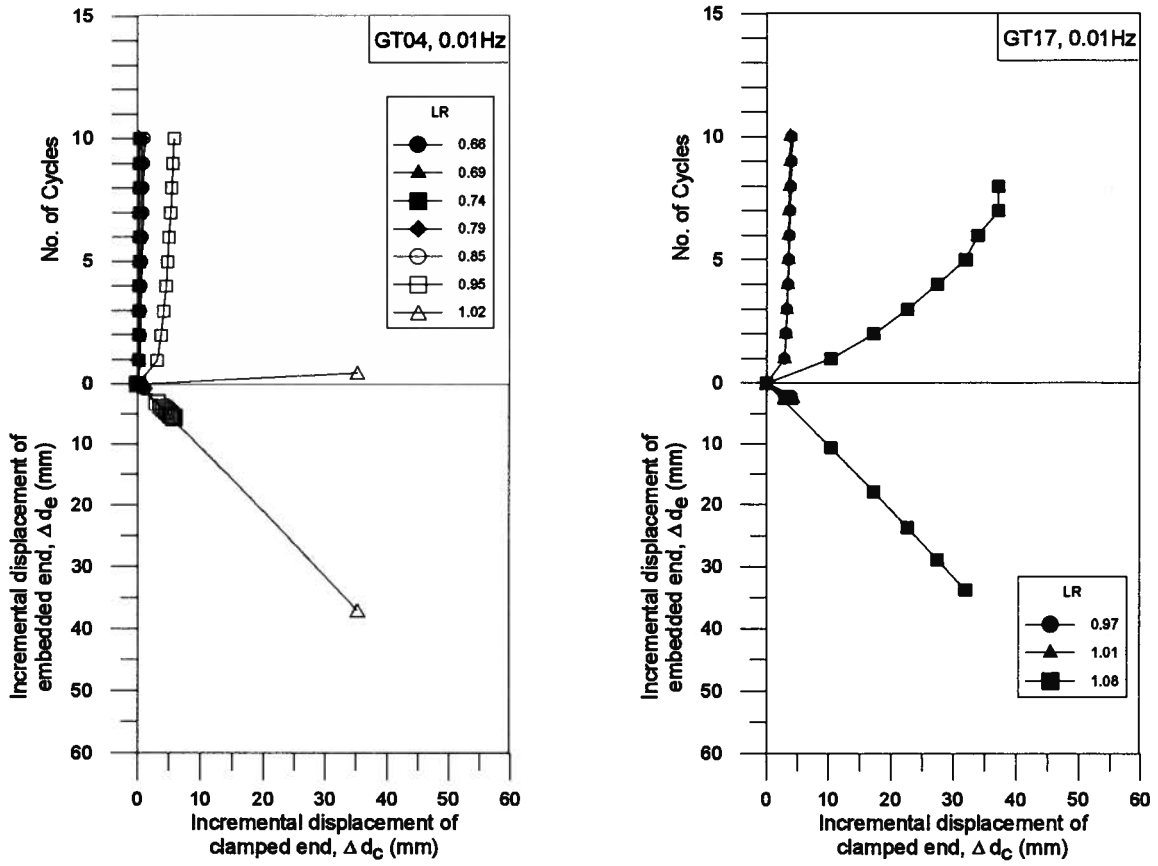


Figure B.11: Relationship between Δd_c and Δd_e for Tensar grid at $\sigma_v=4$ and 17 kPa

Appendix B

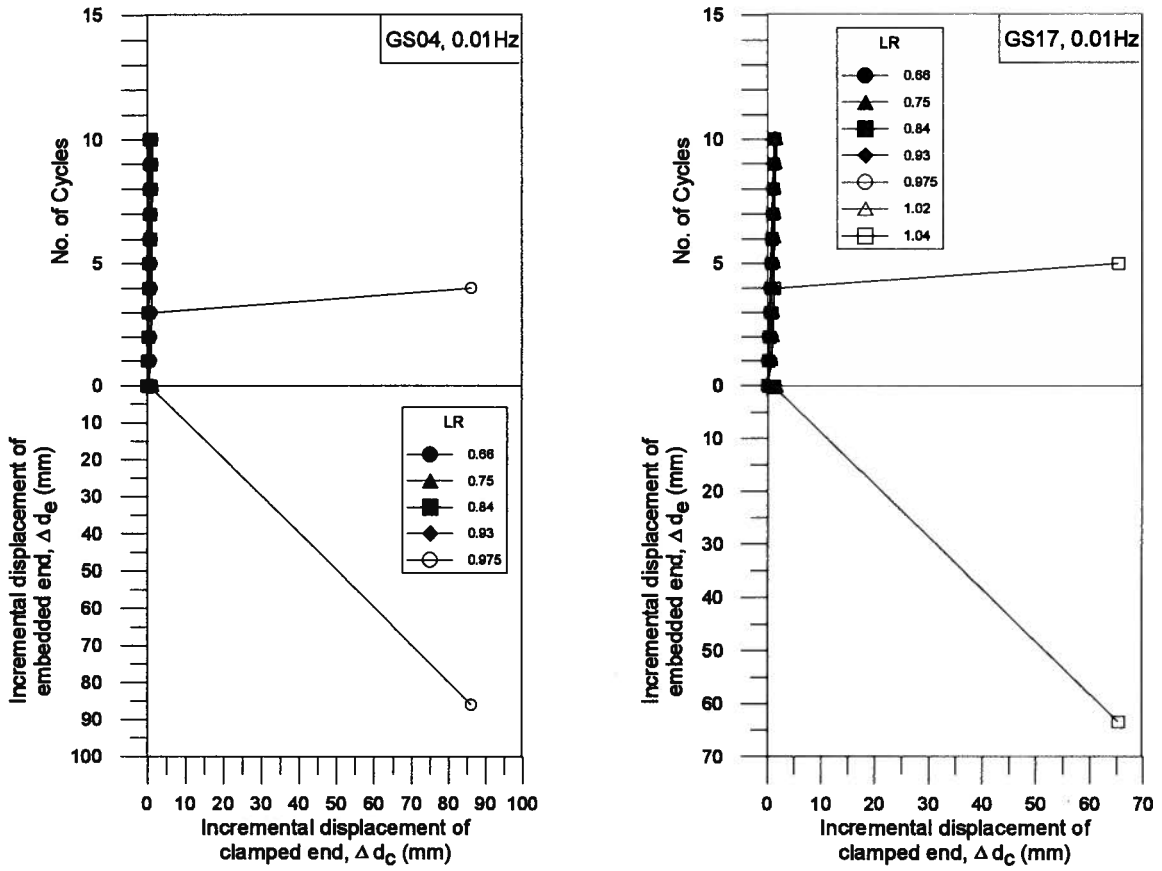


Figure B.12: Relationship between Δd_c and Δd_e for Stratagrid at $\sigma_n=4$ and 17 kPa